JRC Technical Notes

STUDIES OF ELECTROCHEMICAL CORROSION PROCESSES OF UO_2 AND MIXED OXIDE FUELS IN AQUEOUS SOLUTIONS IN THE VIEW OF FINAL STORAGE OF SPENT NUCLEAR FUEL

Cătălin – Gabriel ALECU

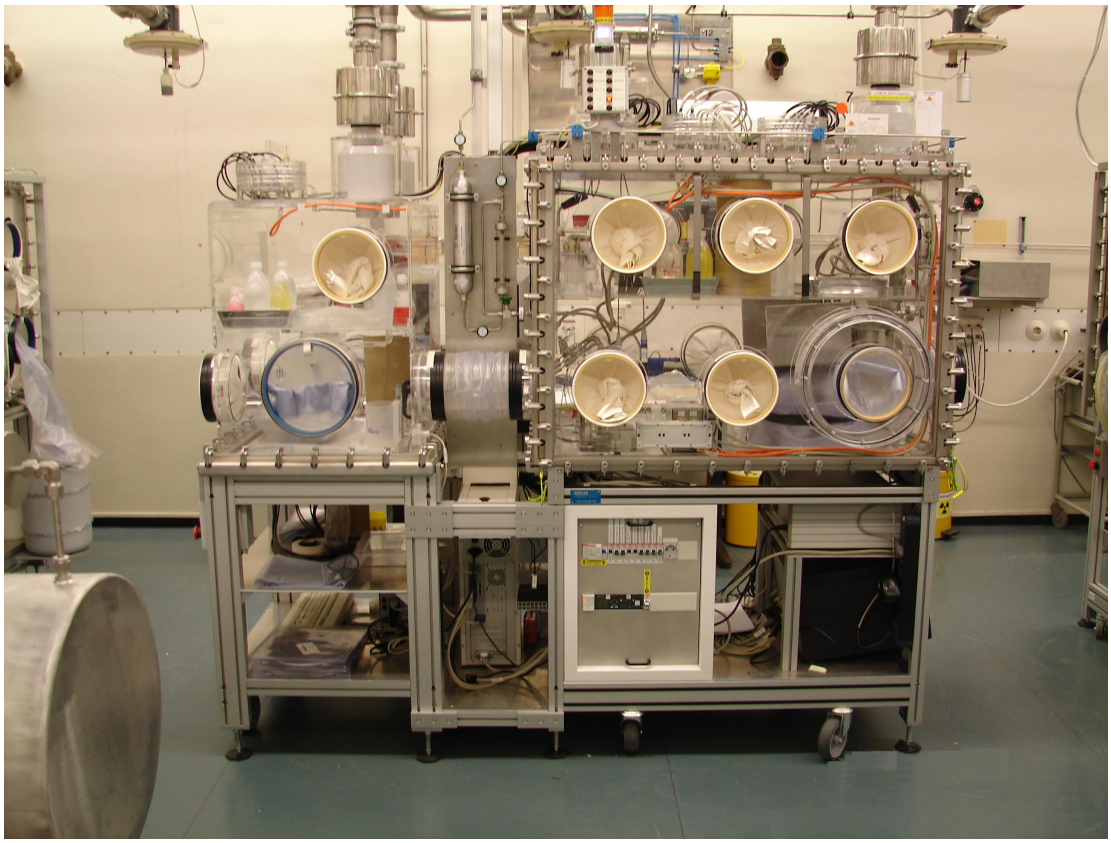

JRC-ITU-TN-2008/55

JRC
EUROPEAN COMMISSION

itu
Institute for Transuranium Elements

The mission of ITU is to provide the scientific foundation for the protection of the European citizen against risks associated with the handling and storage of highly radioactive material. ITU's prime objectives are to serve as a reference centre for basic actinide research, to contribute to an effective safety and safeguards system for the nuclear fuel cycle, and to study technological and medical applications of radionuclides/actinides.

Report No: JRC-ITU-TN-2008/55
Classification: not classified
Type of Report: Doctoral thesis
Unit: Nuclear Chemistry Unit
Action No: 51102

	Name	Date	Signature
Reviewed by the Project Coordinator	D.H. Wegen		
Approved by the Project Leader	V.V. Rondinella		
Approved by the Head of Unit	J.-P. Glatz		
Released by the Director	Th. Fanghänel		

European Commission
Joint Research Centre
Institute for Transuranium Elements

Contact information
Address: P.O. Box 2340, D-76125 Karlsruhe, Federal Republic of Germany
E-mail: catalin_gabriel.alecu@yahoo.com or detlef.wegen@ec.europa.eu
Tel.: +49 (0)7247 951 364
Fax: +49 (0)7247 951 99640

http://itu.jrc.ec.europa.eu/
http://www.jrc.ec.europa.eu/

This research work was carried out in the Nuclear Chemistry Unit of the Institute for Transuranium Elements (ITU) at the European Commission, Joint Research Centre in Karlsruhe, Federal Republic of Germany, from 1st of July 2004 until 15th of April 2008 with a grant from the European Commission.

Scientific supervisor:

Dr. Detlef Wegen (European Commission, Joint Research Centre, Institute for Transuranium Elements)

The defence of the doctoral dissertation will be held at the Combined Faculties of the Natural Sciences and Mathematics of the Ruperto-Carola University of Heidelberg, Federal Republic of Germany on 7th of November 2008.

Examination Commission:

Prof. Dr. Thomas Fanghänel – *chairman* and *referee* (Ruperto-Carola University of Heidelberg, Faculty of Chemistry and Earth Sciences, Institute of Physical Chemistry and European Commission, Joint Research Centre, Institute for Transuranium Elements)

Prof. Dr. Peter Hess – *referee* (Ruperto-Carola University of Heidelberg, Faculty of Chemistry and Earth Sciences, Institute of Physical Chemistry, Physical Chemistry)

Prof. Dr. Hans-Jörg Himmel – *examiner* (Ruperto-Carola University of Heidelberg, Faculty of Chemistry and Earth Sciences, Institute of Inorganic Chemistry)

Prof. Dr. Eva Gutheil – *examiner* (Ruperto-Carola University of Heidelberg, Faculty of Chemistry and Earth Sciences, Institute of Physical Chemistry, Interdisciplinary Centre for Scientific Computing)

STUDIES OF ELECTROCHEMICAL CORROSION PROCESSES OF UO_2 AND MIXED OXIDE FUELS IN AQUEOUS SOLUTIONS IN THE VIEW OF FINAL STORAGE OF SPENT NUCLEAR FUEL

Keywords: Uranium dioxide, electrochemistry, corrosion, radiolysis, leaching, irradiation, Impedance Spectroscopy, polarisation curve

The possible release of toxic and radioactive species from spent nuclear fuel in contact with water in a deep geological repository is expected to depend mainly on the rate of dissolution of the UO_2 matrix. At the depth of the repository very low oxygen concentrations are expected. Moreover, large amounts of hydrogen are expected to be generated from the corrosion of iron containing canisters and containers. In this reducing groundwater environment UO_2 has very low solubility. However, radiolysis of the ground water will produce reactive radicals and molecular products and can thereby alter the redox conditions. In this work different electrochemical techniques were used to study the corrosion behaviour of UO_2 based materials in aqueous solutions in anoxic and reducing conditions. The possible influence of hydrogen on the corrosion mechanism of UO_2 was investigated. In order to study the importance of the alpha activity level on the corrosion of the matrix, UO_2 electrode samples doped with different concentrations of short-lived alpha emitters were used. In the frame of ACTINET Network of Excellence the collaboration between Institute for Transuranium Elements (ITU) in Karlsruhe, Germany and The Centre for Studies and Research by Irradiation (CERI) in Orléans, France made possible the use of a cyclotron generated He^{2+} beam to simulate high levels of alpha activities. Impedance Spectroscopy, together with potentiostatic polarization and cyclic voltammetry measurements were used on a variety of materials, ranging from depleted UO_2 to 10% ^{233}U doped UO_2. A comparison was made between the electrochemical results and the results provided by the solution analysis and surface characterization. The good concordance of the results shows that the electrochemical techniques can be taken into consideration for the safety assessment of the final spent nuclear fuel repository.

ELEKTROCHEMISCHE UNTERSUCHUNG DER KORROSIONSPROZESSE VON UO_2 UND MISCHOXID BRENSTOFFE IN WÄSSRIGE LÖSUNGEN ANGESICHTS DER ENDLAGERUNG VON ABGEBRANNTEM KERNBRENSTOFF

Schlagworten: Urandioxid, Elektrochemie, Korrosion, Radiolyse, Auslaugung, Bestrahlung, Impedanzspektroskopie, Polarisationskurve

Es wird erwartet, dass eine mögliche Freisetzung von giftigen und radioaktiven Substanzen aus abgebrannten Kernbrennstoffen in Kontakt mit Wasser in einem tiefen geologischen Endlager hauptsächlich von der Auflösungsgeschwindigkeit der UO_2-Matrix abhängt. Die Sauerstoffkonzentration in einem solchen Endlager kann als außerordentlich gering angenommen werden. Ferner werden sich große Mengen an Wasserstoff durch die Korrosion von eisenhaltigen Behältern und Kokillen bilden. Unter solchen reduzierenden Bedingungen hat UO_2 eine sehr geringe Löslichkeit in aquatischen Systemen. Allerdings führt die Radiolyse des Grundwassers zur Bildung reaktiver Radikale und Moleküle, die die Redox-Bedingungen beeinflussen können. In dieser Arbeit werden verschiedene elektrochemische Messtechniken eingesetzt, um das Korrosionsverhalten von UO_2 in wässerigen Lösungen unter anoxischen und reduzierenden Bedingungen zu studieren. Ein möglicher Einfluss des Wasserstoffes auf den Korrosionsmechanismus von UO_2 wurde untersucht. Um den Einfluss des α-Aktivitätsniveaus auf die Korrosion der UO_2-Matrix zu untersuchen, wurden UO_2 Proben mit verschiedenen Konzentrationen an kurzlebigen α-Strahlern dotiert. Im Rahmen des ACTINET Network of Excellence machte die Zusammenarbeit des Instituts für Transurane (ITU) in Karlsruhe mit dem Centre for Studies and Research by Irradiation (CERI) in Orléans in Frankreich es möglich hohe α-Aktivitätsniveaus mit einem im Zyklotron erzeugten He^{2+}-Strahl zu simulieren. Impedanzspektroskopie wurde zusammen mit potentiostatischer Polarisation und Zyklovoltammetrie dazu benutzt die verschiedenen Materialien (abgereichertes UO_2, bis zu mit 10% ^{233}U dotiertem UO_2) zu untersuchen. Ergebnisse aus elektrochemischen Messungen wurden mit denen aus Lösungsanalytik und aus Oberflächenuntersuchungen gewonnenen verglichen. Die gute Übereinstimmung zeigt, dass elektrochemische Messtechniken für Sicherheitsbeurteilungen eines nuklearen Endlagers ebenfalls einen wertvollen Beitrag leisten können.

Acknowledgments

This work was realised at the Institute for Transuranium Elements in Karlsruhe under the scientific guidance of Prof. Thomas Fanghänel, Director of the Institute and Professor at University of Heidelberg. I am grateful and deeply honoured to have been granted the chance to make the doctoral thesis at such prestigious institutions and to be guided by a very well known personality in the field of nuclear chemistry. I am also grateful to Prof. Peter Hess for accepting to be examiner for this thesis.

I want to thank especially to Dr. Detlef Wegen for the direct supervision of the experimental work and for the long discussions about electrochemistry and not only. I will forever be grateful to Dr. Eric Mendes for the support and assistance during my last months at ITU. I will also never forget our nights spent in the laboratory near the cyclotron in Orléans. I am grateful to Dr. David Bottomley for all the nice discussions we had and also for the help and support he always offered to me. To Dr. Alice Seibert I am grateful for the advices and suggestions she gave me about electrochemistry.

I have to thank to the person responsible for starting my doctoral work at ITU, Dr. Claudio Ronchi for the strong support and kindness. My kindest regards go to Dr. Jean-Paul Glatz, Head of the Hot Cell Technology Unit and later of Nuclear Chemistry Unit. My special thanks are given also to the new Head of Hot Cell Technology Unit, Dr. Vincenzo Rondinella. I was honoured and I consider myself very lucky for having the possibility to meet Dr. Kastriot Spahiu from SKB. I learned a lot of things from him and for that I thank him very much.

I am very grateful to Dr. Marcus Amme for the very nice discussions we had, for the suggestions and support. One person I will always admire for being a true model for the term "team work". This person is Dr. Paul Carbol, together with whom we shared the office in my first year at ITU. I will forever remember the time we spent working for the hydrogen peroxide determinations and for the alpha spectrometry. I want to thank also to Patrik Fors and Daniel Magnusson for the very nice discussions we had.

My special attention goes to Dr. Joaquin Cobos-Sabate and Dr. Marin Ayranov for the ICP-OES analysis and not only. I want to thank you both for the great discussion we had. I have to mention Stefaan van Winckel, Mariangela Cardinale and Brian Lynch for the ICP-MS analysis. I am very grateful to Dr. Thierry Wiss, Hartmunt Thiele and Bert Cremer for the SEM pictures. Also I want thank to another two wonderful Swedish people, Birgit Christiansen and Rikard Malmbeck for your kindness and understanding. My special regards go to Frank Benneter and Mathias Uhlig for the help and support I was provided by both workshops and also to Markus Ernstberger

During the experiments we made at the cyclotron I had the opportunity to meet some great and wonderful people at CERI, in France. First of all I want to thank to Mrs. Catherine Corbel for offering me the possibility to run the experiments at the cyclotron and also for the great support. I have to mention Mr. Dominique Simon to whom I am grateful for the very good suggestions about impedance spectroscopy. My kindest regards to Mr. Gilbert Blondiaux for offering me the whole support to make the experiments even at late hours.

One very important person that I could not forget to mention is Mr. Sébastien Ancelin who was offering me his best support and not leaving me alone during the never ending experiments. Of course I have to mention a lot of wonderful people from CERI without whom I would have never managed to make a single irradiation. My regards go to Mr. Jean Pascal Rivierre, Christian Lecureux, and Julien Lucas who stayed late into the night to keep the cyclotron running for our irradiation experiments.

I want to thank to all my colleagues for the great time I had at ITU, for being very friendly and supportive. I want to thank to my class mates from the German course and especially to Roberto Tedeschi. I want to thank also to all the members from the basketball club for the great time we spent playing this wonderful sport. I have to mention especially Mr. Jean-Luc Arnoult and thank him for the good mood he brings in every day work and for being a spring of joy and positive energy for all the people around.

I saved for the end some very important persons without whom I would have never achieved anything in my life: my family. My dear beloved parents I am grateful to you for raising me for so many years and always doing all the best you could for my brother and I.

The last person I want to thank is also the most important to me. For being always by my side in the good and in the bad moments, for giving me strength and faith when they were fading, for masking a lot of sacrifice so I could get here, for being the most wonderful miracle in my life I dedicate this work entirely to you, my greatest love of all, my wife and my soul mate, Florentina.

Table of content

1. Introduction and objectives

European projects for the direct disposal of spent nuclear fuel as waste in geological repositories consider that the environment after a short oxic post-closure phase becomes reducing. Reducing environments have shown to favour the stability of natural uraninite minerals for millions of years. Since the bulk part of the matrix of the irradiated fuel is still UO_2 it would be expected, in principle, the same high stability from the matrix (not necessarily for the grain boundaries) of spent fuel. However, the radiation field created by the α-, β- and γ-decay of the radionuclide inventory of this material may establish locally oxidising conditions at the fuel surface due to the radiolytic decomposition of the groundwater and the production of oxidising radicals and molecules. The effect of radiation-generated oxidising conditions on the corrosion of the spent fuel slowly decreases with time.

This poses the principal problem in the experimental testing of long term spent fuel performance: the spent nuclear fuel samples available today are not representative of aged fuel after hundreds or thousands of years of storage in two aspects. Firstly, the decay of fission products and actinides will result in a change of fuel composition; the α-decays will produce increasing amount of He, and also cause the accumulation of micro-structural defects at low temperature, at which less defect recovery occurs than during reactor irradiation. This will alter properties and parameters of the fuel such as thermal conductivity, lattice parameter, or hardness over long time intervals. Secondly, another consequence of the decay process will be the disappearance of the short-lived radionuclides which account for almost all of the β- and γ-decays dominating the activity of the "young" spent fuel available nowadays. As a result, already after a few hundred years of storage, α-decays will dominate the radiation field in and around the spent nuclear fuel.

It is not expected that spent nuclear fuel in a geologic repository will be exposed to groundwater before storage times in the order of a thousand years have elapsed. Upon exposure to ground water, a key factor in determining the dissolution behaviour of the spent fuel exposed to groundwater is the water radiolysis in a film approximately 40 to 50μm thick at the surface of the fuel [1]. This is caused by the α-radiation. The α-particles have high energy, in the range of 5 to 6MeV, but during their travelling path through the water, they lose this energy. One α-particle produces the ionisation of about 50000 water molecules [2]. As an example, in water, 1MeV α-particles lose 190eV/nm [3, 4, 5]. So, the damage inflicted by the α-radiation is high over a small travelling path. Radicals and molecular species radiolytically produced near the fuel surface can oxidise the fuel matrix, thus enhancing its dissolution, in spite of the nominally reducing conditions, which characterise the near field environment of the repository.

The work during the doctoral period was carried out at the Institute for Transuranium Elements in Karlsruhe, Germany. This institute is part of the European Commission's Directorate General – Joint Research Centre. UO_2 containing different fractions of short-lived α-emitters, the so-called α-doped UO_2, simulate the level of activity of spent fuel after different storage times, and can be used to study the effects of radiolysis on the corrosion behaviour of UO_2 matrix exposed to groundwater in a geologic repository.

As short-lived α-emitters, U-233 and Pu-238 are used. The doping range is between 1 to 10% for U-233 and from 0.1 to 1% for Pu-238. In figure 1.1 [6, 7], the α-activity of spent PWR and MOX fuels as a function of time is presented.

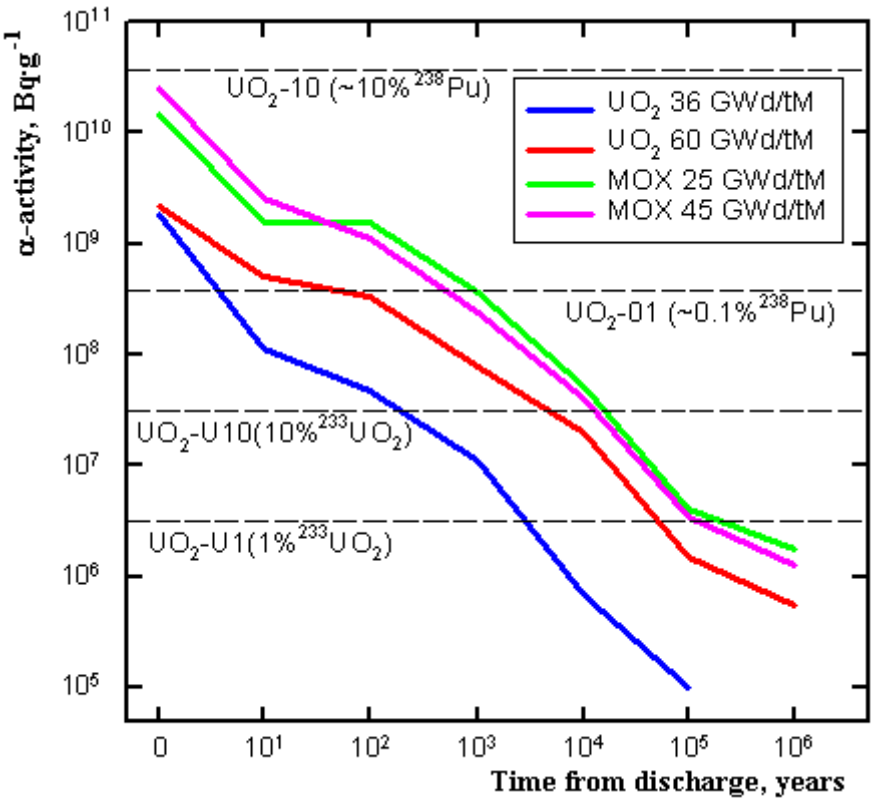

Figure 1.1 Time variation for α-activity of spent PWR and MOX fuels. The horizontal lines indicate the activity of the α-doped UO_2 prepared for the experiments (their activity can be assumed to be constant during the timeframe of the project)

As a result of the water radiolysis by α-radiation and of the container corrosion, large amounts of hydrogen are produced. The consequence is the formation of a more reducing environment that prevents the UO_2 matrix corrosion [8, 9, 10].

This work intends to carry out electrochemical examination of irradiated and non-irradiated UO_2 and MOX fuel corrosion under waste repository conditions. The aims are the determination of the influence of radiolysis, the hydrogen effect and to better understand the behaviour of plutonium. Another important aspect is the comparison between the electrochemical data and the data derived from the solution analysis in order to verify the occurrence of precipitation reactions.

In the frame of the ACTINET 6 Network of Excellence the experience of CNRS-CERI on beam irradiation and UO_2 target preparation was combined with the expertise of ITU on UO_2 electrochemistry and data evaluation. An important part of this work was made in the frame of this collaboration.

The spent nuclear fuel contains fission products which decay under emission of α-particles. The effect of these α-particles on alteration processes occurring at the surface of UO_2 as surrogate for spent fuel is to be investigated. The α-particles are produced at CNRS-CERI by means of a He^{2+} beam. In a repository the α-activity level is not constant. It varies with time. This behaviour is simulated by using different He^{2+} beam fluxes representing the α-activity levels of spent fuel after different storage times.

The objective of these measurements is to better understand the influence of the α-particles on the corrosion of UO_2 matrix. The measurements are to be performed both in anoxic and reducing conditions in order to evaluate the influence of the oxidative and reducing conditions on the corrosion rate of UO_2.

The various electrochemical techniques will be used to investigate the dissolution or corrosion of fuel pellets or pieces under non-oxidising (Ar) or reducing (Ar/H_2) atmospheres in simulated groundwater solutions and to determine the effects of irradiation on fuel dissolution/corrosion mechanisms.

On the solid/solution interface investigations will be conducted using the following techniques:

- Electrochemical Impedance Spectroscopy (EIS)
  - Electrical properties
  - Corrosion behaviour (Polarisation resistance)
  - Processes (surface film, diffusion, etc.)
- Other electrochemical techniques
  - Tafel analysis (corrosion kinetics)
  - Corrosion potential (E_{corr})

The investigations in solution comprise:

- Solution analysis:
  - ICP-MS
  - ICP-OES
- Online monitoring
  - E_h, *p*H, O_2 concentration, E_{corr}
- Comparison of results with those resulted from the electrochemical method
  - Dissolution/precipitation
  - Mass balance

The surface of the solid samples will be analysed by the following methods

- Optical Microscopy:
  - Quantification of surface defects (cracks, pores, etc.) and fuel structure (grain size, grain boundaries etc.)
- Scanning Electron Microscopy (SEM) coupled with Elemental Dispersion X-ray Spectroscopy (EDX)
  - Surface alteration
  - Secondary phases
  - Onset of corrosion (localised attack)

In order to fulfil the intended activities, a new glove box was set-up, equipped and commissioned during the doctoral work. Two electrochemical stations, IM6 (Zahner Elektrik), were used one for the experiments in the glove box and the other one for the experiments the cyclotron.

2. Theoretical aspects and literature review

2.1. Electrochemistry

2.1.1. Thermodynamics

2.1.1.1. Potentials and electrodes

Electrochemical reactions are charge transfer reactions taking place on the interface of two phases.

The interface represents the separation surface of two phases.

Inter-phases are zones on each side o the interface, inside of which the properties are different then the ones inside the phases.

If the two phases placed in contact contain mobile charges (electrons or ions) then, as a consequence of their interaction, in the interface area a rearrangement of the electrically charged particles occurs, a new structure being formed in this area. The interface is loaded with equally and opposite sign charges, q_α and q_β, like a flat capacitor, with the plates situated in the two phases. Consequently, an electrochemical double layer (EDL) is formed on the interface, generating a difference of potential on the interface (the so-called "electrode potential of the interface").

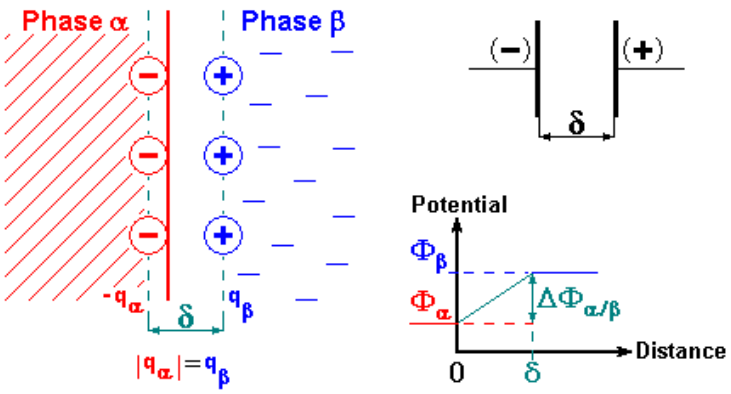

Fig. 2.1 Excess charging of the phases and the electrode potential of the interface

A phase containing mobile charges is characterised by an electrostatic potential called "internal potential" or "galvanic potential" and it is noted as Φ.

Internal potential – effectuated work to bring the elementary positive charge, from infinite, uncharged vacuum, to the interior of the phase.

Internal potential has two components:

- external potential (Volta potential) – noted with ψ, it represents the effectuated work for bringing the elementary positive charge q_α from infinite, uncharged vacuum, to a pointed situated in the vicinity of the phase (at the distance *r* from the phase), but outside the interaction with it; it is determined by the existence of a phase charging excess

$$\Psi_\alpha = \frac{q_\alpha}{r} \text{ in vacuum or } \Psi_\alpha = \frac{q_\alpha}{r \cdot D} \text{ in a medium with dielectric constant D} \qquad (2.1)$$

- surface potential – noted with χ, it represents the effectuated work for introducing the elementary positive charge from outside to the interior of the phase; it is determined by the existence of a dipoles layer on the phase surface

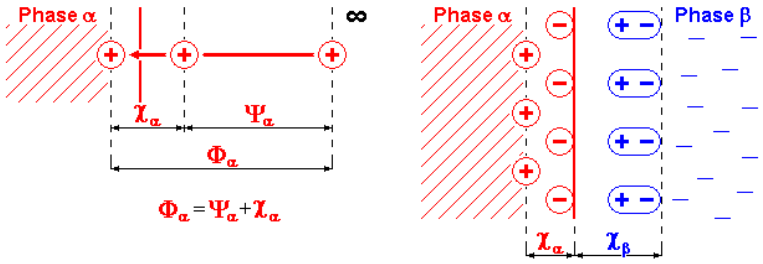

Fig. 2.2 Internal potential for one phase (left) and surface potentials for two phases in contact (right)

Internal potentials are very important for defining of the electrode potential. Absolute electrode potential is given by the difference of the internal potentials of phases that constitute the electrode:

$$\Delta\Phi_{\alpha/\beta} = \Phi_\alpha - \Phi_\beta = (\Psi_\alpha + \chi_\alpha) - (\Psi_\beta + \chi_\beta) = (\Psi_\alpha - \Psi_\beta) + (\chi_\alpha - \chi_\beta) = \Delta\Psi_{\alpha/\beta} + \Delta\chi_{\alpha/\beta} \quad (2.2)$$

The external potential, $\Delta\psi_{\alpha/\beta}$, can be experimentally determined but the surface potential, $\Delta\chi_{\alpha/\beta}$, can not be either experimentally determined or theoretically calculated. This means that also the absolute electrode potential, $\Delta\Phi_{\alpha/\beta}$, can not be known or experimentally determined. In practice, relative electrode potentials are used, being measured in reference to an arbitrary chosen zero value.

2.1.1.2. Equilibrium of the electrochemical systems

In the chemical systems, the equilibrium condition requests that the chemical free enthalpy variation to be null:

$$\Delta G = 0 \quad (2.3)$$

A chemical reaction:

$$\nu_1 S_1 + \nu_2 S_2 + ... + \nu_r S_r \rightleftarrows \nu_{r+1} S_{r+1} + \nu_{r+2} S_{r+2} + ... + \nu_{r+p} S_{r+p} \quad (2.4)$$

can also be represented as:

$$\sum_{i=1}^{r+p} (\nu_i \cdot S_i) = 0, \quad \begin{cases} i = \overline{1,r} < 0 \\ i = \overline{r,r+p} > 0 \end{cases} \quad (2.5)$$

where: - ν_i – stoichiometric coefficient of the substance *i*
- S_i – substance *i*
- r – number of reactants
- p – number of products

Chemical free enthalpy variation is given by the relation:

$$\Delta G = \sum_{i=1}^{r+p} (\nu_i \cdot \mu_i), \quad \begin{cases} i = \overline{1,r} < 0 \\ i = \overline{r,r+p} > 0 \end{cases} \quad (2.6)$$

where μ_i is chemical potential of the substance *i*.

The chemical potential represents the chemical work effectuated for transferring 1 mole of substance inside a solution and it is expressed by the relation:

$$\mu_i = \mu_i^0 + R \cdot T \cdot \ln a_i \tag{2.7}$$

where: - μ^0_i – standard chemical potential of the substance *i*, in $J \cdot mol^{-1}$
- a_i – activity of the substance *i*, in $mol \cdot L^{-1}$
- R – molar gas constant, $8.31 J \cdot mol^{-1} \cdot K^{-1}$
- T – absolute temperature of the chemical system, in K

The free enthalpy variation for a general chemical reaction is:

$$\Delta G = -RT \cdot \ln K \tag{2.8}$$

where K represents the reaction constant defined by the relation:

$$K = \frac{\prod_{i=r+1}^{r+p} a_i^{\nu_i}}{\prod_{i=1}^{r} a_i^{\nu_i}} \tag{2.9}$$

For the electrochemical systems, there is also an electrical energy not just the chemical energy. Because of this, the electrochemical free enthalpy, $\overline{G}$, was introduced, defined by the relation:

$$\overline{G} = G + q \cdot \Phi \tag{2.10}$$

where: - Φ – electrode potential;
- q – corresponding charge for one mole of substance implicated in the reaction

$$q = \pm z \cdot F \tag{2.11}$$

where: - z – number of charges
- F – Faraday constant, 96485C

So, the variation of electrochemical free enthalpy for an electrochemical system is:

$$\Delta \overline{G} = \Delta G + z \cdot F \cdot \Delta \Phi \tag{2.12}$$

The equilibrium condition for an electrochemical system is:

$$\Delta \overline{G} = 0 \tag{2.13}$$

from this resulting the equilibrium electrode potential value:

$$\Delta \Phi_e = -\frac{\Delta G}{z \cdot F} \tag{2.14}$$

or rearranged the free enthalpy variation can be deduced:

$$\Delta G = -z \cdot F \cdot \Delta \Phi_e \tag{2.15}$$

In 1929, the electrochemical potential, $\overline{\mu_i}$, was introduced. It represents the chemical and electrical work effectuated for transferring a charged particle inside a charged phase. The equilibrium condition of an electrochemical system implies that the electrochemical potential gradient is null:

$$\frac{d\overline{\mu_i}}{dx} = 0 \tag{2.16}$$

This means that the electrochemical potential of the two phases forming the electrode must be equal:

$$\left(\overline{\mu_i}\right)_\alpha = \left(\overline{\mu_i}\right)_\beta \tag{2.17}$$

2.1.1.3. Half-cells and Nernst equation

A general redox reaction (electrode reaction) has the form:

$$\nu_{Ox} Ox + z\, e^- \rightleftarrows \nu_{Red} Red \tag{2.18}$$

where: - Ox – oxidised form
- Red – reduced form

Taking into consideration the equations above, for the reduction reaction of the same chemical specie the equilibrium electrode potential is given by the equation:

$$\Delta\Phi_e = \Delta\Phi^0 + \frac{R\cdot T}{z\cdot F}\cdot \ln\frac{a_{Ox}^{\nu_{Ox}}}{a_{Red}^{\nu_{Red}}} \tag{2.19}$$

which is known as Nernst equation. The term $\Delta\Phi^0$ is the standard electrode potential and it represents the equilibrium potential of the electrode reaction in standard conditions (25°C, 1bar, a=1).

If the considered reference is the standard hydrogen electrode, the working temperature is 25°C and exchanging from natural to decimal logarithm the Nernst equation becomes:

$$E_{Ox/Red,e} = E^0_{Ox/Red} + \frac{0.0592}{z}\cdot \lg\frac{a_{Ox}^{\nu_{Ox}}}{a_{Red}^{\nu_{Red}}} \tag{2.20}$$

Conventionally, for half-cell reactions, the reactions are written in the sense of reduction and the equilibrium potentials given in tables are reducing electrode potentials, E_{red}. Nevertheless, the oxidising potential, ε_{ox}, is equal in module with the reducing potential, but has the opposite sign:

$$E_{ox} = -E_{red} \tag{2.21}$$

2.1.1.4. Electrochemical Cells and Potential Scale

The study of electrochemical reactions is only possible by connecting at least two electrodes. An electrochemical cell (system) is obtained connecting two electrodes to the surroundings by two terminals (electronic conductors) of identical composition as the one represented in the figure 2.3. The arrangement of the reactants inside the cell is such that, for a chemical reaction to occur, electrical current must flow in surroundings from one terminal to another.

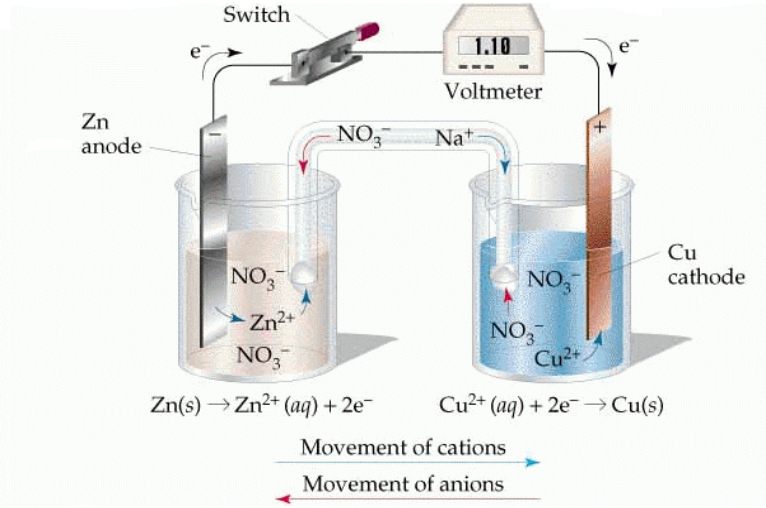

Fig. 2.3 Electrochemical cell

Electrochemical cells are classified as:

- galvanic cells – when the circuit is closed, the chemical reaction occurs spontaneously, resulting in a current flow ($\Delta G<0$)
- electrolytic cells – if an external source of electrical potential is introduced between terminals, with a current produced being accompanied by the chemical reaction ($\Delta G>0$)

The cell reaction for the electrochemical cell presented in fig. 2.3 is represented as:

$$Cu \mid Zn \mid Zn(NO_3)_2\ (a_1) \parallel Cu(NO_3)_2\ (a_2) \mid Cu \mid Cu \qquad (2.22)$$

if the terminals are copper. The double vertical line indicates a liquid-liquid junction across which the electrical potential difference has been eliminated or it is assumed negligible. So long as Cu^{2+} ions do not reach the Zn electrode, direct chemical reaction does not occur. Liquid-liquid junction prevents such mixing while allowing electrical contact between the solutions. This can be accomplished by inserting a concentrated solution or gel containing an inert electrolyte between the two solutions of the cell.

For measuring the potential of an electrode one needs a working electrode, a reference electrode and a voltmeter. The voltmeter measures a sum of potential differences that occur at the terminals of the measuring system. The liquid-liquid junction can be neglected if an inert electrolyte salt bridge is used. The difference of potentials at the contact of terminal with the electrode metal can be neglected for both electrodes if the terminals used are from the same material. In the end the measured difference of potential is:

$$E = \Delta\Phi_{M_1/S} - \Delta\Phi_{M_2/S} \qquad (2.23)$$

where: - $\Delta\Phi_{M_1/S}$ – potential of the electrode where the oxidation reaction take place

- $\Delta\Phi_{M_2/S}$ – potential of the electrode where the reduction reaction take place

The experimentally measured potential is a relative potential with respect to an arbitrary chosen zero. Conventionally, the Standard Hydrogen Electrode (SHE) was chosen to have the standard potential zero. A standard hydrogen electrode is represented in fig. 2.4.

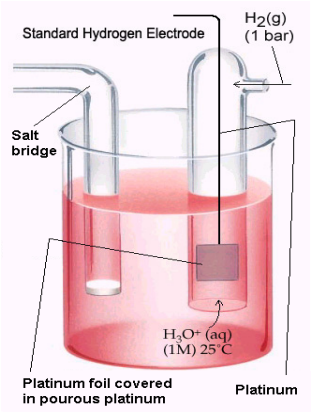

Fig. 2.4 Standard Hydrogen Electrode (SHE)

The standard hydrogen electrode is represented as:

$$Pt \mid H_2 \left(p_{H_2} = 1\,\text{bar} \right) \mid H^+ \left(a_{H^+} = 1 \right) \tag{2.24}$$

The half-cell reaction for the hydrogen electrode is:

$$H^+ + e^- \rightleftarrows 1/2\,H_2 \tag{2.25}$$

The equilibrium potential accordingly to Nernst equation is:

$$E_{e,H^+/H_2} = E^0_{H^+/H_2} + \frac{R \cdot T}{F} \cdot \ln \frac{a_{H^+}}{p^{1/2}_{H_2}} \tag{2.26}$$

For the standard hydrogen electrode the following conditions have to be met:

- protons solution activity – 1 molar
- hydrogen gas pressure – 1 bar

For the above mentioned conditions the hydrogen electrode potential is the standard hydrogen electrode potential and, conventionally, it is zero at any temperature:

$$E_{e,H^+/H_2} = E^0_{H^+/H_2} = 0.000\,V \tag{2.27}$$

The standard hydrogen electrode is used for the experimentally determination of the relative standard potentials. The standard reducing potentials series is obtained by placing the standard reducing electrode potentials from lower to higher potentials (see Table 2.1).

The oxidising or reducing character of different electrodes (electrochemical systems) depends on their position in the standard reducing potentials series. An electrochemical system with a more positive potential has oxidising character against any electrochemical system with a more negative potential and vice-versa.

Table 2.1 Standard Reducing Potentials Series (selection)

Reduction half reaction	**E^o (V_{SHE})**
$Li^+ + e^- \rightarrow Li(s)$	-3.045
$K^+ + e^- \rightarrow K(s)$	-2.924
$Na^+ + e^- \rightarrow Na(s)$	-2.711
$U^{3+} + 3e^- \rightarrow U(s)$	*-1.650*
$UO_2^{2+} + 4H^+ + 2e^- \rightarrow U(s) + 2H_2O$	*-1.444*
$Mn^{2+} + 2e^- \rightarrow Mn(s)$	-1.029

Table 2.1 (cont.)

Reduction half reaction	**E^o (V_{SHE})**
$U^{4+} + e^- \rightarrow U^{3+}$	*-0.553*
$Fe^{2+} + 2e^- \rightarrow Fe(s)$	-0.440
$PbSO_4(s) + 2e^- \rightarrow Pb(s) + SO_4^{2-}$	-0.356
$Ni^{2+} + 2e^- \rightarrow Ni(s)$	-0.230
$Pb^{2+} + 2e^- \rightarrow Pb(s)$	-0.126
$2H^+ + 2e^- \rightarrow H_2(g)$	**0.000**
$UO_2^{2+} + e^- \rightarrow UO_2^+$	*+0.088*
$IO_3^- + 2H_2O + 4e^- \rightarrow IO^- + 4OH^-$	+0.150
$SO_4^{2-} + 4H^+ + 2e^- \rightarrow H_2SO_3 + H_2O$	+0.200
$UO_2^{2+} + 4H^+ + 2e^- \rightarrow U^{4+} + 2H_2O$	*+0.267*
$Cu^{2+} + 2e^- \rightarrow Cu(s)$	+0.342
$O_2(g) + 2H_2O(l) + 4e^- \rightarrow 4OH^-$	+0.401
$UO_2^+ + 4H^+ + e^- \rightarrow U^{4+} + 2H_2O$	*+0.450*
$IO^- + H_2O + 2e^- \rightarrow I^- + 2OH^-$	+0.485
$I_2(s) + 2e^- \rightarrow 2I^-$	+0.535
$Fe^{3+} + e^- \rightarrow Fe^{2+}$	+0.771
$Ag^+ + e^- \rightarrow Ag(s)$	+0.800
$ClO^- + H2O(l) + 2e^- \rightarrow Cl- + 2OH^-$	+0.900
$Br_2(l) + 2e^- \rightarrow 2Br^-$	+1.065
$O_2(g) + 4H^+ + 4e^- \rightarrow 2H_2O(l)$	**+1.229**
$Cl_2 + 2e^- \rightarrow 2Cl^-$	+1.358
$MnO_4^- + 8H^+ + 5e^- \rightarrow Mn^{2+} + 4H_2O$	+1.507
$Au^+ + e^- \rightarrow Au(s)$	+1.680
$F_2(g) + 2e^- \rightarrow 2F^-$	+2.870

But, since the standard hydrogen electrode is difficult to be handled, in laboratories are used other reference electrodes which:

- can be prepared much easier;
- have constant potential over time;
- are hardly to get polarised.

Such kinds of electrodes are for example:

- saturated calomel electrode - SCE (Pt | Hg, Hg_2Cl_2(ins) | KCl);
- silver / silver chloride electrode (Ag | AgCl(ins) | Cl^-)

Attention must be paid at the fact that the potentials measured using other electrodes than SHE are shifted accordingly. For instance:

- 0.000V (SCE) = + 0.244V (SHE) at 25°C;
- 0.000V (Ag/AgCl/3.0M KCl) = + 0.210V (SHE) at 25°C.

2.1.1.5. Pourbaix (potential-pH) Diagrams

The Pourbaix diagram is a graphical representation of thermodynamic information appropriate to electrochemical reactions.

The objective of this diagram is to represent the relative stability of solid phases and soluble ions that are produced by reactions between the electrode and an aqueous environment as function of two parameters, the electrode potential, ε, and the *p*H of the environment. The information needed to construct a Pourbaix diagram are the standard electrode potentials, ε^0, or the equilibrium constants, K, as appropriate for all of the possible reactions considered.

Limitations of Pourbaix diagrams

Pourbaix diagrams are very useful in guiding consideration of corrosion and other problems but they apply only for the conditions assumed in their construction and they are not infallibly predictive because they have limitations, as follows:

- The diagrams are derived from thermodynamic considerations and yield no kinetic information. There are situations in which zones of corrosion suggest that a metal dissolves and yet it does not, due, for example, to the formation of a meta-stable solid phase or to kinetic constraints associated with a complementary cathodic reaction;
- Domains in which solid substances are considered to be the stable species relative to arbitrary soluble ion activities $<10^{-6}$ give good indications of conditions in which a metal may be passive. Whether particular metals are actually passivated within these nominal domains and to what extent a useful passive condition can extend beyond their boundaries depends on the nature, adherence and coherence of the solid substance;
- The diagrams yield information only on the reactions considered in their construction and take no account of known or unsuspected impurities in the solution or of alloy components in the metal that may modify the reactions. For example, Cl^- or SO_4^{2-} ions present in solution may attack, modify or replace oxides or hydroxides in domains of passivity, diminishing the protective power of these substances and small quantities of alloy components can introduce micro-structural features of the metal that resist passivation;
- The form and interpretation of a Pourbaix diagram are both temperature-dependent, the form because T appears in the Nernst equation and the interpretation because *p*H is temperature dependent.

Selection of species and reactions

The reactions significant for the corrosion of uranium [11] are:

R1.	$UO_2^{2+} + 1/2\,H_2 \rightleftarrows UO_2^{+} + H^{+}$	$E^0 = +0.088V$	(2.28)
R2.	$UO_2^{2+} + 4H^{+} + 2e^{-} \rightleftarrows U^{4+} + 2H_2O$	$E^0 = +0.267V$	(2.29)
R3.	$UO_2^{+} + 4H^{+} + e^{-} \rightleftarrows U^{4+} + 2H_2O$	$E^0 = +0.450V$	(2.30)
R4.	$U^{4+} + e^{-} \rightleftarrows U^{3+}$	$E^0 = -0.553V$	(2.31)
R5.	$U^{3+} + 3e^{-} \rightleftarrows U(s)$	$E^0 = -1.650V$	(2.32)
R6.	$UO_2^{2+} + 4H^{+} + 3e^{-} \rightleftarrows U^{3+} + 2H_2O$	$E^0 = -0.010V$	(2.33)
R7.	$UO_2^{+} + 4H^{+} + 2e^{-} \rightleftarrows U^{3+} + 2H_2O$	$E^0 = -0.050V$	(2.34)

In the presence of dissolved oxygen the U(IV) and U(VI) ions suffer different hydrolysis and complexation reactions. In solution, the concentrations of H^+ (as H_3O^+) and of complexation ions (e.g. CO_3^{2-}) have a determining role on the uranium speciation.

In figure 2.5 the potential – *p*H diagram for the system U(IV)/U(VI) in water at 25°C is shown [11]. The covered *p*H domain is between 4.5 and 10. The solubility limiting phases are indicated on the graph. Schoepite is $UO_3{\cdot}2H_2O(cr)$ and uraninite is $UO_2(cr)$. The diagram was calculated for a total uranium concentration $[U]_T = 10^{-5}$M. The relation between *p*e and redox potential is given by the equation:

$$pe = \frac{E_h}{2.303 \cdot R \cdot T} \tag{2.35}$$

At 25°C the equation (2.35) becomes:

$$pe = \frac{E_h}{0.0592} \tag{2.36}$$

where E_h is the redox potential against the Standard Hydrogen Electrode, in volts.

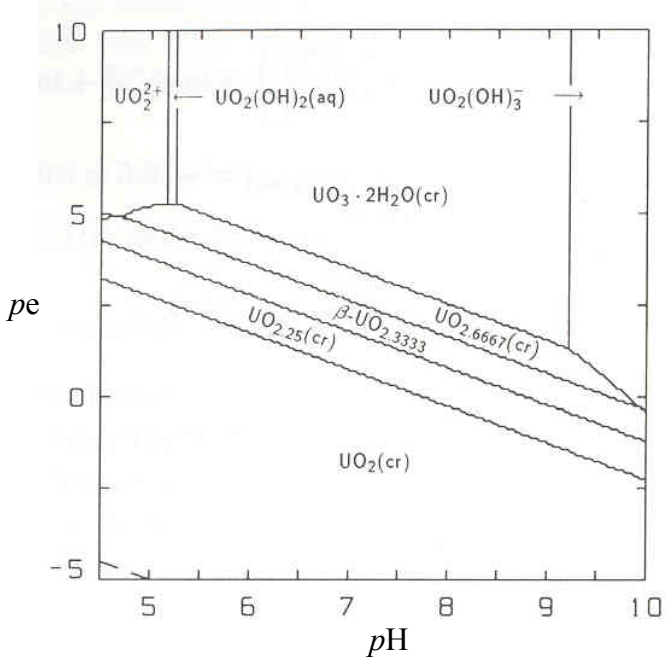

Fig. 2.5 Pourbaix diagram for U(IV)/U(VI) system at 25°C in the *p*H range 4,5-10 for a total U concentration of 10^{-5}M [11]

The domain of stability for water

Superimposing on it the domain enclosing the combinations of the parameters, E and *p*H for which water is stable enhances the usefulness of a Pourbaix diagram. Lines on the diagram representing the decomposition of water define this by hydrogen evolution in reaction W1 or by oxygen evolution in reaction W2:

W1. $2H^+ + 2e^- \rightleftarrows H_2$ $\qquad E^0 = 0.000V$ (2.37)

W2. $1/2\,O_2 + 2H^+ + 2e^- \rightleftarrows H_2O$ $\qquad E^0 = +1.229V$ (2.38)

The gases are evolved against atmospheric pressure, so that $a_{H_2} = a_{O_2} = 1$. The application of Nernst equation yields:

W1. $E = -0.0592 \cdot pH$ (2.39)

W2. $E = 1.229 - 0.0592 \cdot pH$ (2.40)

The two lines enclose a domain in which water is stable. For combinations of potential and *p*H above the top line, water is unstable and decomposes evolving oxygen. For combination bellow the bottom line, it is also unstable and decomposes evolving hydrogen.

2.1.1.6. Corrosion potential (Conditions required for occurrence of corrosion processes)

A corroding system metal/solution forms an aggregation of anodic and cathodic areas on the metal surface. A corrosion element is generated if two processes occur, one delivering electrons (anodic process) and one consuming electrons (cathodic process). Metal dissolution occurs at the surface area with the more negative potential (anode). This anodic reaction (oxidation) is coupled with an electron consuming process (reduction). The most frequently observed cathodic reactions are the hydrogen ion reduction and the oxygen reduction. A measure for the reaction rate is given by the linked partial current densities.

For a homogeneous electrode, the modulus of anodic and cathodic partial current densities of all corrosion elements on the surface is equal and constant. Then the total current density of each element is zero. In case of locally different partial current densities the total current density of the elements is not zero. The electrode is heterogeneous.

The potential of a corroding electrode appears between the equilibrium potentials of the partial reactions. This potential, if not additionally polarised by external currents, is called free corrosion potential. At the free corrosion potential the sum of all occurring partial current densities is zero.

The free corrosion potential is a steady state potential and not an equilibrium potential.

The conditions required for the occurrence of an electrochemical corrosion process are:
- the conjugation, on the material surface, of the ionisation and discharging reactions of its ions, with another electrode reaction which, preferentially, follow the cathodic way
- the more negative reversible potential of the metal than the one of the oxidant from the environment

2.1.2. Kinetics

Electrode processes are phenomena, which occur when an imposed or self-imposed electrical current passes through the electrode.

Electrode processes kinetics deals with establishing of correlation between reaction rate and the force determining the reaction, which is the electrode potential.

2.1.2.1. Reaction rate and Faraday laws

The Faraday law states that the quantity of substance transformed during an electrochemical reaction is proportional with the quantity of implicated current.

Faraday law is the quantitative law of electrochemistry. The definition relation is:

$$m = k_e \cdot Q = k_e \cdot I \cdot t \tag{2.41}$$

where:
- m – mass of the transformed substance, in g
- k_e – electrochemical equivalent (constant of proportionality)
- Q – current quantity, in C
- I – current intensity, in A
- t – reaction time, in s

The electrochemical equivalent represents the quantity of substance transformed during an electrochemical reaction by passing a current quantity equal to 1 Coulomb:

$$k_e = \frac{M}{z \cdot F} \quad \left[g \cdot C^{-1}\right] \tag{2.42}$$

where: - M – molar mass, in $g \cdot mol^{-1}$
- F – Faraday constant and it has the value $96485C \cdot mol^{-1}$ or $26.8A \cdot h \cdot mol^{-1}$
- z – number of transferred electrons

The electrochemical equivalent can be also expressed in units of $mol \cdot C^{-1}$:

$$K_e = \frac{1}{z \cdot F} \quad \left[mol \cdot C^{-1}\right] \tag{2.43}$$

Electrochemical reactions take place on the electrode-electrolyte interface and they depend on the electrode surface area. The electrochemical reaction rate represents the quantity of substance transformed in the unit of time and it is defined by the following equation:

$$r = \pm \frac{dm}{S \cdot dt} = k_e \cdot \frac{dQ}{S \cdot dt} = k_e \cdot \frac{I}{S} = k_e \cdot i \quad \left[g \cdot m^{-2} \cdot s^{-1}\right] \text{or} \left[mol \cdot m^{-2} \cdot s^{-1}\right] \tag{2.44}$$

where: - S – electrode surface area, in m^2
- i – current density, in $A \cdot m^{-2}$

Taking into consideration the general corrosion, the corrosion rate is defined as the material mass corroded reported on the unit of surface and time:

$$r_{corr} = \frac{\Delta m}{S \cdot \Delta t} \quad \left[g \cdot m^{-2} \cdot s^{-1}\right] \tag{2.45}$$

Quantitatively, the general corrosion represents the largest material mass loss because of the corrosion. But it is not a dangerous corrosion because the equipment lifetime can be determined using the penetration index.

The penetration index evaluates the evolution of the corrosion into the depth of the metal material:

$$p_{corr} = \frac{r_{corr} \cdot f}{\rho_{met}} \quad \left[mm \cdot year^{-1}\right] \tag{2.46}$$

where: - ρ_{met} – density of the metal, in kg/m^3
- f – conversion factor between the time unit used for the corrosion rate and year (if corrosion rate is expressed in $g \cdot m^{-2} \cdot h^{-1}$, $f = 8766h \cdot year^{-1}$)

Localised corrosion is more harmful because it occurs on small surfaces but the corrosion rate is much higher. Because the bulk material is not affected the overall metal loss can be neglected. This means that equation (2.43) can not be used for determination of corrosion rates in these cases.

2.1.2.2. Polarisation phenomena

Polarisation represents is the difference of the electrode potential from the corrosion potential due to the action of an electrode current, imposed or self-imposed. It is noted with η and it results from the relation:

$$\eta = E_i - E_e \tag{2.47}$$

where: - E_e – equilibrium potential
- E_i – imposed or self-imposed potential

The electrochemical reactions, even the simple ones, take place in more steps:
- transport
- chemical reactions
- charge transfer

In figure 2.6 the steps of a general electrochemical reaction are presented.

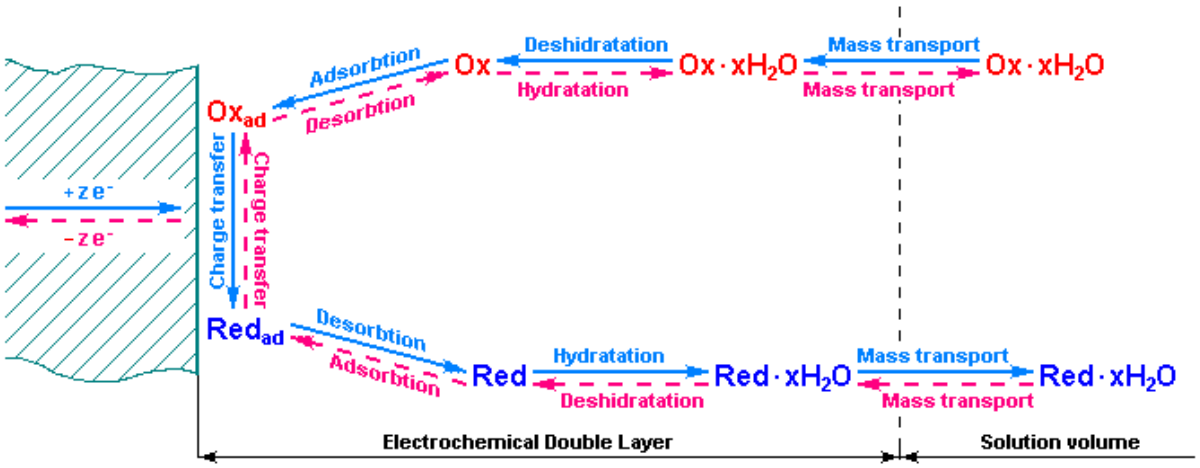

Fig. 2.6 The steps occurring during an electrochemical reaction

During a reaction that takes place in steps, the slowest step is rate determinant and determines the dominant polarisation.

Every step is characterised by a certain polarisation:
- charge transfer – transfer polarisation (activation polarisation), η_T, represents the over potential contributing to the activation energy for the charge transfer to occur
- mass transport – when the transport is slow, a diffusion polarisation, η_D, is generated
  – it determines a concentration modification in the vicinity of the electrode, resulting in modifying the electrode potential, acting as a concentration polarisation, η_C
- chemical reaction – when the reaction that takes place before or after the transport has a slow rate, a reaction polarisation, η_R, occurs
  – it determines a concentration modification in the vicinity of the electrode, resulting in modifying the electrode potential acting as a concentration polarisation, η_C
- ohmic resistance – due to generation of some high resistance layers on the electrode surface, an ohmic polarisation, η_Ω, can occur

If all the steps take place with rates of same order of magnitude, the total polarisation is given by the relation:

$$\eta = \eta_T + \eta_D + \eta_R + \eta_\Omega \tag{2.48}$$

Talking about one pure type of polarisation involves consideration that the rate determinant step, the one giving the polarisation type leading the process, is non-reversible while all the other polarisation types are at equilibrium, their steps being characterised by high rates.

2.1.2.3. Charge transfer polarisation kinetics

Equilibrium conditions charge transfer

When a small metal plate is introduced into a solution, at the initial moment (t = 0), the metal and the solution are not electrically charged:

$$q_M = |q_S| = 0 \tag{2.49}$$

where: - q_M – metal charge, in C
- $|q_S|$ – solution charge, in C

In these conditions, the driving force that determines the charge transfer is represented by the chemical potential gradient of the ions into the two phases. The transfer takes place from the higher chemical potential phase to the lower chemical potential phase:

- if the solution's chemical potential is higher than the metal's chemical potential then, in the beginning, the charge transfer takes place in the cathodic way:

$$\left(\mu_{M^{z+}}\right)_{sol} > \left(\mu_M\right)_{met} \Rightarrow M^{z+} + z\,e^- \xrightarrow{r_c} M \tag{2.50}$$

- if the metal's chemical potential is higher than the solution's chemical potential then, in the beginning, the charge transfer takes place in the anodic way:

$$\left(\mu_M\right)_{met} > \left(\mu_{M^{z+}}\right)_{sol} \Rightarrow M \xrightarrow{r_a} M^{z+} + z\,e^- \tag{2.51}$$

The laws of the chemical kinetics govern this reaction that takes place on an electrically non-charged surface. The following relations determine the cathodic and anodic rates:

$$r_c^0 = \frac{dC_{M^{z+}}}{dt} = k_c^0 \cdot a_{M^{z+}} \cdot e^{-\frac{E_c^0}{R \cdot T}} \tag{2.52}$$

$$r_a^0 = \frac{dC_M}{dt} = k_a^0 \cdot e^{-\frac{E_a^0}{R \cdot T}} \tag{2.53}$$

where: - $C_{M^{z+}}, C_M$ – concentrations of metal ions, M^{z+}, and metal atoms, M, in $mol \cdot L^{-1}$
- k_c^0, k_a^0 – reaction constants for initial chemical cathodic and anodic reaction, in s^{-1}
- E_c^0, E_a^0 – activation energy for initial chemical cathodic and anodic reaction, in $J \cdot mol^{-1}$
- R – molar gas constant, 8.314 $J \cdot mol^{-1} \cdot K^{-1}$
- T – absolute temperature, in K

After the first charge transfer the situation on the interface changes. If the first transfer is in cathodic way, this means the solution looses z positive charges getting negatively charged and the metal looses z e^- getting positively charged.

The electrical field generated by interface charging opposes to the cathodic reaction and favours the anodic reaction. For the charge transfer to continue in the cathodic way, the ion must execute an electrical work against the field, the maximum value being at the metal surface:

$$W_{el} = z \cdot F \cdot E \tag{2.54}$$

Because the charge transfer takes place at a certain distance from the interface the ion must execute just a fraction from this work:

$$W_{el} = (1-\alpha) \cdot z \cdot F \cdot E \tag{2.55}$$

where: - (1-α) – charge transfer coefficient for the cathodic reaction
- α – charge transfer coefficient for the anodic reaction

The potential energy and electrical work profiles for charge transfer in equilibrium condition are presented in figure 2.7:

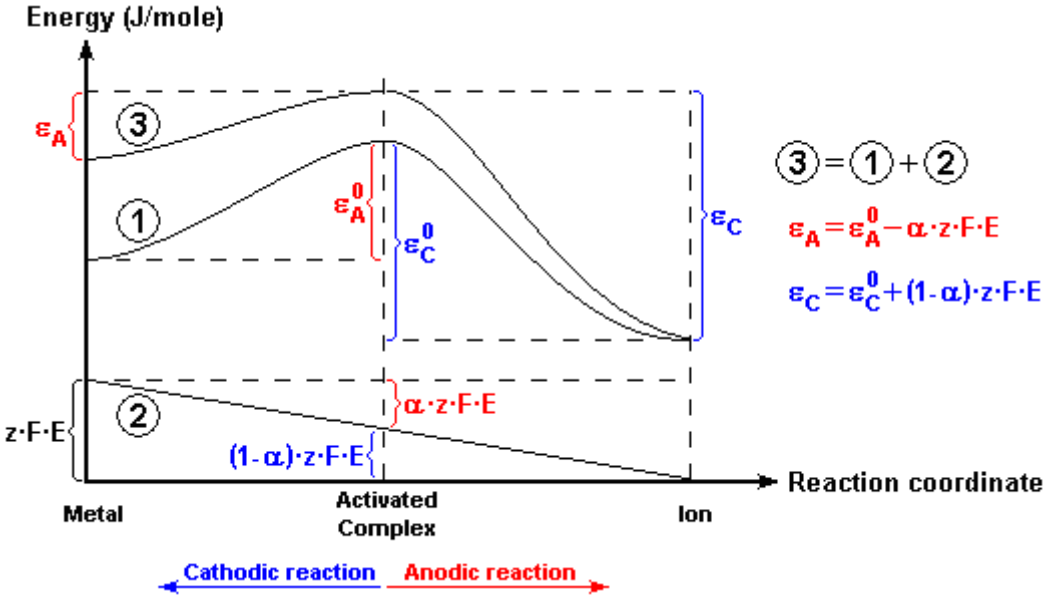

Fig. 2.7 Energy profile for charge transfer in equilibrium conditions

In figure 2.7 ε_A^0 and ε_C^0 represent the activation energies at the first moment, before the interface charging. ε_A and ε_C represent the activation energies after the interface charging. Since the generated electrical field favours the anodic reaction and opposes the cathodic reaction, the relations between activation energy and electrical work are:

$$\varepsilon_A = \varepsilon_A^0 - \alpha \cdot z \cdot F \cdot E \tag{2.56}$$

$$\varepsilon_C = \varepsilon_C^0 + (1-\alpha) \cdot z \cdot F \cdot E \tag{2.57}$$

The relations describing the reaction rates after the interface charging are:

$$r_c = k_c \cdot a_{M^{z+}} \cdot e^{-\frac{(1-\alpha) \cdot z \cdot F \cdot E}{R \cdot T}} \tag{2.58}$$

$$r_a = k_a \cdot e^{\frac{\alpha \cdot z \cdot F \cdot E}{R \cdot T}} \tag{2.59}$$

In the equation (2.58) and (2.59) the electrochemical reaction constants are:

$$k_c = k_c^0 \cdot e^{-\frac{E_c^0}{R \cdot T}} \tag{2.60}$$

$$k_a = k_a^0 \cdot e^{-\frac{E_a^0}{R \cdot T}} \tag{2.61}$$

ε

While the charge transfer continues, ε_C and ε_A increase or decrease until they become equal. In this moment, also the cathodic and anodic reaction rates become equals. This corresponds to the interface equilibrium state, a dynamic equilibrium, characterised by a charge transfer in both ways with equal rates, so no interface modification can be observed, macroscopically. The potential corresponding to this state of equally charge transfer in both ways is the electrode (interface) equilibrium potential, E_e.

Passing of some charged particles through the interface is equivalent to an electrical current flow. At the equilibrium, the interface is passed by an anodic partial current, i_a, and a cathodic partial current, i_c. These currents are equal in absolute value and of different sign, being characterised by the exchange current density, i_0:

$$i_0 = i_a = |i_c| \tag{2.62}$$

Non-equilibrium conditions charge transfer and Butler-Volmer equations

If the equilibrium is disturbed and a predominant way is imposed to the electrode reaction without cancelling the opposite way, the net current passing through the interface is given by the difference between the partial currents in the direct and opposite way. The net current is experimentally measurable. Two cases are possible:

- imposing a current density favourable to the anodic reaction, this is equivalent to a positive polarisation:

  $$\eta_a > 0 \Rightarrow E_i > E_e$$

  $$i_A = i_a - i_c$$

- imposing a current density favourable to the cathodic reaction, this is equivalent to a negative polarisation:

  $$\eta_c < 0 \Rightarrow E_i < E_e$$

  $$i_K = i_c - i_a$$

In this case, the partial anodic and cathodic current densities are:

$$i_a = i_0 \cdot e^{\frac{\alpha \cdot z \cdot F}{R \cdot T} \cdot \eta} \tag{2.63}$$

$$i_c = i_0 \cdot e^{-\frac{(1-\alpha) \cdot z \cdot F}{R \cdot T} \cdot \eta} \tag{2.64}$$

The expressions relating the net anodic and cathodic current densities to polarisation are known as Butler-Volmer equations [12, 13]:

$$i_A = i_0 \cdot \left(e^{\frac{\alpha \cdot z \cdot F}{R \cdot T} \cdot \eta} - e^{-\frac{(1-\alpha) \cdot z \cdot F}{R \cdot T} \cdot \eta} \right) \tag{2.65}$$

$$i_K = i_0 \cdot \left(e^{-\frac{(1-\alpha) \cdot z \cdot F}{R \cdot T} \cdot \eta} - e^{\frac{\alpha \cdot z \cdot F}{R \cdot T} \cdot \eta} \right) \tag{2.66}$$

In Buttler-Volmer equations, net current densities are functions of exchange current density, polarisation and charge transfer coefficient:

$$i_{net} = f(i_0, \eta, \alpha) \tag{2.67}$$

In figure 2.8 the partial and total polarisation curves are presented for a general electrochemical system M^{z+}/M. The exchange current density around the equilibrium potential can be observed. While the value of the exchange current density is different than zero the net current density at the equilibrium potential is zero. It can be observed that at potentials different than the equilibrium potential the net current densities described by the equations (2.65) and (2.66) are different than zero.

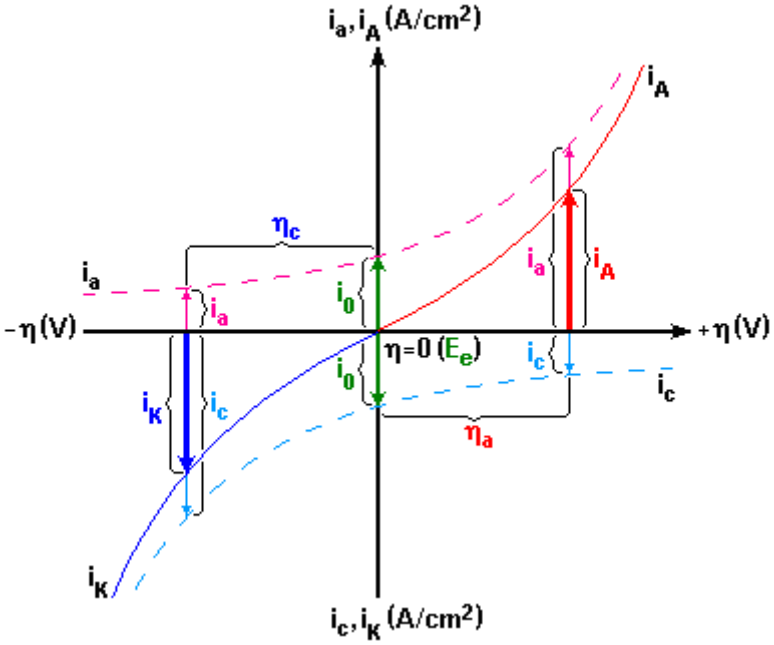

Fig. 2.8 Total polarisation curve and partial polarisation curves

Tafel or High-Field Approximation

The Butler-Volmer equations contain the difference between two exponential terms, the first increases and the second decreases when the polarisation is increasing.

If the absolute value of polarisation is higher than 0.0592V (at 25°C), the first term of the equation is almost 10 times higher than the second one which can be neglected. The net current density is approximatively equal to the partial current density:

$$i_A \cong i_a = i_0 \cdot e^{\frac{\alpha_a \cdot z \cdot F}{R \cdot T} \cdot \eta_a} \tag{2.68}$$

$$i_K \cong i_c = i_0 \cdot e^{-\frac{\alpha_c \cdot z \cdot F}{R \cdot T} \cdot \eta_c} \tag{2.69}$$

where: - α_a – anodic charge transfer coefficient
- α_c – cathodic charge transfer coefficient

The relation between anodic and cathodic charge transfer coefficient is:

$$\alpha_a + \alpha_c = 1 \tag{2.70}$$

In equations (2.68) and (2.69) logarithms can be used for obtaining a linear expression. After exchanging from normal to decimal logarithms, the polarisation can be expressed as a function of net current densities, as follows:

$$\eta_a = -\frac{2.303 \cdot R \cdot T}{\alpha_a \cdot z \cdot F} \cdot \log i_0 + \frac{2.303 \cdot R \cdot T}{\alpha_a \cdot z \cdot F} \cdot \log i_A \tag{2.71}$$

$$\eta_c = \frac{2.303 \cdot R \cdot T}{\alpha_c \cdot z \cdot F} \log i_0 - \frac{2.303 \cdot R \cdot T}{\alpha_c \cdot z \cdot F} \cdot \log i_K \tag{2.72}$$

The following equations, (2.71) and (2.72), represent the Tafel equations:

$$\eta_a = a_a + b_a \cdot \log i_A \tag{2.73}$$

$$\eta_c = a_c - b_c \cdot \log i_K \tag{2.74}$$

where: - $a_a = -\frac{2.303 \cdot R \cdot T}{\alpha_a \cdot z \cdot F} \cdot \log i_0$ (2.75)

- $b_a = \frac{2.303 \cdot R \cdot T}{\alpha_a \cdot z \cdot F}$ (2.76)

- $a_c = \frac{2.303 \cdot R \cdot T}{\alpha_c \cdot z \cdot F} \cdot \log i_0$ (2.77)

- $b_c = \frac{2.303 \cdot R \cdot T}{\alpha_c \cdot z \cdot F}$ (2.78)

a_a and a_c represent the transfer polarisation when the anodic, respectively cathodic, current densities are equal to 1 $A \cdot cm^{-2}$. b_a and b_c are the slopes of the Tafel equations and they represent the change of the transfer polarisation when the anodic, respectively cathodic, current density is changed by one decade. It is expressed in volts per decade.

Also, the exchange current density can be determined:

$$\lg i_0 = \frac{|a_a|}{b_a} = \frac{a_c}{b_c} \tag{2.79}$$

In figure 2.9 the partial polarisation curves and the Tafel curves are presented. The intersection between the extrapolations of the Tafel slopes corresponds to the equilibrium potential and to the exchange current density.

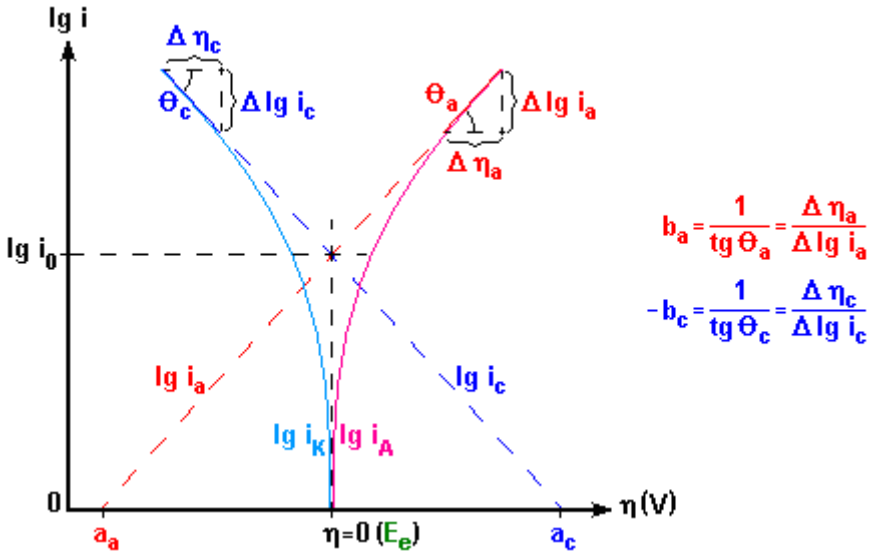

Fig. 2.9 Graphic representation of Tafel equations

Low-field approximation

If the absolute value of the polarisation is lower than 0.010V the exponential terms in Butler-Volmer equations can be developed in series, considering only the first two terms. In these conditions, the following equations are obtained:

$$\eta_a = R_T \cdot i_A \tag{2.80}$$

$$\eta_c = -R_T \cdot i_K \tag{2.81}$$

where R_T is equivalent to an ohmic resistance and it represents the resistance against the charge transfer. It is determined by the relation:

$$R_T = \frac{R \cdot T}{z \cdot F} \cdot \frac{1}{i_0} \tag{2.82}$$

where:
- R – molar gas constant, 8.314J·mol^{-1}·K^{-1}
- T – absolute temperature, in K
- z – number of charges involved in the charge transfer step
- F – Farraday constant, 96485C
- i_0 – exchange current density, in A·m^{-2}

In figure 2.10 the polarisation curves around the equilibrium potential are presented. At low polarisations it can be approximated a linear dependence between the current density and the potential. The slope represents the reciprocal of the charge transfer resistance.

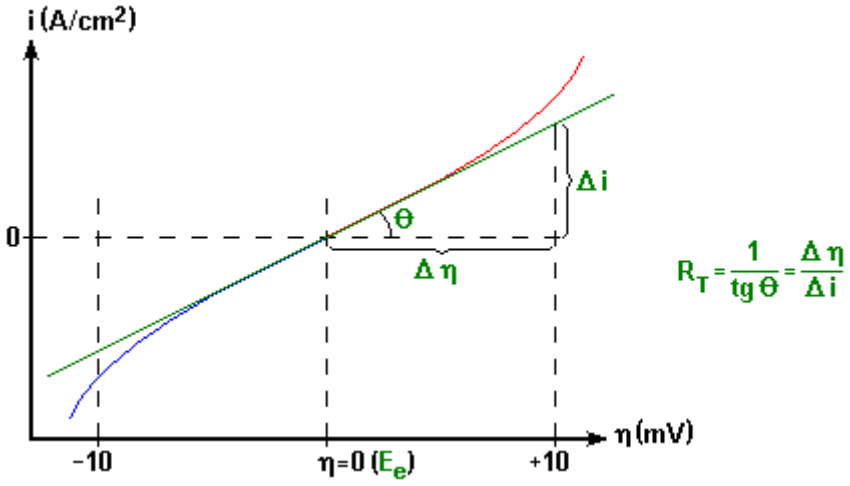

Fig. 2.10 Theoretical polarisation resistance curve

2.1.2.4. Mass transport polarisation kinetics

If the mass transport step to or from the electrode is the slowest step of an electrochemical reaction the concentration of the involved species in the vicinity of the electrode changes. This process occurs when an electrical current passes the interface as a consequence of the charge transfer step. If all the others reaction steps are faster, the variation of the concentration determines the modification of the electrode potential. This potential modification is identified as the diffusion polarisation or mass transport polarisation.

The expression for this type of polarisation depends on ions activities near the electrode and in the solution volume:

$$\eta_D = \frac{R \cdot T}{z \cdot F} \cdot \ln \frac{a_{M^{z+}}}{a^0_{M^{z+}}} \tag{2.83}$$

where: - $a_{M^{z+}}$ – activity of M^{z+} ions near the electrode

- $a^0_{M^{z+}}$ – activity of M^{z+} ions in the solution's volume

For a cathodic reaction, the diffusion polarisation is negative since the M^{z+} ions near the electrode are consumed. For an anodic reaction, the diffusion polarisation is positive since M^{z+} ions are generated near the electrode:

$$\eta_{D,cat} < 0 \tag{2.84}$$

$$\eta_{D,an} > 0 \tag{2.85}$$

The mass transport can be realised by:

- diffusion, caused by a concentration gradient
- convection, caused by a density gradient (it is considered just in some particular cases)
- migration, caused by a potential gradient

Pure diffusion mass transport

The reactant species can be transported to the electrode only by diffusion, in the case of:

- neutral particles (e.g. organic molecules, gases)
- ions, if a chemically inactive indifferent electrolyte is used in a concentration much higher than that of the reactants (i.e. the case for polarography)

Fick's law gives the diffusion rate:

$$r_d = -D \cdot \frac{dC}{dx} \tag{2.86}$$

where: - D – diffusion coefficient, in $cm^2 \cdot s^{-1}$

- $\frac{dC}{dx}$ – concentration gradient, in $mol \cdot L^{-1} \cdot cm^{-1}$

The concentration of the reactant species increases with the distance from the electrode / electrolyte interface and approaches the concentration in the solution volume asymptotically, as shown in figure 2.11. On small distances the concentration and distance vary in a linear manner, so $\frac{dC}{dx}$ can be replaced by $\frac{\Delta C}{\Delta x}$. For this, the tangent to the curve is drawn in the point of concentration on the interface. The intersection between the tangent and the line representing concentration in the solution determines a distance called thickness of the Nernst diffusion layer and noted δ_d.

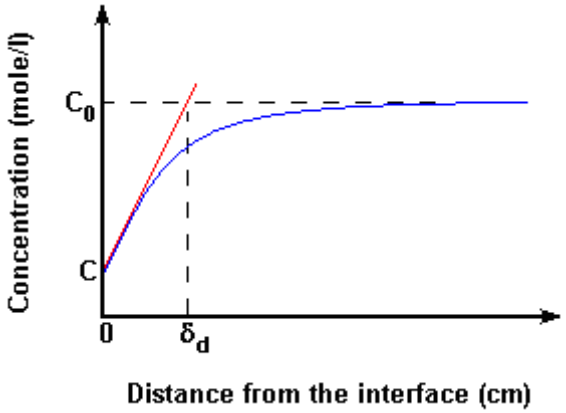

Fig. 2.11 Determination of the thickness of the Nernst diffusion layer

The next relation can express the diffusion current density:

$$i_d = \frac{z \cdot F \cdot D}{\delta_d} \cdot (C_0 - C) \tag{2.87}$$

If the current passing through the interface is so high that the reactant is totally consumed near the electrode, C=0, then the current density is maximal in the given conditions and it is called diffusion limit current density, noted i_D:

$$i_D = \frac{z \cdot F \cdot D}{\delta_d} \cdot C_0 \tag{2.88}$$

If the temperature and stirring conditions are constants, the diffusion limit current density can be determined and also the Nernst diffusion layer thickness. This method is applied in polarography using some standard curves:

$$i_D = K \cdot C_0 \tag{2.89}$$

where K is the polarographic constant:

$$K = \frac{z \cdot F \cdot D}{\delta_d} \tag{2.90}$$

So the relation between diffusion polarisation, η_D, and the diffusion current density, i_d, can be expressed as follows:

$$\eta_D = \frac{R \cdot T}{z \cdot F} \cdot \ln\left(1 - \frac{i_d}{i_D}\right) \tag{2.91}$$

Diffusion and migration mass transport

If diffusion and migration together accomplish the mass transport, the net cathodic current density is influenced by the nature of the ion migrating to the cathode:

- for cations: $i_{K,cat} = i_d + i_K \cdot t_+$ (2.92)
- for anions: $i_{K,an} = i_d - i_K \cdot t_-$ (2.93)

The net cathodic current density is:

- for cations: $i_{K,cat} = \frac{z \cdot F \cdot D}{\delta_d \cdot (1 - t_+)} \cdot (C_0 - C)$ (2.94)
- for anions: $i_{K,an} = \frac{z \cdot F \cdot D}{\delta_d \cdot (1 + t_-)} \cdot (C_0 - C)$ (2.95)

If the whole quantity of reactant species is consumed near the electrode, the limit current density, i_L, is reached:

- for cations: $i_{L,cat} = \frac{z \cdot F \cdot D}{\delta_d \cdot (1 - t_+)} \cdot C_0$ (2.96)
- for anions: $i_{L,an} = \frac{z \cdot F \cdot D}{\delta_d \cdot (1 + t_-)} \cdot C_0$ (2.97)

If cations migrate to the cathode, the limit current density is lower than the diffusion limit current density:

$$i_{L,cat} > i_D \tag{2.98}$$

But if anions migrate to the cathode than the limit current density is higher than the diffusion limit current density:

$$i_{L,an} < i_D \tag{2.99}$$

The diffusion polarisation in this case (which includes also the migration) is:

$$\eta_D = \frac{R \cdot T}{z \cdot F} \cdot \ln\left(1 - \frac{i_K}{i_L}\right) \tag{2.100}$$

If the current density reaches the limit current density value the diffusion polarisation rises theoretically indefinitely. Practically, the potential of another participating species is reached and the concentration near the electrode will increase again.

Only a few reactions have such a high charge transfer rate so that the current increase is rapid. The general polarisation curve for a cathodic reaction contains three areas:

- charge transfer kinetics (low polarisation)
- combined charge transfer and diffusion kinetics
- diffusion kinetics (high polarisation)

In figure 2.12 the general polarisation curve for a cathodic reaction is presented. At lower polarisations the cathodic reaction is controlled by the charge transfer. At high polarisations the cathodic reaction is controlled by the diffusion.

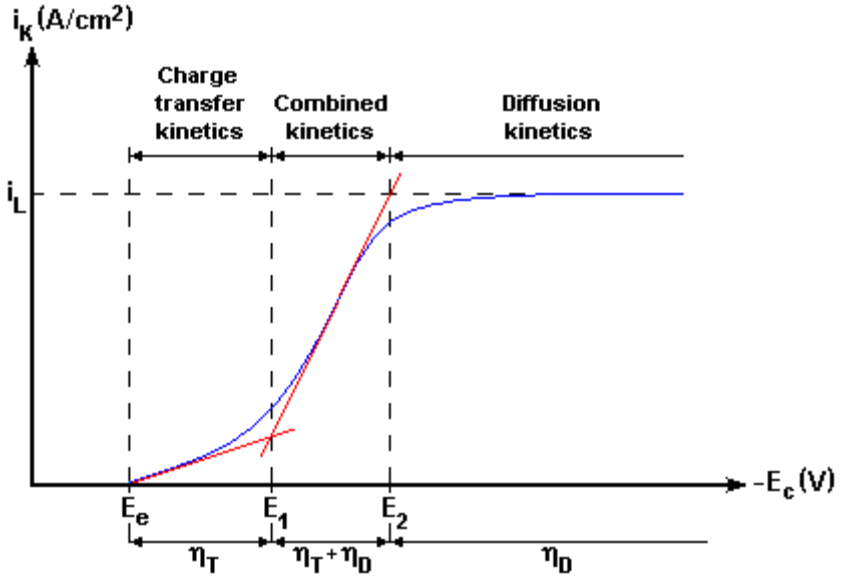

Fig. 2.12 General polarisation curve for the cathodic reaction

2.1.2.5. Reaction polarisation kinetics

Reaction polarisation acts as a concentration polarisation. The difference between diffusion and reaction polarisation can be determined by studying the stirring effect to the limit current density. If it remains unchanged then there is a reaction polarisation.

2.1.2.6. External factors influencing corrosion processes rate

The external factors (environmental dependants) that influence the corrosion rate are:

- *p*H
- temperature
- dissolved O_2 concentration
- complexing agents

2.2. Water radiolysis

2.2.1. Radiolysis mechanism for pure water

One α-particle entering the water loses its energy by a transfer to the surrounding molecules. This energy provided to environment causes the radiolytical decomposition of water. This complex process can be divided into three stages:

- **Physical step** – it takes place between 10^{-18} and 10^{-15} seconds after the energy transfer. This step leads to an ionisation reaction (2.101) or an excitation reaction (2.102) of the water molecule:

$$H_2O \rightarrow H_2O^+ + e^- \quad (2.101)$$

$$H_2O \rightarrow H_2O^* \quad (2.102)$$

- **Physico-chemical step** – between 10^{-15} and 10^{-11} seconds after the energy transfer. The meta-stable species produced in the first step move to give new species such as the electron and solvated radicals H· and HO·. These processes involve on one hand the reaction between H_2O^+ ions and water and on the other hand splitting of the excited species. The splitting of excited species will lead to the formation of oxygen O· in a singlet (·O(^{1}D)) or triplet (·O(^{3}P)) state. The complex mechanism of this step has been proposed by Swiatla [14] and presented in Figure 2.13. It leads to the balance reaction described by the chemical step.

$$H_2O \rightarrow e_{aq}^-, H_3O^+, H\cdot, HO\cdot \quad (2.103)$$

- **Chemical step** - it occurs after 10^{-11} seconds. This step can be described by two phases: a heterogeneous phase followed by a homogeneous one:

  - **Heterogeneous phase** – takes place between 10^{-11} and 10^{-8} seconds after the energy transfer. The species formed in the previous step are still in the clusters formed by the passage of the particle. These clusters are heterogeneous areas whose ionisations and excitement densities are very strong. The species present in this phase lead to reactions generating water (reactions 2.104 to 2.107) and to molecular products, H_2 and H_2O_2 (reactions 2.108 to 2.110)

$$H_3O^+ + e_{aq}^- \rightarrow H\cdot + H_2O \quad (2.104)$$

$$H\cdot + HO\cdot \rightarrow H_2O \quad (2.105)$$

$$e_{aq}^- + HO\cdot \rightarrow HO^- \quad (2.106)$$

$$HO^- + H_3O^+ \rightarrow 2\,H_2O \quad (2.107)$$

$$2\,H\cdot \rightarrow H_2 \quad (2.108)$$

$$2\,H_2O + 2\,e_{aq}^- \rightarrow H_2 + 2\,HO^- \quad (2.109)$$

$$HO\cdot + HO\cdot \rightarrow H_2O_2 \quad (2.110)$$

  At the end of this heterogeneous phase a balance of the produced radiolytical species can be made. It is shown by the following reaction:

$$H_2O \rightarrow e_{aq}^-, H\cdot, HO\cdot, HO_2\cdot, H_2, H_2O_2, H_3O^+ \quad (2.111)$$

- **Homogeneous phase** – occurs between 10^{-8} and 10^{-6} seconds after the energy transfer due to the diffusion of the above mentioned species outside the clusters. During this phase the radicals react with the molecular products according to the following reactions:

$$H_2O_2 + e^-_{aq} \rightarrow HO\cdot + HO^- \quad (2.112)$$

$$H_2O_2 + H\cdot \rightarrow HO\cdot + H_2O \quad (2.113)$$

$$H_2 + HO\cdot \rightarrow H_2O + H\cdot \quad (2.114)$$

$$H_2O_2 + HO\cdot \rightarrow HO_2\cdot + H_2O \quad (2.115)$$

$$2\,HO_2\cdot \rightarrow H_2O_2 + O_2 \quad (2.116)$$

It is interesting to note the production of O_2 during this process even if it can not be defined as a primary product resulting from the radiolysis of water. Its presence in solution comes from the decomposition of H_2O_2. In effect, starting from anoxic conditions it is possible to see that the radiolysis of water lead indirectly to the re-oxygenation of the environment. However, molecular oxygen formed undergoes a decrease from the radical e^-_{aq} and H· as follows:

$$O_2 + e^-_{aq} \rightarrow O_2^- \quad (2.117)$$

$$O_2 + H\cdot \rightarrow HO_2\cdot \quad (2.118)$$

$$HO_2\cdot + H_2O \rightarrow O_2^- + H_3O^+ \quad (2.119)$$

The balance of the O_2 reduction to H_2O_2 can be written as following:

$$HO\cdot + H_2 + \frac{1}{2}O_2 \rightarrow \frac{1}{2}H_2O_2 + H_2O \quad (2.120)$$

During the homogeneous phase the radical products remaining in solution are destroyed by molecular products. Moreover, the lifetime of superoxide O_2^- is very short. Hence, the final outcome of the radiolysis can be summed up in the production of molecular stable species H_2, H_2O_2 and O_2. The concentration of these species in the medium will depend mainly on the dose of energy received and the dose rate.

It is worth noting that in a totally closed system, pure de-aerated water behaves under radiation, as if it was not decomposed. A steady state is rapidly reached in which there is no accumulation of molecular radiolytical products. In this system O_2 is reduced to H_2O_2. Further H_2O_2 is reduced to H_2O (Allen chain reactions 2.113, 2.114 and 2.115). Also H_2 is involved in both processes.

The interaction between radiation and water leads to a process of chain reactions resulting in the formation of radiolytical molecular species such as H_2O_2, O_2 and H_2. These reactions involve chemically very reactive transitional species and will play a major role in the corrosion process. All radiolysis reactions of pure water, taking place in the chemical step are contained in table 2.2. These reactions, with known kinetic constant at 25°C are classified in the order of involved reagents: e^-_{aq}, HO·, H·, HO_2·, O_2^-. The kinetic constants of most of these reactions are about 10^{10}dm^3·mol^{-1}·s^{-1}.

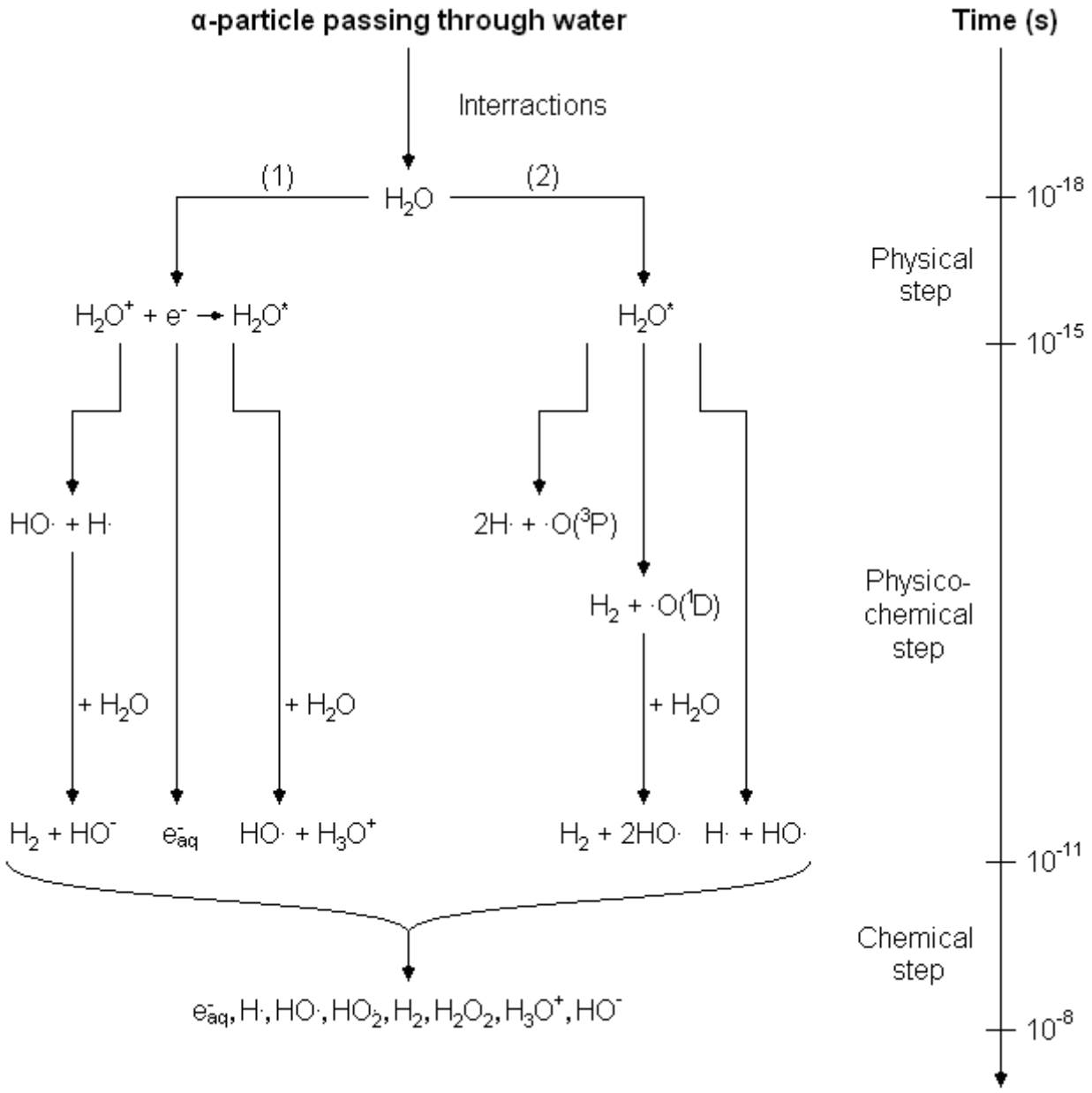

Fig. 2.13 Scheme of the mechanism for water radiolysis [14]

Table 2.2 Reactions balance for the radiolysis of pure water [2]

	Reactions	**E_a (kJ·mol^{-1})**	**k (dm^3·mol^{-1}·s^{-1})**
R1	$e^-_{aq} + H\cdot\left(+ H_2O\right) \rightarrow H_2 + HO^-$	16.3	$3.4\cdot10^{10}$
R2	$e^-_{aq} + e^-_{aq}\left(+2\,H_2O\right) \rightarrow H_2 + 2\,HO^-$	22	$5.5\cdot10^{9}$
R3	$e^-_{aq} + HO\cdot \rightarrow HO^-$		$3.0\cdot10^{10}$
R4	$e^-_{aq} + H_3O^+ \rightarrow H\cdot + H_2O$	14.5	$2.3\cdot10^{10}$
R5	$e^-_{aq} + H_2O_2 \rightarrow HO\cdot + HO^-$	10.0	$1.3\cdot10^{10}$
R6	$e^-_{aq} + O_2 \rightarrow O_2^-$	11.0	$1.9\cdot10^{10}$

Table 2.2 (cont.)

	Reactions	E_a (kJ·mol^{-1})	k (dm^3·mol^{-1}·s^{-1})
R7	$e_{aq}^- + O_2^- \rightarrow O_2^{2-}$		$1.3 \cdot 10^{10}$
R8	$e_{aq}^- + H_2O \rightarrow H\cdot + HO^-$	31.7	$1.0 \cdot 10^{3}$
R9	$2\ HO\cdot \rightarrow H_2O_2$		$5.5 \cdot 10^{9}$
R10	$HO\cdot + H_2O_2 \rightarrow H_2O + HO_2\cdot$	14.0	$2.7 \cdot 10^{7}$
R11	$HO\cdot + H_2 \rightarrow H_2O + H\cdot$		$3.9 \cdot 10^{9}$
R12	$HO\cdot + HO_2\cdot \rightarrow H_2O + O_2$		$1.1 \cdot 10^{10}$
R13	$HO\cdot + O_2^- \rightarrow HO^- + O_2$	17.6	$1.1 \cdot 10^{10}$
R14	$HO^- + H_3O^+ \rightarrow 2\ H_2O$		$3.0 \cdot 10^{10}$
R15	$2\ H\cdot \rightarrow H_2$		$5.0 \cdot 10^{9}$
R16	$H\cdot + HO\cdot \rightarrow H_2O$		$7.0 \cdot 10^{9}$
R17	$H\cdot + H_2O_2 \rightarrow H_2O + HO\cdot$	16.4	$5.0 \cdot 10^{7}$
R18	$H\cdot + HO_2\cdot \rightarrow H_2O_2$		$2.0 \cdot 10^{10}$
R19	$H\cdot + O_2 \rightarrow HO_2\cdot$	6.2	$1.2 \cdot 10^{10}$
R20	$H\cdot + HO^- \rightarrow H_2O + e_{aq}^-$	38.4	$2.2 \cdot 10^{7}$
R21	$2\ HO_2\cdot \rightarrow H_2O_2 + O_2$	20.6	$9.8 \cdot 10^{5}$
R22	$HO_2\cdot + O_2^- \rightarrow HO_2^- + O_2$		$9.7 \cdot 10^{7}$
R23	$H_2O_2 + HO_2\cdot \rightarrow H_2O + O_2 + HO\cdot$		0.5
R24	$O_2^- + H_3O^+ \rightarrow HO_2\cdot + H_2O$		$5.0 \cdot 10^{10}$
R25	$O_2^- + H_2O_2 \rightarrow HO\cdot + HO^- + O_2$		0.13
R26	$HO_2^- + H_3O^+ \rightarrow H_2O_2 + H_2O$		$2.0 \cdot 10^{10}$
R27	$2\ H_2O \leftrightarrow H_3O^+ + HO^-$	$pK_a = 14$	
R28	$HO_2\cdot + H_2O \leftrightarrow H_3O^+ + O_2^-$	$pK_a = 4.8$	
R29	$H_2O_2 + H_2O \leftrightarrow H_3O^+ + HO_2^-$	$pK_a = 11.7$	

*) Kinetic constants determined at 25°C

2.2.2. Physical and chemical properties of radiolytical species

The presence of new radiolytical species in water will affect the physical and chemical properties of the environment. Some of these species will provide acid-base or redox couples. Thus the acid-base or redox balance will be strongly influenced by the production of these new species.

2.2.2.1. Redox potentials

Table 2.3 summarizes the radiolytical species and their redox couples. Also the redox couples and the standard redox potential are presented. This table shows that the radiolysis of water generates places with strongly oxidising conditions due to HO· radical and places with strongly reducing conditions due to e^-_{aq} and H· radical. The extreme values of these redox potentials mean that the radiolytical species, both oxidising and reducing, are very reactive. These species compete within the solution, resulting in the establishing of a redox potential of the solution. The determination of this potential is crucial for determining the corrosion processes that occur at the UO_2 – solution interface.

Table 2.3 Standard redox potentials for the radiolytical species couples [2]

Couple	Reactions	E^0 (V_{SHE})
e^-_{aq} / H_2	$e^-_{aq} + H^+ \leftrightarrow H\cdot$	-2.90
$H\cdot / H_2$	$H\cdot + H^+ + e^- \leftrightarrow H_2$	-2.30
O_2 / O_2^-	$O_2 + e^- \leftrightarrow O_2^-$	-0.30
O_2 / H_2O	$O_2 + 4H^+ + 4e^- \leftrightarrow 2H_2O$	1.23
$HO_2\cdot / H_2O$	$HO_2\cdot + 3H^+ + 3e^- \leftrightarrow 2H_2O$	1.35
H_2O_2 / H_2O	$H_2O_2 + 2H^+ + 2e^- \leftrightarrow 2H_2O$	1.78
$HO\cdot / H_2O$	$OH\cdot + H^+ + e^- \leftrightarrow H_2O$	2.70

2.2.2.2. Acid-base equilibriums

The principal acid-base equilibriums involved in the homogeneous phase of the water radiolysis are presented in the table 2.4.

Table 2.4 Acid-base equilibriums for species involved in the water radiolysis [2]

Couple	Reactions	pK_a (at 25°C)
$HO_2\cdot / O_2^-$	$HO_2\cdot \leftrightarrow O_2^- + H^+$	4.8
$H\cdot / e^-_{aq}$	$H\cdot \leftrightarrow H^+ + e^-_{aq}$	9.6
$HO\cdot / O^-$	$HO\cdot \leftrightarrow H^+ + O^-$	11.9
H_2O_2 / HO_2^-	$H_2O_2 \leftrightarrow H^+ + HO_2^-$	11.9
H_2O / HO^-	$H_2O \leftrightarrow H^+ + HO^-$	14.0

These balances indicate which species will predominate in the water depending on the *p*H. For example, at *p*H value between 5 and 7, the solution contains mostly species O_2^-, H·, HO· and H_2O_2 at the expense of $HO_2\cdot$, e^-_{aq}, O^- and HO_2^-.

2.2.2.3. Diffusion coefficients

In table 2.5 the diffusion coefficients for the species resulted from water radiolysis are presented [15, 16].

The diffusion coefficients have the same order of magnitude for all chemical species and vary between $2 \cdot 10^{-5}$ and $9 \cdot 10^{-5} cm^2 \cdot s^{-1}$. They will quickly spread in the heterogeneous to homogeneous phase. These values are higher by a factor of 10 than the diffusion coefficient of a UO_2^{2+} ion ($0.7 \cdot 10^{-5} cm^2 \cdot s^{-1}$). There is therefore a high mobility of these species in solution.

Table 2.5 Diffusion coefficients of the species produced during water radiolysis (at 25°C) [15, 16]

Radiolytical species	**D ($cm^2 \cdot s^{-1}$)**
e^-_{aq}	$4.9 \cdot 10^{-5}$
HO^-	$5.0 \cdot 10^{-5}$
O_2	$2.0 \cdot 10^{-5}$
H_3O^+	$9.0 \cdot 10^{-5}$
$H\cdot$	$7.0 \cdot 10^{-5}$
$HO\cdot$	$2.2 \cdot 10^{-5}$
H_2O_2	$2.3 \cdot 10^{-5}$
H_2	$4.8 \cdot 10^{-5}$
$HO_2\cdot$	$2.3 \cdot 10^{-5}$
O_2^-	$1.7 \cdot 10^{-5}$
HO_2^-	$1.4 \cdot 10^{-5}$

In conclusion, the production of the radiolytical species results in very important changes of the acid-base and redox properties of the aqueous solutions. These changes have a major influence on the evolution of the solid surface, in contact with the solution.

2.3. Uranium chemistry

2.3.1. Structure and properties of UO_{2+x}

The crystal structure of uranium dioxide stoichiometric is of fluorine type: CaF_2. It consists of a network of face-centred cubic atoms of uranium with the lattice parameter 5.4704 ± 0.0002Å in which oxygen atoms occupy tetrahedral sites [17]. It belongs to the spatial group Fm3m. Its theoretical density is 10.952 $g \cdot cm^{-3}$.

The stoichiometric uranium dioxide $UO_{2.00}$ is difficult to observe because it oxidises spontaneously in air to form on the surface a layer of UO_{2+x} with $0<x<0.33$. These matrices retain the same structure as the stoichiometric ceramics. In this process of altering certain atoms of uranium oxidise to go to the oxidation state +V or +VI.

Oxygen diffuses within the matrix to get to the interstitial positions named O' and O'', as shown in Figure 2.14 proposed by Willis [18]. The result is a decrease of the lattice parameter to 5.44 Å.

If x reaches the value of 0.25 the formula becomes U_4O_9 [19]. If x reaches 0.33 the oxide formula becomes U_3O_7 whose structure is square. The parameter x may continue to rise beyond 0.33. For instance if x is 0.67 the oxide formula is U_3O_8 having an orthorhombic structure.

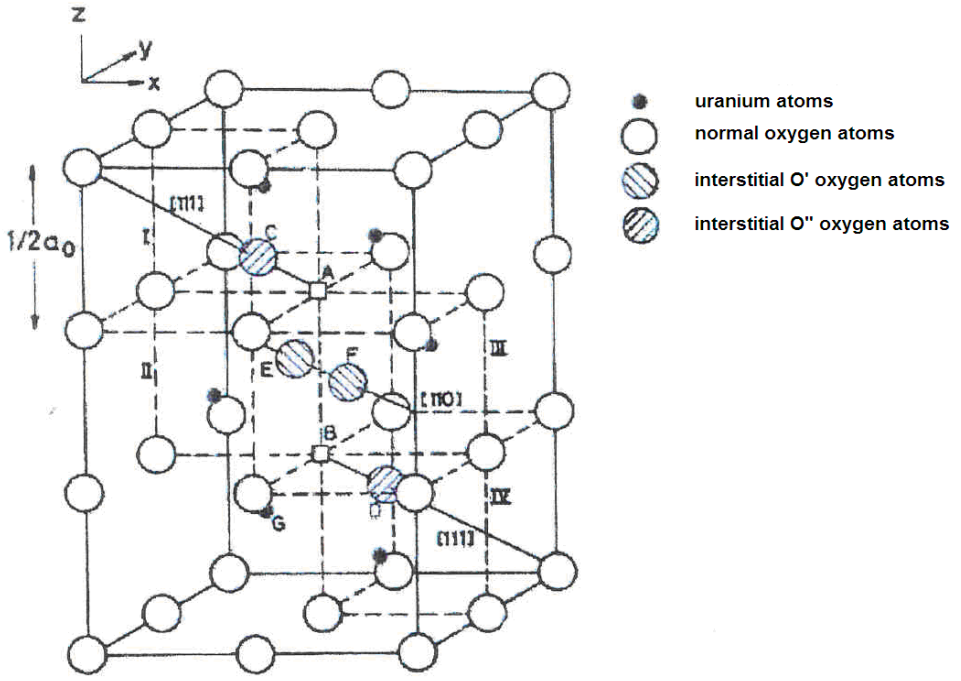

Fig. 2.14 Structure of UO_{2+x} [18]

To each of these compounds corresponds a standard free energy of formation, Δ_fG^0, a standard enthalpy of formation, Δ_fH^0, and standard entropy of formation, Δ_fS^0. In table 2.6 the thermodynamic data for these uranium oxides at 25 ° C are presented [11, 20].

Table 2.6 Thermodynamic data for some uranium oxides at 25°C [11, 20]

Oxides	**Δ_fG^0 (kJ·mol^{-1})**	**Δ_fH^0 (kJ·mol^{-1})**	**Δ_fS^0 (kJ·mol^{-1}·K^{-1})**
UO_2(cr)	-1031.8 ± 1.0	-1085.0 ± 1.0	77.03 ± 0.20
U_4O_9(cr)	-1069.1 ± 1.7	-1128.0 ± 1.7	73.34 ± 0.15
β-U_3O_7	-1080.6 ± 1.4	-1142.0 ± 1.4	83.51 ± 0.2
U_3O_8(cr)	-1123.2 ± 0.8	-1191.6 ± 0.8	94.18 ± 0.17
β-UO_3·H_2O	-1398.7 ± 1.8	-1533.8 ± 1.3	138.00 ± 0.15
UO_3·2H_2O(cr)	-1636.5 ± 1.7	-1826.1 ± 1.7	188.54 ± 0.38

The oxidised layer on the surface of the uranium dioxide is formed by a large range of compounds which have different structures depending on their degree of oxidation.

2.3.2. UO_2 behaviour in solution

In nature the uranium may exists in five oxidation states: 0, +III, +IV, +V and +VI. In water only two of these oxidation states are dominating, +IV and +VI. As shown in table 2.7, U^{III} has a too strong reducing character to be stable and U^{V} undergoes a disproportionation reaction to U^{IV} and U^{VI}.

Table 2.7 Uranium redox couples in water [21]

Redox couple	**Reactions**	**E^0 (V_{SHE})**
U^{VI}/U^{V}	$UO_2^{2+} + e^- \leftrightarrow UO_2^+$	0.09
U^{VI}/U^{IV}	$UO_2^{2+} + 4H^+ + 2e^- \leftrightarrow U^{4+} + 2H_2O$	0.27
U^{V}/U^{IV}	$UO_2^+ + 4H^+ + e^- \leftrightarrow U^{4+} + 2H_2O$	0.45
U^{IV}/U^{III}	$U^{4+} + e^- \leftrightarrow U^{3+}$	-0.52
U^{III}/U^{0}	$U^{3+} + 3e^- \leftrightarrow U_{(s)}$	-1.65
U^{VI}/U^{III}	$UO_2^{2+} + 4H^+ + 3e^- \leftrightarrow U^{3+} + 2H_2O$	-0.01
U^{V}/U^{III}	$UO_2^+ + 4H^+ + 2e^- \leftrightarrow U^{3+} + 2H_2O$	-0.05

Behaviour in oxidative environment

In oxidative environment, U^{4+} and UO_2^{2+} ions may suffer hydrolysis and complexing reactions. In solution, the concentrations of H_3O^+ and of complexing agents like CO_3^{2-} have a determining role in the speciation of uranium. In figure 2.5 the Pourbaix diagram for the system U^{IV}/U^{VI} in aerated water at 25°C is presented. The *p*H domain is between 4.5 and 10 and the total uranium concentration is 10^{-5} M.

If the *p*H is lower than 5.3 the redox potential is higher than 300 mV vs. SHE and no uranium phase will precipitate. If the *p*H is between 5.3 and 9, this is the stability domain for schoepite, $UO_3 \cdot 2H_2O$. As a consequence this phase will precipitate on the surface of the UO_2 matrix.

The figure 2.15 shows the diagram of predominance for the UO_2^{2+} in water and also some hydrolysed compounds as function of *p*H. The precipitation of crystalline species is not presented [11].

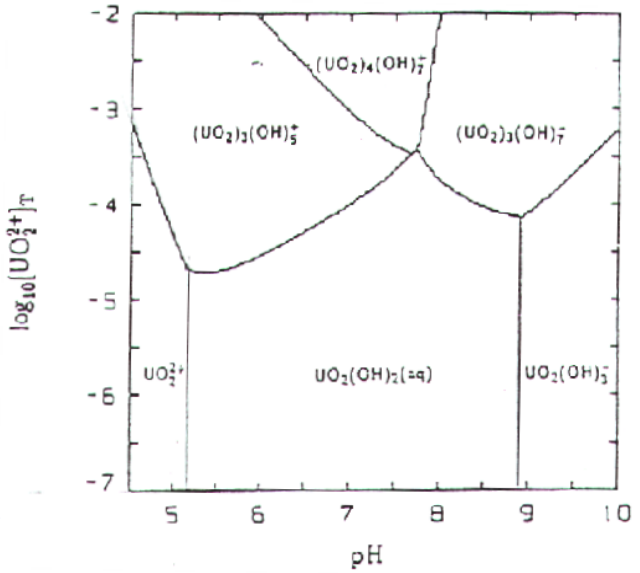

Fig. 2.15 Stability domain for UO_2^{2+} and the hydrolysed species in water, as function of *p*H [11]

In oxidative conditions as aerated water, uranium can be found in solution mainly as U^{VI+}. At *p*H<5.3 it forms UO_2^{2+}. For *p*H>5.3 hydrolysed forms of UO_2^{2+} will dominate. In carbonated solutions, close to 10^{-3}M, the carbonate complexes are dominating.

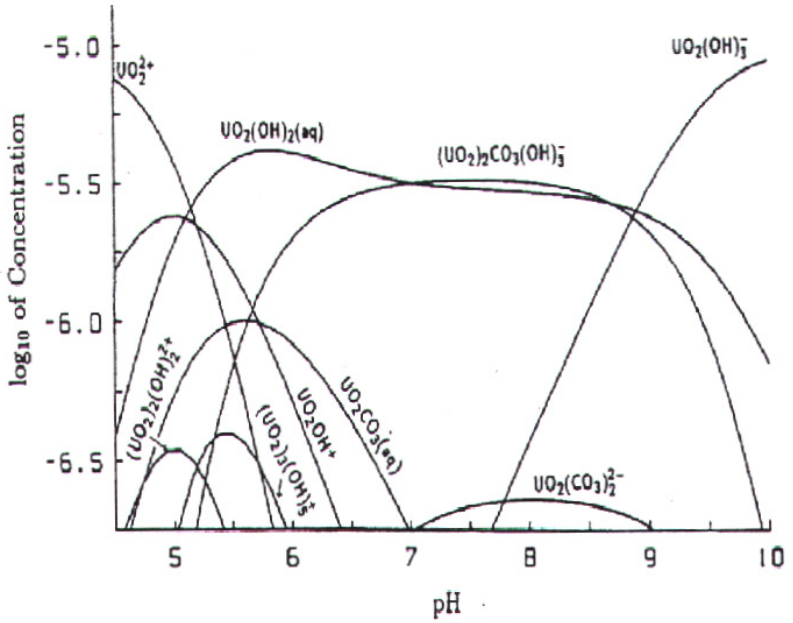

Figure 2.16 Repartition diagram of UO_2^{2+} and carbonate or hydrolysed complexes as function of *p*H

Behaviour in reducing environment

The oxidising or reducing character of an environment is defined by the redox potential. The higher the redox potential the lower is its reducing character.

The knowledge of the behaviour of UO_2 in solution in reducing conditions is important for the storage of the nuclear spent fuel in a geological repository. The redox conditions encountered in these environments are rather simplistic storage because of the presence of species such as Fe^{2+} or S^{2-} [22].

2.3.3. Solubility of UO_2

In solution, uranium can be found mainly as U^{IV} or U^{VI} depending on the conditions. U^{IV} is the main species in solutions with reducing character, while U^{VI} is dominant in neutral or oxidative solutions.

The redox potential plays an important role in the dissolution mechanism of UO_2. In reducing environments, the uranium concentration in solution in equilibrium with UO_2 can be 10^{-8}M. In oxidative conditions, concentrations of uranium in solution are 10^{-6} to 10^{-5}M depending on the concentration of the carbonates.

Solubility of UO_2 in oxidative environment

Because of the dissolved oxygen ($2.7 \cdot 10^{-4}$M), the aerated water can be seen as an oxidative environment. If the UO_2 gets in contact with pure aerated water, a potential difference between the potential of the solid and the potential of the solution is formed at the interface.

As seen in figure 2.17, the two potentials vary to reach a steady state potential at the interface, called corrosion potential,. This change of the potential has as result the decreasing of the concentration of the oxidant in solution on one hand and the increasing of the UO_2^{2+} concentration in solution on the other hand. The interface between the solid and the liquid is the place where the charged particles and the matter are transferred.

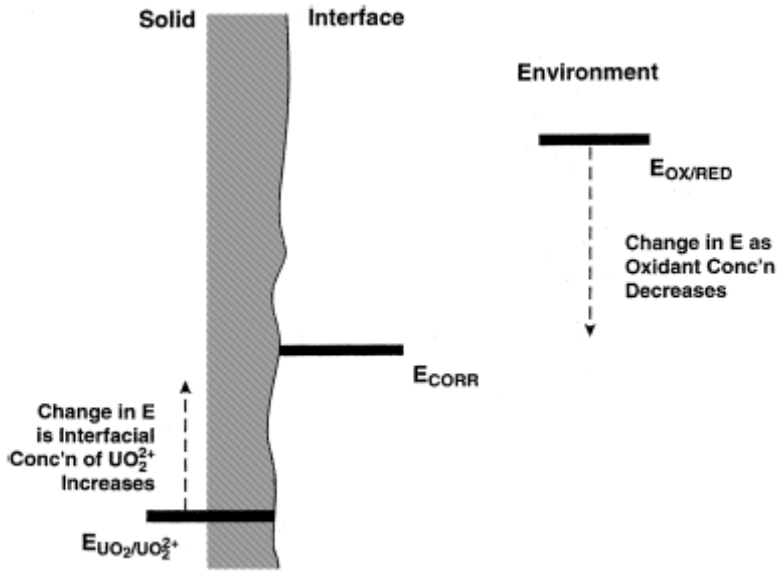

Figure 2.17 Disequilibrium between the redox potential of UO_2 and pure aerated water and the evolution of the corrosion potential on the interface [23]

The *p*H is an important factor which will influence the solubility of UO_2 and the dissolution kinetics. The figure 2.18 shows the dissolution rated of UO_2 as function of *p*H and partial pressure of oxygen at equilibrium. The curves in the graphic separate two *p*H regions in which the dissolution of UO_2 follows different kinetics [24]:

*p*H <6.7 ($[H_3O^+]>2.10^{-7}$M)

The dissolution rate is proportional with the concentration of H_3O^+ ions and with the concentration of the dissolved oxygen. The dissolution kinetic will obey the equation proposed by Torrero [24]:

$$r = (3.5 \pm 0.8)\cdot 10^{-8}\cdot\left[H^+\right]^{0.37\pm0.01}\cdot\left[O_2\right]^{0.31\pm0.01} \qquad (2.121)$$

*p*H >6.7 ($[H_3O^+]<2.10^{-7}$M)

The dissolution rate becomes very slow. It is below 0.2 $mg\cdot m^{-2}\cdot d^{-1}$ and it is impossible to determine a dependence on the *p*H or on the dissolved oxygen [22].

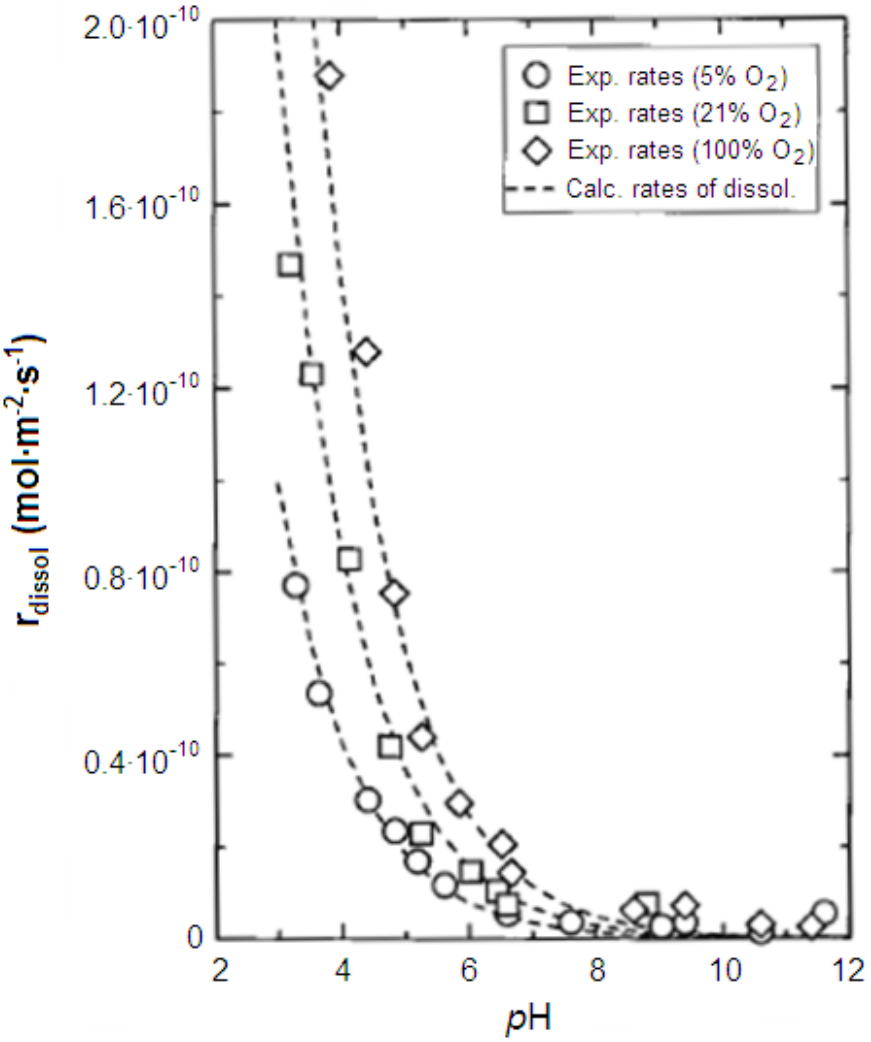

Figure 2.18 UO_2 dissolution rate as function of *p*H and partial pressure of oxygen. The dotted curves correspond to the calculated dissolution rated with equation (2.121) [24]

Other parameters can influence the dissolution of UO_2, for example, temperature, presence of carbonates or other complexing agents. The solubility of the dissolved gases (O_2, H_2, CO_2) in water depends on the temperature [25]. The variation of temperature could increase the effect of these gases on the alteration of UO_2. In the presence of carbonates the dissolution rates could increase with more than one order of magnitude compared with those observed in their absence [26]. The concentration in carbonate can not exceed 10^{-3}M. Also, some complexing agents, like sulphate and phosphates, react with the uranium in the solution [11].

Solubility of UO_2 in reducing environment

The reducing environments are much less favourable to the solubility of uranium dioxide. The concentrations of uranium in solution can reach 10^{-8}M while in oxidative conditions they are between 10^{-6} and 10^{-5}M. However, it is possible to establish reaction mechanisms of the process of dissolution. These mechanisms will involve U^{IV}, which is predominant.

Also, the *p*H is an important factor in the process. Thus, different mechanisms have been proposed depending on the *p*H of the solution by several authors: Rai [27], (reactions a and d), Torrero [28], (reactions c and e) or Yajima [29] (reactions b and e).

For *p*H<2, the proposed mechanisms are:

(a): $UO_2{\cdot}xH_2O_{(am)} + 3\ H^+ \leftrightarrow UOH^{3+} + (x+1)\ H_2O$	log K = 3.5
(b): $UO_{2(s)} + 4\ H^+ \leftrightarrow U^{4+} + 2\ H_2O$	log K = 0.34
(c): $UO_{2(s)} + H^+ + H_2O \leftrightarrow U(OH)_3^+$	K = -2.2

For *p*H>2 the proposed mechanisms are:

(d): $UO_2{\cdot}xH_2O_{(am)} \leftrightarrow U(OH)_4 + (x-2)\ H_2O$	log K = -8.0
(e): $UO_{2(s)} + 2\ H_2O \leftrightarrow U(OH)_4$	log K = -8.7 (log K = -7.1 [30])

Electrochemical approach of the oxidative dissolution

From the electrochemical point of view the oxidative dissolution of UO_2 can be simply represented as a process implying two half-cell reactions:

Anode: $UO_2 \rightarrow UO_2^{2+} + 2\ e^-$

Cathode: oxidant + z e^- → reducing

The complete mechanism allowing the explanation of the process and the formation of the oxidation layers was proposed by Johnson and Shoesmith.

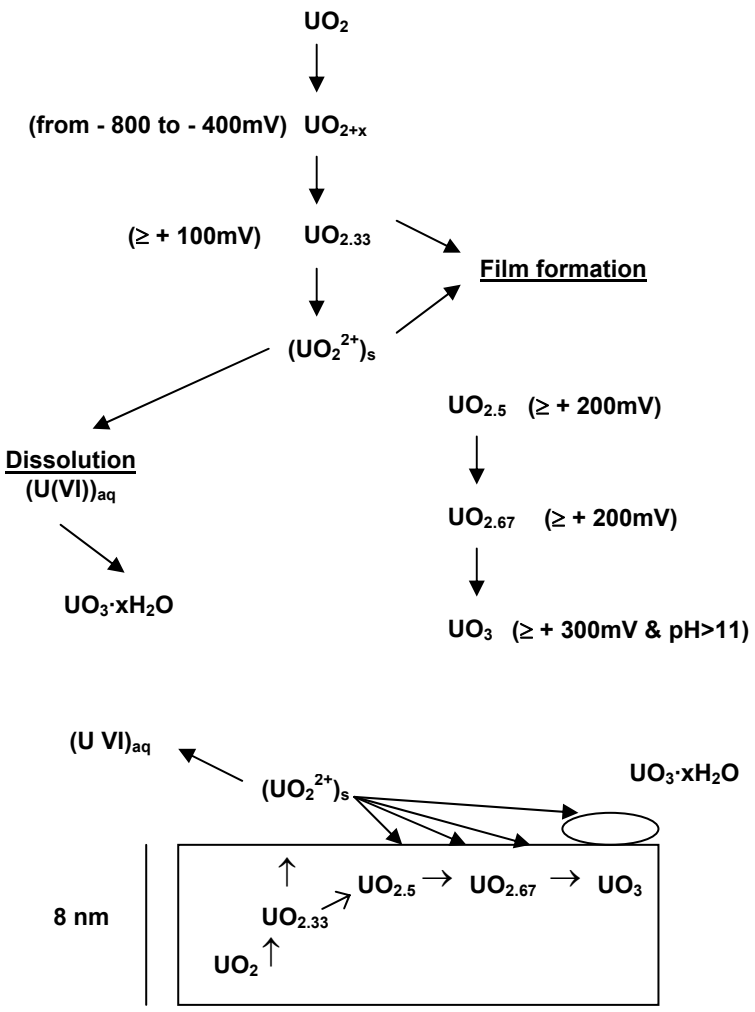

Fig. 2.19 Oxidative dissolution of UO_2 [20]

For *p*H between 5 and 11 and a potential between -550 and -150mV vs. SHE [33], UO_2 can be oxidised to form a super stoichiometric oxide, UO_{2+x}.

$$UO_2(s) + x\ H_2O \rightarrow UO_{2+x} + 2x\ H^+ + 2x\ e^- \quad x < 0.33$$

If the potential is between -150 and +50mV vs. SHE the reaction is:

$$UO_2(s) + 0.33\ H_2O \rightarrow UO_{2.33} + 0.66\ H^+ + 0.66\ e^-$$

At this stage the oxidative dissolution gets in competition with the formation of oxidative layers. The oxidation takes place with the increasing of the potential but <350mV vs. SHE, with the formation of the UO_2^{2+} ions retained on the surface:

$$3\ UO_{2.33} + 2H^+ \rightarrow 3\ (UO_2^{2+})_{surface} + H_2O + 4\ e^-$$

The UO_2^{2+} ions retained on the surface are the intermediates to the transfer of U^{VI} in solution and the oxidation to U_3O_8. According to the composition of the solution and redox conditions, uranium from the solution may precipitate on the surface of the material in the form of ($UO_3 \cdot 2\ H_2O$). This re-crystallisation leads to the formation of a non-passive oxidation layer with solubility between $10^{-6.2}$ and 10^{-5}M for *p*H values between 6 and 9 [34].

The oxidation layer undergoes a series of transformations as shown in figure 2.19:

$$UO_{2.33} + UO_2^{2+}{}_{(s)} + 1.5\ H_2O \rightarrow 2\ UO_{2.5} + 1.33\ H^+$$
$$2\ UO_{2.5} + UO_2^{2+}{}_{(s)} + H_2O \rightarrow 3\ UO_{2.67} + 2\ H^+$$
$$3\ UO_{2.67} + UO_2^{2+}{}_{(s)} + 2\ H_2O \rightarrow 4\ UO_3 + 4\ H^+$$

These transformations take place in a layer of couple of nanometres. They can be influenced by the presence of carbonate.

Dissolution mechanism of UO_2 in reducing environment

In reducing environments, the uranium is in the oxidation state +IV. A two-step mechanism was proposed by Bruno [42, 43] and Johnson [44] to interpret the dissolution UO_2. In a first step the dissolution of uranium increase its concentration in solution. This increase is fast.

In a second step, the concentration of uranium in solution decreases very slowly in parallel with the growth of crystals UO_2.

The dissolution of the UO_2 in the first step can be represented by one of the following reactions:

$$3\ UO_{2.33\ (s)} + H_{2\ (g)} + 5\ H_2O \leftrightarrow 3\ U(OH)_{4\ (aq)}$$
$$3\ UO_{2.33\ (s)} + 5\ H_2O \leftrightarrow UO_2(OH)_{2\ (aq)} + 2\ U(OH)_{4\ (aq)}$$

In the experimental condition used by the authors, the first reaction is significant. Consequently the $U(OH)_4$ (aq) is dominant in the solution.

The second step of the mechanism can be explained by the following reaction:

$$U(OH)_{4aq} \leftrightarrow UO_{2(s)} + 2\ H_2O$$

It allows to explain the decrease of the uranium concentration in solution and also the growth of the UO_2 crystals.

2.3.4. Alteration of UO_2 in solution: consequence of the α-radiolysis

The chemical transformations carried out in the water will induce changes in redox potential by introducing new species. The reactivity of these species will significantly disturb the oxidation / dissolution mechanism of UO_2.

In order to study the radiolysis of water on the alteration of UO_2 three different approaches have been explored in the literature.

A UO_2 – water system is exposed to an external α-source positioned at a variable distance but close enough to the interface for the radiolytical species to react with the matrix [45, 46].

The α-emitters are introduced by doping into the UO_2 matrix. This matrix is then placed in contact with water. In these systems, the flux is changed by the variation of the α-emitters content in the material [47, 48].

The third approach [49, 50] follows the idea of a UO_2 – water system exposed to an external source. Here the source is no longer a radio emitter but a particle accelerator.

Interactions with the surface of UO_2: radiolytical alteration

Sunder and Shoesmith [51] have proposed a sketch for alteration of uranium dioxide by radiolytical species produced by radiation. This pattern is shown in Figure 2.20. It illustrates the formation and interactions of the radiolytical oxidants and reductants with ceramics. This figure reveals three important points in the mechanism of radiolytical alteration.

The surface is attacked by oxidizing species such as $HO^{\cdot}$, $HO_{2\cdot}$ and H_2O_2. These species will oxidise uranium atoms on the surface. This oxidation can lead to the dissolution of uranium as UO_2^{2+} or to formation of alteration layers.

The role of reductive species $H^{\cdot}$, H_2 is less known in the mechanism. It seems they do not interfere at temperatures below 100°C [51]. However, the radical $H^{\cdot}$ and the aqueous electron e_{aq} may reduce U^{VI} to U^{IV} at the interface. However H_2 is not reactive at room temperature and is just diffusing in the solution [20].

The radiolytic species interact with each other on the surface of the material. H_2O_2 can be broken into O_2 and H_2O on the surface of UO_2. The radicals $H^{\cdot}$ and HO• can recombine in H_2O. The presence of impurities in the environment may result in catalytic reactions leading to the recombination of some radicals among them.

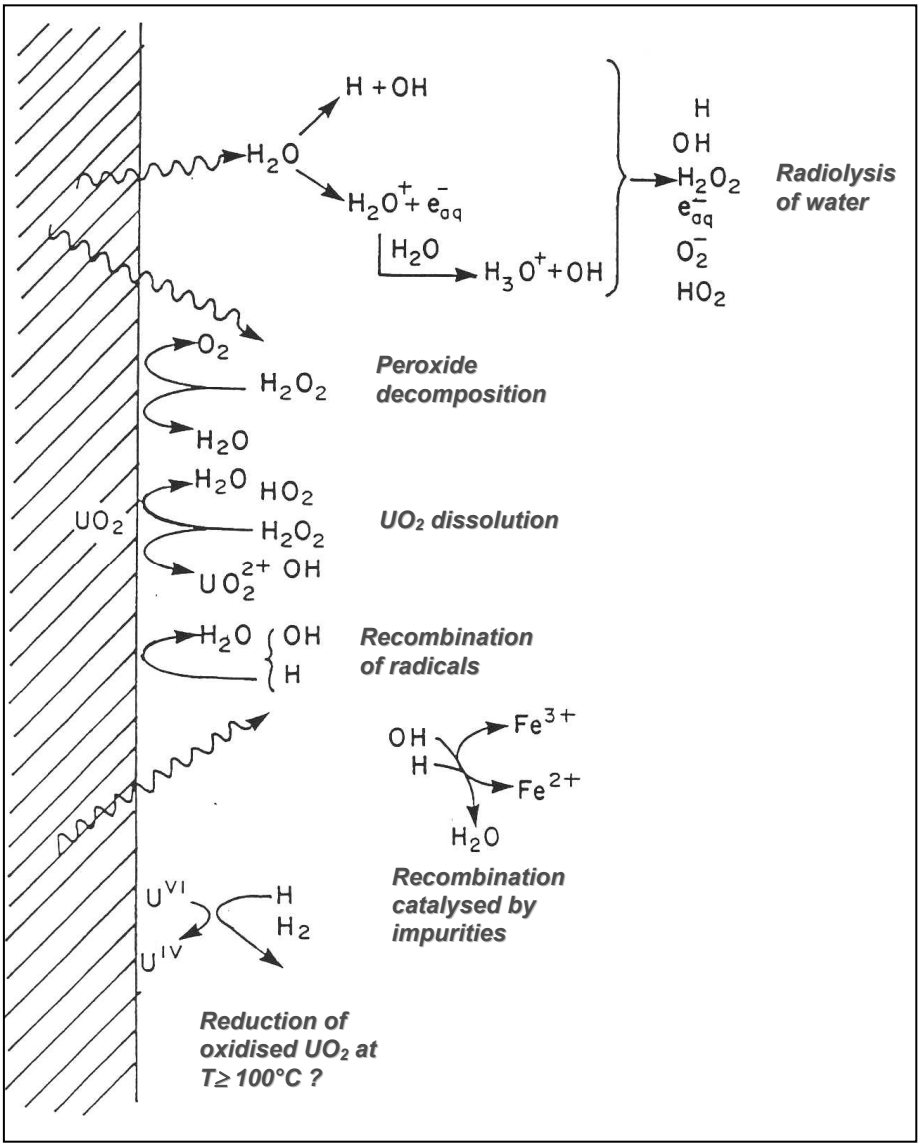

Figure 2.20 Formation and interactions of oxidants and reducers produced by the ground water [51]

Interactions in solution between the radiolytical species and the uranium

Once in solution, uranium can react with different radiolytic species that are present near the solid / water interface. Specific reactions take place depending on the degree of oxidation of uranium. Gordon* [52] and Buxton** [53] have listed a series of reactions involving uranium in different oxidation states and radiolytic products. For each reaction the associate kinetic constant is known.

Reactions with U (+III)

$$*U^{3+} + H_2O_2 \rightarrow U^{4+} + HO\cdot + H_2O \qquad k = (2\pm1)\cdot10^5\ l\cdot mol^{-1}\cdot s^{-1} \text{ at } pH\ 1$$

$$**U^{3+} + HO\cdot \rightarrow UOH^{3+} \qquad k = (4.1\pm0.6)\cdot10^8\ l\cdot mol^{-1}\cdot s^{-1} \text{ at } pH\ 0.3$$

Reactions with U (+IV)

$*U^{4+} + HO\cdot \rightarrow U^{5+} + HO^-$	k = (8.6±0.5)·10^8 l·mol^{-1}·s^{-1} at *p*H 0
$*UOH^{3+} + HO\cdot \rightarrow UOH^{4+} + HO^-$	k = (9.2±0.5)·10^8 l·mol^{-1}·s^{-1} at *p*H 1
$**U^{4+} + e^-_{aq} \rightarrow U^{3+}$	k = 1.0·10^{11} l·mol^{-1}·s^{-1} at *p*H 0
$**UOH^{3+} + e^-_{aq} \rightarrow UOH^{2+}$	k = 5·10^{11} l·mol^{-1}·s^{-1} at *p*H 1

Reactions with U (+V)

$*2UO_2^+ + 4H^+ \rightarrow UO_2^{2+} + U^{4+} + 2H_2O$	k = (3.5±0.1)·10^2 l·mol^{-1}·s^{-1} at *p*H 1

Reactions with U (+VI)

$*UO_2OH^+ + e^-_{aq} \rightarrow UO_2OH$	k = (1.3±0.1)·10^{10} l·mol^{-1}·s^{-1} at *p*H 6.8
$*UO_2^{2+} + H\cdot \rightarrow H^+ + UO_2^+$	k = (4.5±0.5)·10^7 l·mol^{-1}·s^{-1} at *p*H 0
$*UO_2^{2+} + HO_2\cdot /\cdot O_2^- \rightarrow UO_2 - HO_2^{2+}$	k = (1.5±0.1)·10^5 l·mol^{-1}·s^{-1} at *p*H 1
$*UO_2 - HO_2^{2+} + HO_2\cdot /\cdot O_2^- \rightarrow UO_2^{2+} + H_2O_2 + O_2$	k = (9.0±1.5)·10^5 l·mol^{-1}·s^{-1} at *p*H 1
$*UO_2^{2+} + H_2O_2 \rightarrow UO_2^{2+} - H_2O_2$	k = 1.4.10^4 l·mol^{-1}·s^{-1} at *p*H 1
$**UO_2^{2+} + e^-_{aq} \rightarrow UO_2^+$	k = (1.7±0.1)·10^{10} l·mol^{-1}·s^{-1} at *p*H 5.3

Other possible reactions on a thermodynamic plan can supplement the list of these reactions. For example the reaction of hydrolysis of UO_2^{2+} leading to the formation of the meta-studtite (or dehydrated studtite) in the presence of H_2O_2 can be written:

$$UO_2^{2+} + H_2O_2 \rightarrow UO_4 + 2H^+$$

The differences between the redox potential couples involving uranium and those of couples involving radiolytic species reveal that there are many other possible reactions that remain to be determined.

Under radiation and oxidative conditions uranium in solution will be found mainly in the oxidation state +VI in the form of UO_2^{2+}. Taking into account the kinetic constant of the equations presented above it can be stated that the highest are those concerning the reduction of U^{VI} by the aqueous electron e^-_{aq} or H· radical. However, these constants are not enough to predict the evolution of the system. Other factors have to be taken into account such as concentrations of present species.

3. Experimental methods

3.1. Free corrosion potential monitoring (E_{corr})

During the glove box experiments run at ITU and those run at CERI (before, during and after irradiation) the corrosion potential of UO_2 was recorded. The aim was to monitor the UO_2 surface behaviour during the experiments and to determine the influence of the alpha particles on the corrosion of UO_2 and also the possible post-irradiation effects.

The measurement of the corrosion potential during He^{2+} beam irradiation was repeated in order to verify the reproducibility of the measurements or other measurements were made, like electrochemical impedance spectroscopy (EIS) during irradiation or recording of polarisation curves. After the last irradiation measurement the post-irradiation corrosion potential was recorded for 8-10 hours.

3.2. Polarisation curves

Polarisation curves are used for determination of the rate of electrochemical reactions where the current can not be directly measured. In the case of corrosion reactions, at least two different electrochemical couples are involved. Although each process is characterised by different anodic and cathodic current densities the sum of all the current densities is zero. However, the system is not in equilibrium because each system is evolving in only one direction (either reduction or oxidation). The potential at which this process is taking place is known as corrosion potential.

By moving away from the corrosion potential (both in cathodic and anodic range) the current can be measured. If the distance from the corrosion potential is big enough then one process will dominate over the others and the logarithm of the current density will vary linear with the potential. By extrapolating the anodic and cathodic polarisation curves until they intersect the corrosion potential and current density (thus corrosion rate) can be determined for the considered couple. Also by extrapolating one polarisation curve to the already measured corrosion potential one can determine the rate of the considered process at that potential.

Because the UO_2 system is not a fast responding system (the current is not stabilising very fast at an imposed potential), in the effectuated measurements a potential was imposed and the current was measured for a certain period of time (approx. 20 minutes for measurements made at CERI and 2 hours for measurements made in the glove box at ITU).

For the polarisation curves plots the current during last minute of measurement was averaged and the obtained value was used. Because the UO_2 disks have a quite high bulk resistance (5-10kOhm determined by EIS, sometimes even higher) the ohmic drop has to be taken into consideration. It represents a difference between the imposed potential (on the backside of the disk) and the actual potential on the surface in contact with electrolyte due to the resistance of the material to the charge transport. This means that the actual potential on the UO_2-electrolyte interface is lower than the one imposed by the potentiostat.

The anodic and cathodic polarisation curves were recorded on natural and depleted UO_2 samples and under irradiation with He^{2+} beam (at CERI) or 1 and 10% ^{233}U doped UO_2 samples (at ITU) in order to determine the influence of alpha activity on the corrosion rate of UO_2.

3.3. Electrochemical impedance spectroscopy (EIS)

Impedance spectroscopy [54] is a method which has been successfully used in different fields where interfaces need to be studied (e.g. coatings, fuel cells, corrosion studies). A small amplitude signal, usually between 5 and 50mV, is applied over a range of frequencies. Normally for corrosion systems, the frequency range is between 1mHz and 100kHz because in this range most of the relevant information for the corrosion reaction can be found. However in the case of systems corroding with a very small rate this range has to be extended to lower frequencies, even 10μHz. Unfortunately, measurements down to these low frequencies require a long time, even couple of days.

The measured parameter is the current response of the system, which is an alternative current. The advantage of the method is that both the excitation and response signals can be combined in one single function which depends only on the frequency. This function is called impedance and is the equivalent in the alternative current (AC) circuits of the resistance from direct current (DC) circuits. It is characterised by a module and a phase.

$$Z = |Z| \cdot e^{j \cdot \Phi} \tag{3.1}$$

Also it can be represented as complex function having a real (resistive) and an imaginary (capacitive, inductive) component:

$$Z = \mathrm{Re}_Z + \mathrm{Im}_Z \cdot j \tag{3.2}$$

The relations between the two ways of expressing the impedance are presented bellow:

$$|Z| = \sqrt{\mathrm{Re}_Z^2 + \mathrm{Im}_Z^2} \tag{3.3}$$

$$\Phi = \arctan\left(\mathrm{Im}_Z / \mathrm{Re}_Z\right) \tag{3.4}$$

There are more possibilities to represent an impedance spectrum, but two are better known. One is known as Nyquist plot. In this representation the imaginary part, Im(Z) is plotted as function of real part, Re(Z). The other possibility is known as Bode plot and it contains two curves, the impedance module, |Z|, and phase shift, Φ, both being represented as functions of the frequency, f. Although it is easier to read the resistive components on the Nyquist plot, the frequency is implicitly contained and thus not easily available. The Bode plot on the other hand is more complex because it contains two curves instead of one, but the frequency is easily available and different processes can more easily be observed.

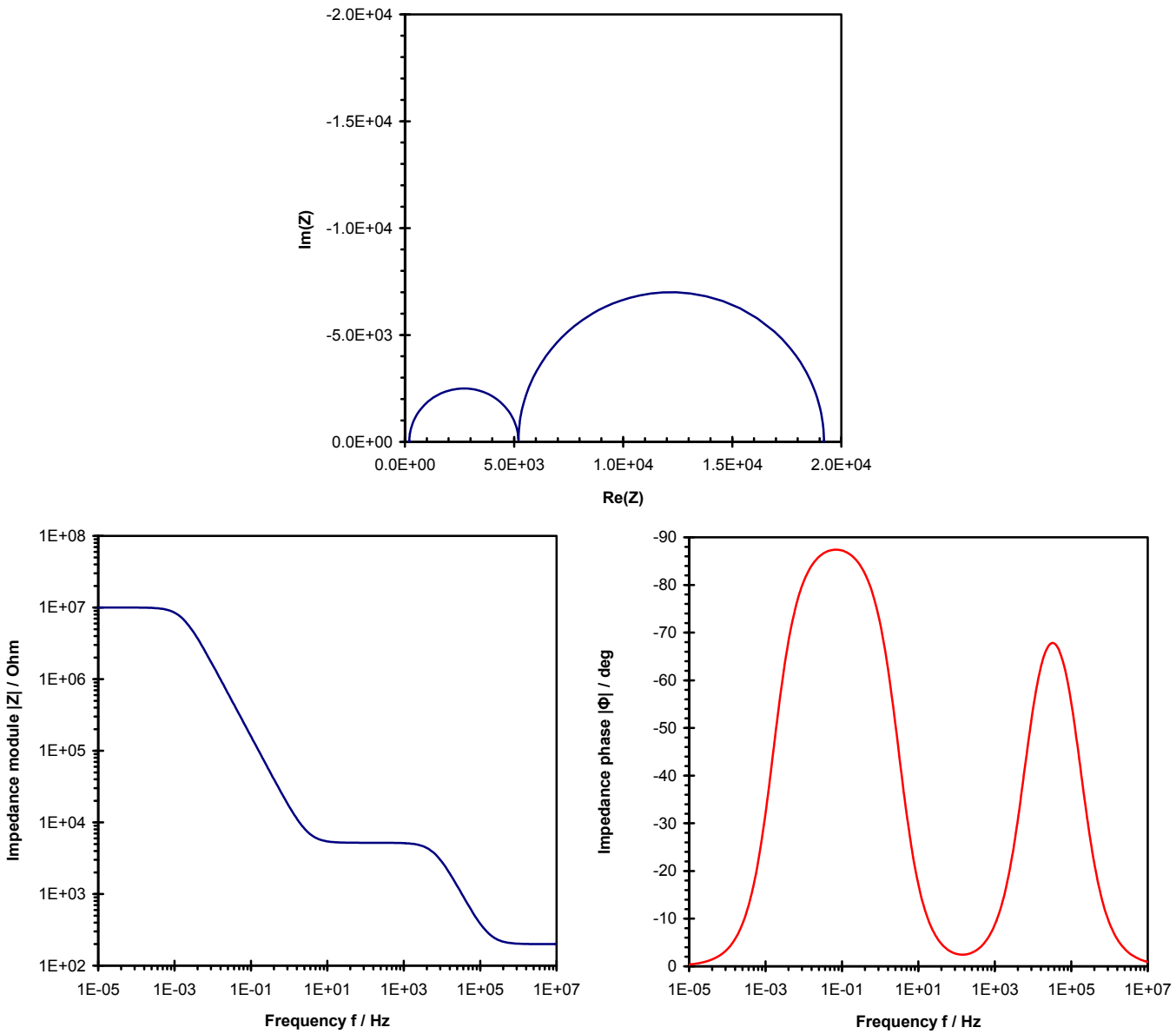

Fig. 3.1 Example of a Niquist plot (up) and Bode plot (down left and right) for an electrochemical system where no leaking occurs

In order to interpret the impedance spectrum an equivalent electrical circuit needs to be associated. This circuit is composed from electrical components, like resistances, capacitors and inductive loops. Also specific "imaginary" impedance elements can be used (e.g. constant phase element, used for non-parallel delimitation surfaces, or Nernst impedance element and Warburg impedance elements used for diffusion representation). Each component from the equivalent circuit is assimilated to a property of the studied electrochemical system.

Different regions in the impedance spectra correspond to different properties. In the high frequency range properties of the electrolyte can be determined (e.g. conductivity). In the medium frequency range the properties of the material (e.g. material resistivity and capacity) and surface film formation can be observed. Also if cracks or leakages occurs, where the electrolyte can get in contact with a more active surface (e.g. stainless steel), they can be seen in this frequency range (see figure 3.2). In the lower frequency range, information related to corrosion rate of the material can be obtained (e.g. polarisation resistance and double layer capacity).

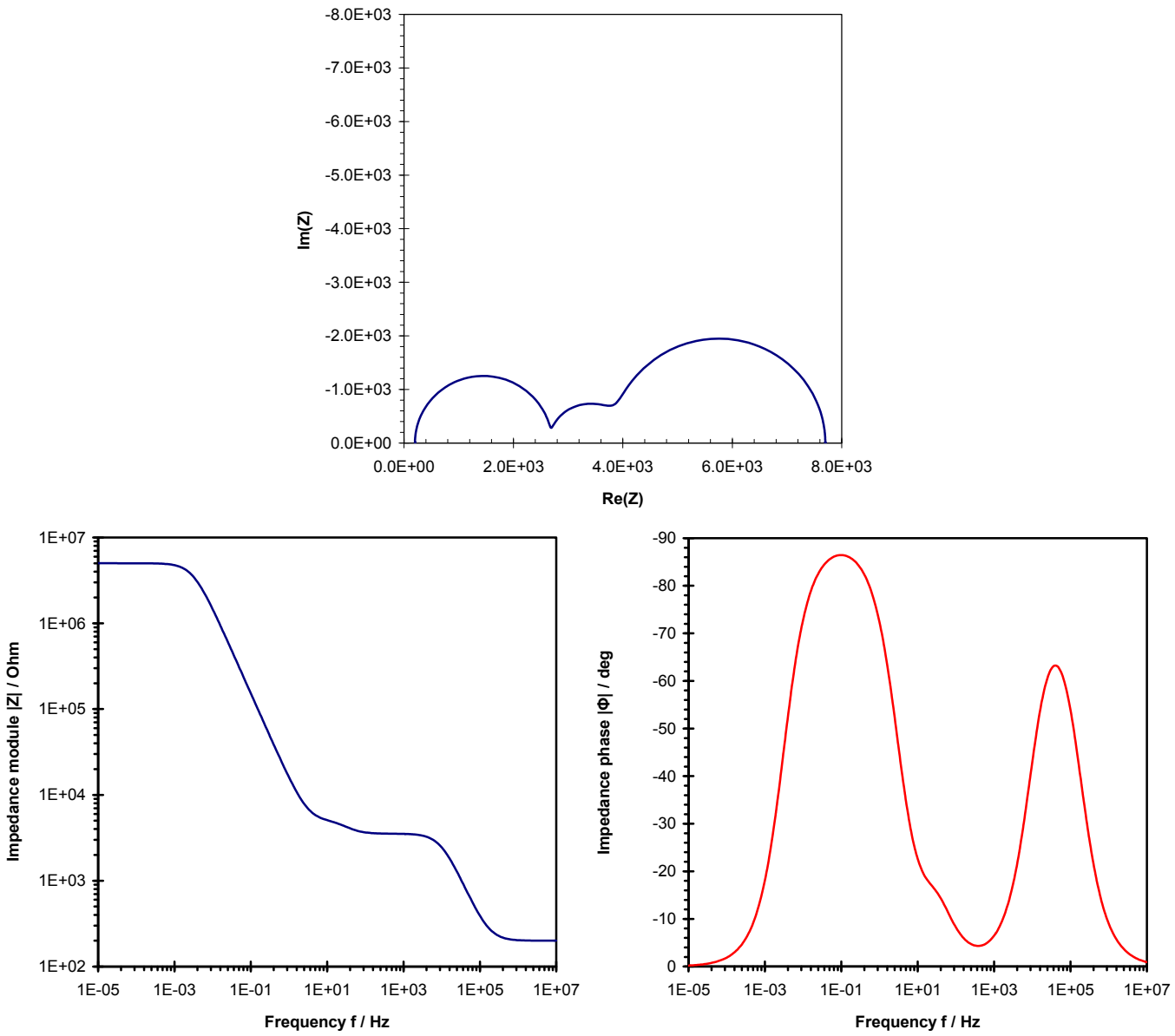

Fig. 3.2 Example of Nyquist plot (up) and Bode plot (down left and right) for an electrochemical system where leaking occurs

During the measurements, EIS was used to check for eventual leakages of the UO_2 electrode (frequency range 1Hz – 10kHz) and to determine the polarisation resistance of the UO_2 corrosion reaction before, during and post-irradiation. It was also used during polarisation measurements to determine the polarisation resistance at different imposed potentials.

3.4. Cyclic voltammetry (CV)

During a cyclic voltammetry measurement, a potential is applied to the electrochemical system, and the current is measured. The current response over a potential window is measured, starting at an initial value and varying the potential in a linear manner up to a pre-defined limiting value. At this potential (switching potential), the direction of the potential scan is reversed, and the same potential window is scanned in the opposite direction. This means that, for example, species formed by oxidation on the first (forward) scan can be reduced on the second (reverse) scan. This technique is commonly used, since it provides a fast and simple method for characterization of a redox-active system. In addition to providing an estimate of the redox potential, it can also provide information about the rate of electron transfer between the electrode and the active species, and the stability of the species in the electrolyzed oxidation states (e.g., whether or not they undergo any chemical reactions).

The collected data are plotted as current vs. potential. As the waveform shows, the forward scan produces a current peak for any species that can be oxidised through the range of the potential scan. The current will increase as the potential reaches the oxidation potential of the species, but then falls off as the concentration of the reactant is depleted close to the electrode surface. As the applied potential is reversed, it will reach a potential that will reduce the product formed in the first oxidation reaction, and produce a current of reverse polarity from the forward scan. This reduction peak will usually have a similar shape to the oxidation peak. As a result, information about the redox potential and electrochemical reaction rates of the compounds is obtained.

If the electronic transfer at the surface is fast and the current is limited by the diffusion of species to the electrode surface, then the current peak will be proportional to the square root of the scan rate. This relationship is described by the Cottrell equation [55]:

$$i = z \cdot F \cdot A_{el} \cdot C^{0}_{Ox} \cdot \sqrt{\frac{D_{Ox}}{\pi \cdot t}} \tag{3.5}$$

where:
- z – number of electrons
- F – Faraday number, 96485 $C \cdot mol^{-1}$
- A_{el} – area of the electrode in cm^2
- C^0_{Ox} – initial concentration of reducible species Ox in $mol \cdot L^{-1}$
- D_{Ox} – diffusion coefficient for species Ox in $cm^2 \cdot s^{-1}$
- t – time in s

This equation describes the change in electric current with respect to time in a controlled potential experiment. For a simple redox event, such as the Ox/Red couple, the current measured depends on the rate at which the analyte diffuses to the electrode. In other words the current is diffusion controlled. The Cottrell equation describes the case for a planar electrode.

Deviations from linearity in the plot of i vs. $t^{-1/2}$ sometimes indicate that the redox event is associated with other processes, such as association or dissociation of a ligand or a change in geometry. In practice the Cottrell equation simplifies to

$$i = k \cdot \sqrt{r_{scan}} \tag{3.6}$$

where:
- k – collection of constants for a given system
- r_{scan} – scanning rate, typical ranges from 20 to 2000 mV/s

4. Experimental set-up

4.1. Equipment

4.1.1. Glove box

The electrochemical work was carried out in a new glove box built and commissioned during this work. A lot of technical problems were encountered and the majority of them were solved.

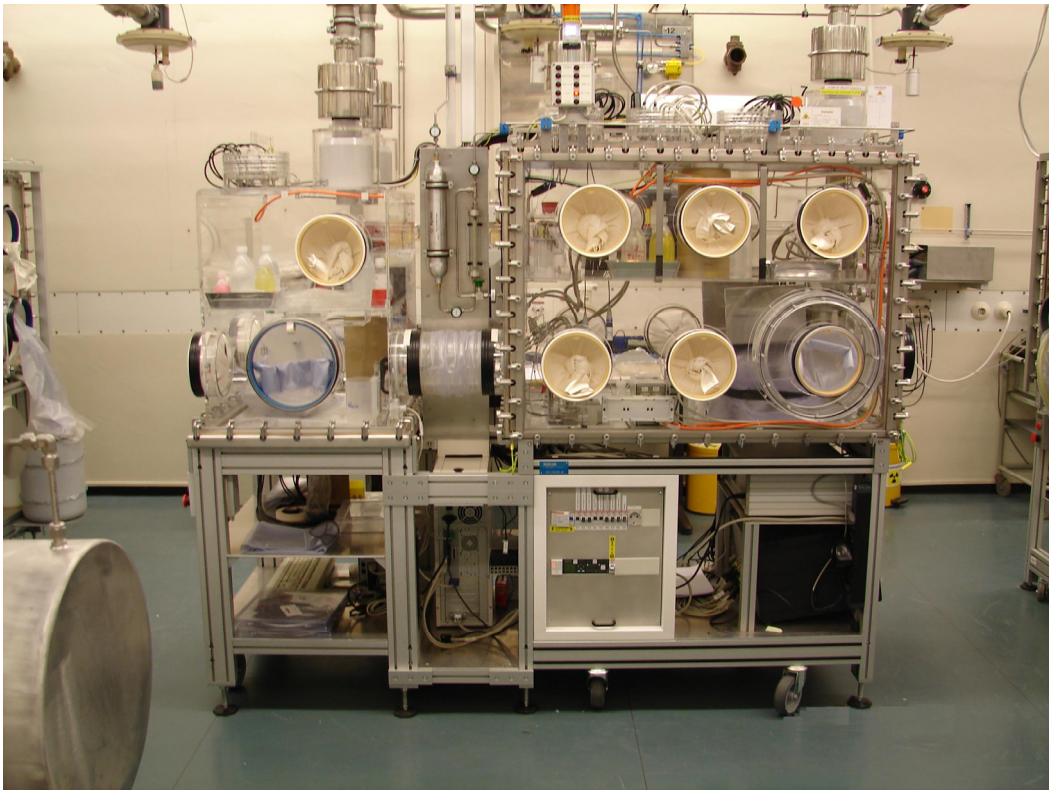

Fig. 4.1 The glove box designed especially for electrochemical experiments

The experimental setup is presented in figure 4.2, together with a list of the equipment used:

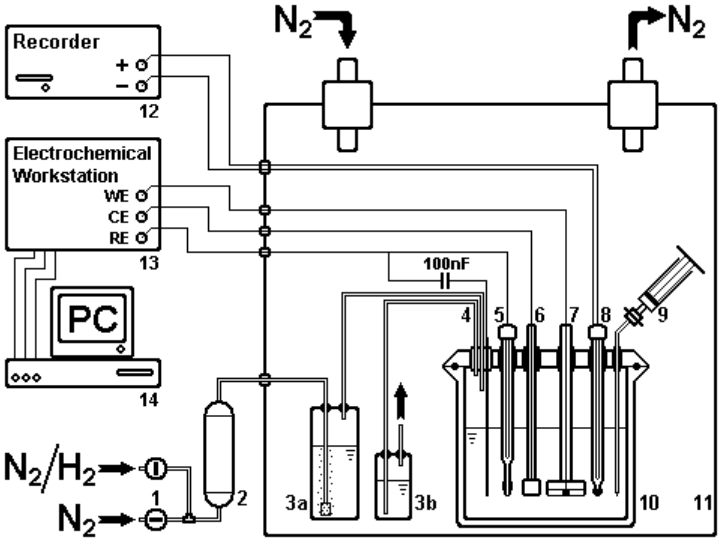

Fig. 4.2 Schematic set-up for electrochemical experiments

1 – Inert gas distribution system
2 – Oxygen trap
3 – Gas bubbler (3a – gas inlet with frit; 3b – gas outlet)
4 – Gas inlet and outlet for cell with Pt-wire auxiliary electrode for short circuiting the reference electrode via a 100 nF capacitor during impedance measurements
5 – Reference electrode, double junction Ag/AgCl electrode (Mettler Toledo InLab®302)
6 – Pt counter electrode
7 – Working electrode with UO_2 sample facing downwards
8 – Redox combined electrode, Pt wire and an internal Ag/AgCl electrode (Mettler Toledo InLab®302)
9 – 5ml syringe for solution sampling
10 – Electrochemical cell with glass vessel (electrolyte volume 100 ml) ad PE cover
11 – Glove box
12 – LSB 36 II recorder for redox potential (Linseis)
13 – IM6 electrochemical workstation (Zahner Elektrik)
14 – Computer to operate the electrochemical workstation

Electrochemical cells

Three electrochemical cells being setup as shown above were available for parallel experiments as shown in figures 4.3 and 4.4.

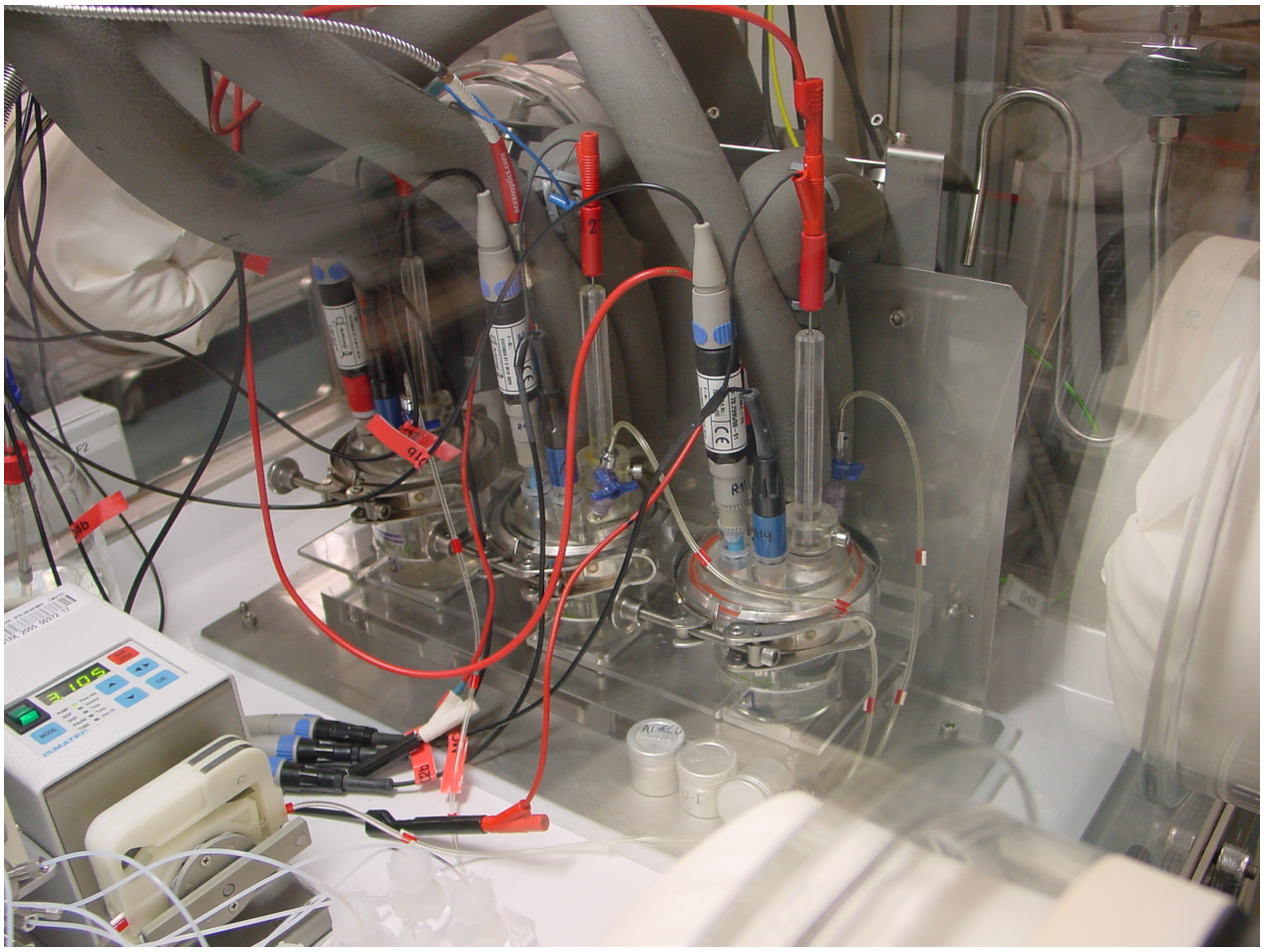

Fig. 4.3 The three electrochemical cells for simultaneous electrochemical experiments

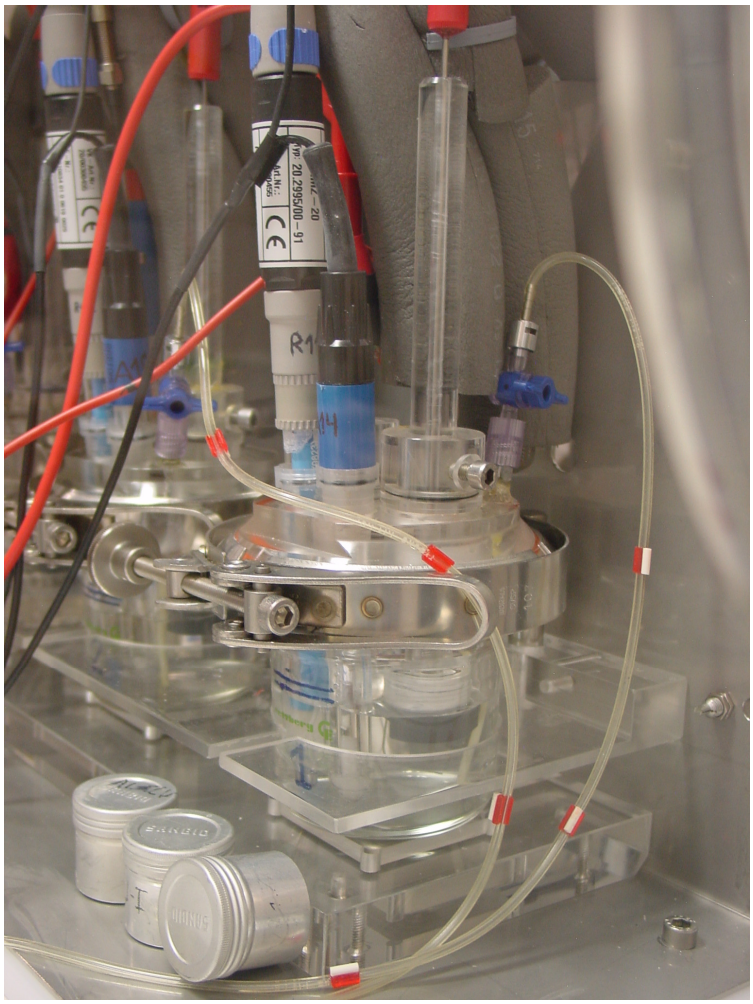

Fig. 4.4 Electrochemical cells during running experiment

The cells are made of Pyrex glass and the covers of Plexiglas. Into the covers holes are drilled in order to accommodate the working electrode, the counter electrode with the auxiliary electrode for EIS, reference and E*h* electrodes, the purging gas inlet and outlet and the needle from the solution sampling system.

4.1.2. Automatic solution sampling system

An automatic sampling system has been developed in order to optimise the running of experiments and will be able to take automatically up to 16 samples.

The sampling system consists of:

- one tubing pump provided by Ismatec (model REGLO Digital ISM 832A – 2channels, 8 rollers)
- one multi-port valve provided by KNAUER (model A1379 – 17-Port-1-Channel Switching Valve)
- one computer with two RS232 ports (i.e. 9-pin COM ports)
- a software program to control both the pump and the multi-valve
- connecting tubes to connect the experimental vessel, the pump, the multi-valve and the sampling vessels (5ml plastic bottles)

This sampling system is in close connection with the IM6 electrochemical station. This is connected via an interface card to the same computer as the pump and multi-valve. Once one set of measurements is complete, the sampling system should take a sample from the experimental vessel and then the next set of measurements should start.

In the figure 4.5 the automatic sampling system is presented:

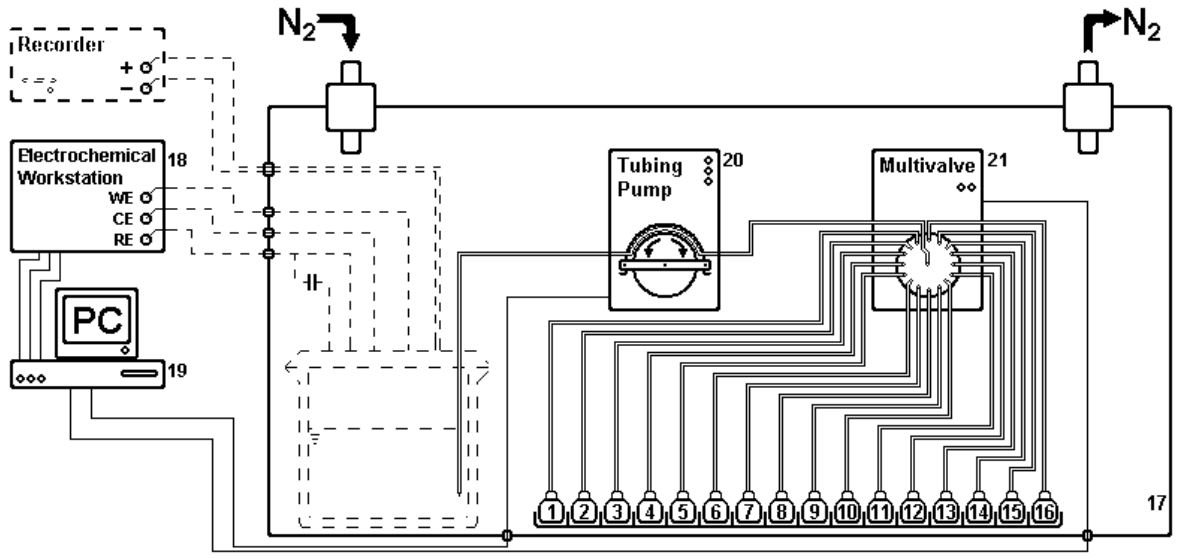

Fig. 4.5 Scheme of the setup for automatic sampling system

1-16 – 10ml PE bottles
17 – Glove box
18 – IM6 electrochemical workstation (Zahner Elektrik)
19 – Computer to operate the electrochemical workstation, the pump and the multi-port valve
20 – Tubing pump REGLO Digital ISM 832A (Ismatec)
21 – Switching multi-port valve 1 inlet, 16 outlets (Knauer)

Fig. 4.6 The automatic solution sampling system inside the glove box

An operating software has been written and developed in Visual Basic in order to run the solution sampling software. Two operating modes are available, manual and automatic. The manual mode allows the setting of the valve position, volume, flow rate and other parameters. Using the automatic mode it is possible to sample subsequently more solutions using a predefined sequence.

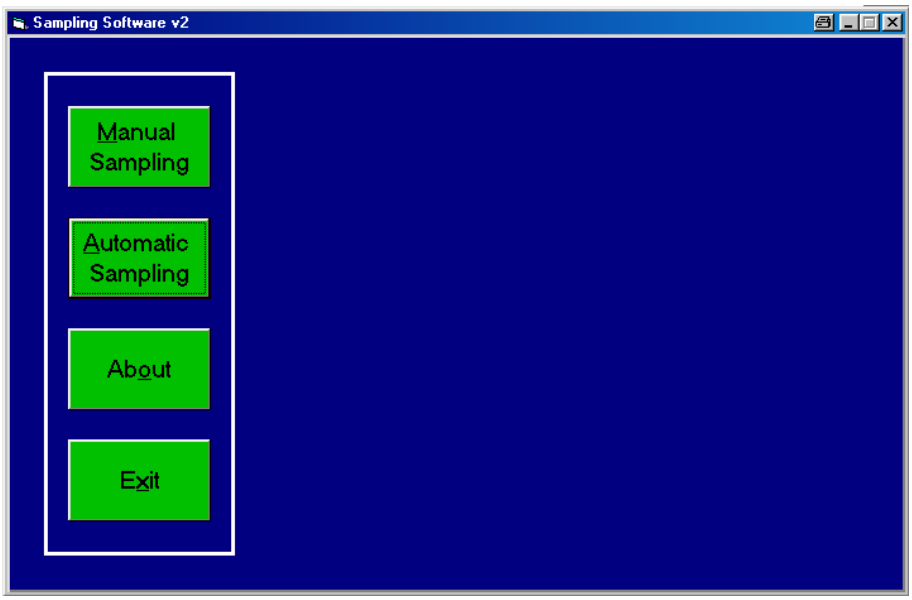

Fig. 4.7 The main menu of the solution sampling software

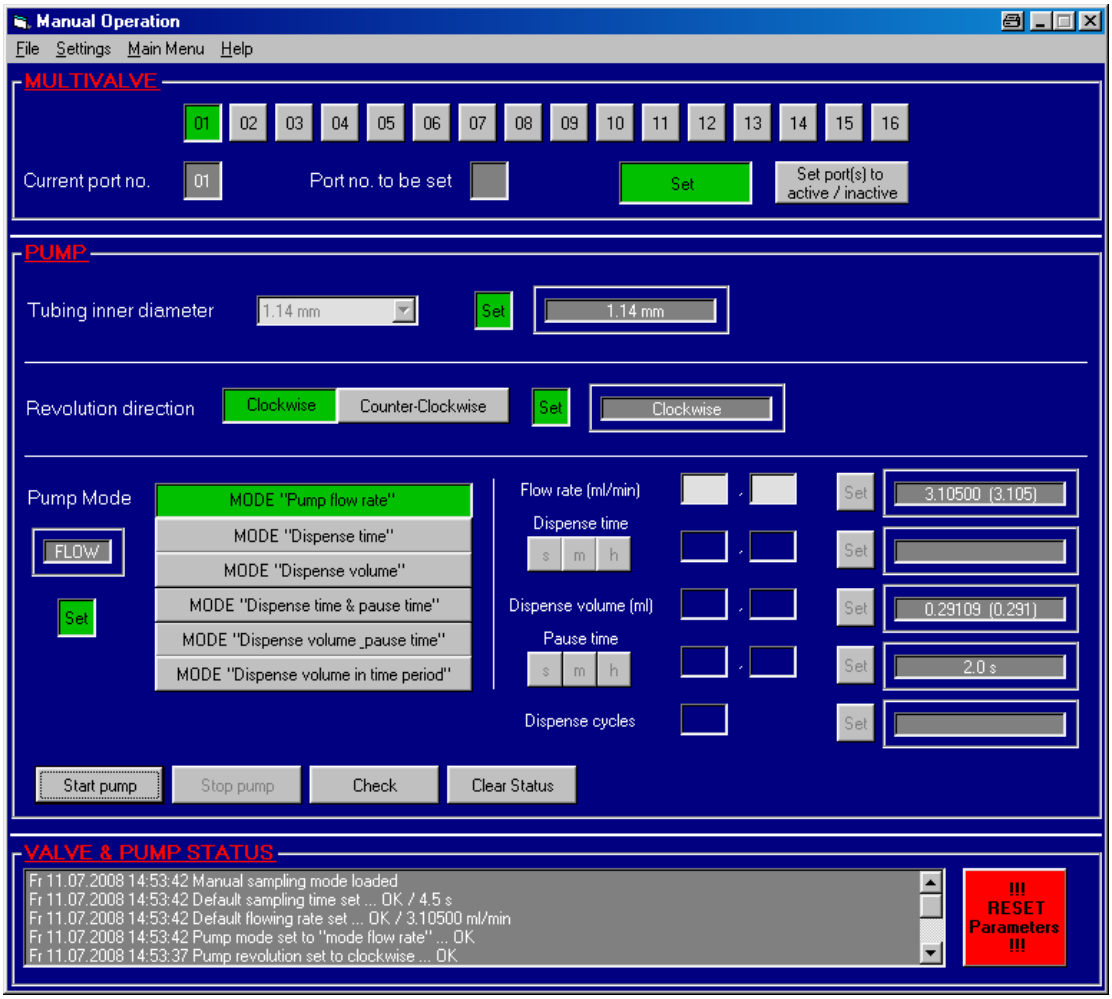

Fig. 4.8 The manual operating mode of the solution sampling software

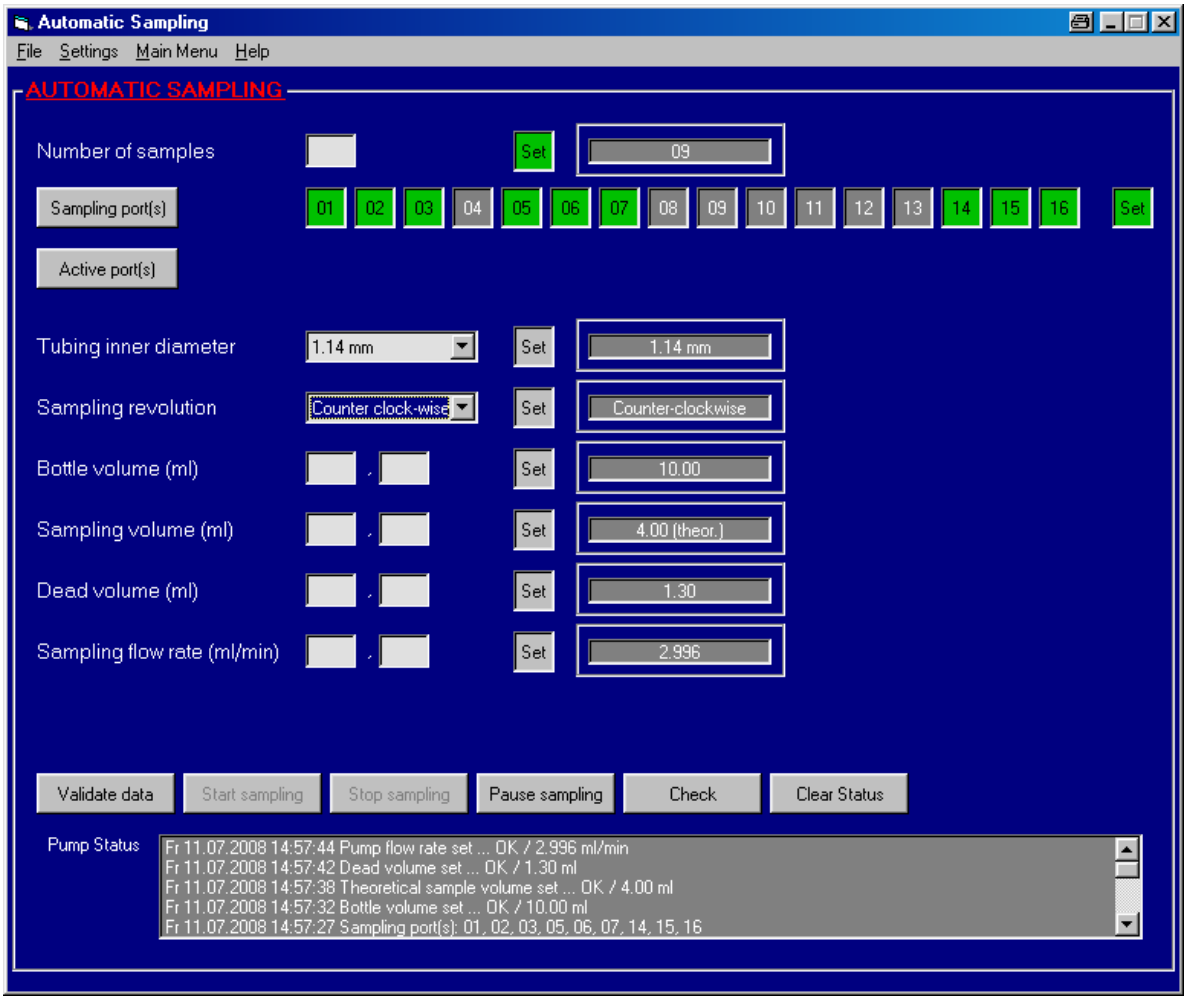

Fig. 4.9 The automatic operating mode of the solution sampling software

4.1.3. Online oxygen measurement

The fibre optical oxygen sensors use the fluorescence of a chemical complex in a sol-gel to measure the partial pressure of oxygen [56, 58, 59]. The pulsed blue LED sends light, at ~475nm, to an optical fibre. The optical fibre carries the light to the probe. The distal end of the probe tip consists of a thin layer of a hydrophobic sol-gel material. A sensor formulation is trapped in the sol-gel matrix, effectively immobilized and protected from water. The light from the LED excites the formulation complex at the probe tip. The excited complex fluoresces, emitting energy at ~600nm. If the excited complex encounters an oxygen molecule, the excess energy is transferred to the oxygen molecule in a non-radiative transfer, decreasing or quenching the fluorescence signal (see Fluorescence Quenching below). The degree of quenching correlates to the level of oxygen concentration or to oxygen partial pressure in the film, which is in dynamic equilibrium with oxygen in the sample. The energy is collected by the probe and carried through the optical fibre to the spectrometer. This data is then displayed on the monitor via the operating software.

Oxygen as a triplet molecule is able to quench efficiently the fluorescence and phosphorescence of certain luminophores. This effect, first described by Kautsky in 1939, is called "dynamic fluorescence quenching". Collision of an oxygen molecule with a fluorophore in its excited state leads to a non-radiative transfer of energy. The degree of fluorescence quenching relates to the frequency of collisions, and therefore to the concentration, pressure and temperature of the oxygen-containing media.

The output (voltage or fluorescent intensity) of the optical oxygen sensors can be expressed in terms of the Stern-Volmer algorithm. The Stern-Volmer algorithm requires at least two standards of known oxygen concentration. The first standard must have 0% oxygen concentration and the last standard must have a concentration in the high end of the concentration range in which you will be working. The fluorescence intensity can be expressed in terms of the Stern-Volmer equation where the fluorescence is related quantitatively to the partial pressure of oxygen:

$$\frac{I_0}{I} = 1 + k \cdot p_{O_2} \tag{4.1}$$

In the equation (4.1) the following notations were used:

- I_0 – intensity of fluorescence at zero pressure of oxygen;
- I – intensity of fluorescence at a pressure p of oxygen;
- k – Stern-Volmer constant.

For a given media, and at a constant total pressure and temperature, the partial pressure of oxygen is proportional to oxygen mole fraction.

The Stern-Volmer constant is primarily dependent on the chemical composition of the sensor formulation. Our probes have shown excellent stability over time, and this value should be largely independent of the other parts of the measurement system. However, the Stern-Volmer constant does vary among probes, and it is temperature dependent. All measurements should be made at the same temperature as the calibration experiments or temperature monitoring devices should be used. The relationship between the Stern-Volmer values and temperature is defined as:

$$I_0 = a_0 + b_0 \cdot T + c_0 \cdot T^2 \tag{4.2}$$

$$k = a + b \cdot T + c \cdot T^2 \tag{4.3}$$

The intensity of fluorescence at zero pressure of oxygen, I_0, depends on details of the optical setup: the power of the LED, the optical fibres, loss of light at the probe due to fibre coupling, and backscattering from the sample. It is important to measure the intensity of fluorescence at zero pressure of oxygen, I_0, for each experimental setup.

It is evident from the equation that the sensor will be most sensitive to low levels of oxygen. The photometric signal-to-noise ratio is roughly proportional to the square root of the signal intensity. The rate of change of signal intensity with oxygen concentration is greatest at low levels. Deviations from the Stern-Volmer relationship occur primarily at higher oxygen concentration levels. By using the Second Order Polynomial algorithm when calibrating corrects these deviations.

The Second Order Polynomial algorithm requires at least three standards of known oxygen concentration. The first standard must have 0% oxygen concentration and the last standard must have a concentration in the high end of the concentration range in which you will be working. The Second Order Polynomial algorithm is considered to provide more accurate data because it requires at least three known concentration standards while the Linear (Stern-Volmer) algorithm requires a minimum of two known concentration standards. The Second Order Polynomial algorithm is defined as:

$$\frac{I_0}{I} = 1 + K_1 \cdot [O_2] + K_2 \cdot [O_2]^2 \tag{4.4}$$

where: - K_1 – first coefficient;
- K_2 – second coefficient.

The relationship between the Second Order Polynomial algorithm and temperature are defined similar to equation (4.2) for I_0 and similar to (4.3) for constants K_1 and K_2.

It is possible to calibrate the system in gas and then use the oxygen sensor in liquid or vice versa. In theory, the sensor probe detects the partial pressure of oxygen. In order to convert partial pressure to concentration, one can use Henry's Law. When the temperature is constant, the weight of a gas that dissolves in a liquid is proportional to the pressure exerted by the gas on the liquid. Therefore, the pressure of the gas above a solution is proportional to the concentration of the gas in the solution. The concentration (mole %) can be calculated if the absolute pressure is known:

$$p_{O_2} = x_{O_2} \cdot P \tag{4.5}$$

where: - p_{O_2} – partial pressure of oxygen;
- x_{O_2} - oxygen mole fraction;
- P – absolute pressure.

Since the sensor detects partial pressure of oxygen, the response in a gas environment is similar to a liquid environment in equilibrium with gas. Therefore, it is possible to calibrate the sensor in gas and then use the system with liquid samples and vice versa by using Henry's Law.

The oxygen probe used during the measurement it of FOSPOR type. The FOSPOR coating is applied to the distal end of the fibre and has a fluorescence-based Pt-porphyrin indicator. The sensor uses fluorescence quenching of the porphyrin to measure the partial pressure of dissolved or gaseous oxygen.

4.1.4. Cyclotron beam line

<u>He^{2+} beam line principle</u>

The He^{2+} beam used for irradiation is generated at the existing cyclotron at CERI. The diameter of the beam is approximately 6mm. For the experiments a He^{2+} beam with the energy of 45MeV is used.

The beam is penetrating the UO_2 disk from the back of the cell. The He^{2+} particles are crossing through the UO_2 disk where they loose energy. When they reach the UO_2 – water interface their energy is approximately 2-5MeV. This is the range of the energy of the α-particles generated by the decay of fission products and their daughters contained in the UO_2 matrix. In figure 4.10 the irradiation principle is presented [61].

<u>He^{2+} beam validation and calibration</u>

Before each experiment the He^{2+} beam is checked, validated and calibrated. The checking and validation are made by irradiation of a Cu plate. If the beam is He^{2+} then Ga-65 is produced by the reaction:

Cu-63 (α, 2n) Ga-65

The half-life of Ga-65 is 15 minutes and it gives a specific γ-line at 115KeV. This line is identified by gamma spectrometry.

The calibration of the beam is made using a Faraday cage at different current intensities: 3, 30 and 300pA corresponding to the associated current to the He^{2+} beam at fluxes of $3.3 \cdot 10^{7}$, $3.3 \cdot 10^{8}$ and $3.3 \cdot 10^{9} cm^{-2} \cdot s^{-1}$. The Faraday cage is simulating the electrochemical cell.

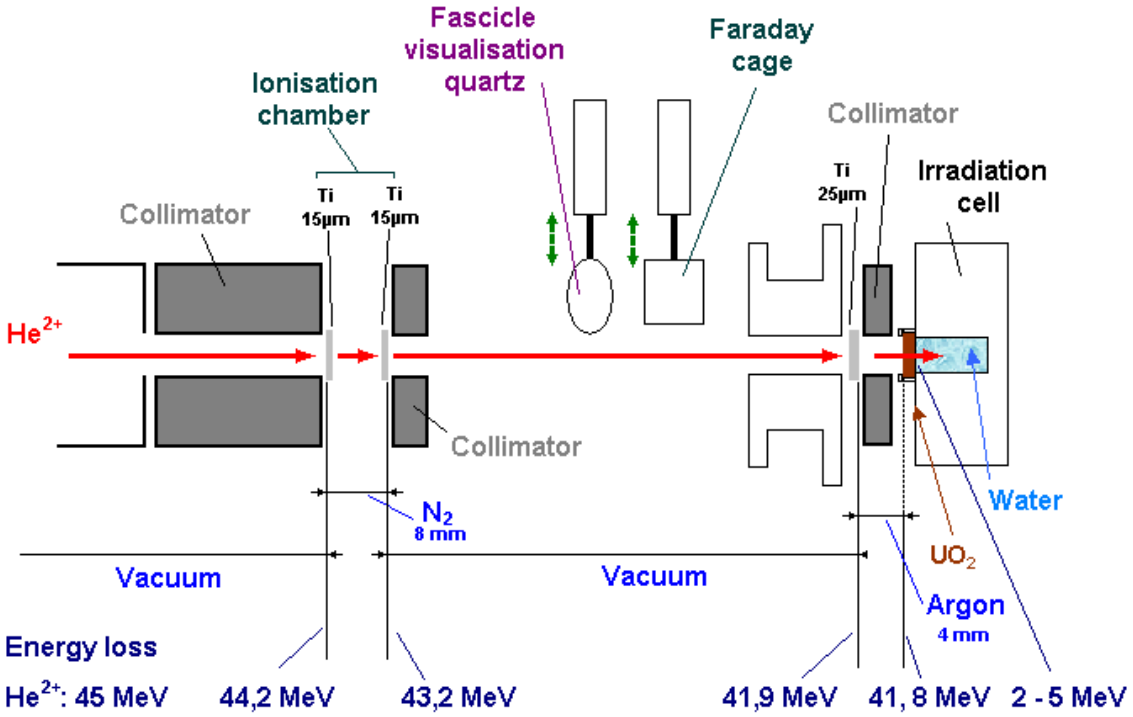

Fig. 4.10 Principle of irradiation method and beam energy distribution along the He^{2+} beam

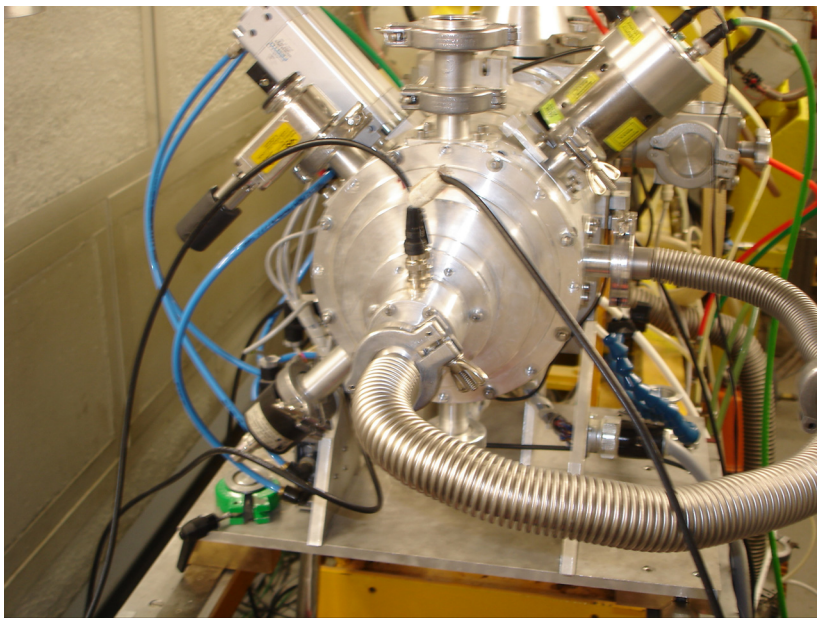

Fig. 4.11 Farday cage used for beam calibration

The electrochemical cell

The cell used for electrochemical measurements is a 3-electrode cell made of Teflon. The working electrode is a natural UO_2 disk with the diameter of 8mm and the thickness of approximately 300µm. As reference a saturated calomel electrode (SCE) was used. The counter electrode consisted of a Pt wire. The volume inside the cell is approximately 20ml. Two electrolyte solutions were used for the measurements: 5mM Na_2SO_4 and 10mM NaCl aqueous solutions.

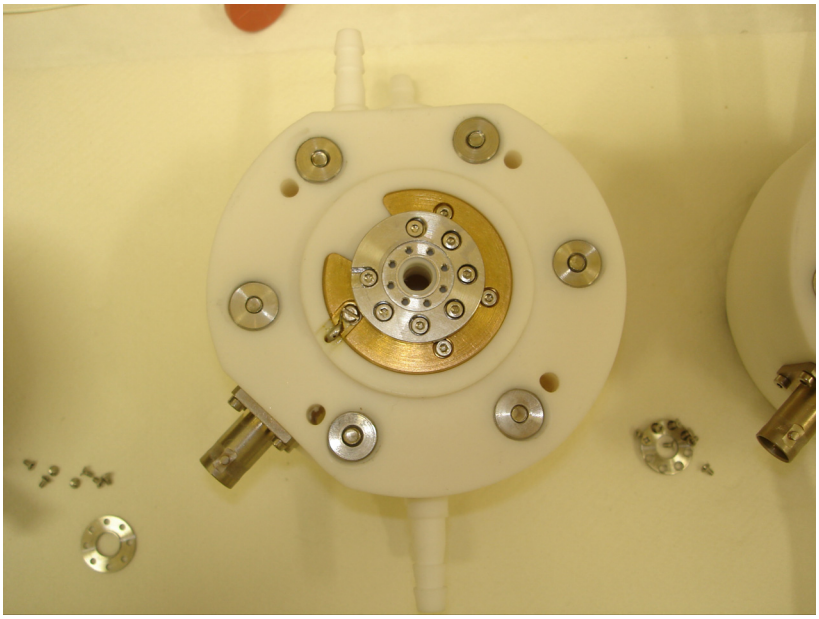

Fig. 4.12 Electrochemical cell used for irradiation experiments

The UO_2 disk is mounted on a Teflon gasket using a stainless steel ring fixed by screws. It is very important that the disk is properly fixed. If too loose then water can leak and get in contact with stainless steel and measurements are influenced by the corrosion reaction of steel. If the ring is pressed too hard the UO_2 disk can break and water will penetrate through the cracks and will get in contact with stainless steel.

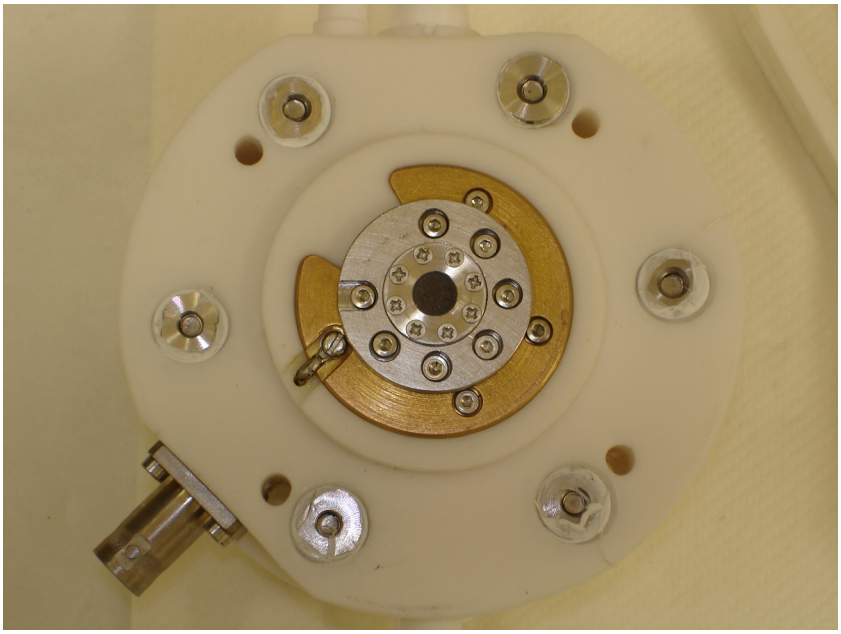

Fig. 4.13 Electrochemical cell with mounted UO_2 disk

The gas chamber

The electrochemical cell is mounted inside a gas chamber that is continuously purged with Ar or Ar/4%H_2 during the measurement. Before filling the cell with solution and starting the experiment, the gas chamber is purged for 40-45 minutes. This is made to remove the oxygen from the gas chamber.

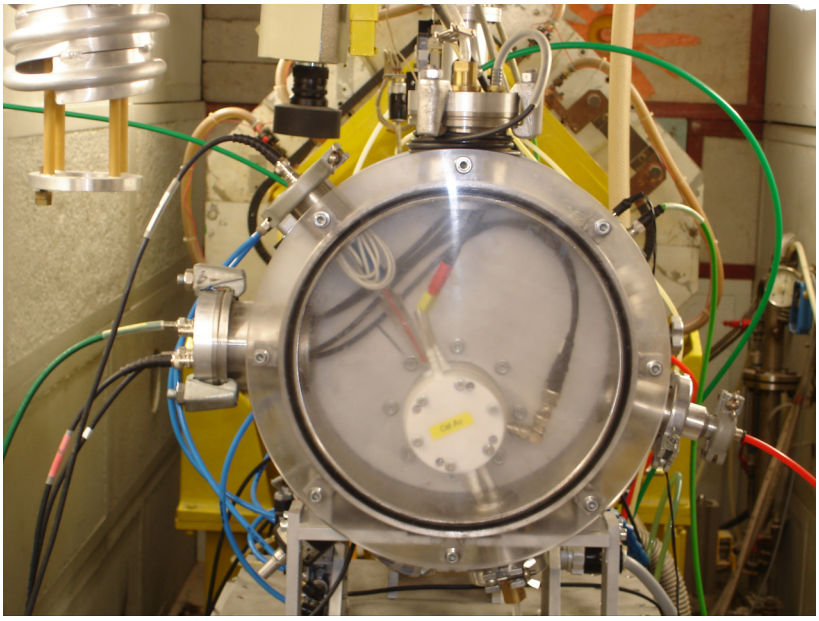

Fig. 4.14 Electrochemical cell mounted inside the gas chamber

The de-aerating & injecting system

Before introducing the electrolyte solution into the cell it needs to be de-aerated. This was realised by purging the solution with Ar for measurements in anoxic conditions and Ar/4%H_2 for measurements in reducing conditions, while steering. According to [62] the residual concentration of oxygen after 30 minutes of Ar purging and solution steering is $2.3 \cdot 10^{-6}$ M (approx. 70ppb).

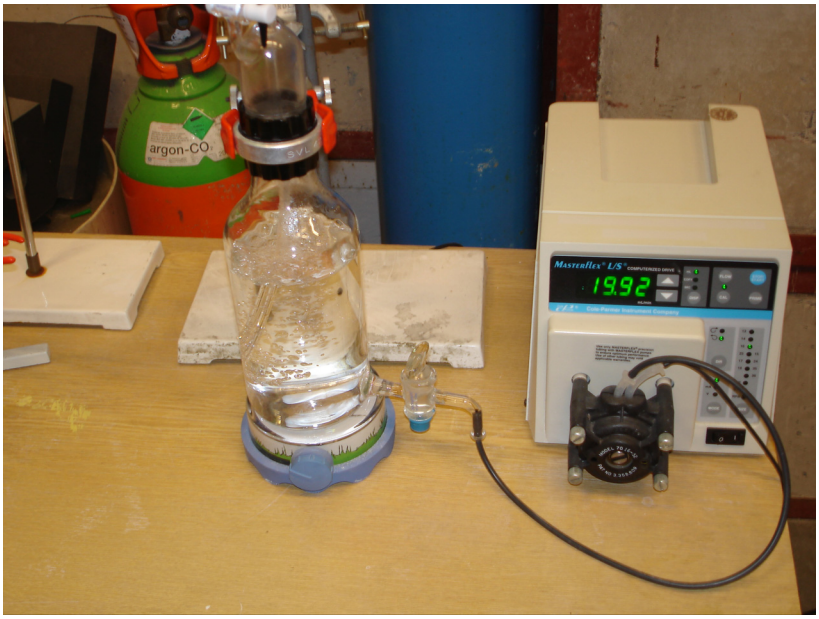

Fig. 4.15 The de-aerating and solution injection system

The de-aerated solution was then injected in the electrochemical cell using a tubing pump. Also, the solution sampling and cell rinsing was realised using another tubing pump similar to the one presented in the figure above.

4.2. Experimental conditions

The overall error for each single data point can be estimated to be in the range of 15–20%, including deviations caused by the solution analysis procedure and leaching equipment. A certain degree of scatter is typical for leaching experiments on these materials especially when trying to achieve/maintain anoxic conditions. Moreover, possible factors interfering with the quantities to be measured have been accounted for.

4.2.1. Glove box experiments

The cleaned vessel is filled with 100ml 0.01M NaCl solution and the cover is mounted in position. One redox electrode (Mettler Toledo InLab®501) and one reference electrode (Mettler Toledo InLab®302) are introduced into the solution together with a Pt auxiliary electrode. The redox electrode is used to monitor the E_h of the solution during the experiment and it is connected to the xt-recorder. The reference electrode is connected later together with the sample electrode and the auxiliary Pt electrode to the IM6 electrochemical station.

A tube is used to purge the solution with N_2 in order to remove the oxygen. One water filled bubbler is used before and one after the experimental cell in order to seal the electrochemical cell from the glove box environment. Also this is done to humidify the purging gas before it comes into contact with the NaCl solution. All the other cover holes are sealed and the solution purging with N_2 is started. The recording of the solution's E_h is started immediately (Linseis LSB 36II).

The potential of the solution drops to more negative values as the oxygen content decreases. This experimental cell is left until the solution's potential settles to a steady state value.

After the sample is pre-cathodised the glove box is purged for 5-10 minutes with ultra pure N_2 so that the atmosphere inside the glove box should have the oxygen content as low as possible.

A sample of the blank solution is taken for analysis. Then the working electrode is immersed in the cell solution and the purging tube is raised so is no longer in the solution, so only the gas phase will be purged with N_2. The electrodes from the experimental cell are connected to the potentiostat except the Pt auxiliary electrode. A capacitor is connected in parallel to the reference electrode using an additional Pt auxiliary electrode. At high frequencies, the high resistance of the reference electrode is bridged and the resulting resistance lowered. The free corrosion potential of the sample in the experimental solution is checked. The ultra pure N_2 purging is stopped and switched to normal N_2.

The corrosion potential measurements are started, measuring the variation of the free corrosion potential with time. When the measurements are finished, a new solution sample is taken. Then the EIS measurements are started at the free corrosion potential. After the EIS measurements are completed further corrosion potential measurements are done. After this set of measurements is finished, a new solution sample is taken. EIS measurements are run again at the free corrosion potential.

When the corrosion potential reached a stable value the solution in the vessel was changed with a fresh one and the purging was changed from Ar to Ar/H_2 6%. The same measurements and solution sampling sequence was repeated. After the potential reached a new stable value in these conditions the anodic polarisation curve was recorded in potentiostatic mode. Also EIS measurements were recorded and solutions were taken at each of the potential step. After the end of the polarisations the corrosion potential was again recorded in order to see the recovering of the electrode in time.

During the free corrosion potential monitoring solution samples are taken. Approx. 4 ml of solution are extracted from the experimental vessel and transferred to 10ml PE bottles containing 2ml HNO_3 2.5 M. The acid is added in order to prevent sorption of uranium inside the walls of the bottles. After the end of the experiments the solutions were analysed for uranium and other elements.

In one cell, an oxygen measurement system was installed. It allows the online measurement of oxygen while other measurements are on-going, for example corrosion potential monitoring or impedance spectroscopy.

The *p*H was also measured from time to time by using a *p*H electrode. Before immersing the *p*H electrode in the electrochemical cell the glove box must be purged with high purity N_2. This is made in order avoid oxygen getting in the experimental vessel.

4.2.2. Cyclotron experiments

Before, during and after irradiation the corrosion potential of UO_2 was recorded. The aim was to determine the influence of the alpha particles on the corrosion of UO2 and also the possible post-irradiation effects.

After the surface being prepared the cell was filled with fresh electrolyte solution. Approx. 5-10 minutes before and during the irradiation the corrosion potential of UO_2 was monitored. The normal irradiation time was approximate 1 hour for each measurement. Also after the irradiation stopped the corrosion potential was recorded for another 5 minutes. Then the solution was removed, the cell was rinsed and then filled with fresh solution. The measurement of the corrosion potential during irradiation was repeated in order to verify the reproducibility of the measurements or other measurements were made, like EIS during irradiation or recording of polarisation curves.

After the last irradiation was made the solution was removed, the cell was rinsed and filled with new solution. Then the post-irradiation corrosion potential was recorded for 8-10 hours.

Also the anodic and cathodic polarisation curves were recorded together with the EIS measurements both in Ar and Ar/H_2 4%. After each measurement at a certain potential the solution was removed and fresh solution was introduced in the cell.

In order to better understand the redox processes cyclic voltammetry measurements were recorded without and during beam irradiation at different fluxes of the He^{2+} beam.

4.3. Electrodes origin and preparation

4.3.1. Glove box experiments

For electrochemical tests electrodes from different materials have been prepared [63]. Slices of ~1 mm thickness were cut from natural and ^{233}U-doped UO_2 pellets. These were then cut into 2 halves (Figure 4.16) [83]. After annealing to maintain UO_2 at stoichiometry the halved slices were mounted upright with conductive resin on a gold coated electrode holder. Then they were impregnated under vacuum in epoxy resin (EPOTHIN) (Figure. 4.17) [83]. The electrodes were mechanically polished after curing.

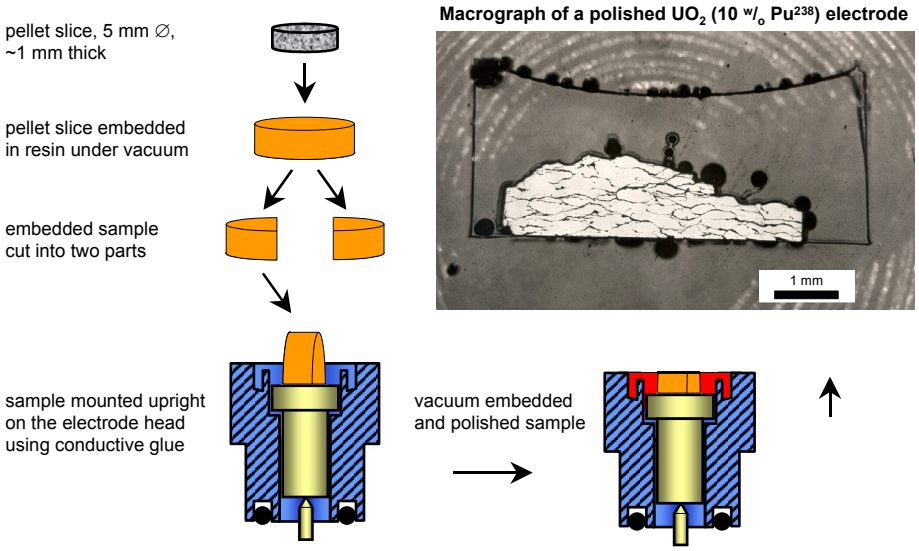

Fig. 4.16 Preparation of UO_2 samples for electrochemical experiments [83]

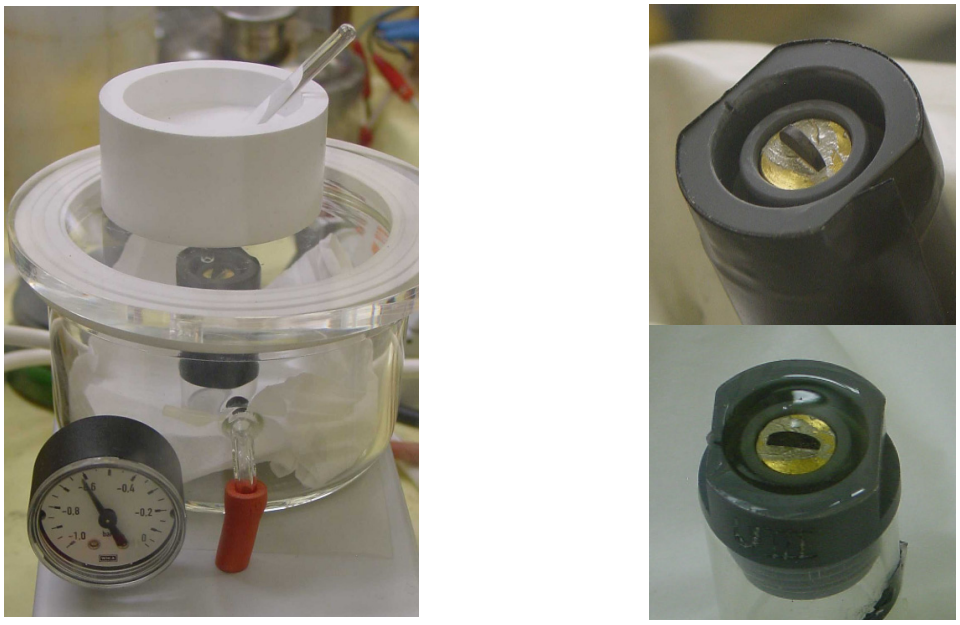

Fig. 4.17 Mounting and embedding of electrochemical samples. Left: Vacuum impregnation chamber for resin embedding. Top right: sample mounted in holder. Bottom right: sample mounted and embedded [83]

Electrochemical long-term testing under static conditions was carried out on vacuum impregnated and polished natural UO_2 (94.4% TD), 1% ^{233}U-doped UO_2 (92.4% TD) and 10% ^{233}U-doped UO_2 (94.6% TD) at room temperature. The electrodes parameters are given in figures 4.18 to 4.20.

material: NUKEM natural UO_2 (sintered pellet) mat.code: nat

description: PVC(grey), advanced design 1/2 slice mounted perpendicular on Au coated brass

4th polishing

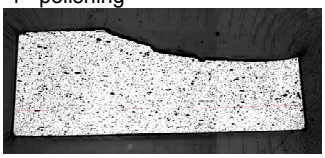

density:	ρ :	10.35	g/cm³
	ρ :	94.43	%
pellet diameter:	D_P :	9.20 ± 0.10	mm
slice thickness:	s_d :	1.84 ± 0.10	mm

geometry:

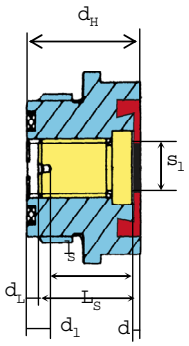

L_S :	16.70 ± 0.10	mm
l_S :	14.77 ± 0.10	mm
d_L :	-0.53 ± 0.09	mm
d_l :	1.40 ± 0.04	mm

		sample thickness		surface area	sample mass
d_H / mm	d_L / mm	d_l / mm	d / mm (d_H-L_S-d_L)	s_l / mm	A_{gp} / cm² (rectangle)	estimated m / g
18.39 ± 0.11	-0.53 ± 0.09	1.40 ± 0.04	2.22 ± 0.17	6.17 ± 0.10	0.114 ± 0.006	0.261 ± 0.013

Fig. 4.18 Geometric parameters of electrode UO_2-X (natural UO_2)

material: depleted UO_2 1% U-233 mat.code: SG101

description: PVC(grey), advanced design 1/2 slice mounted perpendicular on Au coated brass

1st polishing

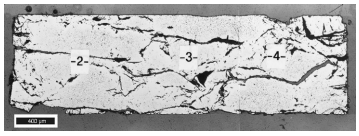

density:	ρ :	10.13	g/cm³
	ρ :	92.40	%
pellet diameter:	D_P :	5.07 ± 0.10	mm
slice thickness:	s_d :	0.96 ± 0.10	mm

2nd polishing

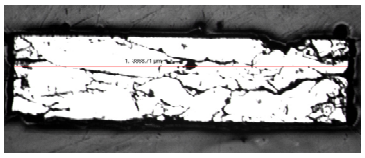

geometry:

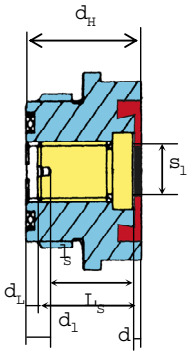

L_S :	16.83 ± 0.10	mm
l_S :	15.00 ± 0.10	mm
d_L :	0.78 ± 0.03	mm
d_l :	2.62 ± 0.06	mm

		sample thickness		surface area	sample mass
d_H / mm	d_L / mm	d_l / mm	d / mm (d_H-L_S-d_L)	s_l / mm	A_{gp} / cm² (rectangle estimate)	estimated m / g
19.25 ± 0.04	0.680 ± 0.03	2.62 ± 0.06	1.64 ± 0.11	3.87 ± 0.10	0.037 ± 0.002	0.075 ± 0.004

Fig. 4.19 Geometric parameters of electrode U-V (1% ^{233}U doped UO_2)

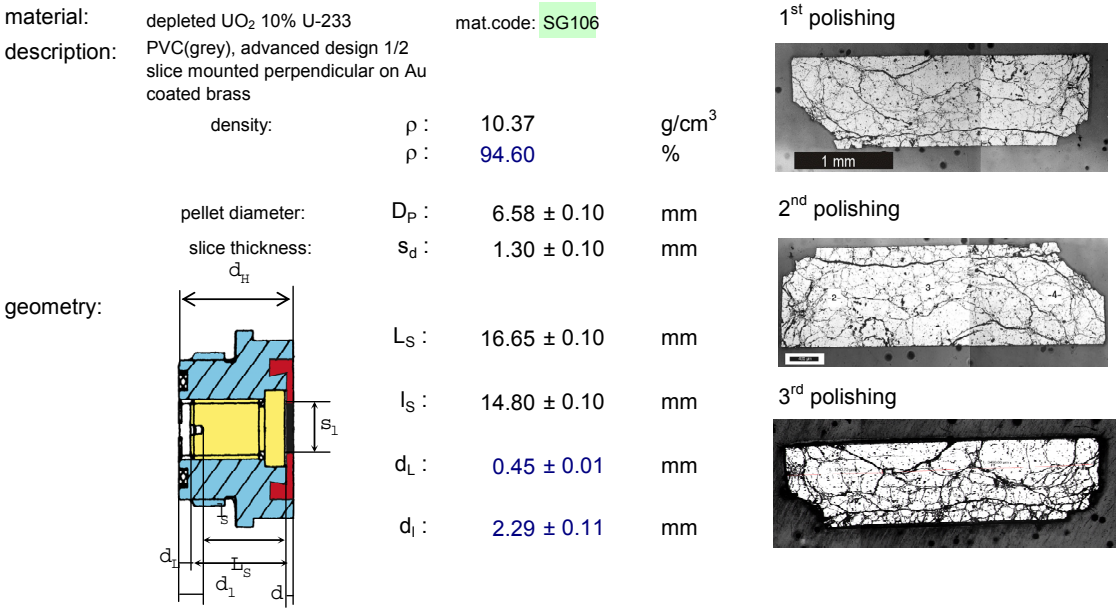

			sample thickness		surface area	sample mass
d_H / mm	d_L / mm	d_I / mm	d / mm (d_H-L_S-d_L)	s_I / mm	A_{gp} / cm^2 (rectangle)	estimated m / g (sample)
19.01 ± 0.10	0.45 ± 0.01	2.57 ± 0.11	1.91	5.05 ± 0.10	0.066 ± 0.003	0.130 0.006

Fig. 4.20 Geometric parameters of electrode U-I (10% ^{233}U doped UO_2)

4.3.2. Cyclotron experiments

Electrodes characteristics

The UO_2 disk electrodes are made from isotopically depleted material and contain 0.2% at. ^{235}U [64]. They were manufactured by The Nuclear Research Centre in Grenoble using the method described in [62]. The total disk diameter was 8mm and the beam exposed diameter 6mm. This corresponds to an irradiated surface of ~0,283cm^2. The surface characterisation of similar UO_2 disks is presented in [61]. In figure 4.21 different UO_2 disks can be seen. Also a broken disk is shown.

In total twenty five UO_2 disks were used. Fifteen electrodes were irradiated and twelve measurements carried out successfully. The other three measurements were influenced by in-leakage of electrolyte from the electrochemical cell. Two successful experiments were made without He^{2+} beam irradiation. The other eight UO_2 disks were not used due to cracking / leaking observed before starting of experiment or due to problems related to the electrical lines. More information regarding the UO_2 disks used for experiments is provided in Table 4.1.

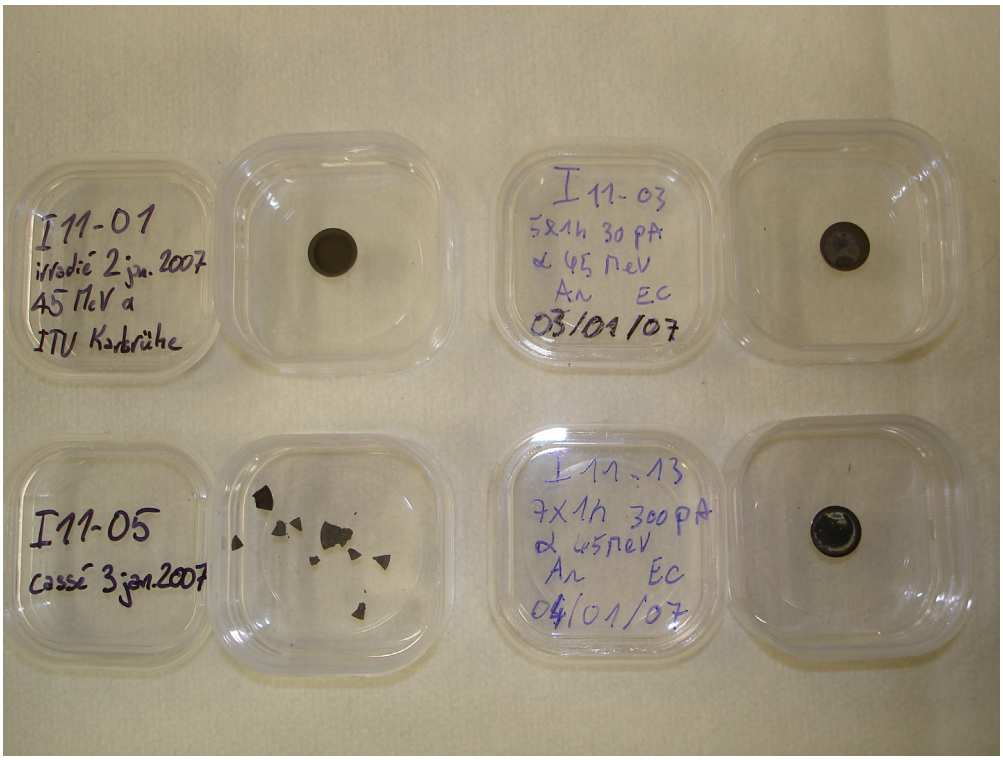

Fig. 4.21 UO_2 disks after irradiation and a broken non-irradiated disk

Table 4.1 Information about UO_2 disks used for experiments

Nr. Crt.	Designation	Thickness (µm)	Mass (g)	Beam flux (if irradiated) ($cm^{-2} \cdot s^{-1}$)	Purging gas	Comments*)
1	G11-01	296 304 305 300	0,16902	-	Ar	Na_2SO_4 5mM Ecorr, EIS, PPol
2	G11-02	305 300 301 303	0,16746	-	-	disk cracked / leakage
3	G11-03	306 307 301 300	0,16873	-	-	disk cracked / leakage
4	G11-04	302 298 302 302	0,16712	$3.3 \cdot 10^7$	Ar	Na_2SO_4 5mM Ecorr, EIS, PPol
5	G11-05	298 291 298 293	0,16608	$3.3 \cdot 10^7$	Ar	Na_2SO_4 5mM Ecorr, EIS, PPol
6	G11-06	300 300 300 296	0,16762	$3.3 \cdot 10^7$	Ar	Na_2SO_4 5mM Ecorr, EIS, PPol leakage during experiment
7	G11-13	305 295 303 301	0,16556	$3.3 \cdot 10^7$	Ar + H_2 (4%)	Na_2SO_4 5mM Ecorr, EIS, PPol leakage during experiment

Table 4.1 (cont.)

Nr. Crt.	Designation	Thickness (µm)	Mass (g)	Beam flux (if irradiated) ($cm^{-2} \cdot s^{-1}$)	Purging gas	Comments*)
8	G11-15	300 296 297 296	0,16402	-	Ar + H_2 (4%)	Na_2SO_4 5mM Ecorr, EIS, PPol
9	G11-16	300 301 295 299	0,16577	$3.3 \cdot 10^7$	Ar + H_2 (4%)	Na_2SO_4 5mM Ecorr, EIS, PPol
10	H11-04	290 291 293 292	0,16046	-	-	big interferences from electrical lines probably due to maintenance works
11	H11-05	290 293 293 287	0,16084	-	-	big interferences from electrical lines probably due to maintenance works
12	H11-06	296 299 294 296	0,16507	$3.3 \cdot 10^7$	Ar	NaCl 10mM Ecorr, EIS, PPol
13	H11-09	300 292 298 296	0,16232	$3.3 \cdot 10^7$	Ar	NaCl 10mM Ecorr, EIS, CV
14	H11-10	296 299 295 294	0,16303	$3.3 \cdot 10^9$	Ar	NaCl 10mM Ecorr, EIS, CV
15	H11-11	296 296 296 296	0,16530	-	-	disk cracked / leakage
16	I11-01	304 298 303	0,16460	$3.3 \cdot 10^7$, $3.3 \cdot 10^8$, $3.3 \cdot 10^9$	Ar	Na_2SO_4 5mM Ecorr, GPol
17	I11-02	302 294 300	0,16250	$3.3 \cdot 10^8$	Ar	Na_2SO_4 5mM Ecorr, EIS disk cracked after 1st irradiation
18	I11-03	295 292 290	0,15864	$3.3 \cdot 10^8$	Ar	Na_2SO_4 5mM Ecorr, EIS, PPol
19	I11-05	302 300 297	0,16390	-	-	disk cracked / leakage
20	I11-08	306 299 298	0,16389	$3.3 \cdot 10^7$	Ar	Na_2SO_4 5mM Ecorr, EIS, PPol
21	I11-10	301 298 297	0,16257	-	-	disk cracked / leakage
22	I11-12	305 301 297	0,16521	$3.3 \cdot 10^7$	Ar	Na_2SO_4 5mM Ecorr, EIS

Table 4.1 (cont.)

Nr. Crt.	Designation	Thickness (µm)	Mass (g)	Beam flux (if irradiated) ($cm^{-2} \cdot s^{-1}$)	Purging gas	Comments*)
23	I11-13	301 302 295	0,16382	$3.3 \cdot 10^{9}$	Ar	Na_2SO_4 5mM Ecorr, EIS, PPol
24	I11-14	295 298 301	0,16163	-	-	disk cracked / leakage
25	I11-15	309 303 302	0,16707	$3.3 \cdot 10^{8}$	Ar	Na_2SO_4 5mM Ecorr, EIS

*) Ecorr – corrosion potential
EIS – electrochemical impedance spectroscopy
PPol – potentiostatic polarisation
GPol – galvanostatic polarisation

Leakage testing

After the disk was mounted as seen in fig. 4.1 the electrochemical cell was tested for any possible leakage of solution during measurements. This is done because in case of leakage the water would come in contact with the stainless steel parts. If this occurs then the corrosion potential is shifted to lower values due to corrosion of steel which is a competitive process to that of UO_2. For a first leakage test the cell is filled with the solution to be used and left for 1 hour.

Surface cleaning

When the UO_2 disk is mounted leak tight the solution is removed and the cell is mounted in the gas chamber. At the end the gas chamber is also closed and the purging starts using N_2. After 45 minutes of purging it is considered that the oxygen content in the gas chamber is at the limit which can be achieved inside the gas chamber. Qualitative measurement by gas chromatography indicated that residual peak for O_2 remain constant after approx. 45 minutes of purging [61]. The cell is filled with electrolyte solution and the corrosion potential is measured for 15 minutes. Then a second more sensitive leakage test is performed. An impedance spectrum is recorded which is able to detect even micro-cracks in the UO_2 disk. The measurement is made in the frequency range between 1Hz and 10kHz. After the EIS measurement the solution is removed and the cell is filled with new solution. This sequence of measurements and solution changing is repeated 3 more times. The last impedance spectrum is recorded in the frequency range between 2mHz and 10kHz. This measurement gives also indications about the corrosion rate.

After these successive dissolutions (3 of approx. 15-20 minutes and 1 of approx. 1 hour) the corrosion potential is not varying considerable in time and thus the surface is considered to be clean.

5. Results

5.1. Electrochemical results

5.1.1. Redox potential and *p*H

The redox potential was monitored continuously during long time experiments made on natural, 1% and 10% ^{233}U doped UO_2 electrodes. Before the immersion of electrodes each of the electrochemical vessels was purged using Ar in order to remove as much as possible the oxygen from the system. For a higher efficiency and faster oxygen removal the liquid phase was purged.

After the redox potential reaching a stable value, the sample electrodes were immersed in 10mM NaCl aqueous solution. Also during the experiments only the gas phase above the solution was purged. First measurements were made under anoxic conditions. These conditions were ensured by continuously purging the experimental vessels with Ar. The redox potentials values decreased from 484 to 410mV vs. SHE for the natural UO_2. In case of 1% ^{233}U doped sample it decreased from 442 to 361mV vs. SHE. The same tendency was observed for the 10% ^{233}U doped sample. In this case the E_h values dropped from 527 to 428mV vs. SHE.

After 900 hours since the beginning of the experiments the solution was removed from all three vessels and fresh solution was introduced. Also the purging gas was changed to Ar/H_2 6% in order to ensure reducing conditions. The initial E_h values under the new conditions were similar to the starting values under purging with Ar.

A fast drop in the redox potential was observed in the first 5 hours to 207mV vs. SHE for the natural UO_2 sample. During and immediately solution sampling the E_h increased to 337mV vs. SHE. Then it decreased to 42mV vs. SHE. In the next approx. 100 hours the redox potential increased up to 353mV vs. SHE. During this time the purging gas was stopped due to technical problems in the central gas facility. After Ar/H_2 purging restarting the redox potential decreased. After another 500 hours the E_h value was 287mV vs. SHE. Problems in the gas lines led to stopping the purging. After consecutive turnings off and on again the redox potential increased to 429mV vs. SHE. After the gas purging was stable again the E_h decreased to 320mV vs. SHE. Some technical problems occurred in the ventilation lines of the glove boxes. As a result the glove box ventilation was interrupted. Consequently the Ar/H_2 purging was stopped due to safety reasons related to accumulation of hydrogen in the upper part of the glove box. After the problems were solved the gas purging was restarted. The redox potential in the natural UO_2 experimental vessel decreased to 330mV vs. SHE. The measurement ended after almost 3100 hours.

The E_h variation in the electrochemical cell running the 1% doped ^{233}U doped UO_2 sample showed the tendency as mentioned for the natural UO_2 sample. The redox potential increased during times when the Ar/H_2 purging was interrupted. After the gas purging restarted it decreased. However it has to be mentioned that the lowest E_h value of -210mV vs. SHE was achieved after 50 hours from replacing the solution. During the time when the gas purging was interrupted it increased to 232 and then further to 336mV vs. SHE. Afterwards the E_h showed a continuous decreasing tendency. At end of the almost 3300 hours of measurement, the E_h value was 296mV vs. SHE. In 50 hours of measurement in reducing conditions, the redox potential in the experimental vessel containing the 10% ^{233}U doped UO_2 sample decreased initially from 529 to -8 mV vs. SHE. Solution sampling and then interruption of gas purging led to the increase of the E_h to 308mV vs. SHE. Although the redox potential was affected by the successive purging gas interruptions the variations were only about 20mV.

At the end of the 3300 hours of measurement the redox potential was 249mV vs. SHE. The variations of the redox potential in all three experiments can be seen in figure 5.1.

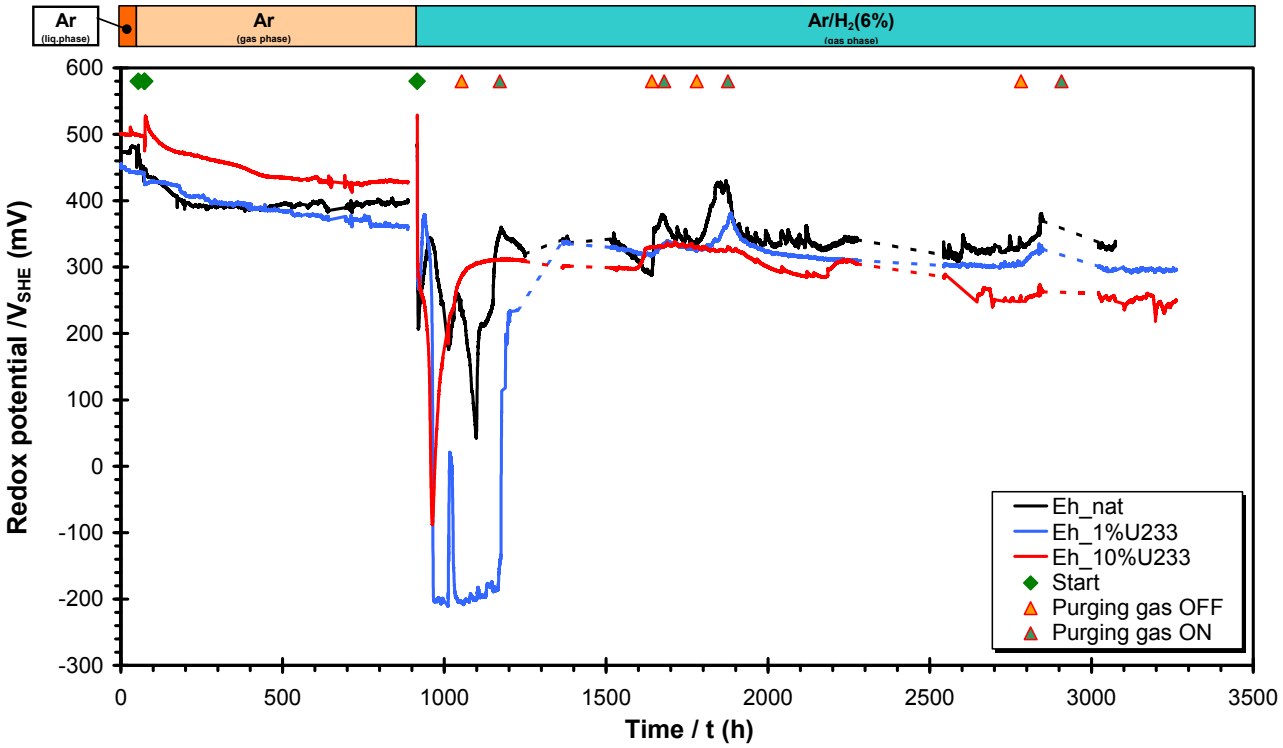

Fig. 5.1 Redox potential variation during glove box experiments

In figure 5.2 the changes on the *p*H of the solutions in the electrochemical cells are presented. The *p*H was not measured continuously but only from time to time.

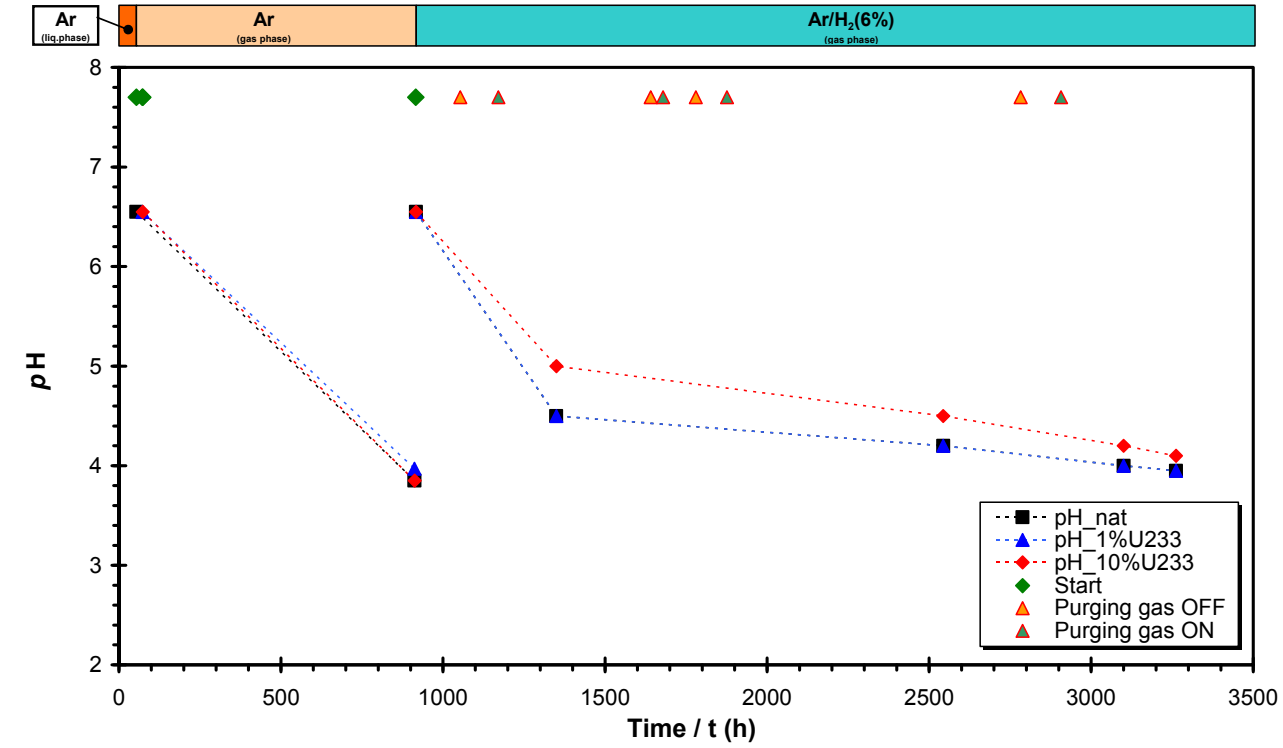

Fig. 5.2 *p*H variation during glove box experiments

In all three vessels, the *p*H dropped from 6.55 in the fresh 10mM NaCl solution to 3.85 for natural UO_2 and 4.06 for 10% ^{233}U doped sample. In case of 1% ^{233}U doped sample the *p*H value dropped to 3.97.

After changing the solutions and the purging gase from Ar (anoxic) to Ar/H_2 6% (reducing) the *p*H in all three vessels decreased again from 6.5 to approx. 4. A higher value was recorded for the high level doped UO_2 sample for which the *p*H was 4.2.

5.1.2. Free corrosion potential

Glove box experiments

In general, the free corrosion potential showed similar variation as the redox potential in the solution in all the three electrochemical cells. Before the starting of the experiments each electrode was pre-cathodised in another cell, at an imposed potential of -2V vs SHE. This opration was made in order to clean the UO_2 surface and to reduce it as close as possible to the stoichiometric $UO_{2.00}$. Then the clean electrodes were immersed in the 10mM NaCl solution previously purged with Ar. In the first 500 hours the corrosion potential increased constantly for all three electrodes. Then it stabilised in case of natural UO_2. For the 1% ^{233}U doped sample after a short stabilisation period it decreased approx. 40mV. The 10% ^{233}U sample continued to increase and started to stabilise after 800 hours. However an important role in the time needed for the corrosion potential to stabilise it is played by the electrical resistance of the electrodes. Since they were initially polarised to a very low imposed potential if the bulk resistance of the electrode was lower then the real polarisation potential was closer to the imposed one because the lower ohmic drop. The impedance spectroscopy measurements pointed the fact that the high doped sample had a lower resistance while low doped sample had the highest bulk resistance.

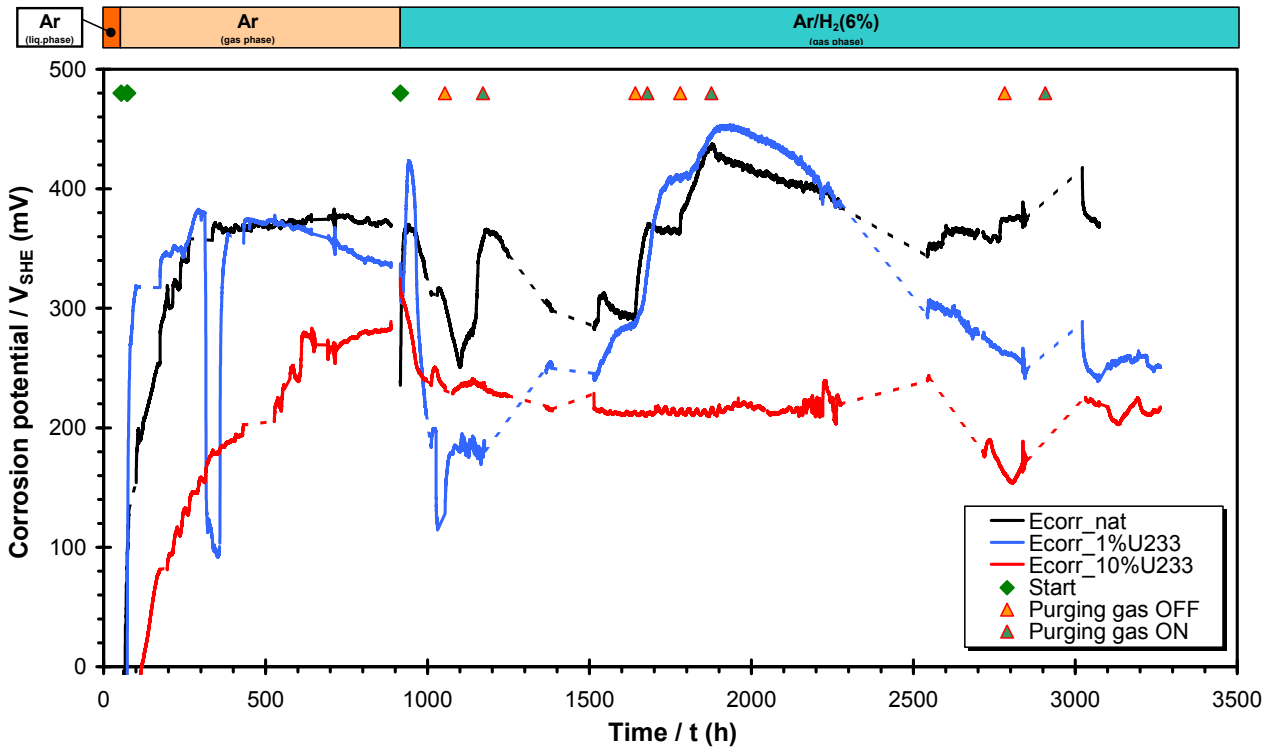

Fig. 5.3 Free corrosion potential monitored during glove box experiments

After changing the solution and the purging gas from Ar to Ar/H_2 the corrosion potentials decreased. But as the reducing conditions were not kept constant the corrosion potential increased or decreased as the concentration of hydrogen varied. Moreover not only the hydrogen concentration decreased during the time when the purging gas was not functioning but also oxygen entered into the cells. As a result the corrosion potential increased. After the Ar/H_2 gas line started to be operational the corrosion potential started to decrease again.

Cyclotron experiments

The results of the measured UO_2 corrosion potential without and under 45MeV He^{2+} irradiation are presented in Table 5.1. The graphics showing the corrosion potential variation during the measurements are presented in the Appendix A.1.

Table 5.1 UO_2 free corrosion potential during cyclotron experiments

Nr. Crt.	**Designation**	**Purging gas**	**Corrosion potential (mV_{SHE})**				
			10^3 $cm^{-2}\cdot s^{-1}$ (no beam) *)	**$3.3\cdot10^7$ $cm^{-2}\cdot s^{-1}$**	**$3.3\cdot10^8$ $cm^{-2}\cdot s^{-1}$**	**$3.3\cdot10^9$ $cm^{-2}\cdot s^{-1}$**	**post irradiation** **)
1	G11-01	Ar	285				-
2	G11-04	Ar	256	470 470			307
3	G11-05	Ar	219 300	373 405			212 -
4	G11-06	Ar	248	*330*			*170*
5	H11-06	Ar	184	380			285
6	H11-09	Ar	258	470 474			245
7	H11-10	Ar	245			580 580	369
8	I11-01	Ar	261	478	516	562	416
9	I11-02	Ar	274		503 *380* *176*		*-258*

Table 5.1 (cont.)

Nr. Crt.	Designation	Purging gas	Corrosion potential (mV_{SHE})				
			$10^3 cm^{-2} \cdot s^{-1}$ (no beam)*)	**$3.3 \cdot 10^7 cm^{-2} \cdot s^{-1}$**	**$3.3 \cdot 10^8 cm^{-2} \cdot s^{-1}$**	**$3.3 \cdot 10^9 cm^{-2} \cdot s^{-1}$**	**post irradiation**)**
10	I11-03	Ar	*74*		449		254
11	I11-08	Ar	*78*	*377*			*173*
12	I11-12	Ar	239	426 433 420			186
13	I11-13	Ar	*159*			549	297
14	I11-15	Ar	282		548 548 546		-
15	G11-13	Ar + H_2 4%	228	426 420 415			261
16	G11-15	Ar + H_2 4%	221				-
17	G11-16	Ar + H_2 4%	247	467 467 458			329

*) These measurements were made without beam irradiation. However $10^3 cm^{-2} \cdot s^{-1}$ is the maximum flux possible to be generated by the specific α-activity of the UO_2 ($1.23 \cdot 10^4$Bq/q) [65] in the given conditions.
**) Values in italics indicate cracking/leakage. Consequently water got in contact with stainless steel and the combined process potential was measured.

An increase of the corrosion potential with increase of the beam intensity was observed as shown in figure 5.4. Also no influence of the hydrogen was observed for the purging gas used and for the measured period (1 hour) at a beam flux of $3.3 \cdot 10^7 cm^{-2} \cdot s^{-1}$. A small decrease of the corrosion potential was observed for the measurements made without and before irradiation under reducing conditions.

The corrosion potential measured after irradiation was in general higher than the initial corrosion potential, before irradiation. This observation is valid for both type of purging gases, Ar and Ar/H_2 4%.

Also the *p*H of all solution samples was measured by using a *p*H indicator paper. The *p*H for all the solutions was in the range of 4.5 to 5.0. The values close to *p*H 4.5 were recorded for the solutions coming from the polarisation measurements. The other solutions had a *p*H close to 5.0.

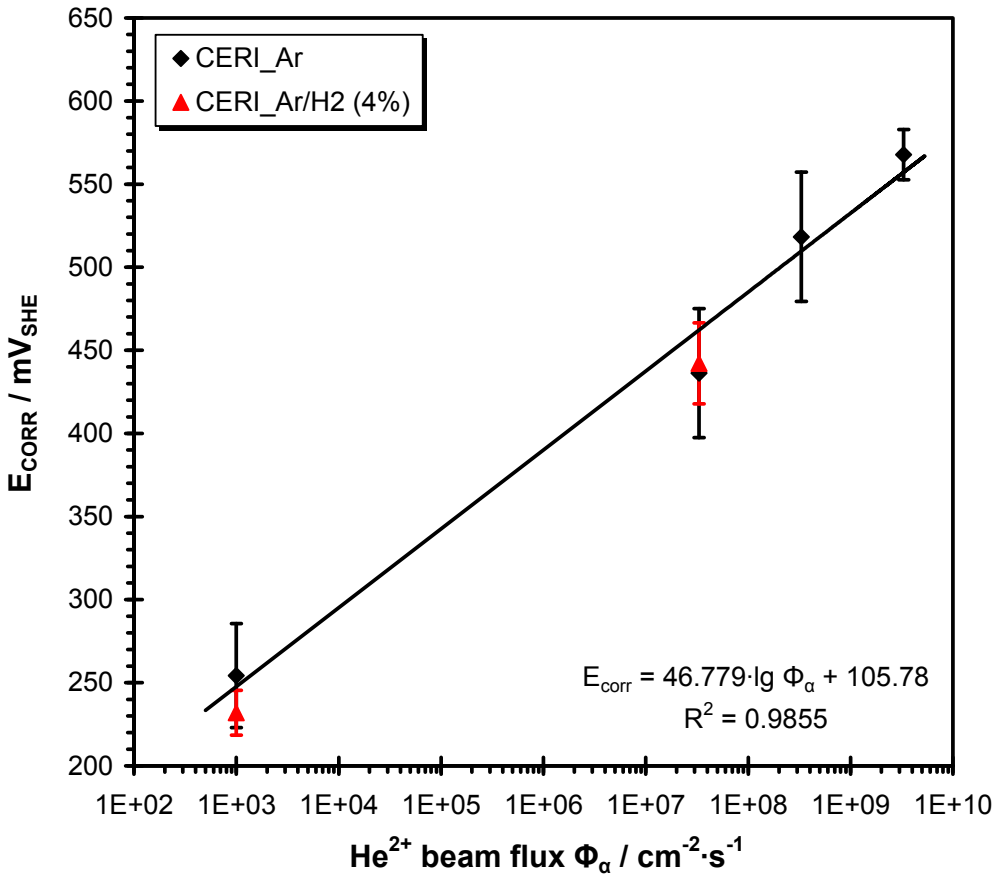

Fig 5.4 Corrosion potential dependence of the He^{2+} beam flux

5.1.3. Polarisation curves

Glove box experiments

The anodic polarisation curves were recorded under reducing conditions (Ar/H_2 6%). They were recorded in "quasi" steady state mode. The polarisation potential was imposed and the current variation was recorded for 2 hours. The value of the current after stabilisation was used further for the polarisation curves. The polarisation curves are presented in Appendix A.2.

The bulk resistance of the UO_2 electrode, R_{bulk}, determined from EIS measurements was used to correct the polarisation potential for the ohmic drop.

The calculated values are presented in the Appendix A.3 and the polarisation curves are presented in figure 5.5. The calculated Tafel slopes were approx. 42mV/decade for natural UO_2 sample and approx. 51mV/decade for the 1 and 10% ^{233}U doped samples.

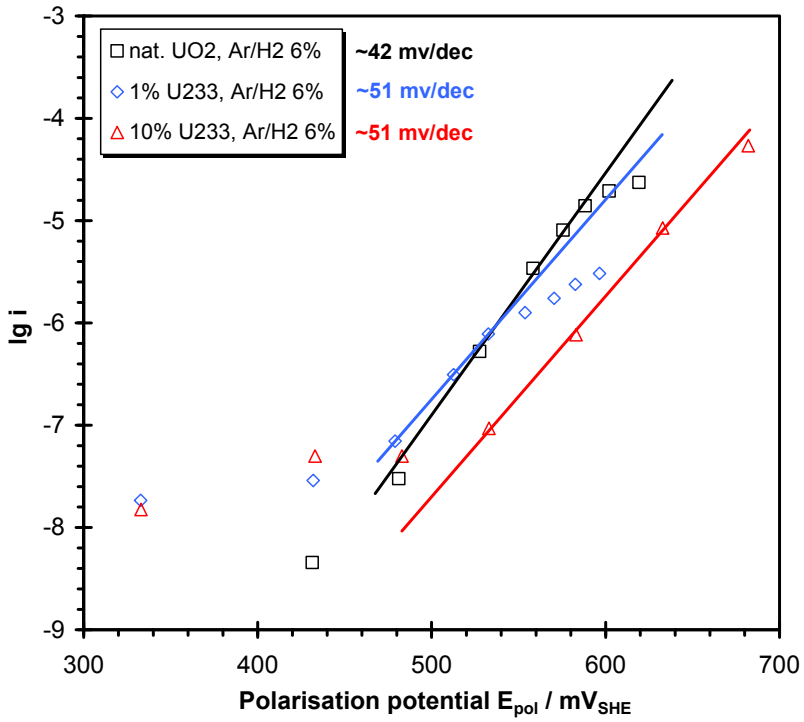

Fig. 5.5 Anodic polarisation curves recorded under Ar/H_2 6% purging
(polarisation potential was corrected for the ohmic drop due to UO_2 bulk resistance)

Cyclotron experiments

The cathodic polarisation curves were recorded in anoxic conditions (Ar purging) under He^{2+} beam irradiation with a particle flux of $3.3 \cdot 10^7 cm^{-2} \cdot s^{-1}$ and also without irradiation. The determined slopes showed values of -370mV/decade under irradiation and -357mV/decade without irradiation.

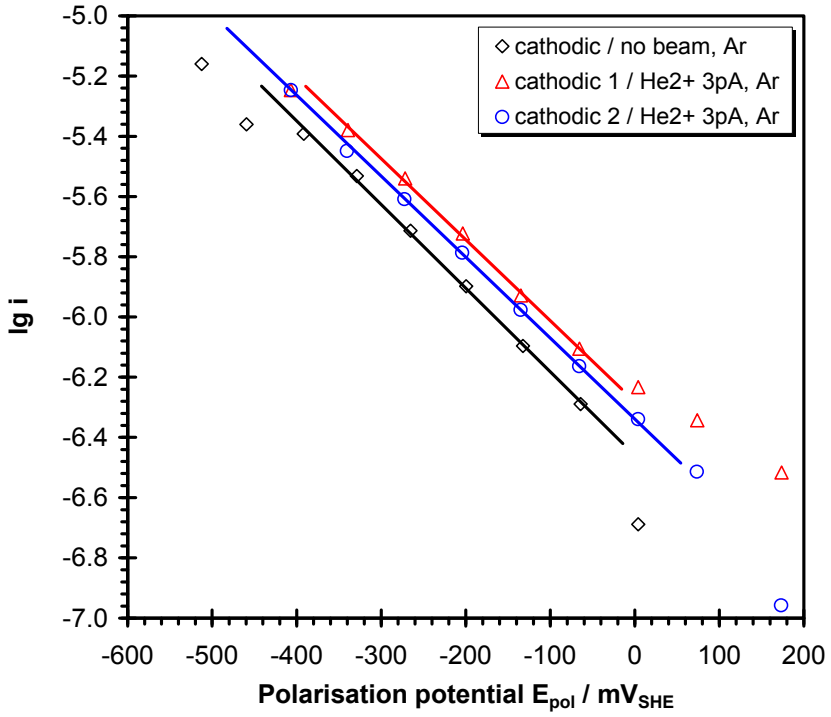

Fig. 5.6 Cathodic polarisation curves recorded under Ar purging
(polarisation potential was corrected for the ohmic drop due to UO_2 bulk resistance)

The anodic polarisation curves were recorded in anoxic conditions (Ar purging) and slightly reducing conditions (Ar / 4% H_2 purging) both under $3.3 \cdot 10^7 cm^{-2} \cdot s^{-1}$ He^{2+} beam irradiation and also without irradiation. No influence of the beam was observed in both anoxic and reducing conditions for the used beam flux. The slopes were 45mV/decade for anoxic conditions and 65mV/decade for reducing conditions.

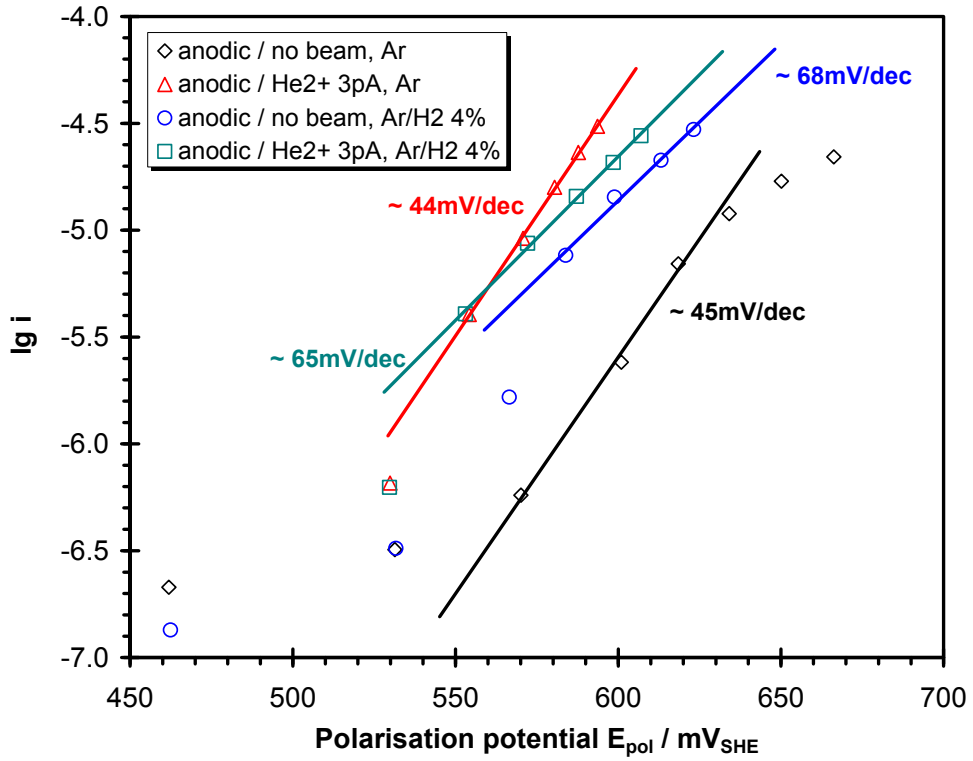

Fig. 5.7 Anodic polarisation curves under Ar and Ar/H_2 purging
(polarisation potential was corrected for the ohmic drop due to UO_2 bulk resistance)

5.1.4 Electrochemical Impedance Spectroscopy (EIS)

The impedance spectra were fitted using electrical equivalent circuits for measurements made around free corrosion potential and for measurements made during anodic polarisations [66].

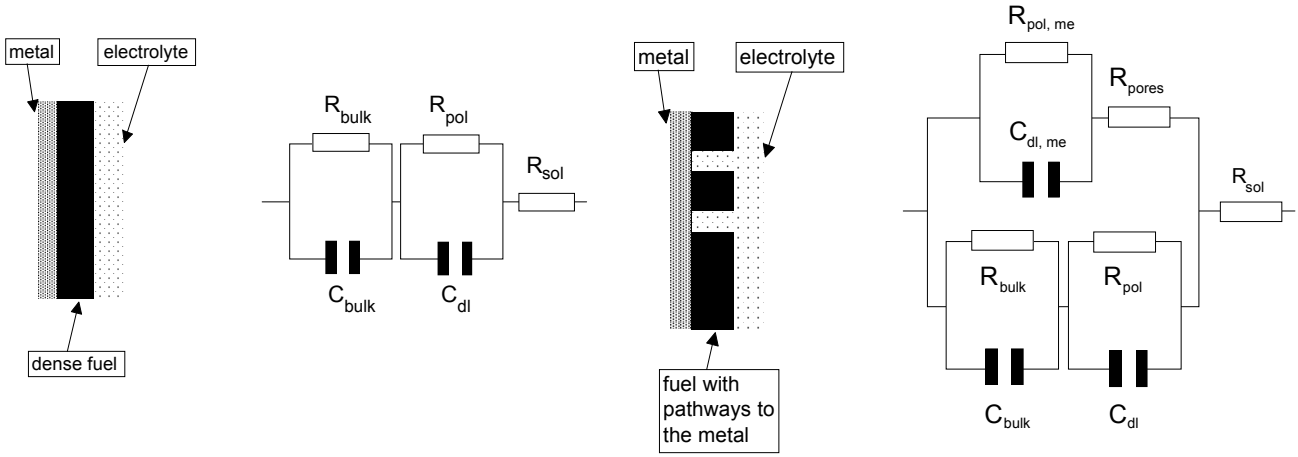

Fig. 5.8 Electrochemical systems and equivalent electrical circuits(left – no leakage; right – leakage) for EIS measurements at free corrosion potential

In figure 5.8 the symbols have the following semnification:

- R_{bulk} – bulk resistance of the UO_2 electrode, in Ohm
- C_{bulk} – bulk capacity of the UO_2 electrode, in F
- R_{pol} – polarisation resistance for the reaction at UO_2 surface, in Ohm
- C_{dl} – double layer capacity for the reaction at UO_2 surface, in F
- R_{sol} – solution resistance, in Ohm
- $R_{pol,me}$ – polarisation resistance for the leakage reaction at metal surface, in Ohm
- $C_{dl,me}$ – double layer capacity for the leakage reaction, in F
- R_{pores} – pores resistance along the leakage path, in O

The parallel circuit made from R_{bulk} and C_{bulk} is the electrical equivalent of the UO_2 electrode. The paralellel circuit made from R_{pol} and C_{dl} characterises the UO_2 – water interface inside which the charge transfer reaction takes place. The electrical conductivity of the solvent is represented by the inverse of the R_{sol}. The serial connection of the two RC parallel circuits together with R_{sol} represents the electrical equivalent circuit for the corrosion of UO_2 in aqueous solution. If a leakage occurs for instance due to a possible crack in the UO_2 material a secondary "defective" path develops. In this case the water can get in direct contact with the metal conductor on which the UO_2 is glued. The cracks will be characterised by a resistance, R_{pore}. On the interface formed at the surface of the metal a charge transfer reaction will take place, being characterised by a RC parallel circuit formed by $R_{pol,me}$ and $C_{dl,me}$. Since both reactions take place at the same time the two equivalent circuits are connected in parallel. Since the reaction on the metal will be much faster than the one on the UO_2 this will have as result the passivation of UO_2.

During polarisation a relaxation of the electrochemical system could occur especially at high polarisation potentials. This is to be taken into account as relaxation impedance, represented by relaxation resistance, R_{relax} and by relaxation inductivity, L_{relax}, coupled in serial connection.

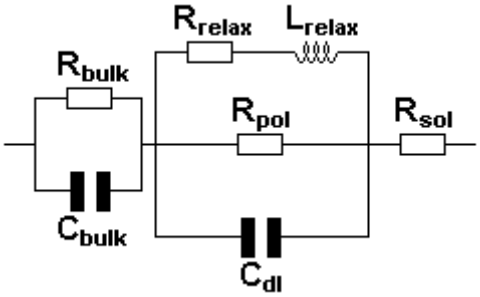

Fig. 5.9 Equivalent electrical circuit used for EIS spectra during polarisation

The inverse of polarisation resistance determined from the EIS spectra is directly related to the corrosion rate. However, this corrosion rates includes also the changes inside the electrode without transferring material into the solution, for instance partial oxidation of UO_{2+x} up to $UO_{2.33}$ or surface processes. As shown in Cap. 2 the current density can be determined if the polarisation resistance, R_p, and the Tafel coefficients are known. By using of the Faraday law, then the corrosion rate can be determined.

The EIS spectra and the fitted parameters are presented in Appendices A.4.

Glove box experiments

By use of the Electrochemical Impedance Spectroscopy the impedance spectra were recorded during free corrosion potential monitoring and also during the potentiostatic polarisation.

In figure 5.10 the bulk properties of the electrodes during the monitoring of the free corrosion potential are presented. For better comparison they are expressed in terms of resistivity (Ohm·cm) and relative capacitance ($F \cdot cm^{-2}$).

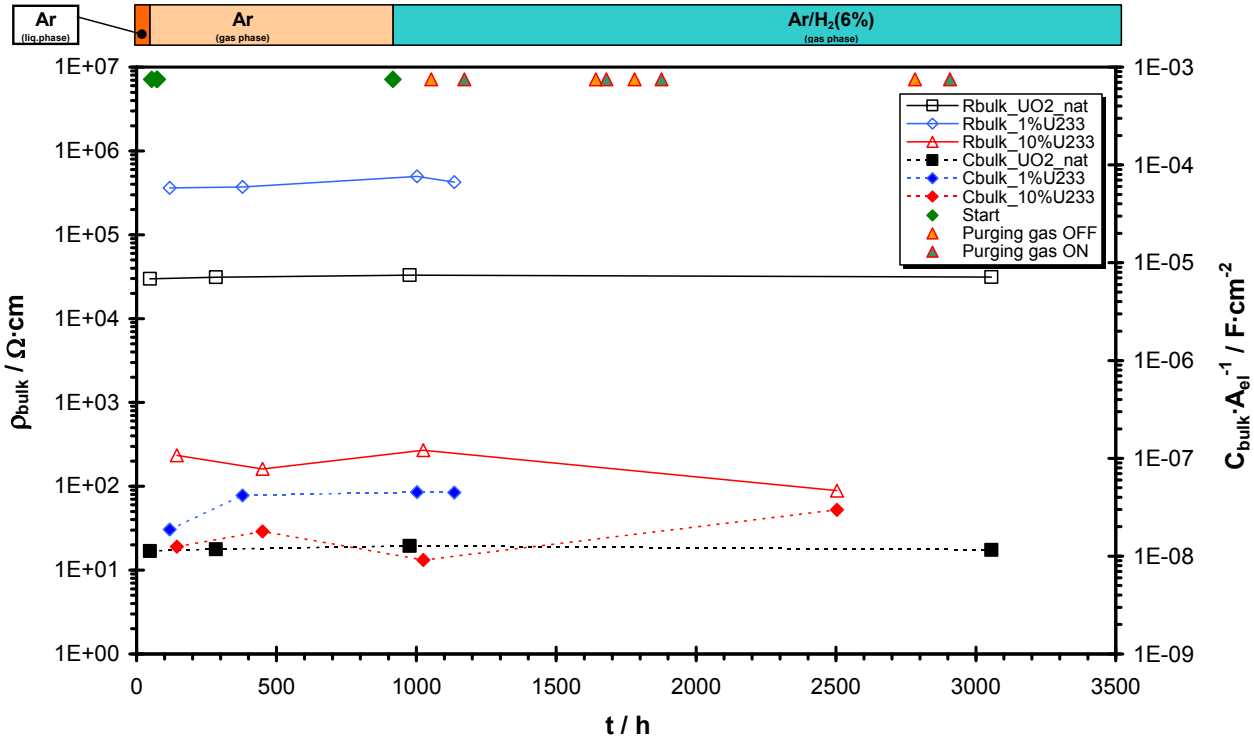

Fig. 5.10 Electrical properties of the natural and doped UO_2 electrodes during the long term experiments

It can be observed that the bulk resistivity of the 10% ^{233}U doped UO_2 sample is very low, below 1 KOhm·cm. At the opposite site the 1% ^{233}U doped UO_2 electrode shows a resistivity of more than 0.5MOhm·cm.. The relative bulk capacitances are for all thre electrodes in the range of $10^{-8}F \cdot cm^{-2}$. The low ^{233}U doped electrode showed the highest value of approx. $4 \cdot 10^{-8}F \cdot cm^{-2}$.

In figure 5.11 the polarisation resistance is presented. Also the inverse of the polarisation resistance normalised to the electrode surface is presented in $Ohm^{-1} \cdot cm^{-2}$. In general it can be observed that the polarisation resistance is decreasing with time. One exception is the case of 10% doped ^{233}U sample.

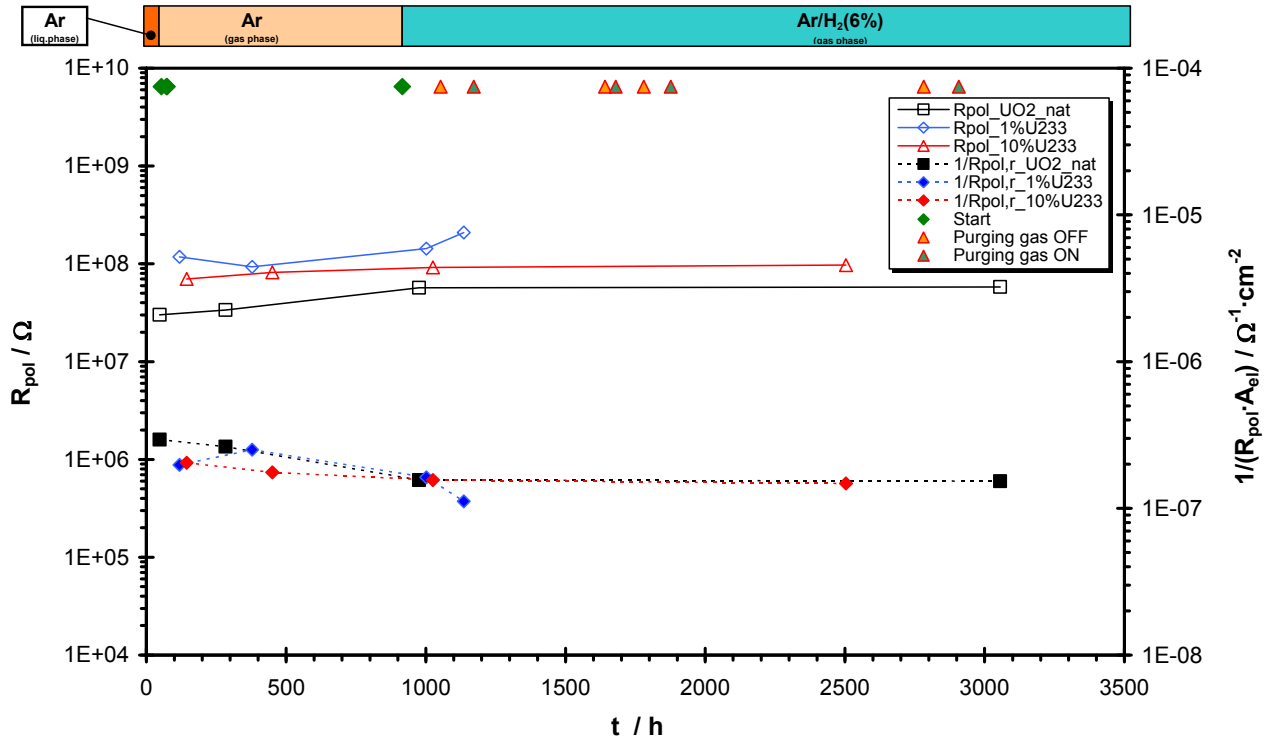

Fig. 5.11 Polarisation resistance comparison during the long term experiments

The comparison of the double layer capacitances during the measurements in the glove box can be seen in figure 5.12.

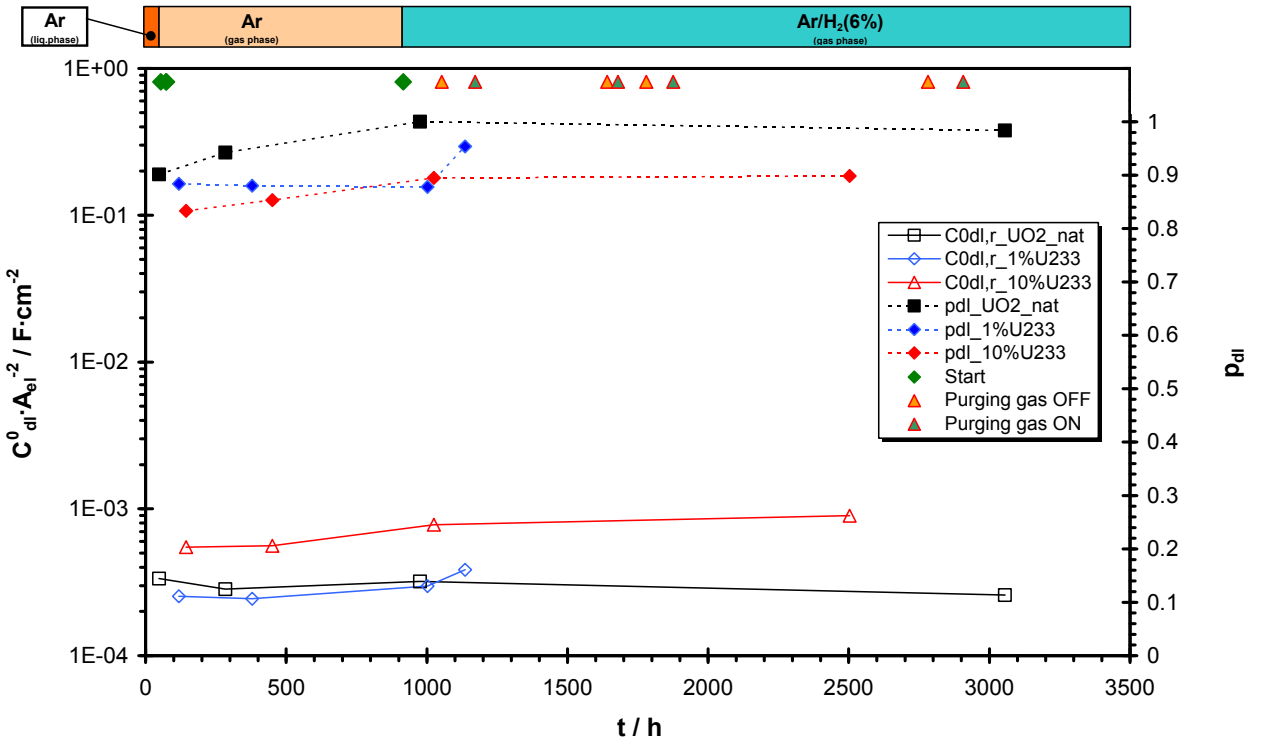

Fig. 5.12 Double layer capacitance and exponential coefficient comparison during the long term experiments

It has to be mentioned that the real double layer has a certain deviation from an ideal capacitor. This is due to the rugosity of the UO_2 surface and also to the fact that not all the surface is active (only a certain percentage of the surface is participating to the reaction). Thus it can be imagined as a capacitor with non-parallel plates. For fitting the EIS data the C_{dl} capacitor from figure 5.8 was replaced with a constant phase element (CPE). This virtual element is characterised by a module C^0_{dl} and an exponential coefficient, p, showing the deviation from an ideal capacitor.

For the long time measurements made inside the glove box it has to be taken into consideration that the solution is not steered. As a consequence the chemical species to and from the UO_2 – water interface are transported only by diffusion. This is taken into account by adding a virtual circuit element in a serial connection to the circuit presented in figure 5.8. The circuit element is called "Nernst Diffusion Impedance Element". Its role is to consider diffusion of chemical species in a finite diffusion layer inside the solution. The impedance of this element is expressed by the following equation [54]:

$$Z_N = \frac{A_N}{\sqrt{j \cdot \omega}} \cdot \tanh \sqrt{\frac{j \cdot \omega}{k_N}} \tag{5.1}$$

A_N is called Warburg parameter and k_N is called reaction constant. They are expressed by the following equations:

$$A_N = \frac{|\nu_i| \cdot p_i \cdot R \cdot T \cdot a}{z^2 \cdot F^2 \cdot C_i \cdot \sqrt{D_i} \cdot A_{el}} \tag{5.2}$$

$$k_N = \frac{D_i}{d_N{}^2} \tag{5.3}$$

The inverse of the reaction constant, $1/k_N$, corresponds to the time needed by the specie to diffuse through the Nernst layer. In the equations (5.1) to (5.3) the following notations were used:

- j – imaginary unit
- ω – angular frequency
- $|\nu_i|$ – stoichiometric coefficient the chemical specie i
- p_i – reaction order
- R – universal gas constant, 8.314 $J \cdot mol^{-1} \cdot K^{-1}$
- T – absolute temperature, in K
- a – inverse of the charge transfer coefficient
- z – number of electrons transferred during the reaction
- F – Faraday constant, 96485 $C \cdot mol^{-1}$
- C_i – concentration of the chemical specie i at the surface of the electrode, in $mol \cdot m^{-3}$
- D_i – diffusion coefficient of the chemical specie i, $m^2 \cdot s^{-1}$
- A_{el} – electrode area, in m^2
- d_N – thickness of the Nernst diffusion layer

In figure 5.13 the two parameters of the Nernst diffusion impedance are presented for all three UO_2 electrodes. It can be observed that the reaction constant is lower for the natural UO_2 sample while for the doped samples it is almost two orders of magnitude higher. The values of the Warburg parameters are within one order of magnitude for all three samples.

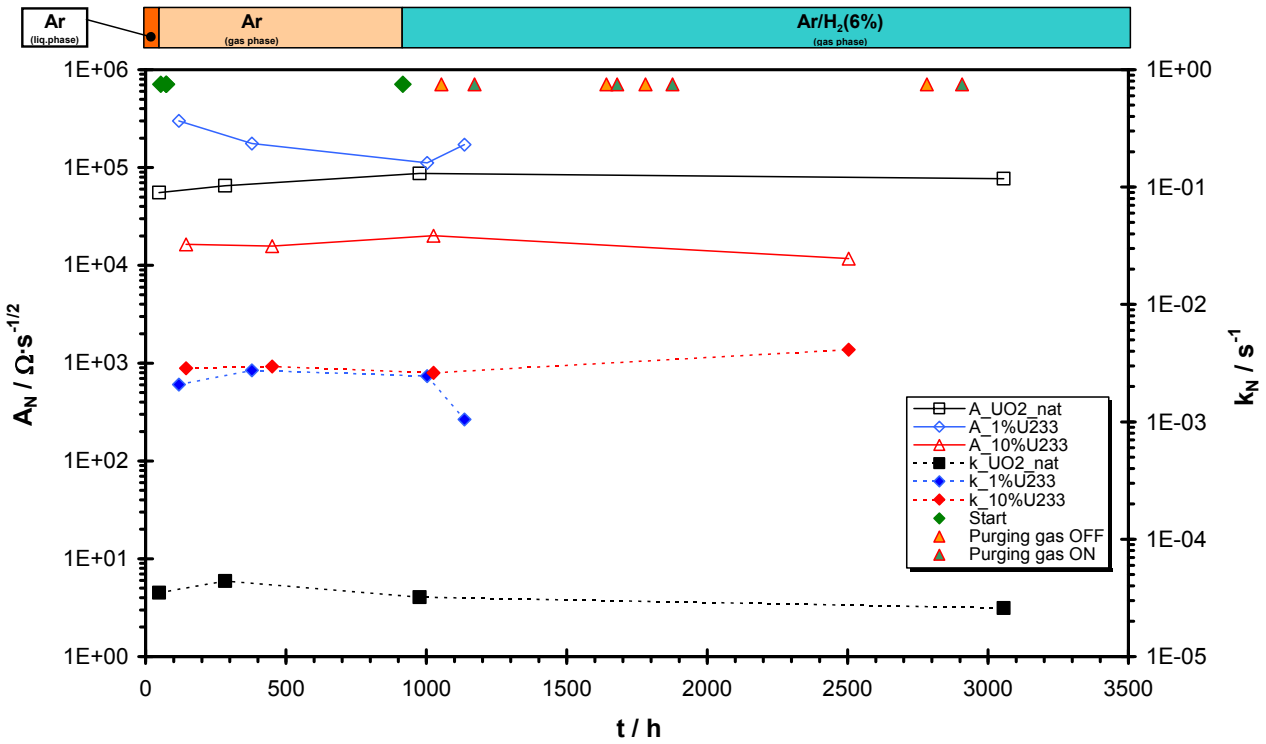

Fig. 5.13 Warburg parameter, A_N, and reaction constant, k_N, comparison during the long term measurements

The electrical properties of each of the electrodes during the polarisation sequences are presented in the figure 5.14.

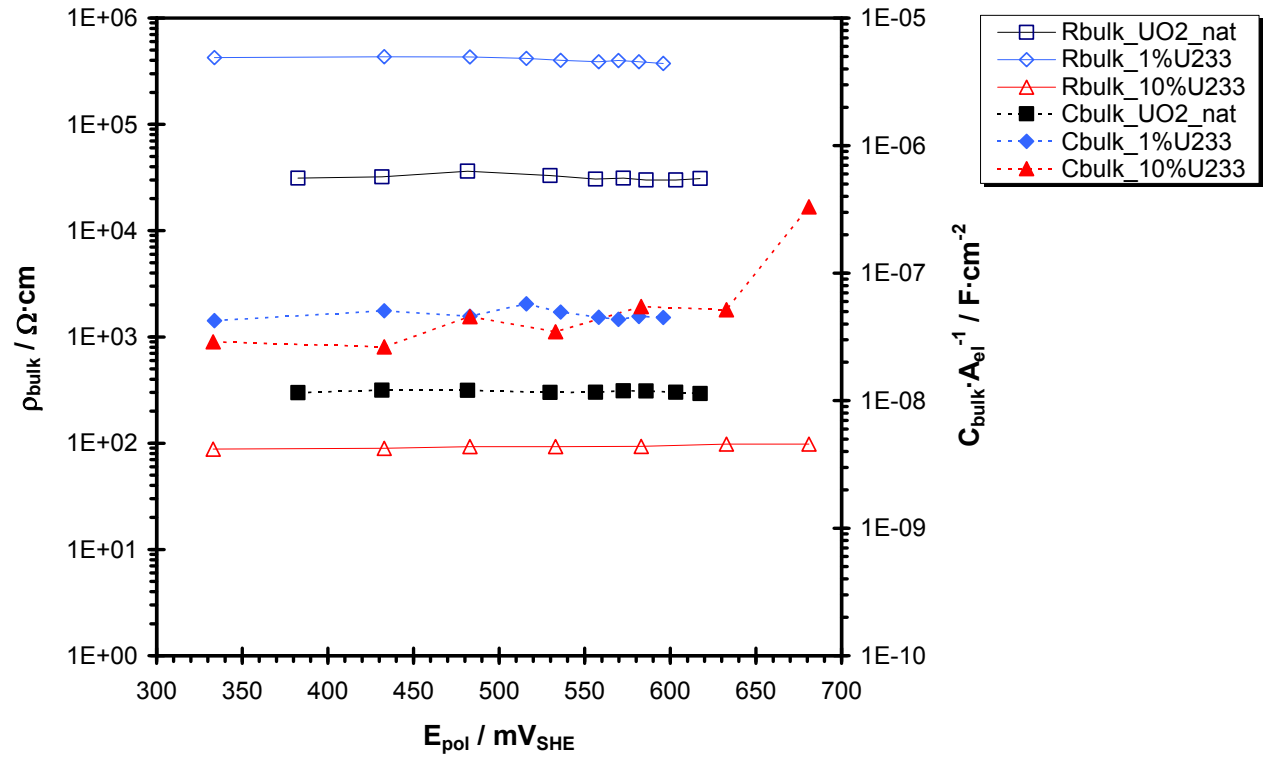

Fig. 5.14 Electrical properties of the natural and doped UO_2 electrodes during polarisation under Ar/H_2 atmosphere

It can be observed that the resistivity of the electrodes doesn't change during polarisation. However there are almost four orders between the resistivity of the 1% and 10% ^{233}U doped samples. The bulk capacity is also not changing too much, exempt for the 10% ^{233}U doped UO_2 electrode. In this case the value of the bulk capacity increases at 680 mV vs. SHE.

In figure 5.15 the variation of the polarisation resistance during the polarisation is presented. It is presented in the form of the decimal logarithm of its reciprocal normalised to the area of the electrode. It is presented in this form for a better comparison between the three electrodes and also for a comparison to the data obtained by potentiostatic polarisation method.

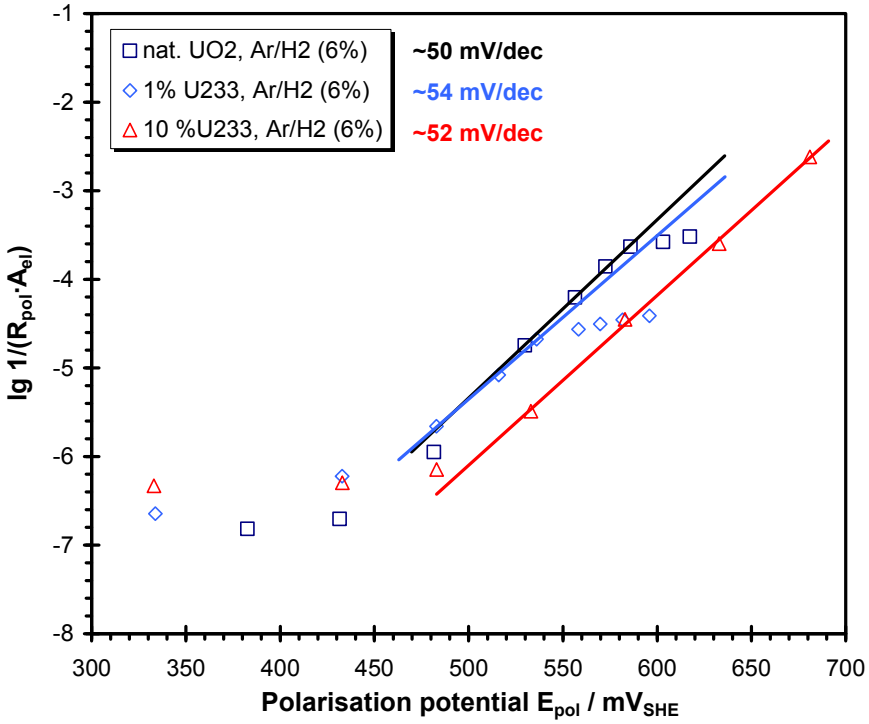

Fig. 5.15 Decimal logarithm of reciprocal of the polarisation resistance normalised to the surface area during polarisation under Ar/H_2 atmosphere

Cyclotron experiments

The corrosion rate was determined from the EIS data recorded at different fluxes of α-particles resulted from the natural radioactivity of uranium itself or simulated by irradiation using a He^{2+} beam. As observed in figure 5.16, the corrosion rate increases as the flux of the He^{2+} beam increases. Also, after irradiation the corrosion rate decreases but is higher then the one before irradiation.

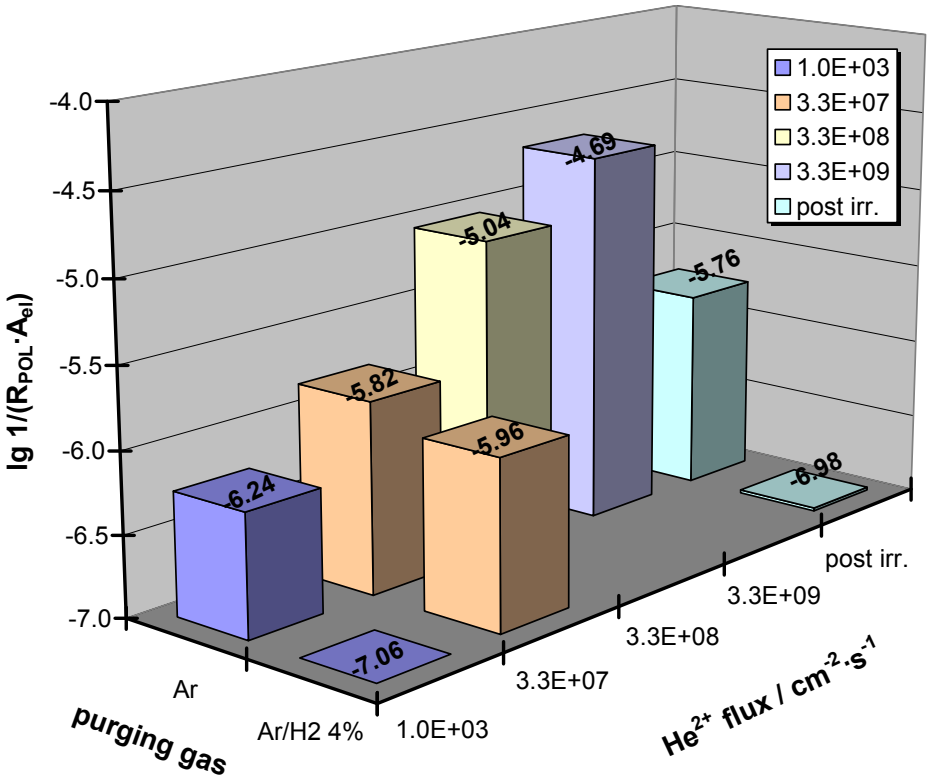

Fig. 5.16 Variation of the inverse of polarisation resistance normalised to the area of the electrode (R_{POL}) as the flux of the He^{2+} beam changes

The invert of polarisation resistances resulted from fitting of EIS spectra were plotted against the potential. Under Ar purging and irradiating with 45MeV He^{2+} beam at $3.3 \cdot 10^{7} cm^{-2} \cdot s^{-1}$ the curve slope was 52mV/decade. Under Ar/ 4% H_2 purging without beam irradiation the curve slope was 69mV/decade, while under irradiation with the same beam energy and flux the slope was 61mV/decade.

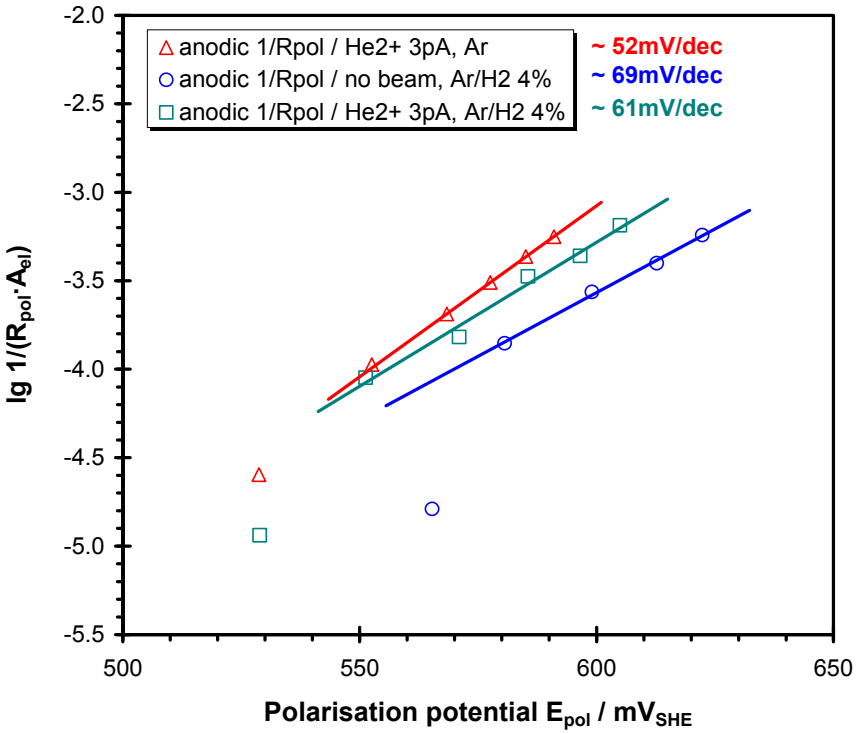

Fig. 5.17 Inverse of polarisation resistance (normalised to the electrode area) as function of polarisation potential

EIS was used also to determine electrical properties (resistivity, capacitance) of the UO_2 electrode and the influence of the He^{2+} beam irradiation on these properties. The observed values for the resistivity before and during irradiation varied between 0.05 and 0.4MOhm·cm. The variation was noticed between different UO_2 disks. However for all UO_2 samples the value of resistivity after a couple of hours from the end of irradiation decreased and in some cases even to half of the value before irradiation, the lowest value being 0.02MOhm·cm. Also during polarisation it was noticed the decrease of the electrodes resistivity, as seen in figure 5.18

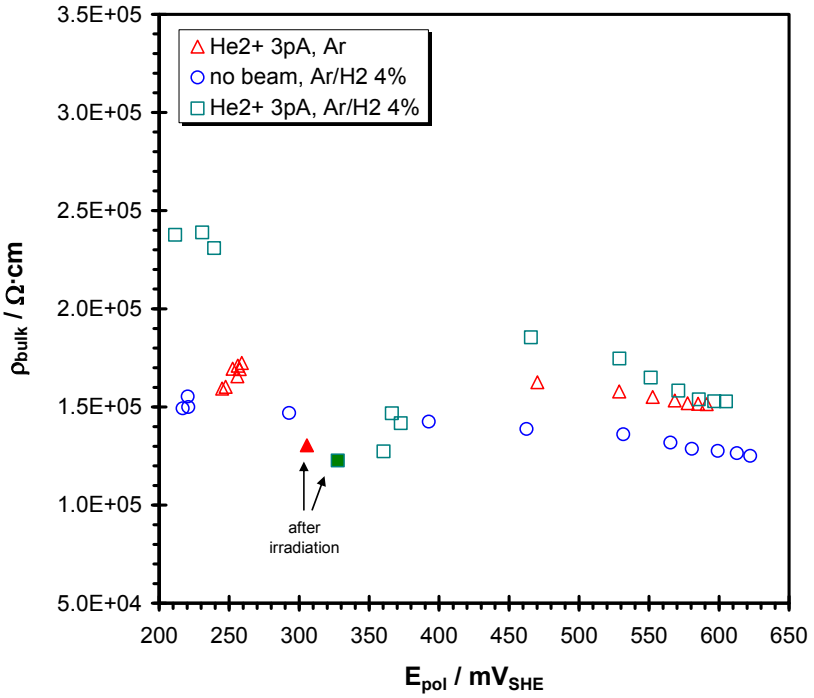

Fig- 5.18 Electrode bulk resistivity during polarisation under 45 MeV He^{2+} beam

The values of the bulk capacitance varied between 1.7 and 3.5 $nF \cdot cm^{-2}$. Again no influence of the beam was observed. A slight modification of the bulk capacitance after irradiation was noticed.

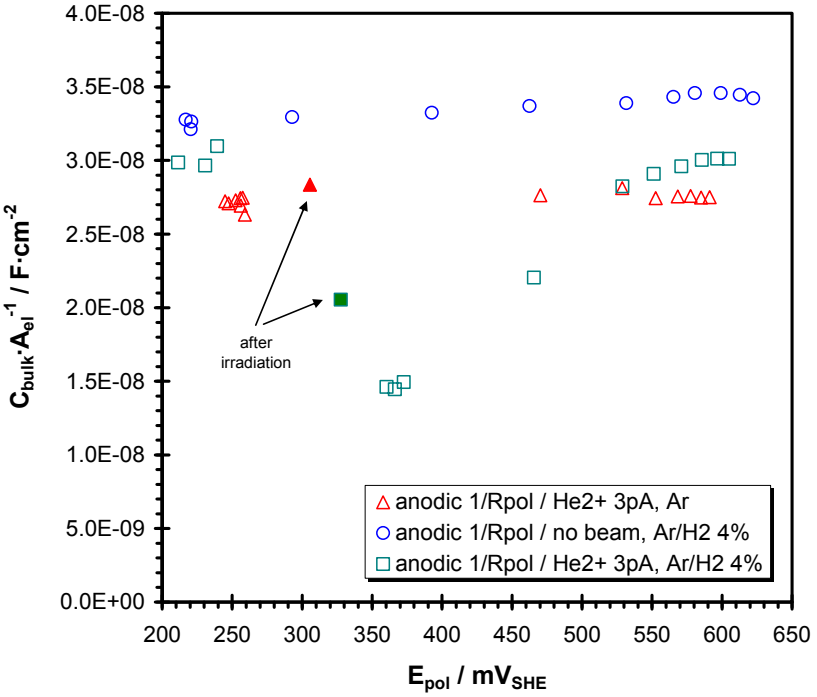

Fig- 5.19 Electrode bulk capacity normalised to the area during polarisation during 45 MeV He^{2+} beam irradiation

5.1.5 Cyclic voltammetry (CV)

Cyclic voltammograms on UO_2 before, during and after irradiation using the He^{2+} beam were recorded. The CV's were recorded using scanning rates of 10, 50 and 100mV/s. However, noticeable results were obtaining only at scanning rate of 10mV/s. For these measurements the electrolyte used was a 10mM NaCl solution, in order to avoid the possible interference of different sulphur species.

Figure 5.20 shows a cyclic voltammogram recorded on UO_2 in 10mM NaCl solution at *p*H=7 at a scan rate of 10mV/s. The obtained data are in good concordance with the literature data [67, 68, 69]. The letters indicate the various stages of oxidation which occur on the surface of the electrode. The scanning starts first in the cathodic sense from the corrosion potential established under He^{2+} beam irradiation at flux $3.3 \cdot 10^7 cm^{-2} \cdot s^{-1}$. A reduction reaction is observed in the region O corresponding to the reduction of the pre-oxidised layers ($UO_{2.33} \rightarrow UO_{2+x}$). The scanning potential is swept at -1.002V vs. SHE. Region A corresponds to a reversible oxidation of non-stoichiometric areas of the surface (UO_{2+x}). This could be associated to the grain boundaries of the sintered UO_2 pellet. Region B corresponds to the oxidation of the UO_2 matrix ($UO_2 \rightarrow UO_{2+x}$). In region C, further oxidation of the surface takes place to produce soluble U^{VI} species ($UO_{2+x} \rightarrow UO_2^{2+} + 2e^-$). In neutral solutions it is expected that these species precipitate on the electrode surface as a hydrated deposit ($UO_2^{2+} \rightarrow UO_3 \cdot xH_2O$). The potential sense is switched at +0.838mV vs. SHE to cathodic sense. The U^{VI} deposit and the oxidised surface layer are reduced in region D ($UO_3 \cdot xH_2O \rightarrow UO_{2.33} \rightarrow UO_{2+x}$). Reaching region E a further reduction of the oxidised layers takes place.

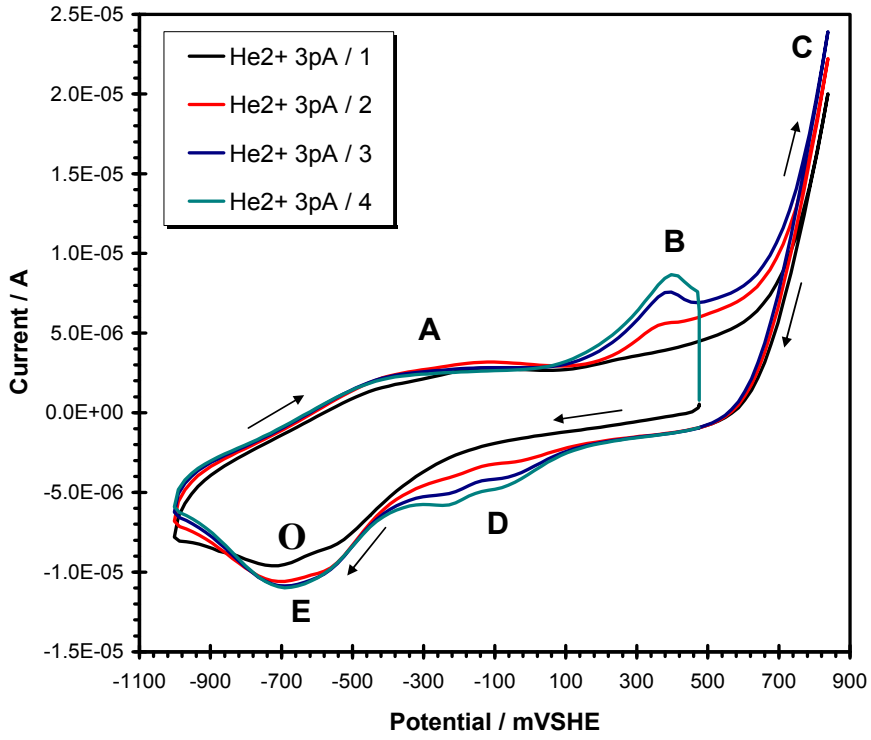

Fig. 5.20 Cyclic voltammogram (scanning rate 10mV/s) during He^{2+} beam irradiation at $3.3 \cdot 10^7 cm^{-2} \cdot s^{-1}$ flux (beam current 3pA)

No big difference can be observed in the cyclic voltammogram recorded after the end of irradiation (figure 5.21).

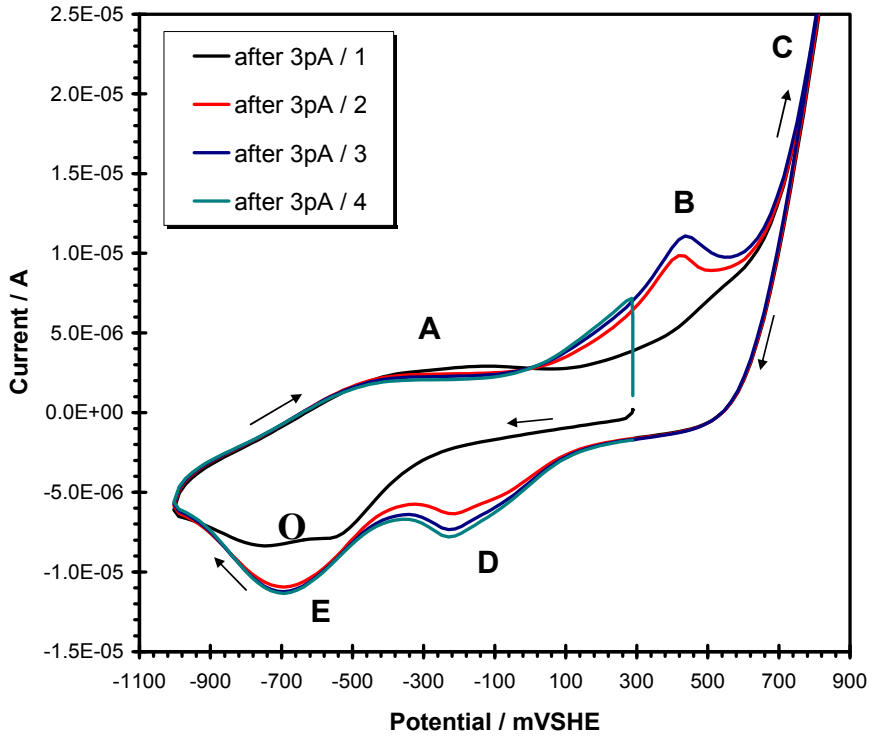

Fig. 5.21 Cyclic voltammogram (scanning rate 10mV/s) after He^{2+} beam irradiation at $3.3 \cdot 10^{7} cm^{-2} \cdot s^{-1}$ flux (beam current 3pA)

In the cyclic voltammogram recorded before irradiation (figure 5.22) one could observe that the oxidation of the UO_2 lattice (region B) and the reduction of the U^{VI} are not so dominant. This could be due to slower processes taking place at the surface in the absence of the high α-activity field. The fact that different electrodes were used may also play a role.

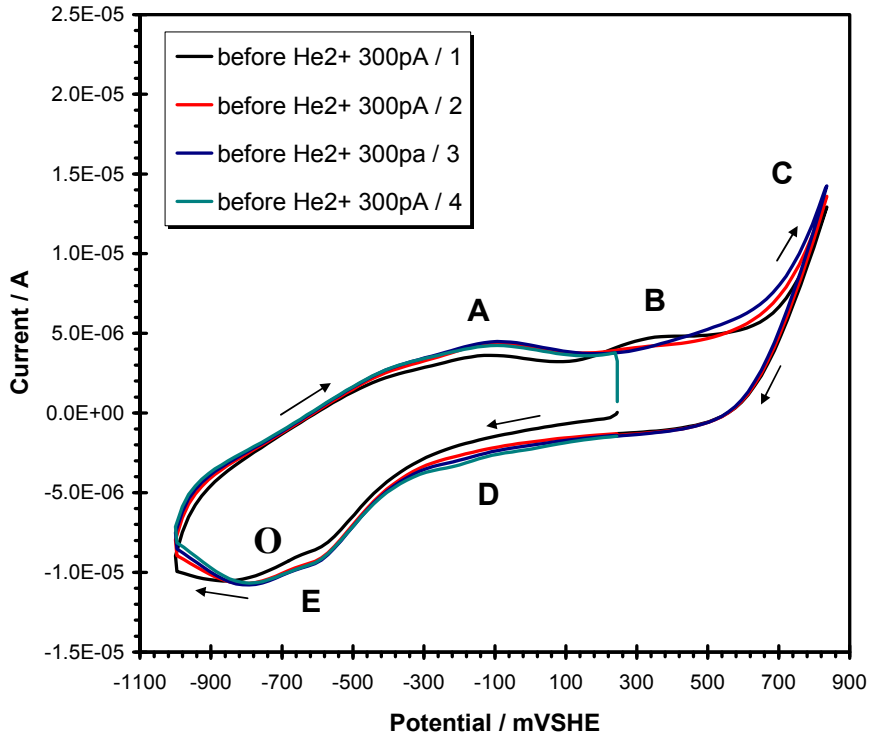

Fig. 5.22 Cyclic voltammogram (scanning rate 10mV/s) before He^{2+} beam irradiation at $3.3 \cdot 10^{9} cm^{-2} \cdot s^{-1}$ flux (beam current 300pA)

A big change in region E is noticed in the cyclic voltammogram recorded during irradiation with He^{2+}beam at flux of $3.3 \cdot 10^{9} cm^{-2} \cdot s^{-1}$, as seen in figure 5.23

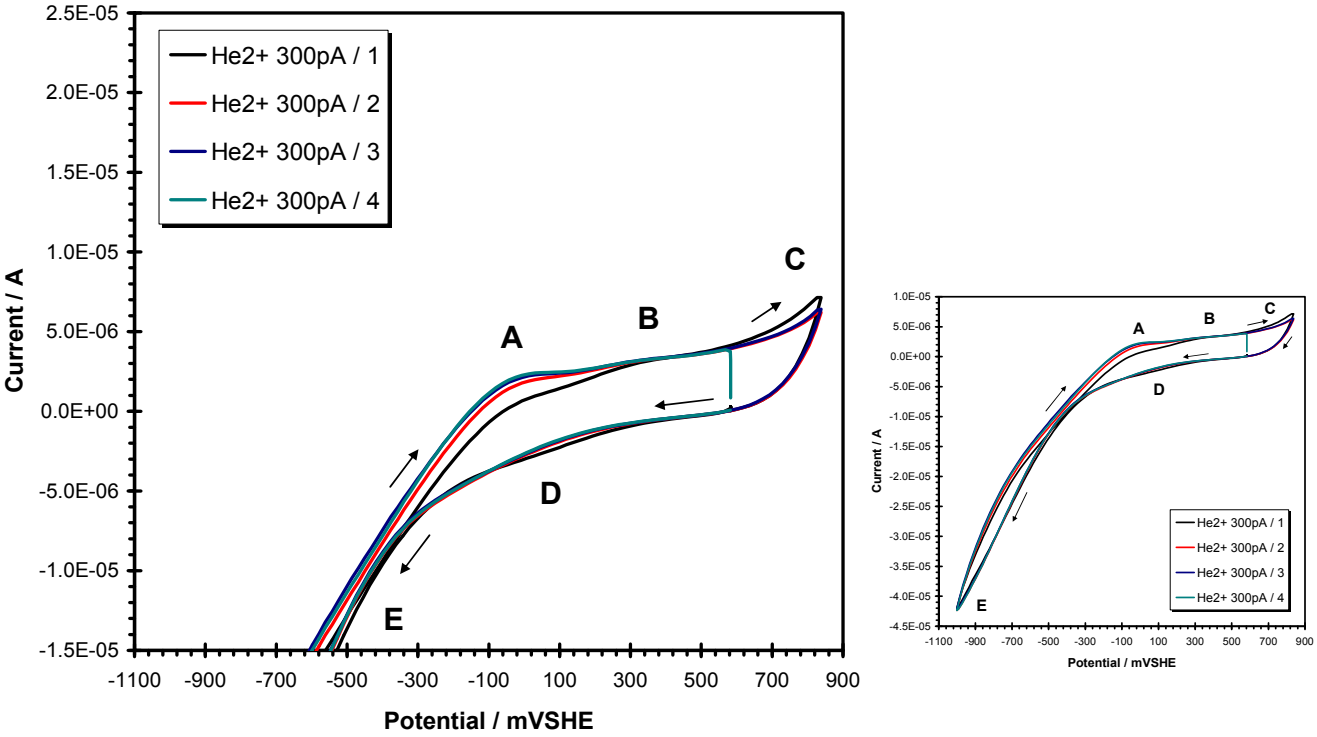

Fig. 5.23 Cyclic voltammogram (scanning rate 10mV/s) during at $3.3 \cdot 10^{9}$ $cm^{-2} \cdot s^{-1}$ flux (beam current 300pA)

5.2. Solution analysis

5.2.1. Uranium content

Glove box experiments

The solution sampled during the long term monitoring of the free corrosion potential and during the polarisation sequences were analysed by ICP-MS. Because the solution was sampled in bottles already containing approx. 2ml HNO_3 2.5M the concentration was back calculated to the original value. Furthermore it was taken into account also the fact that the volume of solution in the vessel is decreasing with every sample. In appendix A.6 the table containing the ICP-MS results and the calculated values are presented. In figure 5.24 the evolution of uranium concentration in the solution during the long term measurements is presented for all three electrodes.

It can be observed that under Ar the concentration increases and after approx. 500 hours a steady state is reached. During the following 400 hours the concentrations in all three vessels change very little. For the 1% and 10% ^{233}U doped UO_2 samples the concentrations increased from $2.88 \cdot 10^{-8}$M to $7.35 \cdot 10^{-8}$M, respectively from $1.50 \cdot 10^{-8}$M to $2.98 \cdot 10^{-8}$M. For the natural UO_2 sample the initial concentration was $2.41 \cdot 10^{-6}$M and the final one was $3.00 \cdot 10^{-6}$M.

After changing the solutions and purging to Ar/H_2 initial concentrations were $3.79 \cdot 10^{-11}$M for natural UO_2, $5.61 \cdot 10^{-11}$M for the 1% ^{233}U doped UO_2 and $3.63 \cdot 10^{-10}$M for the 10% ^{233}U doped UO_2. The uranium concentration in all three electrochemical cells slowly increased even after 2000 hours.

However, the final concentrations were below those measured in Ar atmosphere with almost one order of magnitude. The highest concentration $2.96 \cdot 10^{-7}$M was for the natural UO_2. For the low level doped UO_2 sample it was $1.28 \cdot 10^{-8}$M while for the high level doped UO_2 was $9.31 \cdot 10^{-9}$M.

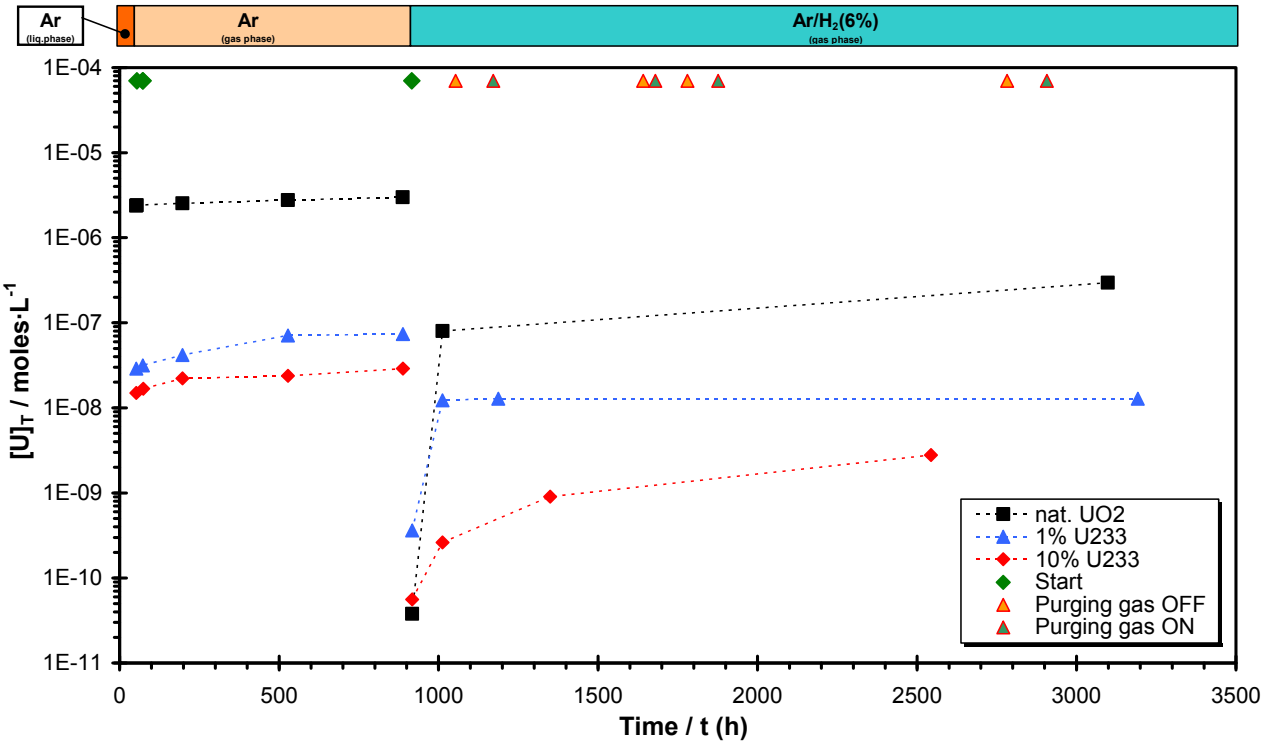

Fig. 5.24 Uranium concentration during the long term experiments

The variation of the uranium concentration in the solution during polarisation measurements is presented in figure 5.25.

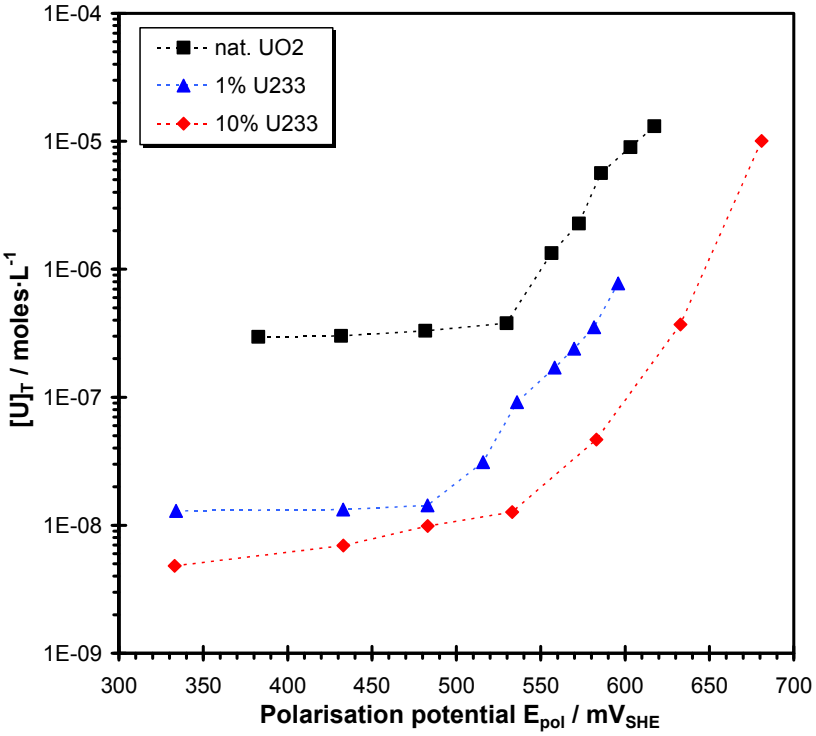

Fig. 5.25 Uranium concentration variation during anodic polarisation

It can be observed that the increase in the uranium concentration becomes significant at a polarisation higher than 520 mV vs. SHE.

Cyclotron experiments

The solutions sampled during the experiments made at the CERI cyclotron were analysed both by ICP-MS and also by ICP-OES. Both type of analysis were made at ITU. A short description of the ICP-OES method is presented bellow.

ICP-OES is a multi-element analytical technique, which is widely used [70]. The analysis of the samples requires an instrument with high resolution to avoid inter-element interference and to obtain low detection limits.

ICP-OES (Inductive Coupled Plasma – Optical Emission Spectroscopy) also known as ICP-AES (Inductive Coupled Plasma – Atomic Emission Spectroscopy) is a type of emission spectroscopy that uses the inductively coupled plasma to produce excited atoms and ions that emit electromagnetic radiation at wavelengths characteristic of a particular element. The intensity of this emission is indicative of the concentration of the element within the sample.

The ICP-OES is composed of two parts, the inductive coupled plasma (ICP) and the optical spectrometer. The ICP torch consists of 3 concentric quartz glass tubes that is water cooled and a coil of the radio frequency (RF) generator which surrounds part of this torch. Argon gas is typically used to create the plasma. When the torch is turned on, an intense magnetic field from the RF generator is turned on. The argon gas flowing through is ignited with a Tesla unit (typically a copper strip on the outside of the tube). The argon gas is ionized in this field and flows in a particular rotationally symmetrically pattern towards the magnetic field of the RF coil. A stable high temperature plasma of about 7000K is then generated as the result of the inelastic collisions created between the neutral argon atoms and the charged particles.

A peristaltic pump delivers a liquid sample into a nebulizer where it is atomized and introduced directly inside the plasma flame. The sample immediately collides with the electrons and other charged ions in the plasma and is broken down into charged ions. The various molecules break up into their respective atoms which then lose electrons and recombine repeatedly in the plasma, giving off the characteristic wavelengths of the elements involved.

A shear gas, typically nitrogen or dry compressed air is used to “cut” the plasma flame at a specific spot. One or two transfer lenses are then used to focus the emitted light on a diffraction grating where it is separated into its component radiation in the optical spectrometer. The light intensity is then measured with a photomultiplier tube at the specific wavelength for each element line involved.

The intensity of each line is then compared to previous measured intensities of known concentrations of the element and its concentration is then computed by extrapolation along the calibration line.

This technique was applied under standard conditions for the analysis of the dissolution behaviour and secondary phase formation of uranium dioxide in corrosion experiments. The system has to be calibrated before its use accordingly.

Due to the complexity of the matrix, the uranium concentration in solution and the number of samples to be analysed the application of ICP-OES as analytical technique for uranium determination has been chosen.

The uranium analysis was undertaken by Inductively Coupled Plasma Optical Emission Spectrometry (ICP-OES Horiba Jobin Yvon Ultima 2 spectrometer [71]). The setup of the spectrometer is presented in the figure 5.26.

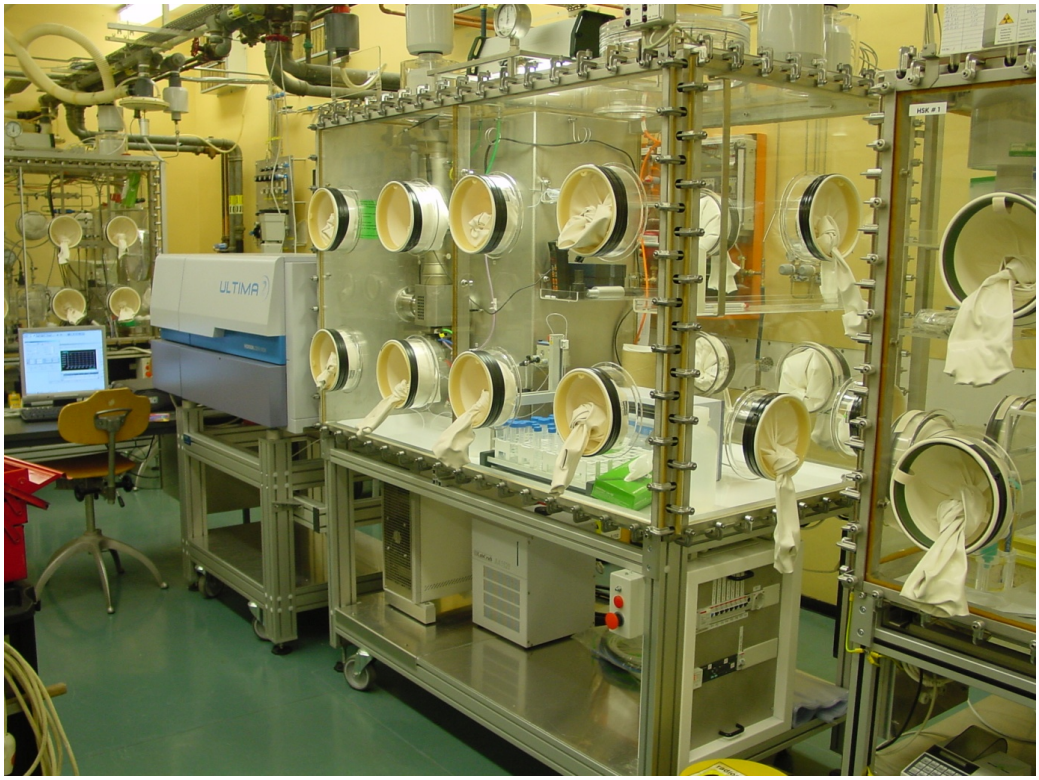

Fig. 5.26 Picture of the IPC-OES. The sampling part is installed inside a glove box

The samples were fed to the Meinhard nebulizer fitted to a conical spray chamber via a peristaltic pump, then transferred to argon plasma. Here the sample is decomposed, atomized and ionized whereby the atoms and ions are excited. The intensity of the light emitted when the atoms return to lower energy levels is measured. Each element emits light at characteristic wavelength and these lines can be used for quantitative analysis after a calibration. During the analysis 3 replicas per line and element were performed for each sample.

The samples were acidified with nitric acid up to a concentration of 1M HNO_3. Appropriate blanks following the same scheme of sample preparation were used for the analysis. External calibration was performed using a series of dilutions of certified uranium standard solutions (Alfa Aesar Specpure) in the concentration range between 0 - 3000ppb. Since the calibration is undertaken in 1M HNO_3 and the samples have various matrices, a high generator power is used to minimize the matrix effects.

The wavelength was detected using the profile function, and by using Win-IMAGE which is rapid semi-quantitative analysis mode using multiple wavelengths. After semi-quantitative analysis two analytical lines for uranium were used. The lines at 367.007 and 409.014 nm have the best limits of detection of 1.11ppb and 4.31ppb, respectively.

The limit of detection (LOD) was determined as:

$$LOD = \frac{3 \cdot SD \cdot C}{I - I_o} \tag{5.4}$$

where:
- SD – standard deviation of the blank
- C – Analytical concentration
- I – Signal for the sample concentration
- I_0 – Signal for the blank

In the table 5.2 the parameters of the ICP-OES instrument during the uranium analysis are presented

Table 5.2 Operational conditions of the ICP-OES instrument during uranium analysis

Instrumental Conditions for Sample Introduction Systems	
RF Power	1000 W
Reflect power	4 W
Plasma Gas Flow	12 L/min
Auxiliary Gas Flow	0.4 L/min
Nebulizer Gas Flow	2.6 bar
Solution Pump Rate	0.8 mL/min
integration time	0.5 s
Spray chamber	cyclonic
Optical purge for analysis < 190 nm Nitrogen	3 L/min
Equilibration Time	10 s

In figures 5.27 and 5.28 the solution analysis is presented for the irradiations using a He^{2+} beam flux of $3.3 \cdot 10^7 cm^{-2} \cdot s^{-1}$ under Ar and Ar/H_2 4%. The solutions sampled during free corrosion monitoring were analysed by ICP-MS. The samples taken during polarisation measurements were analysed by ICP-OES.

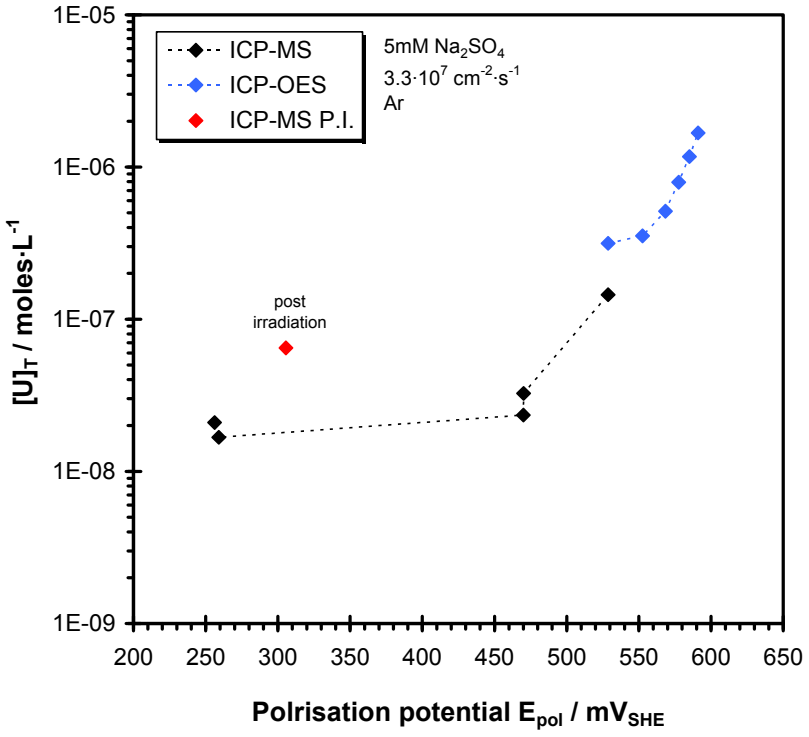

Fig. 5.27 Uranium concentration variation during measurement at low He^{2+} beam flux under Ar

It can be observed that the uranium concentration in solutions coming from the experiment under Ar/H_2 is lower than in those sampled during the experiment under Ar.

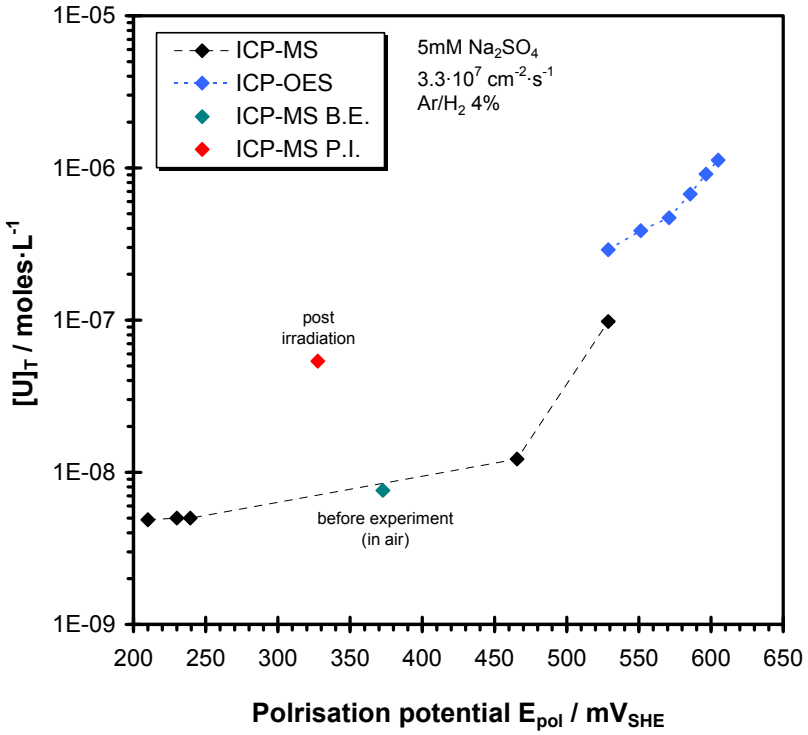

Fig. 5.28 Uranium concentration variation during measurement at low He^{2+} beam flux under Ar/H_2 4%

5.2.2. Other elements

Due to the fact the *p*H was very low, approx. 4, in stead of the expected value around 7, the solutions sampled during the long term measurements in the glove box were analysed also for Fe, Si, Ag and Au.

High amounts of iron could be observed in all three experiments. The higher concentration in the case of 1% ^{233}U doped sample, especially in the beginning of the experiment could be due to the oxygen probe because the outer part of the probe is made of stainless steel.

In figure 5.29 the variation of Fe concentration during the free corrosion monitoring is presented.

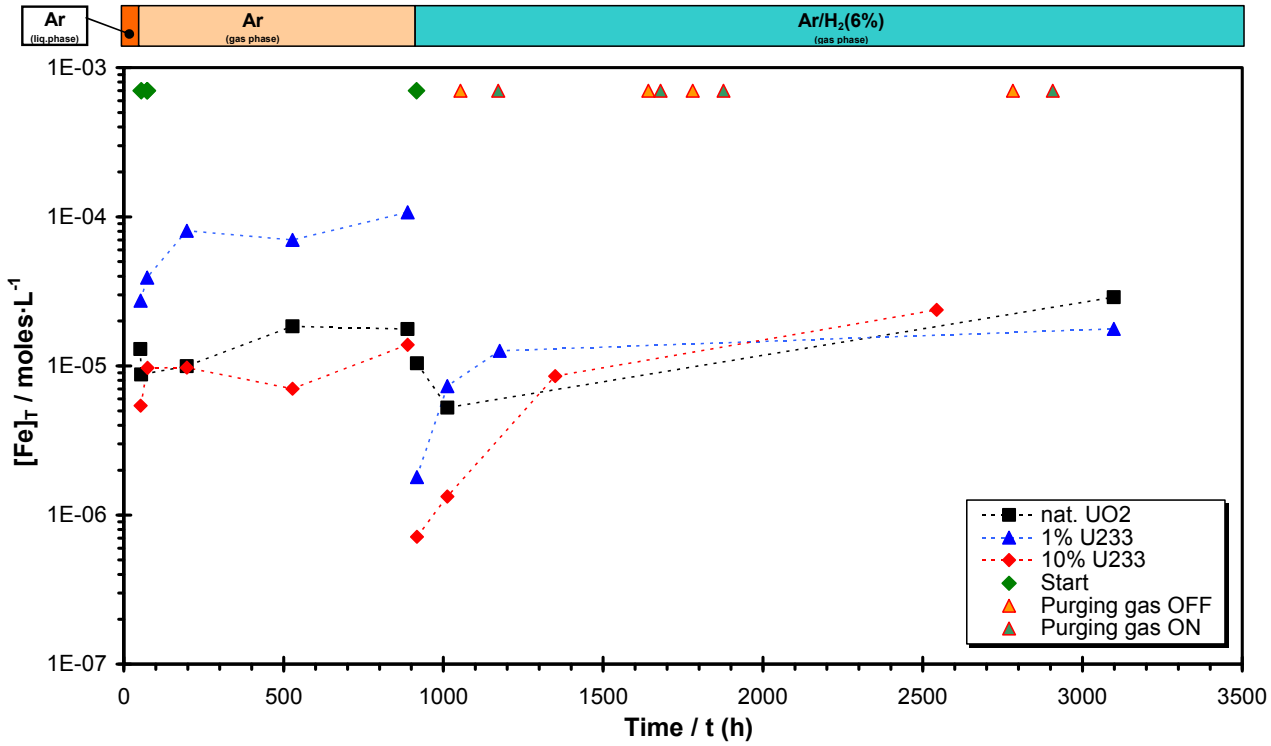

Fig. 5.29 Iron concentration during long term experiments

In figure 5.30 the variation of Fe concentration during the polarisation measurements is presented. The total Fe concentration is not varying significantly, in general being around 2-3·10^{-5}M. Only two samples, one from the 1% and the other from the 10% ^{233}U doped UO_2, showed values around 10^{-4}M. In these cases the contamination with Fe containing particles may be the cause of higher total Fe concentration.

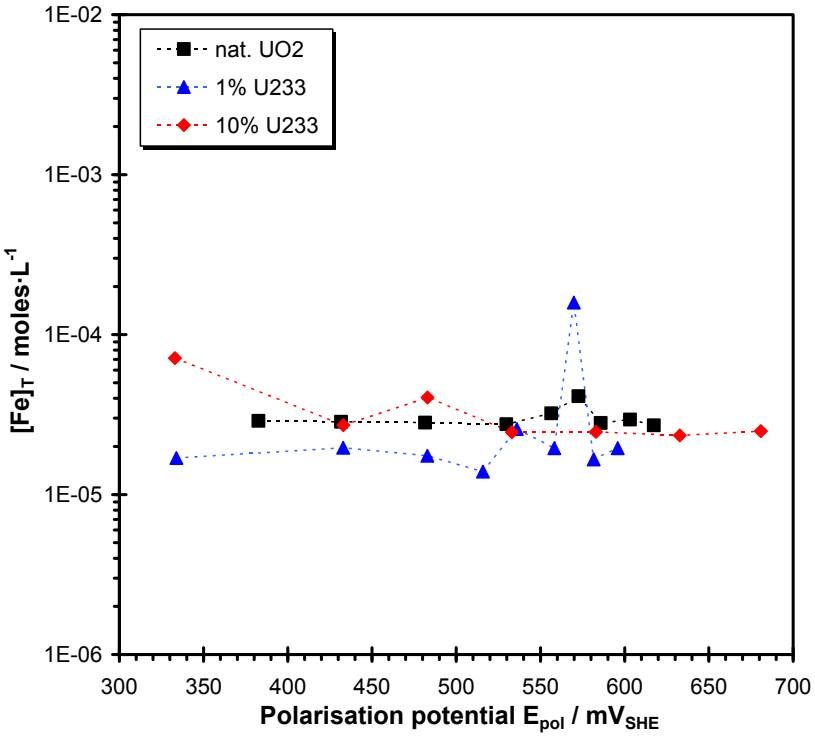

Fig. 5.30 Iron concentration during anodic polarisation

In figure 5.31 the variation of silicon concentration during the experiments is presented. Also high concentrations of silicon were measured for all three experiments. It was observed that the concentrations increase constantly, reaching values higher then 10^{-4}M.

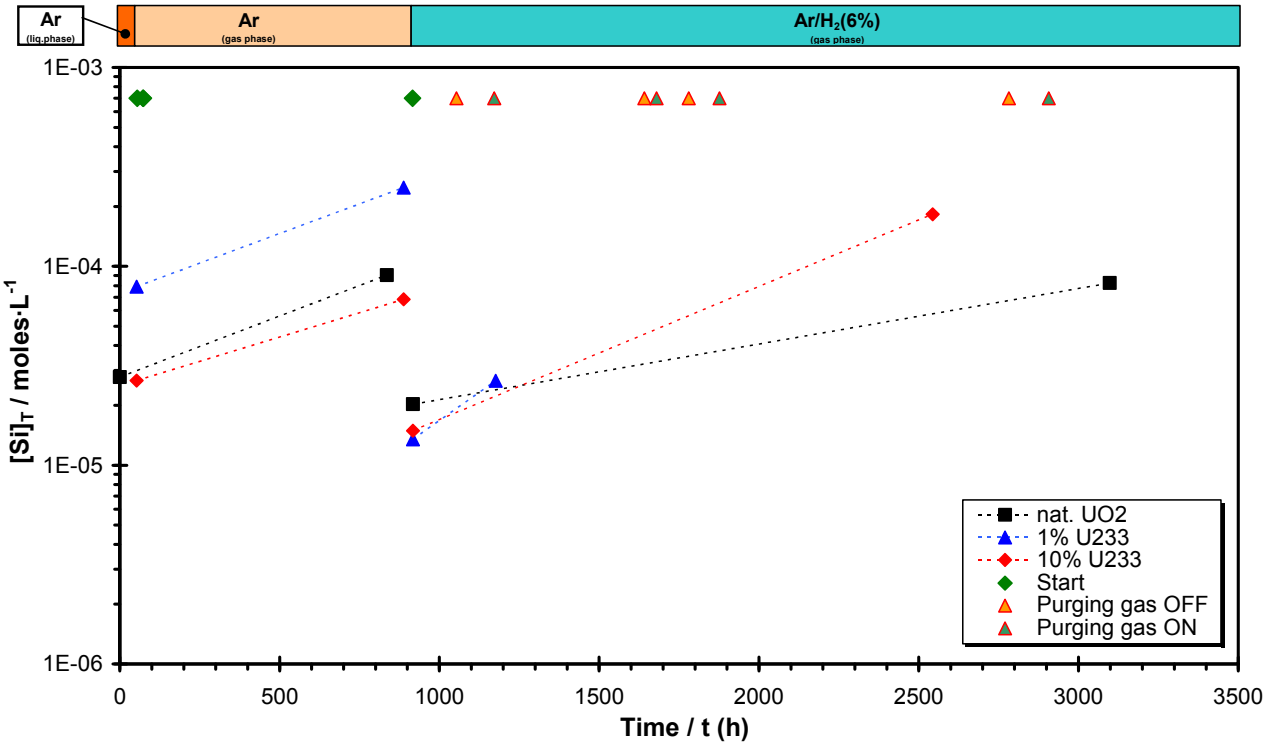

Fig. 5.31 Silicon concentration during long term experiments

In figures 5.32 and 5.33 the concentration of silver during the measurements of corrosion potential and recording of the anodic polarisation curves is presented.

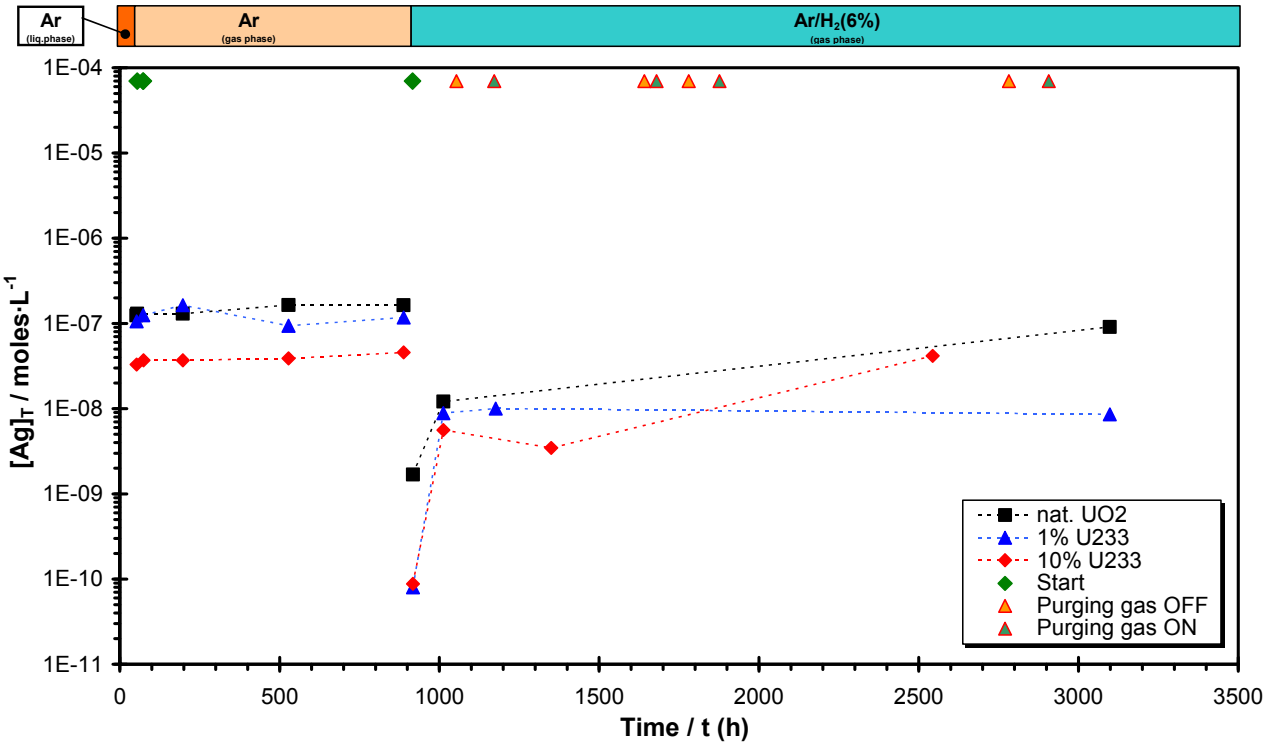

Fig. 5.32 Silver concentrations during long term measurements

Most of the silver is coming from the E_h electrodes which are combined Pt – Ag/AgCl redox electrodes. The concentrations of silver are quite constant during Ar purging measurements. For natural and 1% ^{233}U doped UO_2 it was around $1.50 \cdot 10^{-7}$M, while for the 10% ^{233}U doped UO_2 it was around $4.00 \cdot 10^{-8}$M.

After changing the solutions and purging gas to Ar/H_2 the silver concentration for the natural UO_2 sample was $1.69 \cdot 10^{-9}$M. For the doped UO_2 samples it was around $8.00 \cdot 10^{-11}$M. At the end of the measurements the silver concentration was $9.14 \cdot 10^{-8}$M for the natural UO_2 sample, $8.61 \cdot 10^{-9}$M for the 1% ^{233}U doped UO_2 sample and $4.17 \cdot 10^{-8}$M for the 10% ^{233}U doped UO_2 sample.

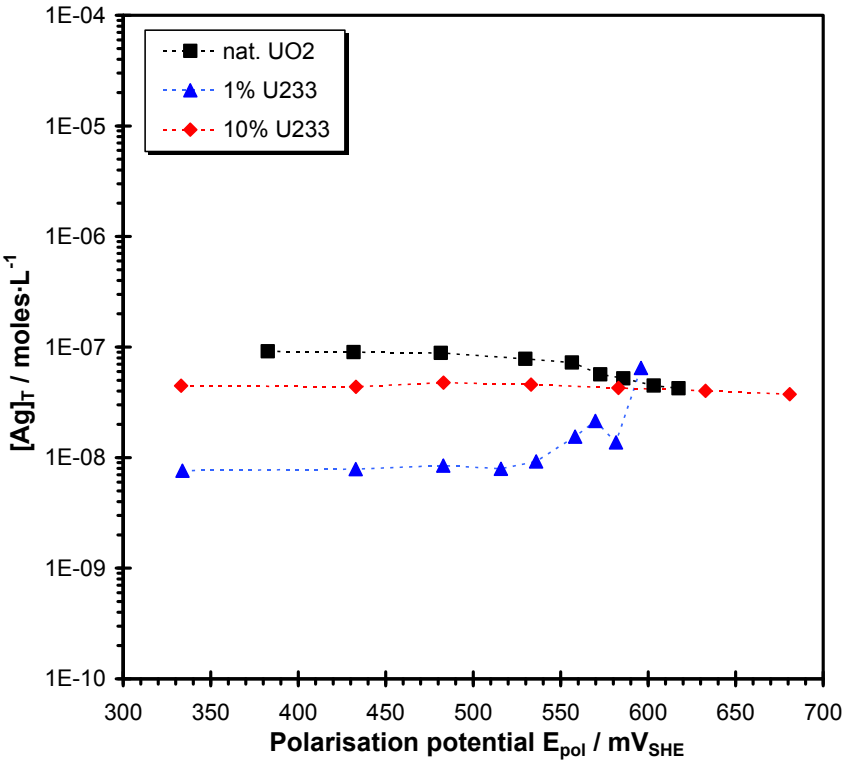

Fig. 5.33 Silver concentrations during anodic polarisation

During the polarisation measurements, the concentrations were not varying significantly until the polarisation potential passed 550mV. At higher potential in case of natural UO_2 it decreased slowly to $4.24 \cdot 10^{-8}$M, it increased in case of the 1% ^{233}U doped UO_2 sample up to $6.49 \cdot 10^{-8}$M and it remained almost constant for the 10% ^{233}U doped UO_2 around $4 \cdot 10^{-8}$M.

In case of gold, although it was measured, it was not possible to measure or the few values obtained are below the detection limit of the ICP-MS which is 10 times the standard deviation of the blank sample.

5.2.3. Online oxygen determination

The dissolved oxygen was monitored inside the electrochemical cell in which the 1% ^{233}U doped UO_2 electrode was installed. During the whole experiment the oxygen sensor was mounted. It was kept in the gaseous phase above the liquid. By determining the oxygen partial pressure in the gaseous phase the dissolved oxygen concentration was then deduced from the Henry law.

The calibration of the oxygen sensor and the calculations are presented in the Appendix A.7. In figure 5.34 the dissolved oxygen concentration is presented for the 1% ^{233}U doped UO_2.

The initial dissolved oxygen concentration was $9.37 \cdot 10^{-7}$M. Until approx. 350 hours since the start of the experiment the oxygen concentration showed a small variation around the $1.50 \cdot 10^{-6}$M value. After approx. 350 hours the oxygen concentration increased suddenly and reached $6.40 \cdot 10^{-6}$M. After changing the solution and switching the purging gas to Ar/H_2 it remained around the same value with small variations during the periods the purging gas was not working.

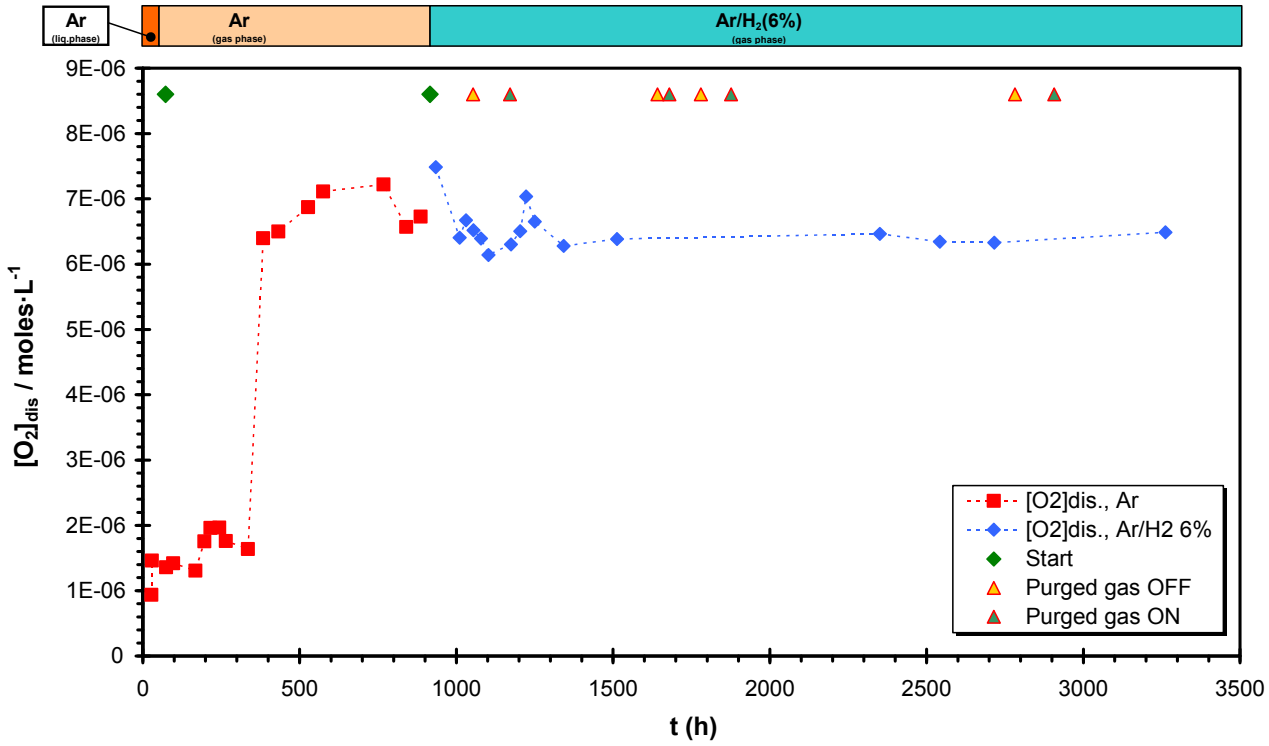

Fig. 5.34 Dissolved oxygen concentration inside the electrochemical cell with 1% ^{233}U doped UO_2

5.3. Surface characterisation

Glove box experiments

The three electrodes used for the experiments in the glove box, after the end of the experiment were analysed by Scanning Electron Microscopy (SEM) coupled with Energy Dispersive X-Ray Spectroscopy (EDX).

Energy dispersive X-ray spectroscopy is an analytical technique used for the elemental analysis or chemical characterization of a sample. As a type of spectroscopy, it relies on the investigation of a sample through interactions between electromagnetic radiation and matter, analyzing x-rays emitted by the matter in response to being hit with the electromagnetic radiation. Its characterization capabilities are due in large part to the fundamental principle that each element has a unique atomic structure allowing x-rays that are characteristic of an element's atomic structure to be identified uniquely from each other.

To stimulate the emission of characteristic X-rays from a specimen, a high energy beam of charged particles such as electrons or protons, or a beam of X-rays, is focused into the sample being studied.

At rest, an atom within the sample contains ground state (or unexcited) electrons in discrete energy levels or electron shells bound to the nucleus. The incident beam may excite an electron in an inner shell, ejecting it from the shell while creating an electron hole where the electron was. An electron from an outer, higher-energy shell then fills the hole, and the difference in energy between the higher-energy shell and the lower energy shell may be released in the form of an X-ray. The number and energy of the X-rays emitted from a specimen can be measured by an energy dispersive spectrometer. As the energy of the X-rays is characteristic of the difference in energy between the two shells, and of the atomic structure of the element form which they were emitted, this allows the elemental composition of the specimen to be measured.

In the figure 5.35 the EDX results are presented for the natural UO_2 and for the 10% ^{233}U doped electrodes. No other elements besides uranium could be determined at the surface of the samples.

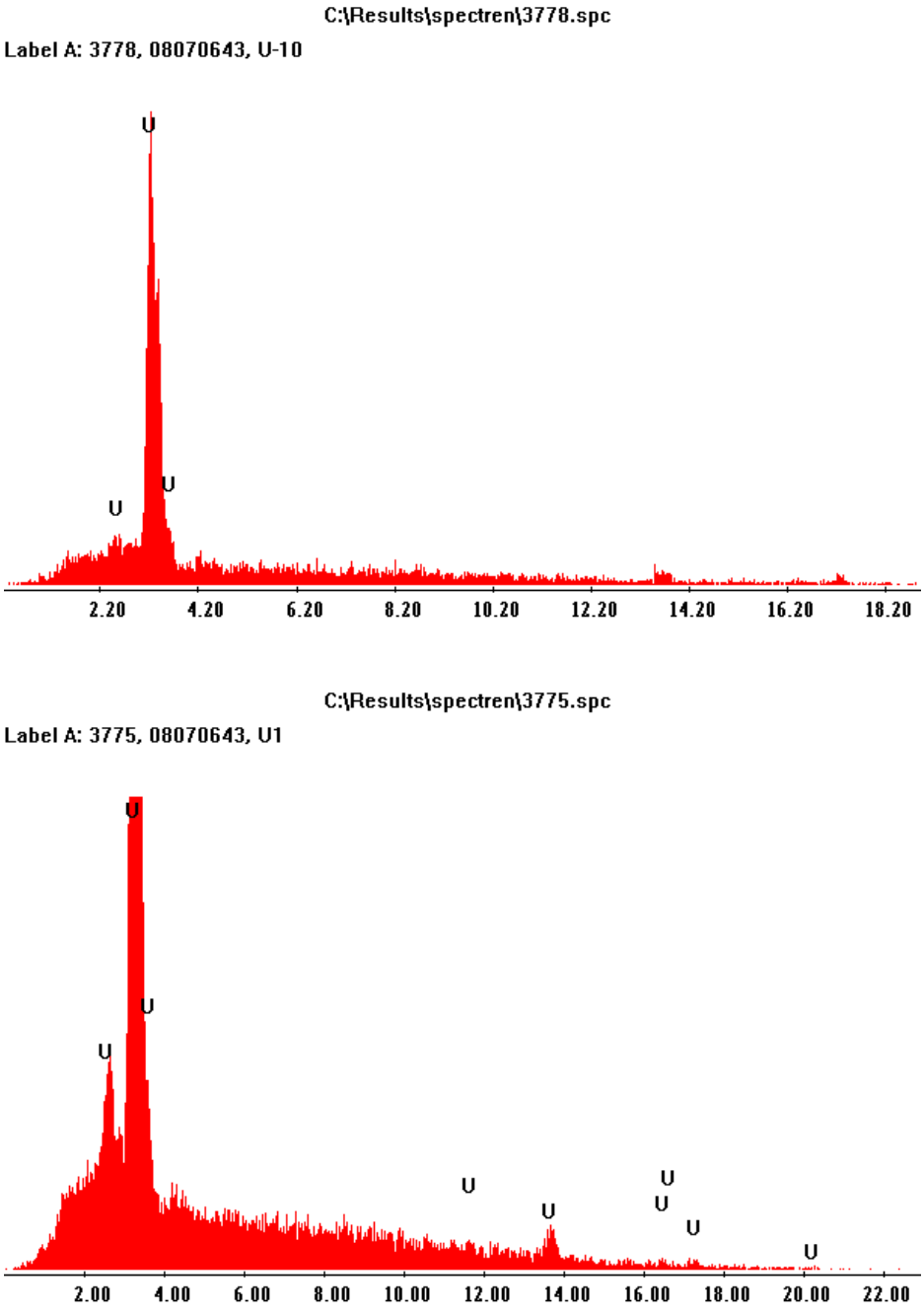

Fig. 5.35 EDX analysis for the natural UO_2 electrode (up) and the 10% ^{233}U doped UO_2 electrode (down)

In the following figures the SEM pictures of the three electrodes at different magnification scales are presented. Cracks of different sizes and etched empty place due to polarisation can be observed on all samples. However, no formation of secondary phases could be noticed.

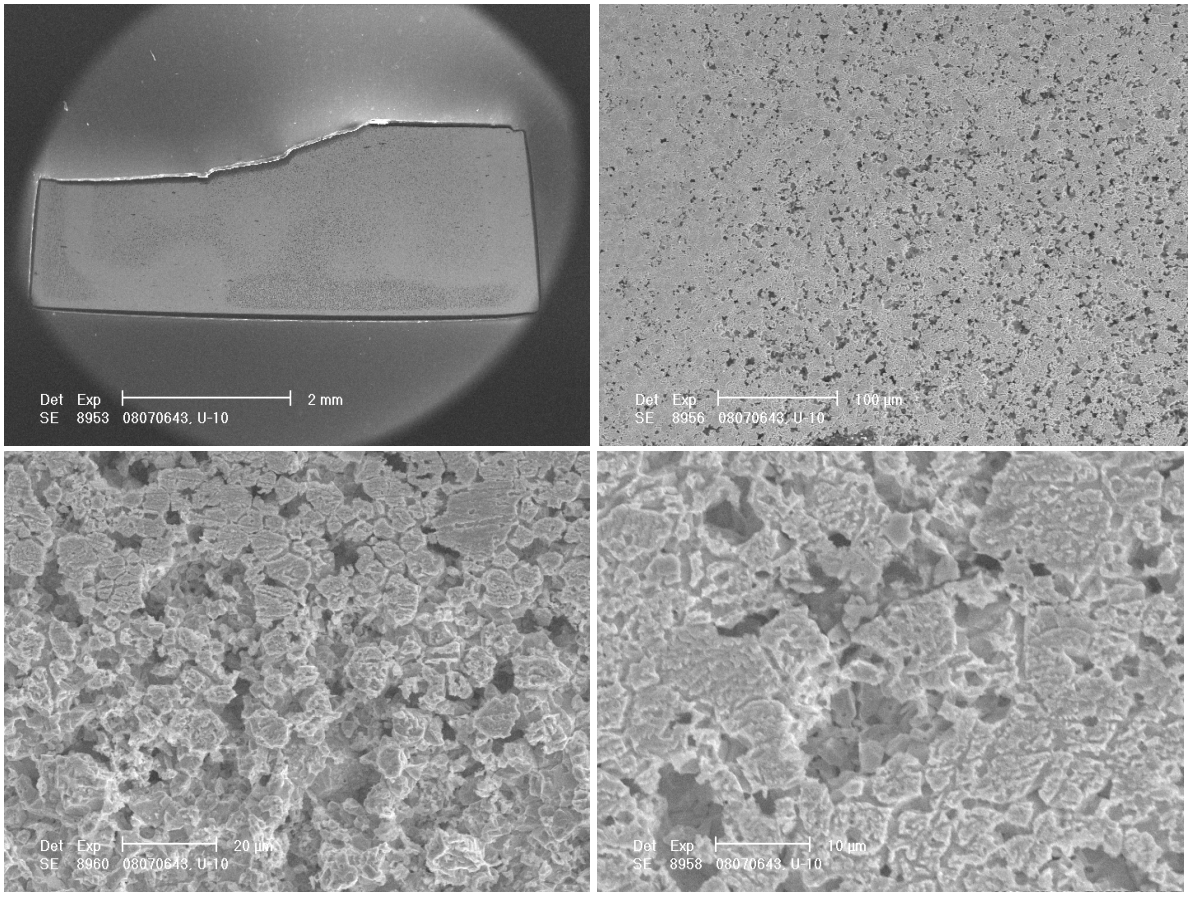

Figure 5.36 Natural UO_2 electrode after polarisation

The SEM pictures of the 1% ^{233}U doped UO_2 show the corrosion was concentrated around cracks and on the grain boundaries.

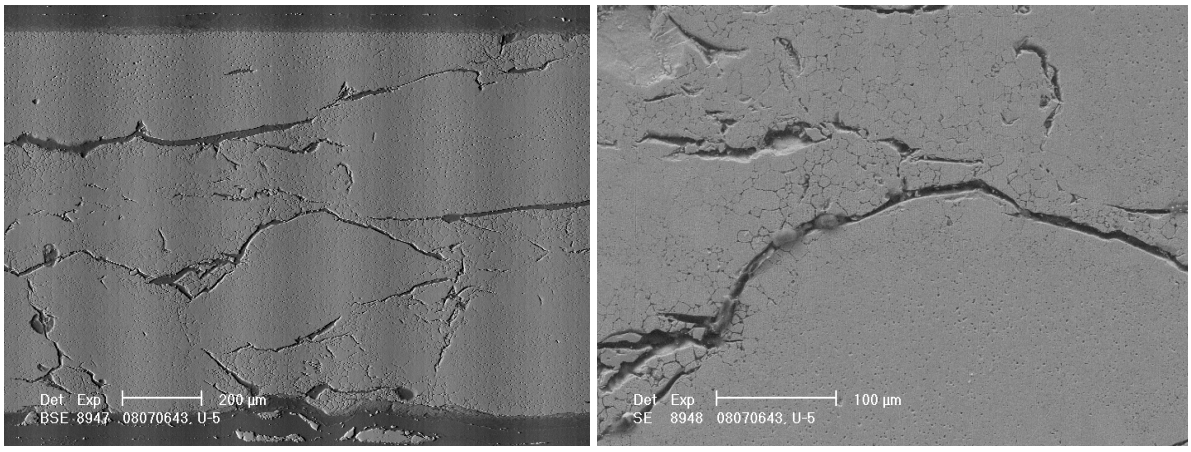

Figure 5.37 1% ^{233}U doped UO_2 electrode (back scattering electrons image – left; evidence of corrosion along cracks – right)

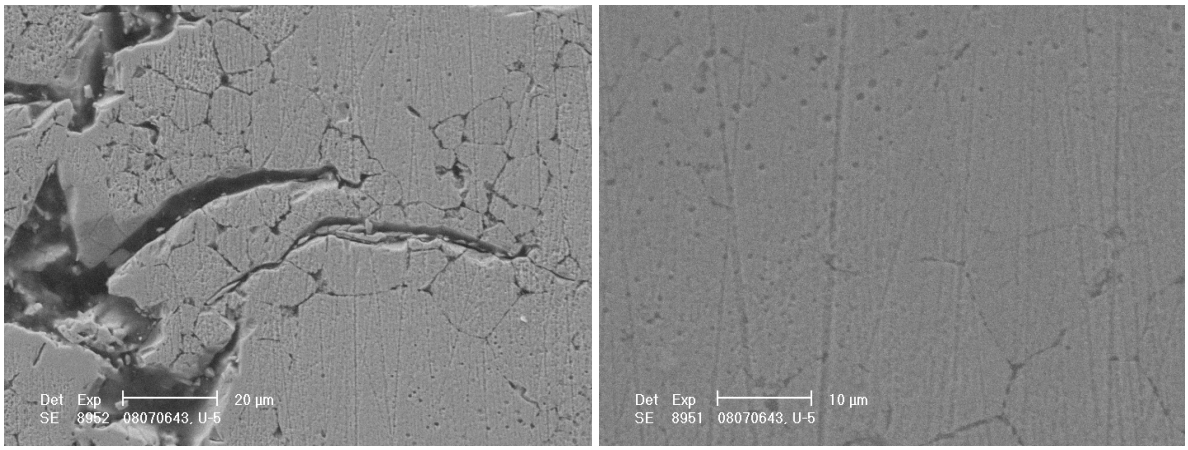

Figure 5.38 1% ^{233}U doped UO_2 electrode (magnification and evidence of corrosion around grain boundaries)

The high level doped UO_2 has a lot of cracks. Signs of corrosion can be observed on the grain boundaries and also inside the grains. Also in some regions the corrosion the corrosion attack was much stronger.

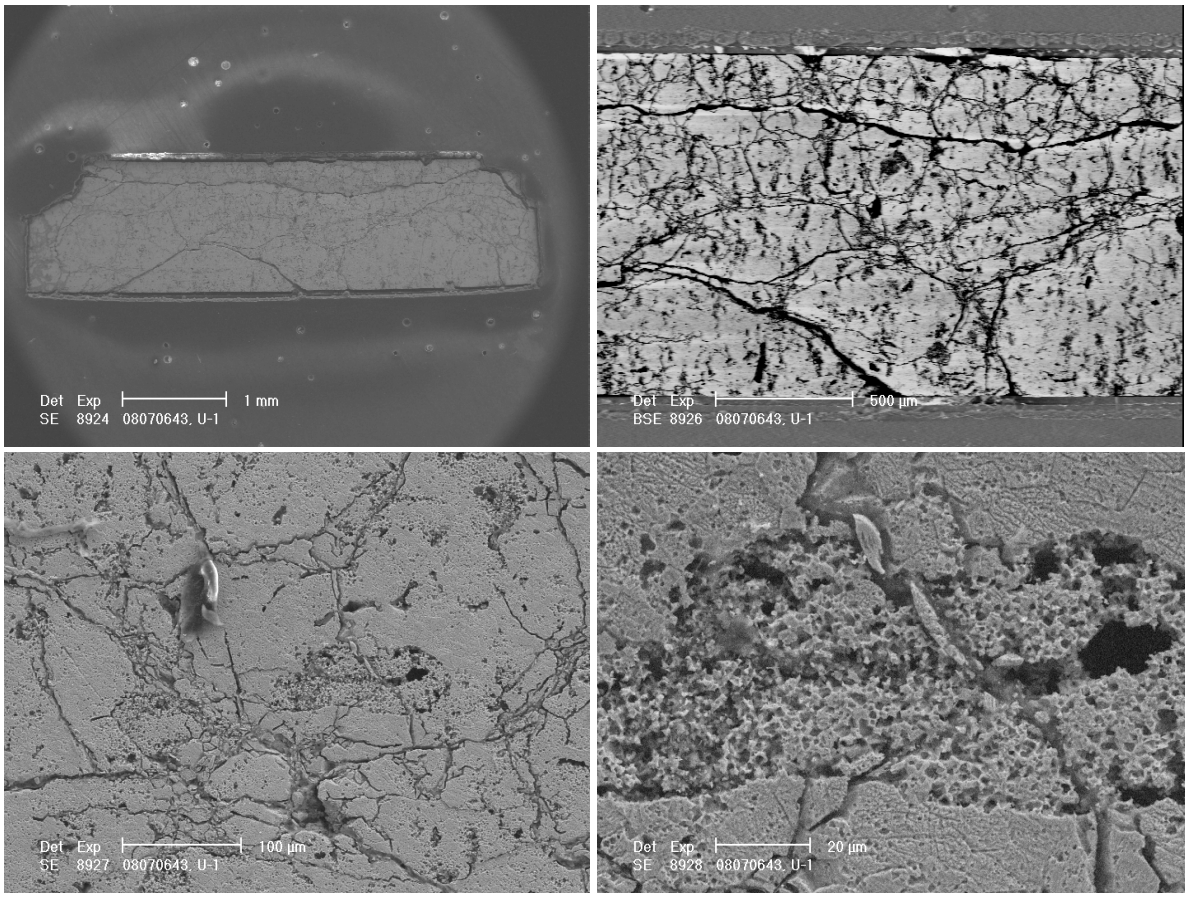

Figure 5.39 10% ^{233}U doped UO_2 electrode (general view and back scattering electrons image – up; localised corrosion evidence along cracks and grain boundaries)

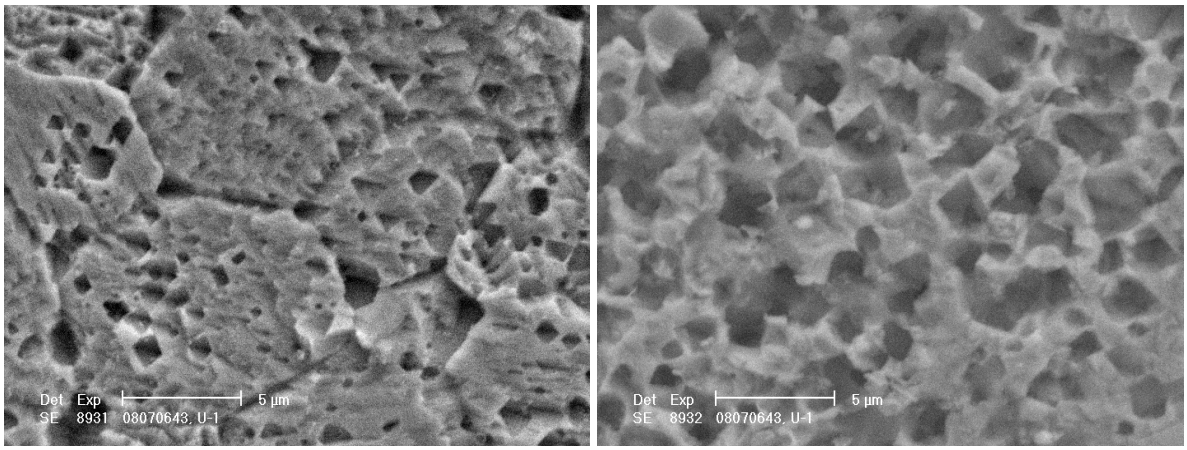

Figure 5.40 10% ^{233}U doped UO_2 electrode (evidence of localised attack inside the grains)

Cyclotron experiments

After irradiation the surface of the UO_2 disks was investigated using an optical microscope. In figure 5.41 pictures of an irradiated disk (I11-01) are presented. A film formation can be observed on the surface of the irradiated area. A comparison can be made with the margins of the disk which were not in contact with water or with the 45 MeV He^{2+} beam.

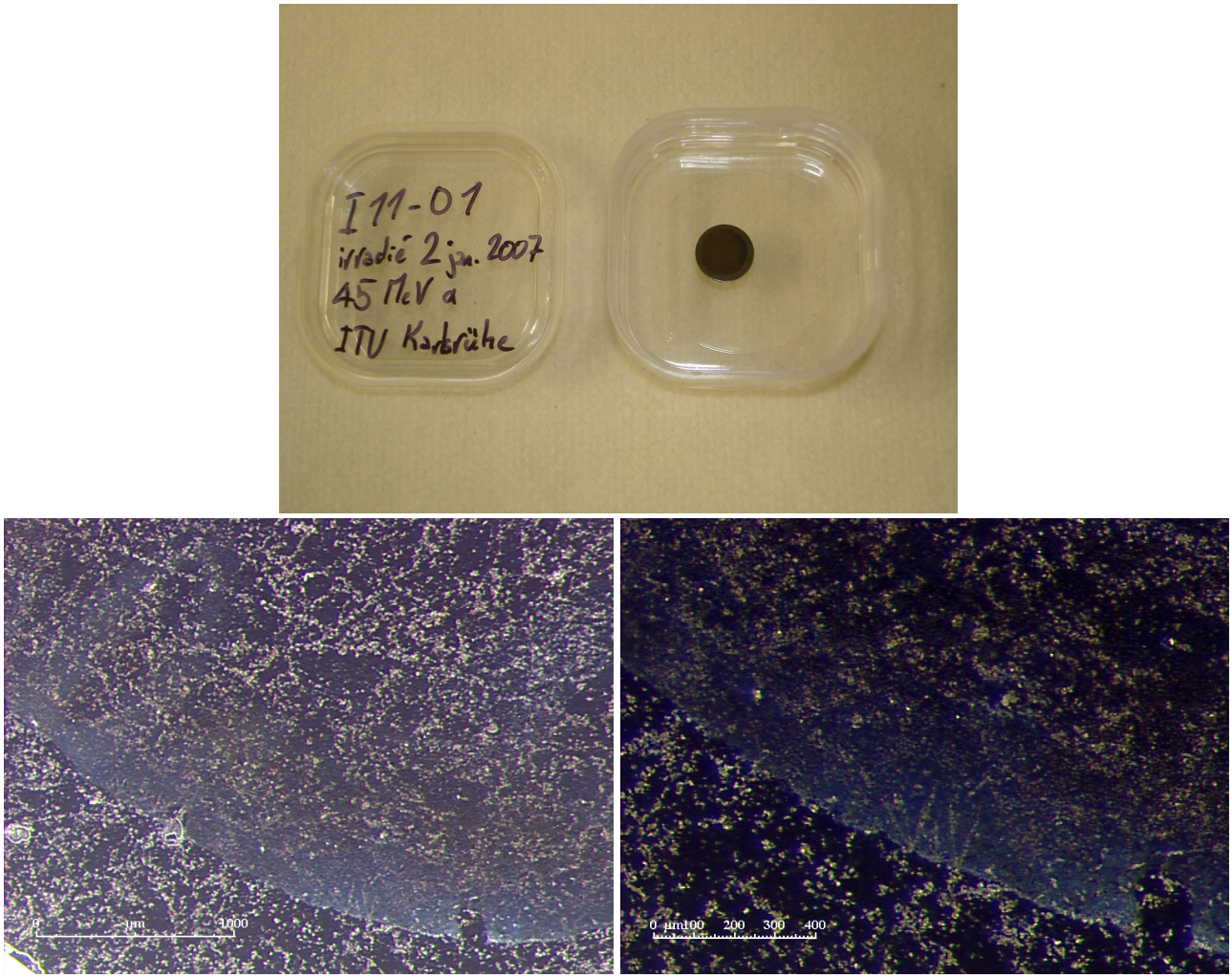

Fig. 5.41 Camera picture (up) and optical microscope pictures (down) of UO_2 after corrosion monitoring under 45MeV He^{2+} beam irradiation (beam flux $3.3 \cdot 10^7$ $cm^{-2} \cdot s^{-1}$)

In figure 5.42 the pictures of an irradiated UO_2 disk after polarisation under 45 MeV He^{2+} beam are presented.

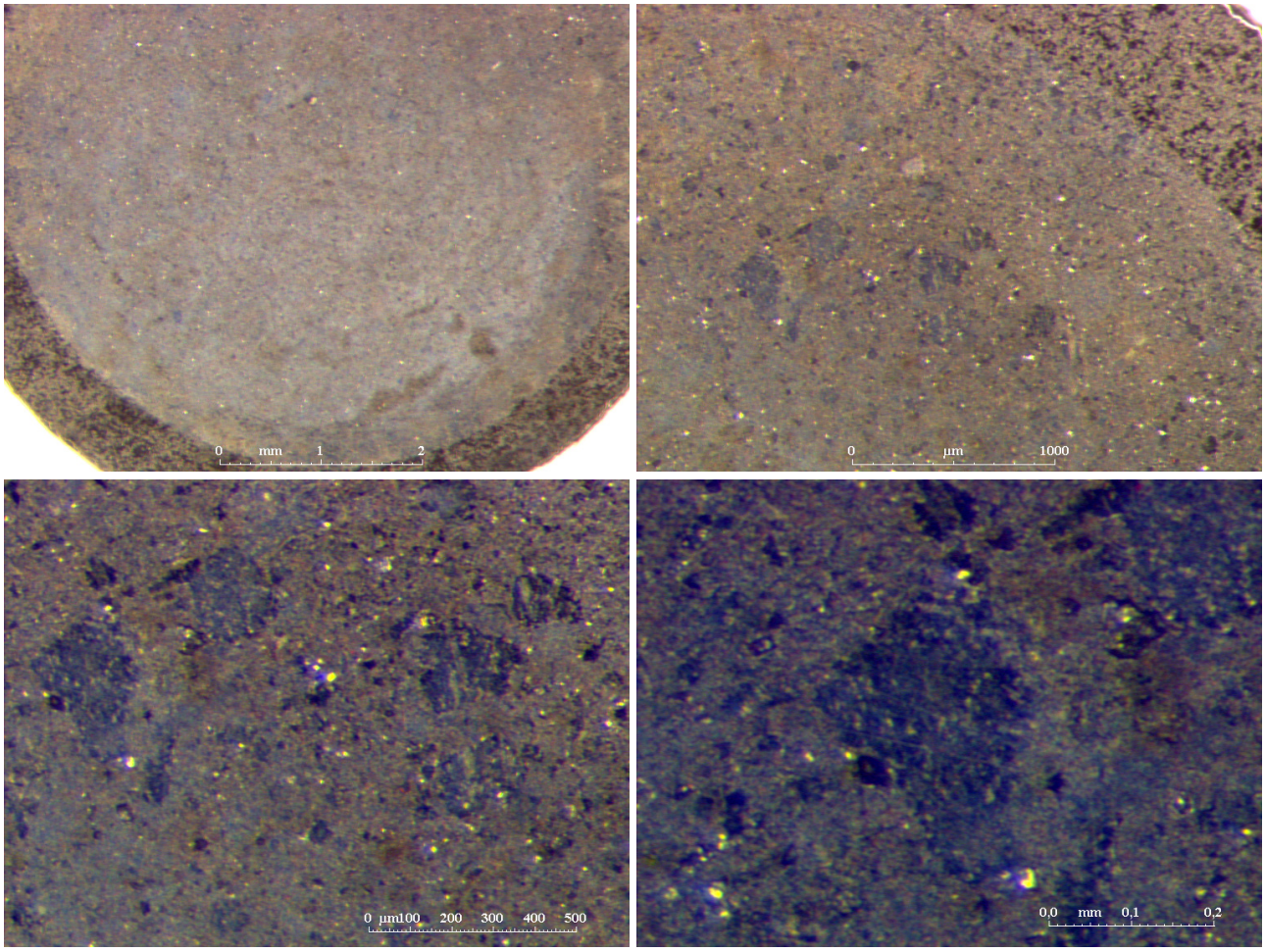

Fig. 5.42 UO_2 disk pictures after polarisation under 45MeV He^{2+} beam irradiation (beam flux $3.3 \cdot 10^7$ $cm^{-2} \cdot s^{-1}$)

Under the oxidation layer formed during irradiation the localised attack areas due to polarisation can be observed.

6. Discussions

6.1. Electrochemical data

6.1.1. Redox potentials and *p*H

The redox potentials and the corrosion potentials recorded during the long term experiments inside the glove box showed higher values than initially expected [23]. The very low *p*H values of around 4, sometimes even lower, could be an explanation for these values. From the solution analysis high concentration of iron and silicon were found. These high concentrations, in the order of 10^{-5} to 10^{-4}M for iron and even higher than 10^{-4}M for silicon can be an explanation.

The tubing for the transport of the purging gases to and from the electrochemical cells is made from stainless steel. Previously problems were encountered, the water from the inlet bubblers being transported into the experimental vessels. The inlet bubblers were manufactured from plastic. It is possible due to the temperature variations from day and night, that the tubes to act as condensers. The incoming gas being humidified in the bubblers could be cooled during the passing through the tubes. As a consequence water could condensate into the tubes and then by gravity to get into the experimental vessels. However some water could have been left on walls of the tubes and in time could start to corrode them. Even if later the system was cleaned it is impossible to clean the tubing. In order to prevent the further condensation the tubing was insulated. Since after that no water have been transported to the electrochemical cells led to the conclusion that temperature difference was the cause of this problem. However it is possible that iron left on the inner side of the tubing to get into the vessels.

It is impossible that the high amount of silicon to come from the leaching of the glass vessels. The same type of cells was used before for other experiments and no such high amount of silicon could be found. It is thought that silicon could be transported from the oxygen trap to the vessels. The analysis of the water from the inlet bubbler showed an amount of silicon of 10^{-5}M and a *p*H of approx. 4.5.

Since the measurements are made in non-buffered system the redox potential is driven by the dominating species.

The standard reducing potential for Fe^{3+} to Fe^{2+}, $\varepsilon^0_{Fe^{3+}/Fe^{3+}}$, is 771mV. Considering the redox potential of the solution 400mV vs. SHE the ratio between the activities of Fe^{2+} and Fe^{3+} can be calculated from the Nernst equation (2.20):

$$\lg\frac{a_{Fe^{2+}}}{a_{Fe^{3+}}}=\frac{771-400}{59.18}=6.269\Rightarrow\frac{a_{Fe^{2+}}}{a_{Fe^{3+}}}=10^{6.269}\Rightarrow\frac{a_{Fe^{2+}}}{a_{Fe^{3+}}}=1.858\cdot10^{6}$$

Taking into consideration the relative low total iron concentration of 10^{-5}M the concentrations of the two iron species can be calculated:

$$\left.\begin{aligned}&\left[Fe^{2+}\right]+\left[Fe^{3+}\right]=10^{-5}M\\&\left[Fe^{2+}\right]=1.858\cdot10^{6}\cdot\left[Fe^{3+}\right]\end{aligned}\right|\Rightarrow\left[Fe^{3+}\right]=\frac{10^{-5}}{1.858\cdot10^{6}+1}M\Rightarrow\left[Fe^{3+}\right]=5.383\cdot10^{-12}M$$
$$\left[Fe^{2+}\right]=10^{-5}-5.383\cdot10^{-12}\Rightarrow\left[Fe^{2+}\right]\cong10^{-5}M$$

The Fe^{2+} is stable only in a non-oxidising environment. Its high concentration compared to Fe^{3+} could only be a proof of the anoxic environment and low oxygen concentration.

In the absence of any buffering species the redox potential in the presence of hydrogen at equilibrium the redox potential is:

$$E_{H^+/H_2,e} = -59.18 \cdot \lg \frac{p_{H_2}^{0.5}}{a_{H^+}} mV \Rightarrow E_{H^+/H_2,e} = -59.18 \cdot \left(pH + \frac{1}{2} \lg p_{H_2} \right) mV$$

Under Ar/H_2 6% purging at 25°C and a total gas pressure of 1.2 bar the redox potential should be:

$$E_{H^+/H_2,e} = -59.18 \cdot \left(7 + \frac{1}{2} \cdot \lg\left(7.2 \cdot 10^{-2}\right) \right) mV_{SHE} \Rightarrow E_{H^+/H_2,e} = -380 mV_{SHE}$$

The initial decrease of the redox potential in all three electrochemical cells under Ar/H_2 could be due to the low iron concentration after changing the solution. The later increase of the E_h could be to the increase of the iron concentration which is buffering the potential. However, the lower redox potential under Ar/H_2 could be an indication of the more reducing environment. At a redox potential of 300mV and a total iron concentration of 10^{-5}M the concentration of Fe^{3+} is $1.10 \cdot 10^{-13}$M.

6.1.2. Corrosion potentials

During the long term measurements in the glove box the corrosion potential was monitored. As seen in figure 5.3 the corrosion potential is stabilising during measurements under Ar purging. Under reducing conditions, initially, the corrosion potential drops. However, the successive interruption of the purging gas had an important role on the variation of the corrosion potential. During the time the purging was stopped the corrosion potential increased even with more than 150mV, as seen for the natural and 1% ^{233}U doped UO_2 samples. After the purging restarted the corrosion potential decreased significantly. However, only in the case of 10% ^{233}U doped UO_2 the potential reached a value close to the one before the first gas interruption.

For the measurements made at CERI the corrosion potential recorded before, during and after the irradiation with 45MeV He^{2+} beam was monitored. The results showed a logarithmic dependence with the He^{2+} beam flux. A slope of approx. 47mV/decade was determined for He^{2+} beam fluxes up to $10^9 cm^{-2} \cdot s^{-1}$.

The corrosion potentials measured in the glove box and also during irradiation with He^{2+} beam were compared. The comparison is presented in figure 6.1.

It can be observed that the corrosion potential from the electrodes investigate in the glove box do not match the logarithmic dependency shown by the UO_2 under He^{2+} beam irradiation. The reasons might be the difference in the experimental conditions and also the electrical properties of the electrodes. The disk electrodes used at CERI had electrical properties relative close to each other. On the contrary the properties of the investigated samples inside the glove box at ITU were quite different, for example the material resistivity being spread over almost four orders of magnitude.

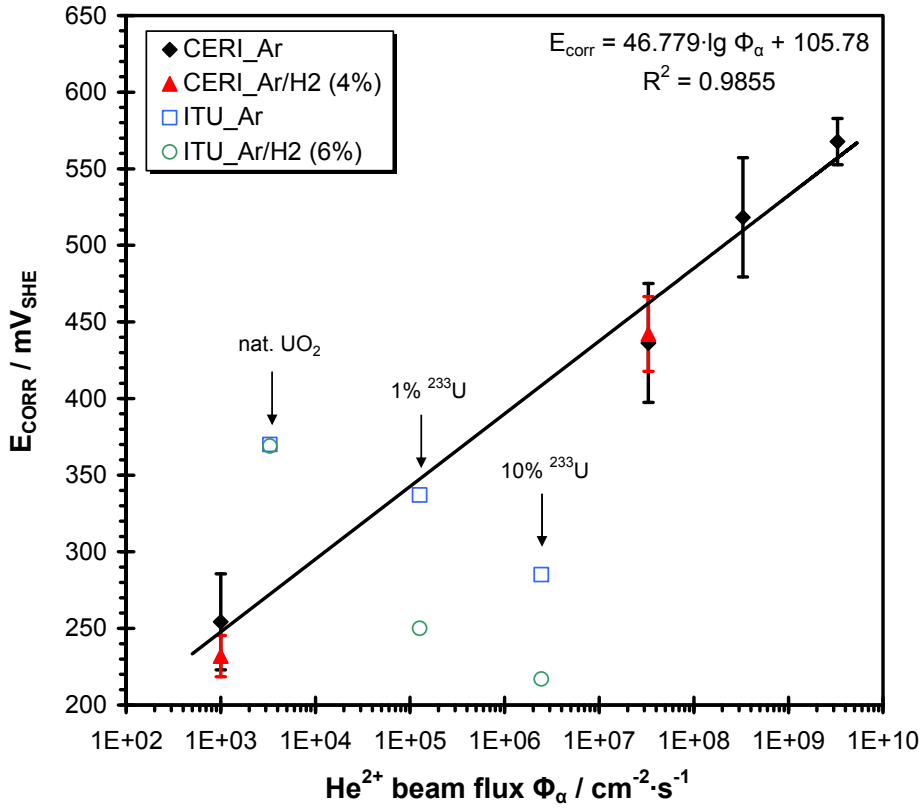

Fig. 6.1 Comparison between corrosion potentials measured for doped samples and under irradiation with 45 MeV He^{2+} beam

6.1.3. Polarisation curves

The anodic polarisation curves were recorded by potentiostatic polarisation. A potential was fixed and the current was measured for a period of time long enough to let the polarisation current to stabilise. Due to time limitations at the CERI cyclotron each polarisation point was recorded for maximum one hour, 20 minutes for the measurement of the polarisation current and 40 minutes for the recording of the impedance spectra. At ITU each polarisation point was recorded for more than 8 hours, 2 hours for the polarisation current and over 6 hours for the impedance spectra.

The cathodic polarisation curves recorded without and under irradiation showed values of approx. -370mV/decade, close to the literature presented data. The high negative value is due to the formation of the negative species like HO^- and e^-_{aq}, which are evolving fast on the surface.

For the anodic polarisation curves values between 60 and 80mV/decade were expected [69]. However under anoxic conditions (Ar purging) values of approx. 45 mv/decade were recorded during the polarisation with and without beam irradiation. The Tafel slopes determined from measurements under reducing conditions (Ar/H_2 4%) without and during He^{2+} beam irradiation showed values of approx. 65mV/dec.

The Tafel slopes determined by the anodic polarisation under Ar/H_2 6% made inside the glove box turned out values of approx. 51mV/decade for the 1 and 10% ^{233}U doped UO_2 electrodes. For the natural UO_2 electrode the value of the Tafel slope was approx. 42mV/decade.

The comparison between the anodic polarisation curves recorded under Ar/H_2 atmosphere is presented in figure 6.2.

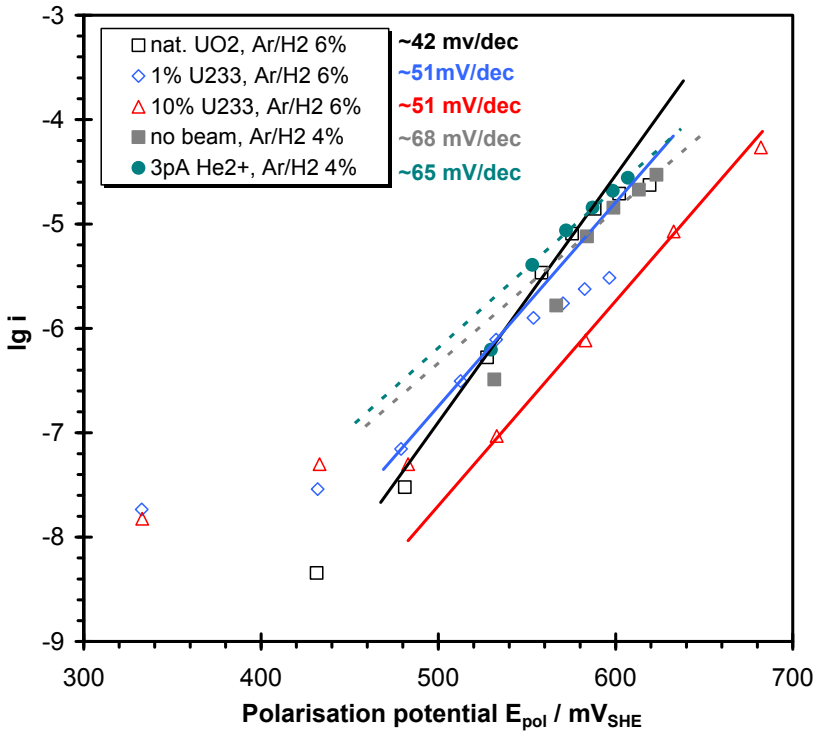

Fig. 6.2 Comparison between anodic polarisation curves measured for doped samples and under irradiation with 45 MeV He^{2+} beam in Ar/H_2 atmosphere

The explanation for these results is the low value of the *p*H especially for the samples investigated in the glove box. The effect of the surface acidification is the enhancing of the corrosion as already mentioned in the literature [72, 73]. It was seen that the *p*H during the experiments on natural and ^{233}U doped UO_2 was around 4.0, compared to approx. 5.0 for the solutions coming from the He^{2+} irradiated samples. A lower *p*H value can be the associated to a lower value of the slope. This being taken into consideration there is a good agreement between the slopes of the anodic polarisation curves and the *p*H in solution.

6.1.4. Electrochemical impedance spectroscopy

By using of the EIS electrode properties or kinetic data can be obtained. As seen in figure 5.1 the resistivity of the UO_2 electrodes used during the long term measurements have electrical properties which are quite different. The 1% ^{233}U doped UO_2 sample had a very high resistivity, approx. 0.5 MOhm·cm. This means a low conductivity of the electrons through the material. This also leads to high ohmic drop especially at high polarisation potentials. As consequence real potential on the surface of the electrode will be much lower than the initially imposed one.

The situation is different with the 10% ^{233}U doped UO_2 electrode. It has a very low resistivity of 0.2 KOhm·cm. This electrode will allow a high conductivity of the electrons. Due to the low ohmic drop the real polarisation potential on the surface will close to the imposed one. From all the UO_2 electrodes used for polarisation measurements this one was polarised at the highest real potentials. Although a leak was initially suspected the solution analysis removed this doubt. The UO_2 piece is glued on a gold coated brass screw before being embedded in resin and polished.

If a crack in the electrode or the separation between the UO_2 and resin would have led to the formation of a "defective" path to the gold coated screw then Au could have been seen in the solution analysis. As already mentioned in section 5.2.2 in the majority of the solution no gold could be detected. In the few samples in which it was detected the recorded values were bellow the detection limit (10 times the standard deviation of the blank sample).

The resistivity of the UO_2 disks used for measurements under He^{2+} beam irradiation was in the range of 0.05 to 0.4MOhm·cm. Here are included also UO_2 disks that later led to leaking. It can be observed that in this case the resistivity values are within one order of magnitude, unlike the doped UO_2 electrodes. There the values were separated by almost four orders of magnitude.

The polarisation resistances can be used in the calculation of the corrosion rates. In section 6.3 a comparison between the corrosion rated derived from electrochemical methods and from solution analysis is presented.

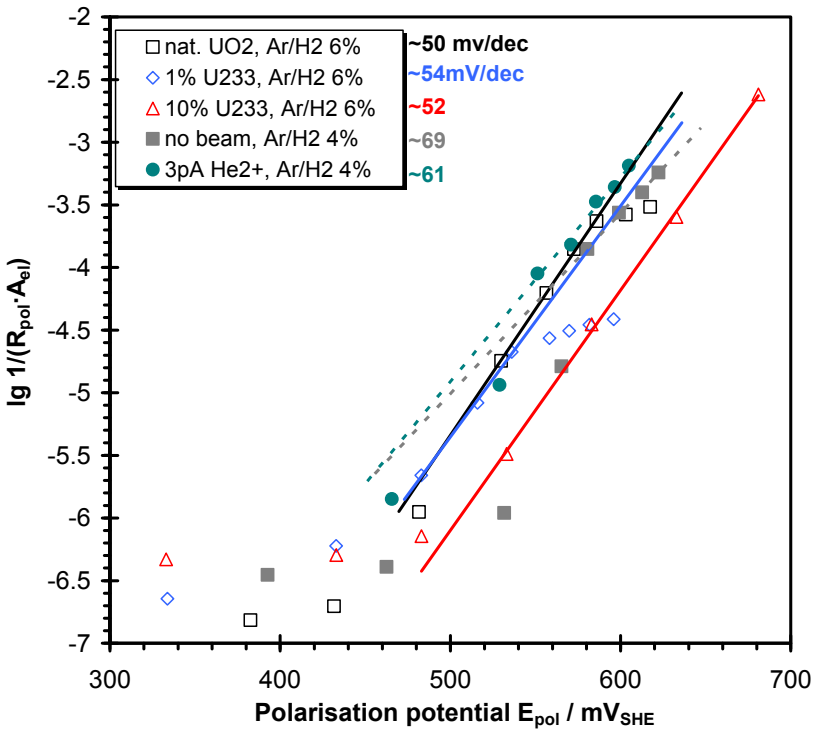

Fig. 6.3 Comparison between reciprocal of the polarisation resistance normalised to the electrode surface at different potentials for doped samples and under irradiation with 45 MeV He^{2+} beam in Ar/H_2 atmosphere

In figure 6.3 the same it can be observed that the slopes of the curves corresponding to the measurements made in the glove box are smaller than those recorded during He^{2+} beam irradiation. The values of the slopes are comparable with those already discussed in the previous section. There is a good agreement between the two sets of data which can only increase the level of confidence in the obtained results.

In figure 5.16 the influence of the α-particles flux and of the purging gas can be observed. The polarisation resistance is represented as the logarithm of its inverse normalised to the electrode area. Concerning influence of the α-particles flux it can be seen that the corrosion rate is increasing together with the flux. It was also observed that the corrosion rate after the end of irradiation is higher then the one before irradiation. These observations are valid for both type of gases, Ar and Ar/H_2. However the corrosion rates under Ar/H_2 are smaller than the corresponding ones under Ar.

However as the α-particles flux increases the difference is smaller. The corrosion rate under reducing conditions is almost one order of magnitude slower before and after irradiation compared with the ones under anoxic conditions. Under irradiation with a He^{2+} beam flux of $3.3 \cdot 10^{7}$ $cm^{-2} \cdot s^{-1}$ the corrosion rate under Ar/H_2 4% purging is only 1.5 times slower than the one under Ar purging.

The double layer capacitance resulted from the EIS spectra can be used in the calculation of the thickness of the electrochemical double layer. For a plane plane capacitor with parallel plates is expressed by the following equation:

$$C = \frac{\varepsilon_0 \cdot \varepsilon_r \cdot A}{\delta} \tag{6.1}$$

In the equation (6.1) the following notations were used:

- ε_0 – permeability of vacuum, in F/m;
- ε_r – relative static permeability of the medium (dielectric constant);
- A – surface of the plates, in m^2;
- δ – distance between the plates, in m.

Te double layer can be compared with a plane capacitor with parallel plates. The surface of the plates is equal to the surface of the electrode, and the distance between the plates is the thickness of the double layer. In figure 6.4 the thickness of the double layer is presented for the three long term experiments during the free corrosion potential monitoring period. The calculated values of approx. 10^{-10}m are in the ranged of expected values for the electrochemical double layer inside an electrolyte [12].

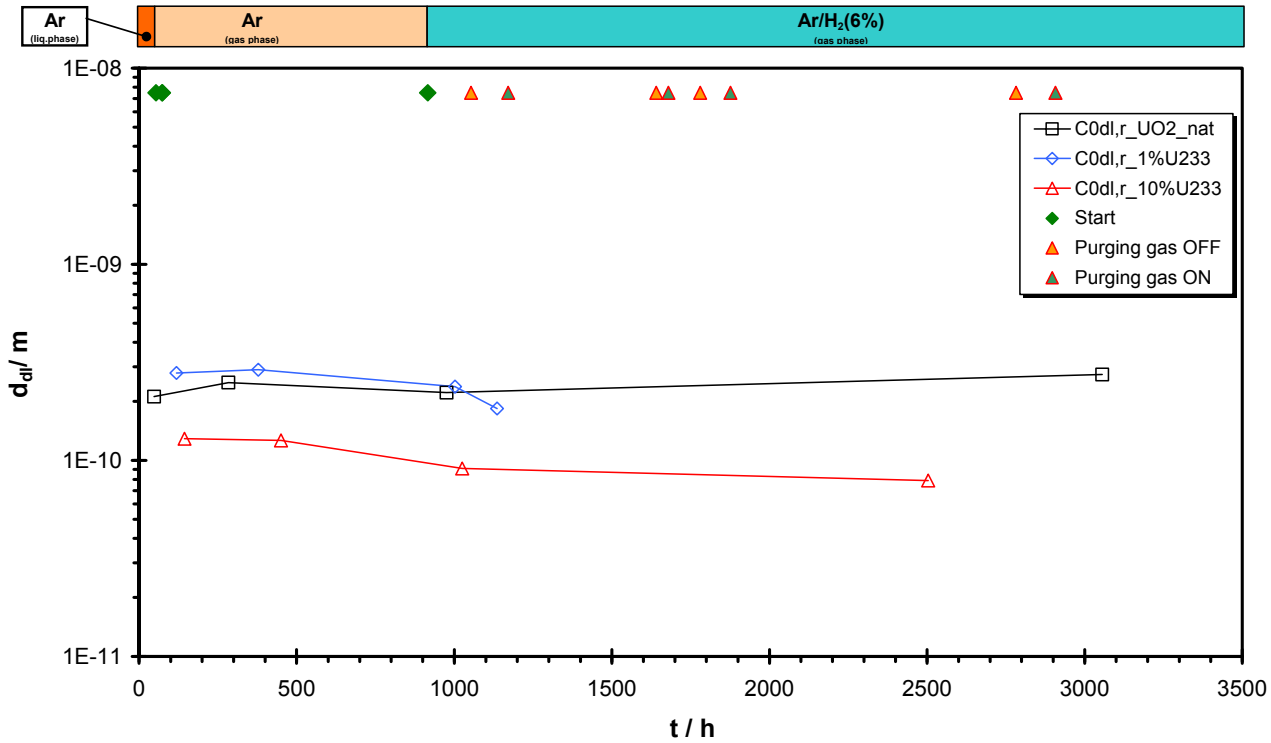

Fig. 6.4 Electrochemical double layer thickness during long term experiments

From the fitted parameters of the Nernst diffusion impedance the concentration of oxygen at the surface of the electrode and the thickness of the Nernst diffusion layer can be calculated. Also the time needed by the molecule of oxygen to diffuse through the Nernst diffusion layer to the surface of the electrode is presented. The results are presented in figures 6.5 and 6.6.

The calculated oxygen concentrations at the surface of the electrode were around $3.00 \cdot 10^{-6}$M for the natural and 1% ^{233}U doped UO_2 samples. For the 10% ^{233}U doped UO_2 sample the calculated oxygen concentration was about $3.00 \cdot 10^{-5}$M. The measured oxygen concentration in the electrochemical cell containing the 1% ^{233}U doped UO_2 sample during the free corrosion potential monitoring can be seen in figure 5.32. After the first 100 hours of measurements the measured oxygen concentration was around $1.40 \cdot 10^{-6}$M. From the EIS spectra a value of $2.11 \cdot 10^{-6}$M was calculated. After 400 hours of measurement the measured oxygen concentration was $6.4 \cdot 10^{-6}$M. The calculated oxygen concentration was $3.58 \cdot 10^{-6}$M. After changing the solution and starting the Ar/H_2 6% purging the measured oxygen concentration was $6.40 \cdot 10^{-6}$M while the calculated one was $5.66 \cdot 10^{-6}$M. The last calculated value for the oxygen concentration was $3.69 \cdot 10^{-9}$M after 220 hours of purging with Ar/H_2 6%. The measured concentration of oxygen for the same period of time was $6.30 \cdot 10^{-4}$M.

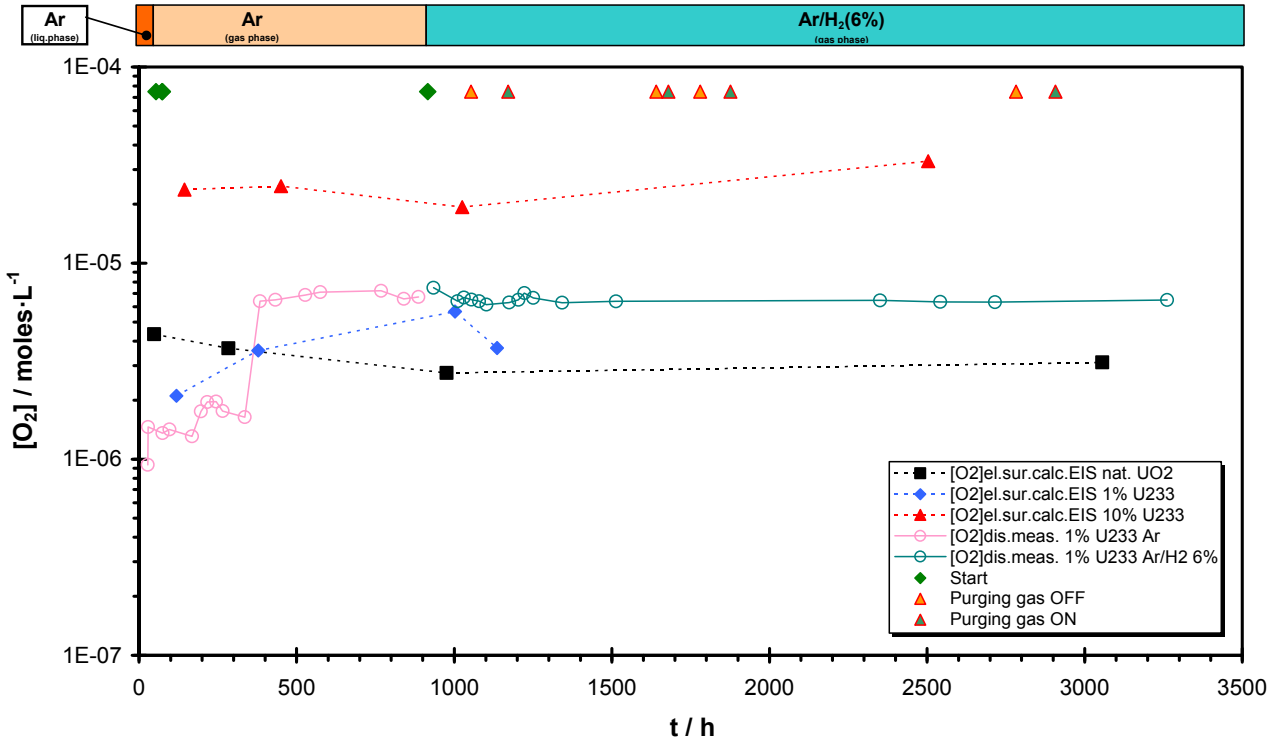

Fig. 6.5 Measured and calculated oxygen concentration variation during long term experiments

The comparison between the thicknesses of the Nernst diffusion layer and the diffusion times through this layer is presented below. For the doped UO_2 electrodes the calculated thickness of the layer is approx. 10^{-3} m and in general is stable in time. In the case of the natural UO_2 sample the diffusion layer has a thickness of approx. 10^{-2} m. After a small variation in the beginning it showed a constant thickness during the measurement period.

The diffusion time needed for the oxygen molecules to diffuse through the Nernst diffusion layer increases with the thickness of the layer. In consequence the diffusion time will be the longest in case of natural UO_2 electrode. The calculated time needed for the oxygen molecules to diffuse to the surface of the UO_2 was $3.86 \cdot 10^4$ s (almost 11 hours).

For the ^{233}U doped samples the diffusion time was much shorter because the diffusion layer was also thinner. The calculated diffusion times were around 400 seconds (approx. 7 minutes). An increase in the diffusion time of the 1% ^{233}U doped UO_2 was observed in the last calculated value which was 960 seconds (16 minutes).

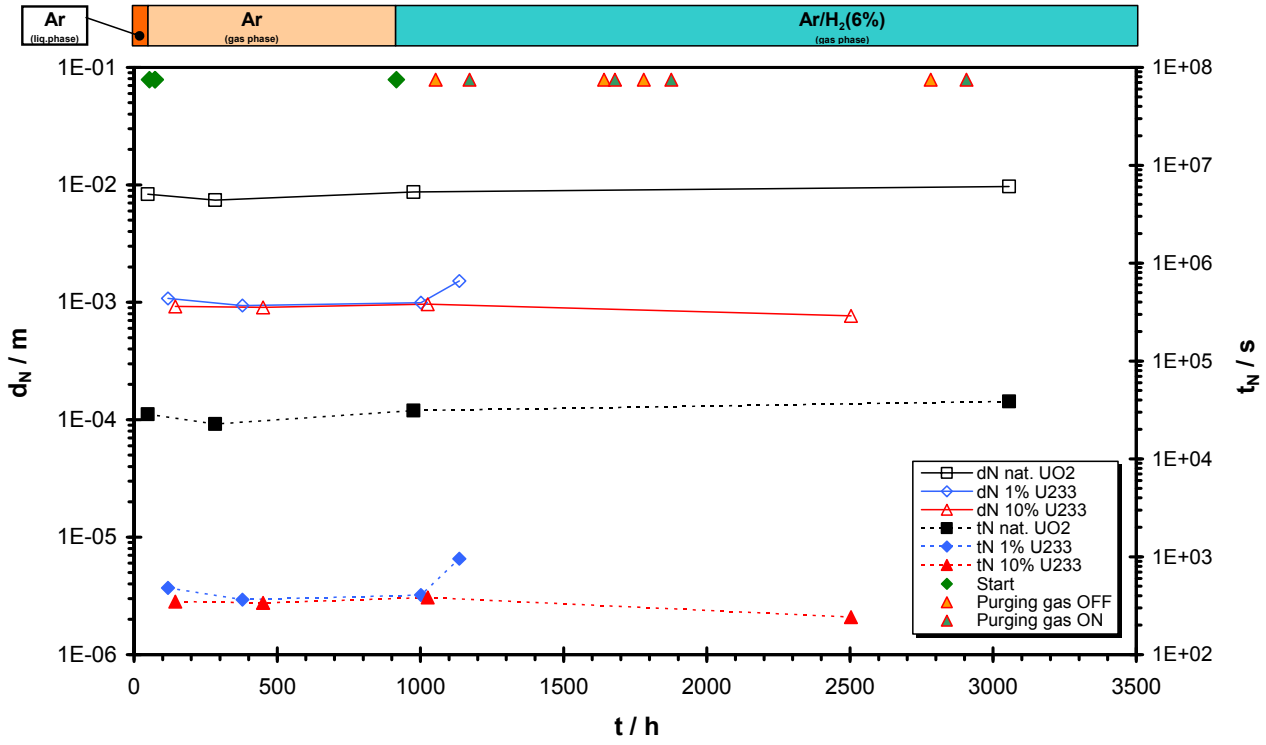

Fig. 6.6 Thickness of Nernst diffusion layer and the diffusion time of oxygen through the diffusion layer during long term experiments

6.1.5. Cyclic voltammetry

No significant differences could be seen in the cyclic voltammograms recorded during and after He^{2+} beam irradiation at $3.3 \cdot 10^7$ $cm^{-2} \cdot s^{-1}$. A difference can be observered when compared with the cyclic voltammogram recorded before irradiation. The current increase in in regions B (associated to the process $UO_2 \rightarrow UO_{2+x}$) and D (associated to the processes $UO_3 \cdot xH_2O \rightarrow UO_{2.33} \rightarrow UO_{2+x}$) is is very small. During irradiation an oxidation layer is growing on the surface of the UO_2 (as seen in figures 5.38 and 5.39). This is produced by the oxidative action of the radiolysis products generated by the interaction between He^{2+} nuclei and water. The reduction of this oxidation layer can be seen in region D, where two peaks are visible associated to the processes mentioned above. Since during the cathodic scan not all oxidised layers could be reduced during the next anodic scan a further increase of these layers can be recorded in region B. A small difference can be observed between the scans made during and after irradiation at this low flux. After irradiation the second peak in the region D which can be associated to the reduction process $UO_{2.33} \rightarrow UO_{2+x}$) is increasing in intensity compared to the one corresponding to the transformation $UO_3 \cdot xH_2O \rightarrow UO_{2.33}$. In the absence of the He^{2+} beam the radiolysis is generated only by the decay of the uranium. The flux of the α-particles generated by decay is almost 30.000 times smaller than the one used for irradiation. In such conditions the generation of $UO_3 \cdot xH_2O$ can be neglected.

The situation is different under irradiation with a He^{2+} beam at a flux of $3.3 \cdot 10^9$ $cm^{-2} \cdot s^{-1}$. The strong reducing current can be observed in region E compared to the previous cyclic voltammograms. This is due to the high concentration of oxidised uranium present on the surface of the electrode which is reduced during the scanning at this potential.

6.2. Comparison between the electrochemical data and results from solution analysis

6.2.1. Corrosion rate comparison during the long term measurements

The polarisation resistance determined from the fitting of the EIS spectra can be used to calculate the corrosion rate. The Stern-Geary equation [74]:

$$i_{corr} = \frac{b_a \cdot b_c}{2.303 \cdot (b_a + b_c)} \cdot \left(\frac{\partial i}{\partial E} \right)_{E_{corr}} \tag{6.2}$$

it is derived from the linearization of the Buttler-Volmer equation (see Capter 2). The terms b_a and b_c represent the anodic, respectively the cathodic Tafel slopes of the polarisation curves.

The polarisation resistance is defined as:

$$R_{pol} = \left(\frac{\partial E}{\partial i} \right)_{E_{corr}} \tag{6.3}$$

and it represents the slope of the linear polarization curve around the corrosion potential.

The proportionality constant B is defined as:

$$B = \frac{b_a \cdot b_c}{2.303 \cdot (b_a + b_c)} \tag{6.4}$$

From the equations (6.2) to (6.4) the relation between the corrosion current density and polarisation resistance is:

$$i_{corr} = B \cdot \frac{1}{R_{pol}} \tag{6.5}$$

From the Faraday law the corrosion rate can be calculated:

$$r_{corr} = \frac{1}{z \cdot F} \cdot \frac{B}{R_{pol}} \tag{6.6}$$

The corrosion rate was calculated from the impedance spectroscopy data as shown before and also from the results of the solution analysis. In figure 6.7 the comparison of the corrosion rate from electrochemical measurements (EIS) and from the solution analysis during the long term measurements was made.

For the natural and 1 % ^{233}U doped UO_2 electrodes the calculated values from EIS were bellow those obtained from the solution analysis. However, it has to be mentioned that the differences are within one order of magnitude.

In the case of the 100 % ^{233}U doped UO_2 electrode the calculated values from the impedance spectroscopy were higher than the data derived from the solution analysis. During Ar purging the differences are smaller than one order of magnitude. During the Ar/H_2 6% purging the differences increase up to almost two orders of magnitude. This different situation compared to the other two electrodes might be because of the low resistivity of the electrode. This means that the electrode is more conductive, allowing more charges to be transferred on the surface.

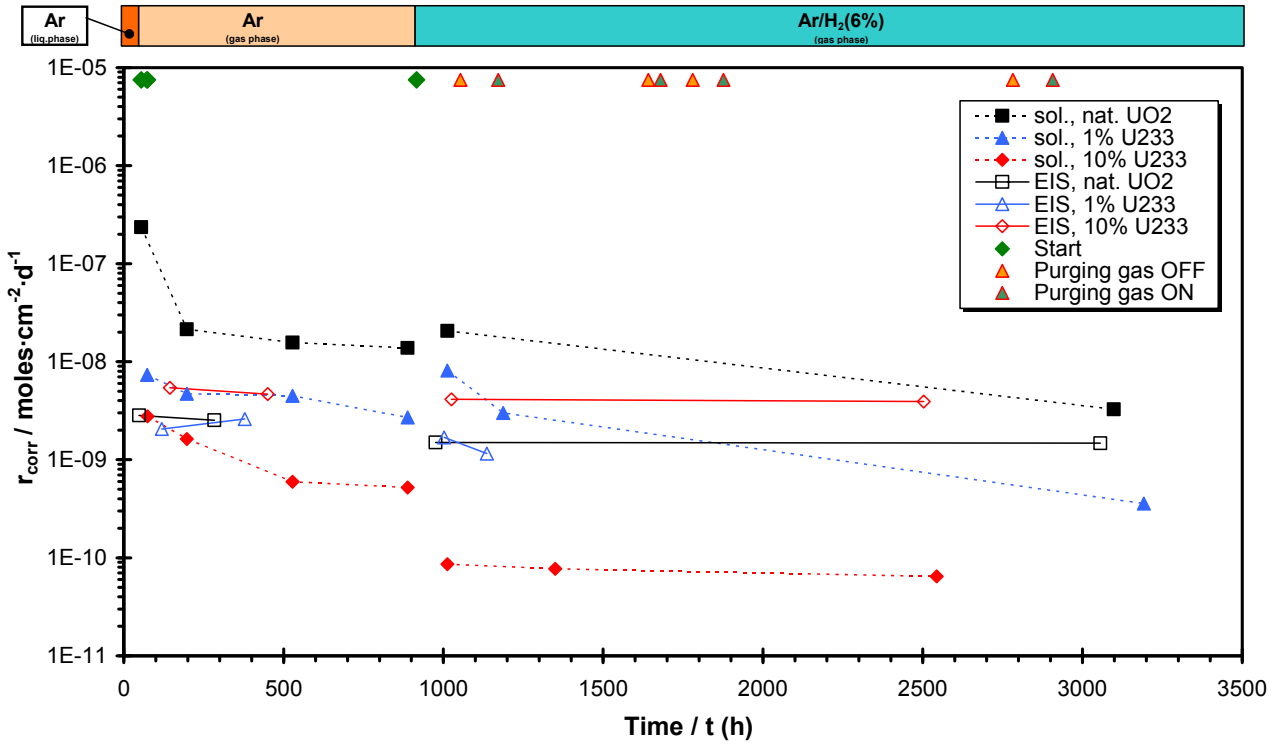

Fig. 6.7 Comparison between the corrosion rates determined from the EIS and from the solution analysis during long term measurements

6.2.2. Corrosion rate comparison during polarisation measurements

For an easier understanding the comparison is presented for each experiment separated. On each graph the corrosion rates calculated from the solution analysis, polarisation currents and impedance spectra are presented. The calculated values for the corrosion rates are presented in Appendices A.3, A.5 and A.6.

From the uranium concentration determined from the solution analysis the corrosion rate at a fixed potential is calculated using the equation:

$$r_{corr,sol,E_{pol}} = \frac{[U]_{E_{pol}} - [U]_{ref}}{A_{el} \cdot \Delta t} \qquad (6.7)$$

In the above mentioned equation the following notations where used:

- $[U]_{E_{pol}}$ – uranium concentration after the polarisation at the potential E_{pol}, in $mol \cdot L^{-1}$
- $[U]_{ref}$ – uranium concentration for the reference, in $mol \cdot L^{-1}$
- A_{el} – electrode area, in cm^2
- Δt – measurement time period, in days

As a reference the uranium concentration before starting the polarisation measurements was used.

For the calculation of the corrosion rate from the impedance spectroscopy data equation (6.6) was used. Also, the Faraday law was used for calculation of the corrosion rate from the measured polarisation currents:

$$r_{corr,pol,E_{pol}} = \frac{1}{z \cdot F} \cdot i_{pol,E_{pol}} \tag{6.8}$$

In figure 6.8 a comparison is made between the corrosion rates determined by the different mentioned methods for the experiments using natural, 1% and 10% ^{233}U doped UO_2 electrodes.

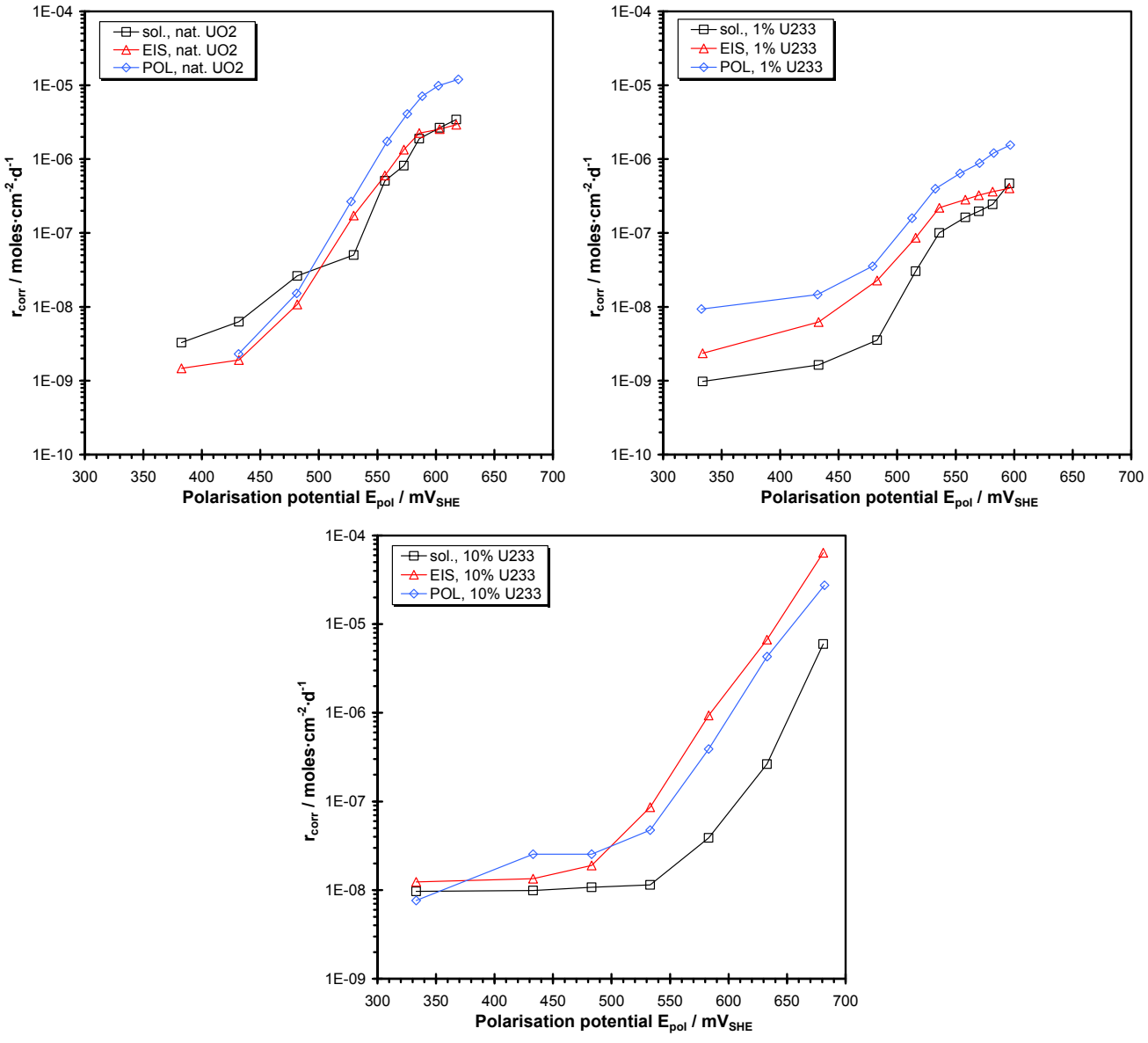

Fig. 6.8 Comparison between the corrosion rates obtained from solution analysis, impedance spectra and polarisation currents (upper left – natural UO_2; upper right – 1% ^{233}U doped UO_2;bellow - 10% ^{233}U doped UO_2)

A good correlation between the results of all three methods was observed. All the results are within one order of magnitude. Differences between the values can be due to more reasons specific for each method.

During the measurement of the polarisation current it is possible that a longer would have been needed until the steady state would be reached, especially at low polarisation potentials.

For the recording of the impedance spectra at the open circuit potential and also at low polarisation potentials measurements at lower frequencies would have reduced the uncertainty in the values of the polarisation resistance, but this would have required a longer measurement time. At high polarisation potentials the uncertainty in the determination of the polarisation resistance increases due to the small signal change in the spectrum.

In order to reduce the probability of the uranium to be adsorbed in the walls of the sampling bottles before sampling HNO_3 is added to the bottles. Although the bottles were weighted a decrease in the amount of solution in the bottles during storage in the glove box is possible. The bottles were also weighted after solution sampling from the experimental vessels. After the solution analysis the concentrations were back-calculated to the concentrations inside the electrochemical cells. However, an error due to possible loss of water or uranium sorption in the walls of the bottles during storage might influence the calculated rates.

In the figure 6.9 the same comparison between corrosion rate is made for the polarisation measurements under He^{2+} beam irradiation of UO_2 electrodes in aqueous solutions purged with Ar and Ar/H_2.

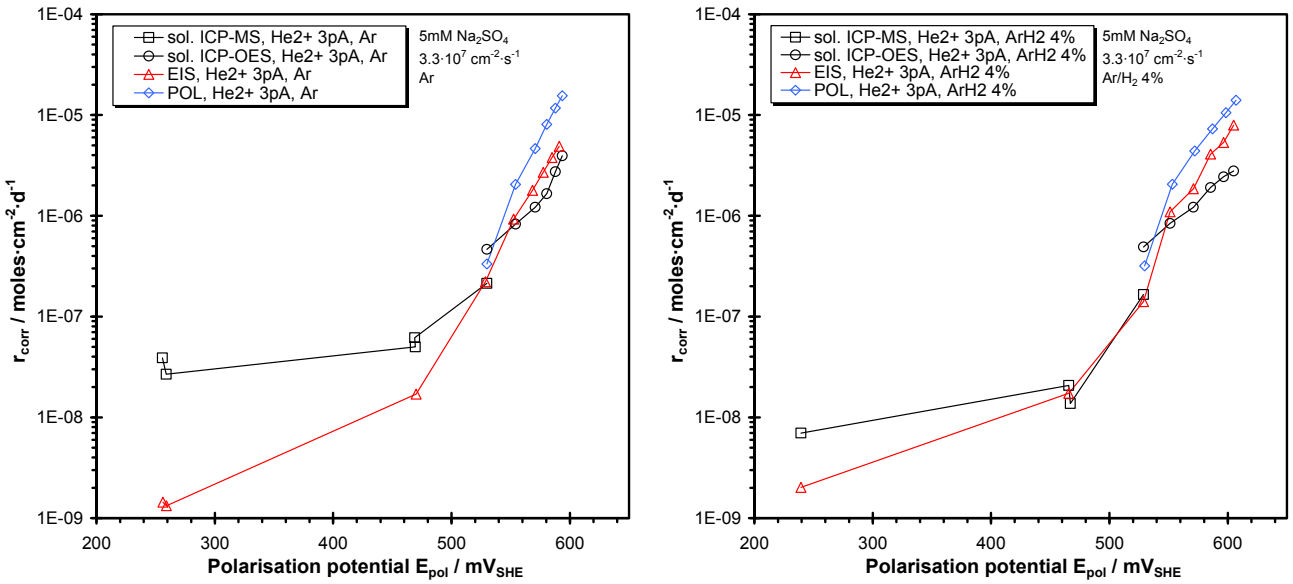

Fig. 6.9 Comparison between the corrosion rates obtained from solution analysis, impedance spectra and polarisation currents during irradiation with 45 MeV He^{2+} $3.3 \cdot 10^7$ $cm^{-2} \cdot s^{-1}$ (left – Ar purging; right – Ar/H_2 4% purging)

Also a good correlation between the values can be observed for these measurements. The bigger difference between the rates derived from impedance spectroscopy and solution analysis is due to the bigger uncertainty in the fitting of the polarisation resistance. Because of time limitations long impedance spectroscopy measurements can not be run. It is possible that measurements at lower frequencies would have reduced the differences between the values.

6.3. Surface characterisation

The Scanning Electron Microscopy coupled with Energy Dispersive X-ray Spectroscopy helped in the creating of a complete image on the corrosion processes together with the different electrochemical measurements and solution analysis.

The pictures show the strong localised corrosion attacks. The attacks were concentrated on the grain boundaries and along the pre-existing cracks. However, as seen in the figures 5.39 and 5.40 the corrosion attacked also inside the grains. It is mentioned that the 10% ^{233}U doped UO_2 electrode presented in these figures had the lowest resistivity from all the investigated samples.

The other doped sample, the 1% ^{233}U doped UO_2 electrode had the highest resistivity. In figures 5.37 and 5.38 the traces of the corrosion can be seen along the cracks and o the grain boundaries. However, no corrosion inside the grains was observed.

The natural UO_2 electrode shows on the whole surface the consequences of the pitting corrosion. Corrosion pathways going deep inside the UO_2 matrix can be observed in figure 5.36.

After the end of polarisation measurements the ^{233}U doped electrodes were left for a longer time in the solution. However, no evidence of secondary phases could have been observed on the SEM pictures. Also the EDX analysis revealed only the presence of uranium on the surface of the electrodes.

The situation was different with the UO_2 disks used for the electrochemical investigations during He^{2+} beam irradiation. As seen in figures 5.41 and 5.42 the optical microscope pictures taken after irradiation, a film was formed on the irradiated surface. Most probably this film is a studtide layer produced due to the oxidative action of the radiolysis products on the surface of UO_2. On the surface of the UO_2 disk used for the polarisation measurements also evidences of localised corrosion can be seen.

7. Conclusions

In this work proportionality has been found between the redox potential, expressing how reducing or oxidative the solution is, and the corrosion potential. Under reducing conditions both parameters varied in the same way during the interruption of the purging gas. In presence of hydrogen the corrosion potential together with the redox potential decreased, as already shown in [91, 98].

The measured values of the free corrosion potential of depleted UO_2 disks in aqueous solutions under de-aerated conditions were approx. 250mV vs. SHE, being in good agreement with the literature data [68, 69, 72].

A logarithmic dependence between the corrosion potential of UO_2 and the flux of α-particles simulated by the use of 45MeV He^{2+} beam was found. The corrosion potential increases with 47mV/decade together with the decimal logarithm of the α-particle flux. This dependence was observed to be valid up to a flux of $3.3 \cdot 10^{9} cm^{-2} \cdot s^{-1}$. However, the differences between the physical properties of the UO_2 electrodes made a further comparison between the corrosion potentials measured during He^{2+} beam irradiation and those measured using α-doped UO_2 samples impossible.

The low value of the *p*H (approx. 4) had a significant influence on the redox and corrosion potentials measured during the electrochemical measurements conducted on natural UO_2 and on different levels of α-doped UO_2 samples. This low *p*H value can be explained by presence in solution of iron and silicon in concentrations around 10^{-5} to 10^{-4}M.

In presence of hydrogen the corrosion potentials decreased in experiments involving natural and α-doped UO_2. The same behaviour was observed for depleted UO_2 with and without He^{2+} beam irradiation. A decrease of the corrosion potential in these cases means that the corrosion process of UO_2 was slowed down. Nevertheless, at higher He^{2+} beam fluxes the influence of hydrogen on the corrosion potential decreased. This can be due to the oxidising effect of the radiolysis products which exceeds the effect of hydrogen. The difference between the corrosion potentials measured in Ar and Ar/H_2 4% was small already at flux of $3.3 \cdot 10^{7} cm^{-2} \cdot s^{-1}$. After the irradiation was ended the effect of hydrogen could be seen again. The post-irradiation measured corrosion potential under reducing conditions was lower than the one under anoxic conditions.

The cathodic polarisation curves recorded in anoxic conditions (Ar purging) without irradiation and at low He^{2+} beam flux ($3.3 \cdot 10^{7} cm^{-2} \cdot s^{-1}$) gave slopes of -357mV/decade and -370mV/decade, respectively. These high values of the slopes is due to the fact that at high negative polarisation potentials the concentration of negative species (like solvated electrons) is significant and has a big impact on the mechanism of the reactions taking place at the interface. However, no influence of the He^{2+} beam and consequently of the α-activity field could be observed on the cathodic polarisation curve under these experimental conditions.

Also, no influence of the α-activity could be observed on the slopes of the anodic polarisation curves both under anoxic conditions (Ar) and slightly reducing conditions (Ar/H_2 4%). This means that at a He^{2+} beam flux of $3.3 \cdot 10^{7} cm^{-2} \cdot s^{-1}$, the α-radiolysis does not influence the oxidation/dissolution mechanism of UO_2.

However, an influence of the purging gas was observed during the potentiostatit polarisation measurements under He^{2+} beam irradiation. The values of the Tafel slopes recorded under Ar/H_2 4% purging were found to be 65mV/decade, in good concordance with the literature data [69, 72, 73]. In contrast, the slopes of 45mV/decade were observed Ar purging.

The Tafel slopes for the natural and α-doped UO_2 under reducing conditions (Ar/H_2 6%) were 50mV/decade. This difference in slopes be explained by a local acidification of the interface [72, 73]. Local acidification can occur at high polarisation potentials especially if there is no stirring of the solution. The acidification of the surface was supported by the fact that during the experiments the *p*H decreased from 6.5 to 4.

Impedance spectroscopy allows the determination of parameters like: resistivity and capacitance of the electrode, polarisation resistance, thicknesses of the double layer, oxygen concentration at the electrode surface and the thickness of the diffusion layer. A good correlation was found between the measured and calculated oxygen concentration.

In all long term impedance measurements diffusive mass transport of oxygen to and from the UO_2 surface needed to be taken into calculations independently of the redox conditions in the solution.

Tafel slopes derived from the measurement of the reciprocal polarisation resistance vs. polarisation potential by impedance spectroscopy gave comparable values with the ones deduced from the polarisation curves.

The corrosion rates were calculated from the polarisation resistance measured by impedance spectroscopy, from the potentiostatic polarisation currents and additionally obtained from solution analysis. The rates derived from these three different methods were in good agreement.

The cyclic voltammograms indicate different redox reactions taking place at the the surface of UO_2. These reactions take place under distinct conditions and at different rates. At higher beam fluxes ($3.3 \cdot 10^9$ $cm^{-2} \cdot s^{-1}$), the influence of the He^{2+} beam is significant on the rate of the redox reactions taking place on the surface of UO_2 while no big differences could be observed during and after irradiation at low flux ($3.3 \cdot 10^7$ $cm^{-2} \cdot s^{-1}$).

The SEM-EDX investigations of the electrode surface after the experiments showed evidence of corrosion especially along cracks and grain boundaries. No formation of secondary phases was observed in case of UO_2 samples at low fluxes of α-particles, below $10^7 cm^{-2} \cdot s^{-1}$. In the case of UO_2 samples irradiated with a 45MeV He^{2+} beam at fluxes between $3.3 \cdot 10^7$ and $3.3 \cdot 10^9$ $cm^{-2} \cdot s^{-1}$, a formation of a white layer was observed, probably studtite.

Setting up and commissioning of a newly designed and built glove box is some time much more time consuming than expected. It was intended during this doctoral work to investigate also other aspects which may influence the corrosion process of spent UO_2 and mixed fuels inside the underground repository in the presence of ground water.

The comparison between natural UO_2 single crystal and sintered pellets would help in the understanding of the structure influence on the corrosion process. It is expected that the dissolution rate of the matrix to be much slower in case of the UO_2 single crystal, since it was already observed that the corrosion take place mostly at the ground boundaries or fractures in the material.

Using of Pu doped UO_2 electrodes would help the simulation of different ages of spent nuclear fuel by providing higher fields of α-activity, as already shown in figure 1.1. Also the influence of plutonium could be investigated helping to a better understanding of the corrosion processes of the mixed oxide fuels.

Electrodes made from natural UO_2 single crystals and Pu doped UO_2 have already been prepared and characterised. Future experiments may be conducted using these samples. Also additional electrochemical techniques, like the Electrochemical Noise Analysis or Electrochemical Atomic Force Microscopy could be used for the investigation of the localised corrosion processes.

The behaviour of UO_2 and α-doped UO_2 in aqueous solutions was investigated by different electrochemical and analytical techniques. A good agreement of the obtained results was found.

In this thesis, it is shown that the electrochemical methods can be used to study the corrosion behaviour of UO_2 under repository conditions. The methods have a low detection limit and deliver real-time data reflecting the reaction at the UO_2 – H_2O interface. In comparison with classical leaching experiments the electrochemical methods are faster and give the possibility to impose redox conditions which can be similar to those in a repository.

It can be concluded that the electrochemical methods contribute to a reliable understanding of the reactions governing the corrosion of UO_2 which is crucial for the safety assessment of the final repository for spent nuclear fuel.

8. Bibliography

[1] H. Christensen and H.J. Sunder: "An evaluation of water layer thickness effective in the oxidation of UO_2 fuel due to radiolysis of water", *J. Nucl. Mat.*, **238**, (1996), 70-77

[2] B. Pastina: "Study on the radiolysis of water in the primary cooling system from pressurised water reactors", Doctoral thesis, University Paris XI Orsay, (1997)

[3] G. Choppin, J. Rydberg and J.O. Liljenzin: "Radiochemistry and Nuclear Chemistry", 2nd edition, Butterworth-Heinemann Ltd., Oxford, (1995)

[4] K.H. Lieser: "Nuclear and Radiochemistry: Fundamentals and Applications", VCH, Weinheim, (1997)

[5] J.F. Ziegler, J.P. Biersack and U. Littmark: "The Stopping and Range of Ions in Solids", edited by J.F. Ziegler, Pergamon Press, New York, (1985)

[6] V.V. Rondinela, Hj Matzke, J. Cobos and T.Wiss: "Leaching behaviour of UO_2 containing α-emitting actinides", *Radiochim. Acta*, **88**, 527-531, (2000)

[7] C.Cachoir, P. Carbol, J. Cobos-Sabate, J.P. Glatz, B. Grambow, K. Lemmens, A. Martinez-Esparza, T. Mennecart, C. Ronchi, V.V. Rondinella, D. Serrano-Purroy, K. Spahiu, D.H. Wegen and T. Wiss: "Effect of alpha irradiation field on long-term corrosion rates of spent fuel", *Technical Report JRC-ITU-SCA-2005/01*, (2005)

[8] D.W. Shoesmith, W.H. Hocking, B.M. Ikeda, F. King, J.J. Noel and S. Sunder: "Application of electrochemical methods in the development of models for fuel dissolution and container corrosion under nuclear waste disposal conditions", *Can. J. Chem.*, **75**, (1997), 1566-1584

[9] K. Spahiu, L. Werme and U.-B. Eklund: "The influence of near field hydrogen on actinide and spent fuel leaching", *Rad. Chem. Acta*, **88**, (2000), 507-511

[10] M.E. Broczkowski, J.J. Noel and D.W. Shoesmith: "The inhibiting effects of hydrogen on the corrosion of uranium dioxide under nuclear waste disposal conditions", *IYNC 2004*, (2004)

[11] I. Grenthe, J. Fuger, R.J.M. Konings, R.J. Lemire, A.B. Muller, C. Nguyen-Trung and H. Wanner: "Chemical Thermodinamics. Vol. 1. Chemical Thermodinamics of Uranium", edited by H. Wanner and I. Forest, North-Holland, Amsterdam, (1992)

[12] J.O'M. Bockris and A.K.N. Reddy: "Modern Electrochemistry", Vol. 2, Plenum Press, New York, (1997)

[13] A.J. Bard and L.R. Faulkner: "Electrochemical Methods", John Wiley and Sons, New York, (1980)

[14] D. Swiatla-Wojcik and G.V. Buxton: "Modeling of radiation spur processes in water at temperatures up to 300°C", *J. Phys. Chem.*, **99**, (1995), 11464-11471

[15] Y. Frongillo, M.J. Fraser and V. Cobut: "Evolution of the species produced by the slowing down of rapid protons in liquid water", *J. Chim. Phys.*, **93**, (1996), 93-102

[16] W.G. Burns and H.E. Sims: "Effect of radiation type in water radiolysis", *J. Chem. Soc. Faraday Trans.*, **77**, (1981), 2803

[17] P. Buisson, P. Pïluso and M. Pernet: "Determination by X-ray diffraction of the compositional distribution of $U_{1-y}Ce_yO_2$ solid in UO_2 - $U_{1-y}Ce_yO_2$ composite", *J. Phys. IV*, **8**, (1998), 77-84

[18] B.T.M. Willis: "Crystallographic studies of anion excess uranium oxides", *J. Chem. Soc. Faraday Trans. II*, **83**, (1987), 1073-1081

[19] D.K. Smith, B.E. Scheetz, C.A.F. Anderson and K.L. Smith: "Phase relations in the uranium-oxygen-water system and its significance on the stability of nuclear waste forms", Ed. Elsevier, (1982)

[20] L.H. Johnson and D.W. Shoesmith: "Radioactive waste forms for the future", Edited by W. Lutze and R.C. Ewing, (1988)

[21] P. Vitorge: "Actinides chemistry. Engineering techniques", Presentation for Scientific and Technical Evaluation Committee of nuclear fuel cycle (1999)

[22] S. Sunder, D.W. Shoesmith, R.J. Lemire, M.G. Bailey and G.J. Wallace: "The effect of *p*H on the corrosion of nuclear fuel (UO_2) in oxygenated solutions", *Corr. Sci.*, **32-4**, (1991), 373-386

[23] D.W. Shoesmith: "Fuel corrosion processes under waste disposal conditions – review", *J. Nucl. Mat.*, **282**, (2000), 1-31

[24] M.E. Torrero, E. Baraj, J. de Pablo, J. Gimenez and I. Casas: "Kinetics of corrosion and dissolution of uranium dioxide as a function of *p*H", *Int. J. Chem. Kinet.*, **29**, (1997), 261

[25] W. Stumm and G. Furrer: "The dissolution of oxides and aluminium silicates; examples of surface-coordination-controlled kinetics", in "Aquatic surface chemistry. Chemical processes at the particle-water interface", edited by John Wiley and Sons, (1987)

[26] S.A.Steward and W.J. Gray: "Comparison of uranium dissolution rates from spent fuel and uranium dioxide". Proceedings of "5th Annual Intl. High-Level Radioactive Waste Management Conf. (Waste Management 94)", Las Vegas, Nevada, **4**, (1994), 2602

[27] D. Rai, A.R. Felmy and J.L. Ryan: "Uranium (IV) hydrolysis constants and solubility product of $UO_2 \cdot xH_2O_{(am)}$", *Inorg. Chem.*, **29**, (1990), 260-264

[28] M.E. Torrero, I. Casas, M. Aguilar, J. de Pablo, J. Gimenez, and J. Bruno: "The solubility of unirradiated UO_2 in both perchlorate and chloride test solutions. Influence of the ionic medium", *Mat. Res. Soc. Symp. Proc.*, **212**, (1991), 229-234

[29] T. Yajima, Y. Kawamura and S. Ueta: "Uranium (IV) solubility and hydrolysis constants under reduced conditions", *Mat. Res. Soc. Symp. Proc.*, **353**, (1995), 1137-1142

[30] J. Bruno, I. Casas, I and Puigdomènech: "The kinetics of dissolution of UO_2 under reducing conditions and the influence of an oxidized surface layer (UO_{2+x}): Application of a continuous flow-through reactor", *Geochim. Cosmochim. Acta.*, **55**, (1991), 647-658

[31] J. Bruno: "A reinterpretation of the solubility product of solid uranium (IV) dioxide", *Acta Chem. Scandin.*, **43**, (1989), 99-100

[32] I. Casas, J. De Pablo, J; Gimenez, M.E. Torrero, J. Bruno, E. Cera, R.J. Finch and R.C. Ewing: "The role of pe, *p*H and carbonate on the solubility of UO_2 and uranite under nominally reducing conditions", *Geochim. Cosmochim. Acta.*, **62**, (1998), 2223-2231

[33] D.W. Shoesmith, S. Sunder and W.H. Hocking: in "Electrochemistry of Novel Materials", J. Lipkowski, P.N. Ross (Eds.), VCH, New York, (1994)

[34] J. De Pablo, J. Gimenez, M.E. Torrero and I. Casas: "Mechanism of unirradiated UO_2(s) dissolution in NaCl and $MgCl_2$ brines à 25°C", *Mat. Res. Soc. Symp. Proc. Series*, **353-1**, (1995), 609

[35] I.Casas, J. Gimenez, V. Marti, M.E. Torrero and J. de Pablo: "Kinetic studies of unirradiated UO_2 dissolution under oxidizing conditions in batch and flow experiments", *Radiochim. Acta*, **66/67**, (1994), 23

[36] B. Grambow, A. Loida, P. Dressler, H. Geckeis, J. Gago, I. Casas, J. de Pablo, J. Gimenez and M.E. Torrero: "Long-term safety of radioactive waste disposal: chemical reaction of fabricated and high burnup spent UO_2 fuel with saline brines", *Kernforschungszentrum Karlsruhe Report KfK 5702*, (1996)

[37] H. Christensen and S. Sunder: "Current state of knowledge of radiolysis effects on spent nuclear fuel corrosion", *Nucl. Techn.*, **131**, (2000), 102

[38] H. Christensen, R. Forsyth, R. Lundqvist and L.O. Werme: "Radiation induced dissolution of UO_2", *Studsvik Report NS-90/85*, (1990).

[39] J. Gimenez, E. Baraj, M.E. Torrero, I. Casas and J. de Pablo: "Effect of H_2O_2, NaClO and Fe on the dissolution of unirradiated UO_2 in NaCl 5 $mol.kg^{-1}$. Comparison with spent fuel dissolution experiments", *J.Nucl. Mat.*, **238**, (1996), 64

[40] B. Grambow, A. Loida, P. Dressler, H. Geckeis, P. Diaz, J. Gago, I. Casas, J. de Pablo, J. Gimenez and M.E. Torrero: "Long-term safety of radioactive waste disposal : reaction of high burnup spent fuel and UO_2 in saline brines at room temperature", *Kernforschungszentrum Karlsruhe Report KfK 5377*, (1994)

[41] P. Diaz-Arocas, J. Quinones, C. Maffiotte, J. Serrano, J. Garcia, J.R. Almazan and J. Esteban: "Effect of secondary phases formation in the leaching of UO_2 under simulated radiolytic products", *Mat. Res. Soc. Symp. Proc.*, **353**, (1995), 641

[42] J. Bruno and A. Sandino: "The thermodynamics and kinetics of co-precipitation and its effect on radionuclide solubility", *Radiochim. Acta*. **44**, (1988), 17-21

[43] J. Bruno, I. Grenthe and B. Lagerman: "On the UO_2^{2+}/U^{4+} potential", *Acta. Chem. Scand.*, **44**, (1990), 896-901

[44] L.H. Johnson, D.W. Schoesmith, G.E. Lunansky, M.G. Bailey and P.R. Tremaine: "Mechanisms of leaching and dissolution of UO_2 fuel", *Nucl. Techn.*, **56**, (1982), 238-253

[45] D.W. Shoesmith, S. Sunder, L.H. Johnson and M.G. Bailey: "Oxidation of CANDU UO_2 fuel by the alpha radiolysis products of water", *Mat. Res. Soc. Symp. Proc.*, **50**, (1985), 309

[46] S. Sunder, D.W. Shoesmith and N.H. Miller: "Oxidation and dissolution of nuclear fuel (UO_2) by the products of the alpha radiolysis of water", *J. Nucl. Mat.*, **24**, (1997)**4**, 66

[47] W.J. Gray: "Effect of surface oxidation, alpha radiolysis, and salt brine composition on spent fuel and UO_2 leaching performance", *Report PNL/SRP-6689*, (1988)

[48] V.V. Rondinella, Hj. Matzke, J. Cobos and T. Wiss: "α-radiolysis and α-radiation damage effects on UO_2 dissolution under spent fuel storage conditions", *Mat. Res. Soc. Symp. Proc.*, **556**, (1999), 447

[49] J.F. Lucchini: "Influence of the α-radiolysis of the water on the alteration of the UO_2 matrix from spent nuclear fuel", Doctoral Thesis, University Paris XI Orsay (2001)

[50] G. Sattonay, C. Ardois, C. Corbel, J.F. Lucchini, M.-F. Barthe, F. Garrido and D. Gosset: "Alpha-radiolysis effects on UO_2 alteration in water", *J. Nucl. Mat.*, **288**, (2001), 11-19

[51] S. Sunder and D.W. Shoesmith: "Chemistry of UO_2 fuel dissolution in relation to the disposal of used nuclear fuel", AECL-10395, (1991)

[52] S. Gordon, J.C. Sullivan and A.B. Ross: "Rate constants for reactions of radiation-produced transients in aqueous solutions of actinides", *J. Phys. Chem. Ref. Data*, **15-4**, (1986), 1357

[53] G.V. Buxton, CL Greenstock, W.P. Helman and A.B. Ross: "Critical review of rate constants for reactions of hydrated electrons, hydrogen atoms and hydroxyl radicals ($OH\cdot/\cdot O^-$) in aqueous solution", *J. Phys. Chem. Ref. Data*, **17-2**, (1988), 513

[54] J.R. Macdonald, "Impedance Spectroscopy", John Wiley & Sons, Inc., New York, (1987)

[55] A. J. Bard and L.R. Faulkner, "Electrochemical methods. Fundamentals and Applications", 2nd edition, John Wiley & Sons, Inc., New York, (2001)

[56] W, Wang, C.E. Reimers, S.C. Wainright, M.R. Shahriari and M.J. Morris: "Applying fiber-optic sensors for monitoring dissolved oxygen", *Sea Technology*, **40-3**, (1999), 69-74

{57] M.R. Shahriari, M.T. Murtaugh and H.C. Kwon: "Ormosil thin films for chemical sensing platforms", *Chem., Biochem. and Environ. Fiber Sensors IX*, **3105**, (1997), 40-51

[58] M. Krihak and M.R. Shahriari: "A highly sensitive, all solid state fiber optic oxygen sensor based on the sol-gel coating technique", .*Electronic Letters*, **32-3**, (1996)

[59] M. Krihak, M.T. Murtaugh and M.R. Shahriari: "Fiber optic oxygen sensors based on the sol-gel coating technique", *Chem., Biochem. and Environ. Fiber Sensors VIII*, **2836**, (1996)

[60] C.B. Allen, B.K. Schneider and C.J. White: "Limitations to oxygen diffusion in-vitro cell exposure systems in hyperoxia and hypoxia", *.Am. J. of Physiol. Lung Cell Molec. Physiol*, **281**, (2001), 1021-1027

[61] E. Mendes: "Behaviour of high purity UO_2/H_2O interfaces under a He^{2+} irradiation beam in de-aerated media", Doctoral Thesis, University Paris XI Orsay (2005)

[62] S. Guilbert: "Behaviour of UO_2 / clay water interfaces. Spectroscopical approach", Doctoral Thesis, (2000)

[63] J. Somers, R.Voet, C.Fuchs, H.Hein, C.Boshoven, S. Fourcaudot, N. Modery and M. Murray-Farthing: "Fabrication of UO_2 pellets doped with ^{233}U for α-radiolysis investigations", *Technical Report JRC-ITU-TPW-2001/12*, (2001)

[64] C. Corbel, G. Sattonnay, S. Guilbert, F. Carrido, M.-F. Barthe and C. Jegou: "Addition versus radiolytic production effects of hydrogen peroxide on aqueous corrosion of UO_2", *J. Nucl. Mat*, **348**, (2006), 1-17

[65] E. Sauter: "Grundlagen des Strahlenschutzes", 2nd edition, Karl Thiemig AG, München, (1983)

[66] F. Miserque, T. Gouder, D.H. Wegen and P.D.W. Bottomley: "Use of UO_2 films for electrochemical studies", *J. Nucl. Mat*, **298**, (2001), 280-290

[67] S. Sunders, N.H. Miller and D.W. Shoesmith: "Corrosion of uranium dioxide in hydrogen peroxide solutions", *Corr. Sci.*, **46**, (2004), 1095–1111

[68] S. Sunders, D.W. Shoesmith and N.H. Miller: "Oxidation and dissolution of nuclear fuel (UO2) by the products of the alpha radiolysis of water", *J. Nucl. Mat.*, **244**, (1997), 66–74

[69] D.W. Shoesmith, S. Sunders and W.H. Hocking: "Electrochemistry of UO_2 nuclear fuel", in J. Lipkowski, P.N. Ross (Eds.), "Electrochemistry of novel materials", VCH Publishers, New York, 297–338, (1994)

[70] J.M. Mermet: "Atomic Emission Spectroscopy. Inductively Coupled Plasma", *Encyclopedia of Analytical Services* (1995), 210-215

[71] "ICP Optical Emission Spectroscopy application note", Horiba Jobin Yvon S.A.S., Group, Longjumeau, France (2003)

[72] M.E. Broczkowski, J.J. Noël and D.W. Shoesmith: "The influence of dissolved hydrogen on the surface composition of doped uranium dioxide under aqueous corrosion conditions", *J. Electroanal. Chem.*, **602**, (2007), 8-16

[73] M.J. Nicol and C.R.S. Needs: "The anodic dissolution of uranium dioxide in perchlorate solutions", *Electrochim. Acta*, **20**, (1975), 585-589

[74] M. Stern and A.L. Geary: "Electrochemical Polarisation", *J. Electrochem. Soc.*, **104**, (1957), 56

[75] S. Sunders, N.H. Miller and D.W. Shoesmith: "Corrosion of uranium dioxide in hydrogen peroxide solutions", *Corr. Sci.*, **46**, (2004), 1095–1111

[76] "Uhlig's Corrosion Handbook", 2nd edition, R.W. Revie (Ed.), John Wiley & Sons, Inc., New York, (2000)

[77] F. Mansfeld: "Electrochemical Impedance Spectroscopy (EIS) as a New Tool for Investigation Methods of Corrosion Protection", *Electrochim. Acta*, **35**, (1990), 1533

[78] M.G. Bailey, L.H. Johnson and D.W. Schoesmith: "The effects of alpha-radiolysis of water on the corrosion of UO_2", *Corr. Sci.*, **25**, (1985), 233-238

[79] S. Sunder, G.D. Boyer and N.H. Miller: "XPS studies of oxidation by alpha radiolysis of water at 100°C.", *J. Nucl. Mat.***, 175**, (1990), 163

[80] H. Christensen: "Radiation induced dissolution of UO_2", *Mat. Res. Soc. Symp. Proc.*, **212**, (1991), 213

[81] F. Clarens, J. De Pablo, J. Diez-Perez, I. Casas, J. Gimenez and M. Rovira: "Formation of Studtite during the oxidative dissolution of UO_2 by hydrogen peroxide. A SFM study", *Environ. Sci. Technol*., **38**, (2004), 6656-6661

[82] B. MacNamara, E. Buck and B. Hanson: "Observation of Studtite and Metastudtite on Spent Fuel", *Mat. Res. Soc. Symp. Proc.*, **757**, 2003

[83] P. Carbol, J. Cobos-Sabate, J.-P. Glatz, C. Ronchi, V. Rondinella, D.H. Wegen, T. Wiss, A. Loida, V. Metz, B. Kienzler, K. Spahiu, B. Grambow, J. Quinones and A. Martinez Esparza Valiente (edited by K. Spahiu): "The effect of disolved hydrogen on the dissolution of ^{233}U doped UO_2(s), high burn-up spent fuel and MOX fuel", *SKB Technical Report TR-05-09*, Stockholm, Sweden, (2005)

[84] L.O. Rasmussen and E. Bjergbakke: "CHEMSIMUL, a program package for numerical simulation of chemical reaction systems", *Risö-R-395*, (1984).

[85] H. Christensen and E. Bjergbakke: "Application of Chemsimul for Groundwater Radiolysis", *Nucl. Chem. Waste Managem.* **6**, (1986), 265

[86] D.W. Shoesmith and S. Sunder: "The prediction of nuclear fuel (UO_2) dissolution rates under waste disposal conditions", *J. Nucl. Mat.*, **190**, (1992), 20-35

[87] Hj. Matzke: "Radiation damage-enhanced dissolution of UO_2 in water", *J. Nucl. Mat*, **190**, (1992), 101-106

[88] S. Sunder, D.W. Shoesmith, M. Kolar and D.M. Leneveu: "Calculation of used nuclear fuel dissolution rates under anticipated Canadian waste vault conditions", *J. Nucl. Mat*, **250**, (1997), 118-130

[89] D. Labroche, O. Dugne and C. Chatillon: "Thermodynamics of the O–U system. I – Oxygen chemical potential critical assessment in the UO_2–U_3O_8 composition range", *J. Nucl. Mat*, **312**, (2003), 21-49

[90] A. Leenaers, L. Sannen, S. Van den Berghe and M. Verwerft: "Oxidation of spent UO2 fuel stored in moist environment", *J. Nucl. Mat*, **317**, (2003), 226-233

[91] M.E. Brockzkowski, J.J. Nöel and D.W. Shoesmith: "The inhibiting effects of hydrogen on the corrosion of uranium dioxide under nuclear waste disposal conditions", *J. Nucl. Mat*, **346**, (2005), 16-23

[92] J.S. Goldik, J.J. Nöel and D.W. Shoesmith: "Surface electrochemistry of UO2 in dilute alkaline hydrogen peroxide solutions. Part II. Effects of carbonate ions", *Electrochim. Acta*, **51**, (2006), 3278-3286

[93] B.G. Santos, J.J. Nöel and D.W. Shoesmith: "The influence of potential on the anodic dissolution of SIMFUEL (UO_2)", *Electrochim. Acta*, **51**, (2006), 4157-4166

[94] B.G. Santos, J.J. Nöel and D.W. Shoesmith: "The effect of pH on the anodic dissolution of SIMFUEL (UO_2)", *J. Electroanal. Chem*, **586**, (2006), 1-11

[95] B.G. Santos, J.J. Nöel and D.W. Shoesmith: "The influence of silicate on the development of acidity in corrosion product deposits on SIMFUEL (UO_2)", *Corr. Sci.,* **48**, (2006), 3852-3868

[96] Olivia Roth, Tobias Bönnemark and Mats Jonsson: "The influence of particle size on the kinetics of UO_2 oxidation in aqueous powder suspensions", *J. Nucl. Mat*, **353**, (2006), 75-79

[97] Ella Ekeroth, Olivia Roth and Mats Jonsson: "The relative impact of radiolysis products in radiation induced oxidative dissolution of UO_2", *J. Nucl. Mat*, **355**, (2006), 38-46

[98] M.E. Brockzkowski, J.J. Nöel and D.W. Shoesmith: "The influence of dissolved hydrogen on the surface composition of doped uranium dioxide under aqueous corrosion conditions", *J. Electroanal. Chem*, **602**, (2007), 8-16

[99] Sara Nilsson and Mats Jonsson: "On the catalytic effects of UO2(s) and Pd(s) on the reaction between H_2O_2 and H_2 in aqueous solution", *J. Nucl. Mat*, **372**, (2008), 160-163

[100] Mohammad Mohsin Hossain and Mats Jonsson: "Effects of ionic strength on the kinetics for UO2 oxidation", *J. Nucl. Mat*, **373**, (2008), 190-193

APPENDICES

A.1. Corrosion potential monitoring curves (under He^{2+} beam)

Corrosion potentials during irradiation with 45 MeV He^{2+} beam (flux $3.3 \cdot 10^7$ $cm^{-2} \cdot s^{-1}$) under Ar atmosphere (samples G11-04, G11-05, H11-06, H11-09, I11-08, I11-12)

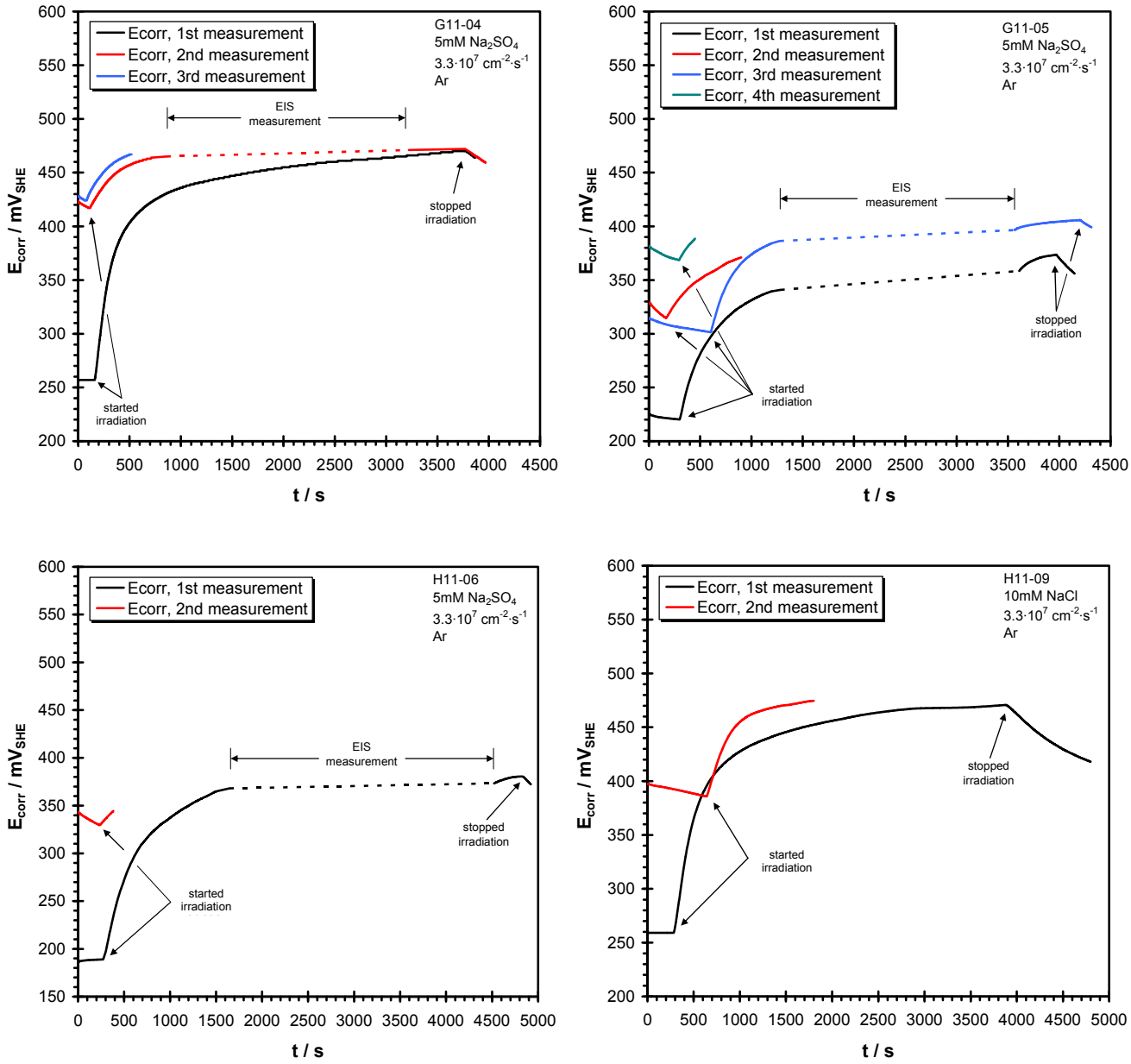

Fig. A.1a Corrosion potentials during irradiation with 45MeV He^{2+} beam (flux $3.3 \cdot 10^7$ $cm^{-2} \cdot s^{-1}$) under Ar atmosphere

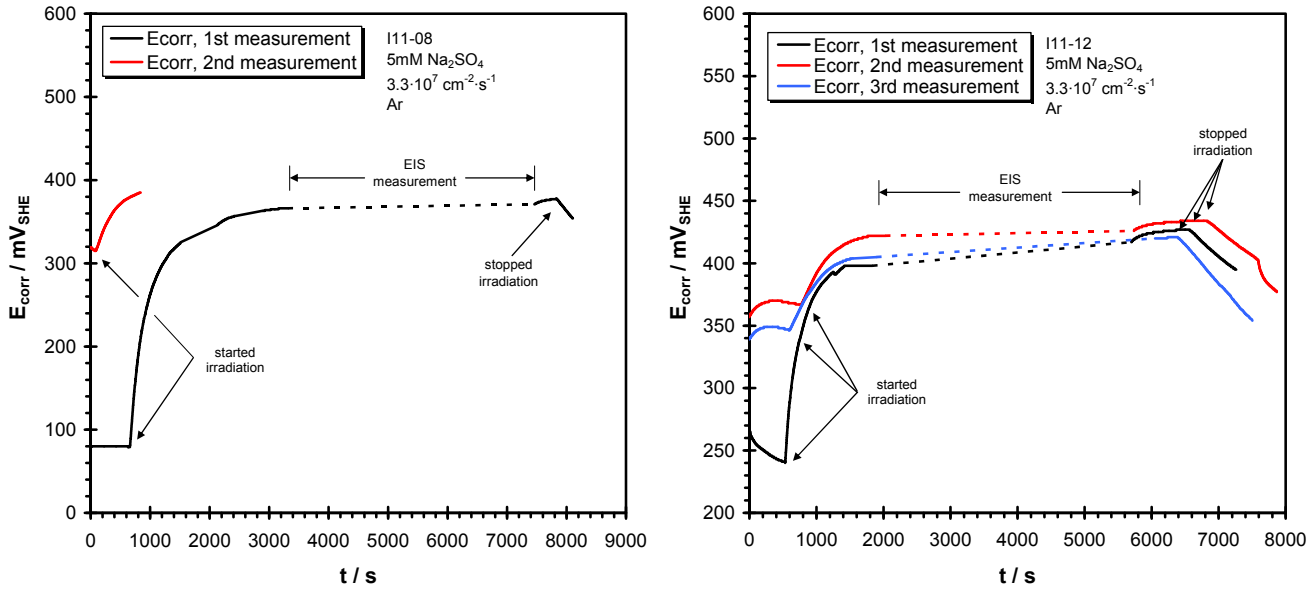

Fig. A.1.b Corrosion potentials during irradiation with 45MeV He^{2+} beam (flux $3.3 \cdot 10^7$ $cm^{-2} \cdot s^{-1}$) under Ar atmosphere

Corrosion potentials during irradiation with 45 MeV He^{2+} beam (flux $3.3 \cdot 10^8$ $cm^{-2} \cdot s^{-1}$) under Ar atmosphere (samples I11-03, I11-15)

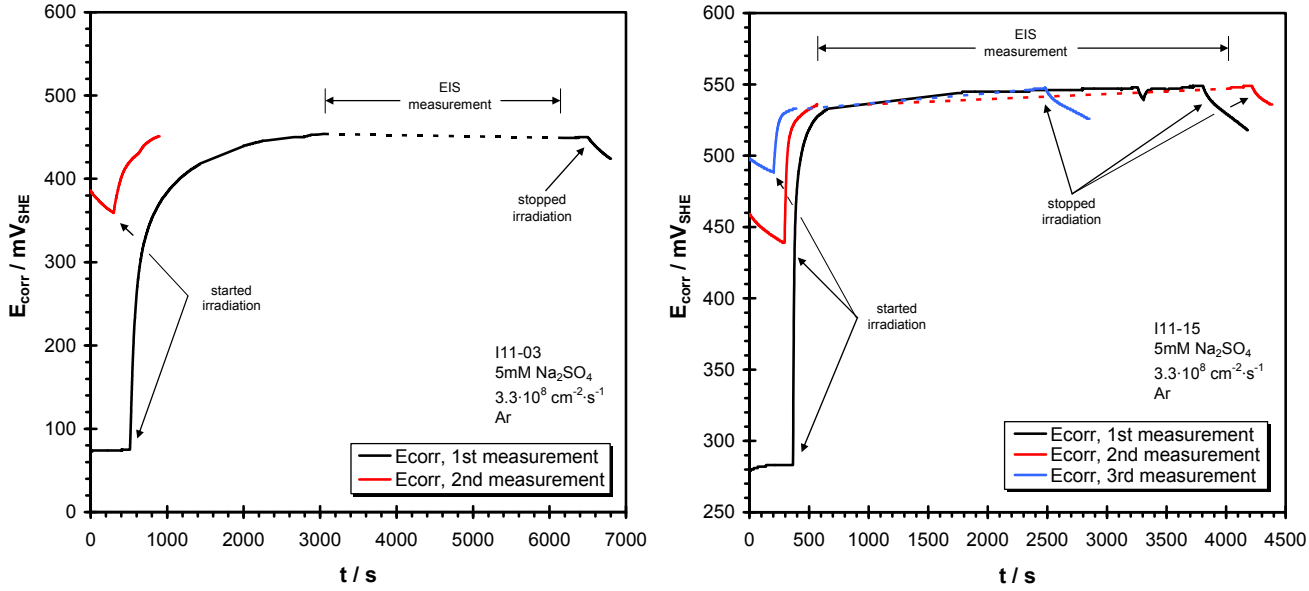

Fig. A.2 Corrosion potentials during irradiation with 45MeV He^{2+} beam (flux $3.3 \cdot 10^8$ $cm^{-2} \cdot s^{-1}$) under Ar atmosphere

Corrosion potentials during irradiation with 45 MeV He^{2+} beam (flux $3.3 \cdot 10^9$ $cm^{-2} \cdot s^{-1}$) under Ar atmosphere (samples H11-10, I11-13)

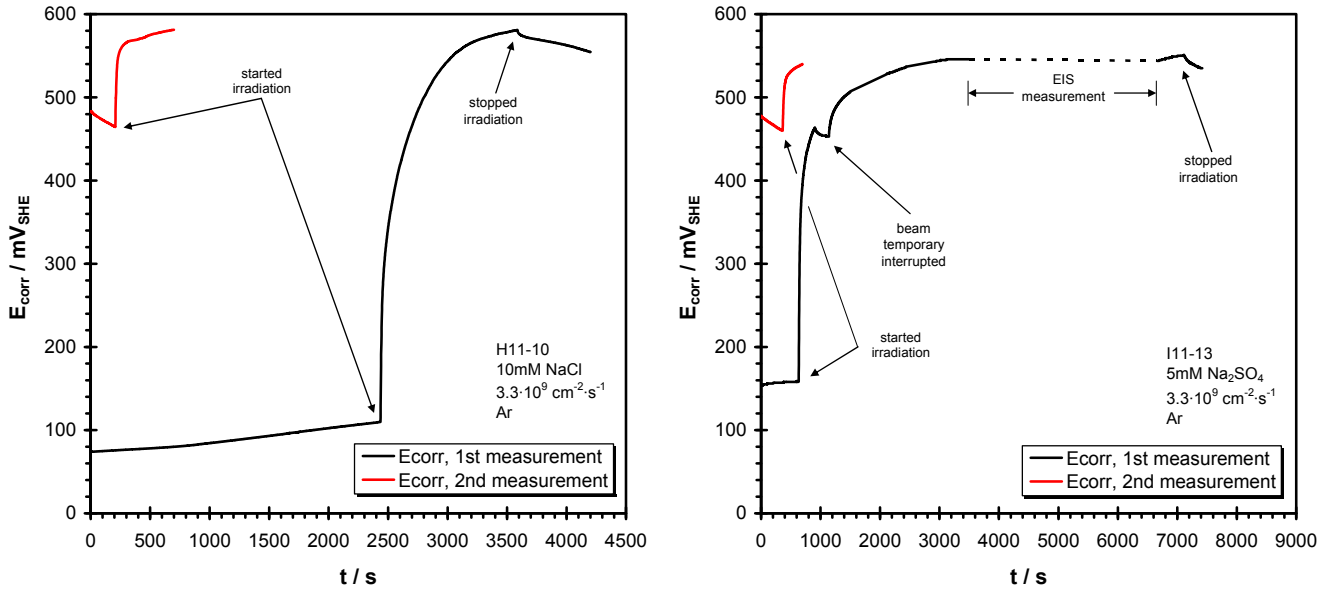

Fig. A.3 Corrosion potentials during irradiation with 45MeV He^{2+} beam (flux $3.3 \cdot 10^9$ $cm^{-2} \cdot s^{-1}$) under Ar atmosphere

Corrosion potentials during irradiation with 45 MeV He^{2+} beam (flux increased successively from $3.3 \cdot 10^7$ to $3.3 \cdot 10^9$ $cm^{-2} \cdot s^{-1}$) under Ar atmosphere (sample I11-01)

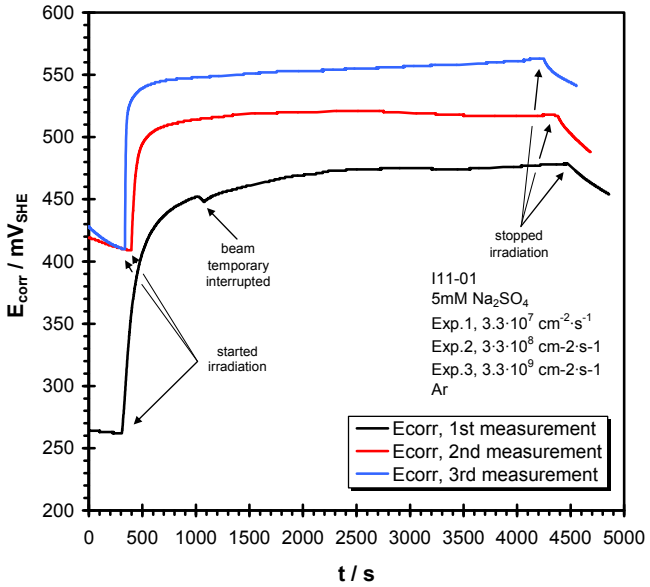

Fig. A.4 Corrosion potential during irradiation with 45MeV He^{2+} beam (flux increased from $3.3 \cdot 10^7$ $cm^{-2} \cdot s^{-1}$ to $3.3 \cdot 10^9$ $cm^{-2} \cdot s^{-1}$) under Ar atmosphere

Corrosion potentials during irradiation with 45 MeV He^{2+} beam (flux $3.3 \cdot 10^7$ $cm^{-2} \cdot s^{-1}$) under Ar/H_2 4% atmosphere (samples G11-13, G11-16)

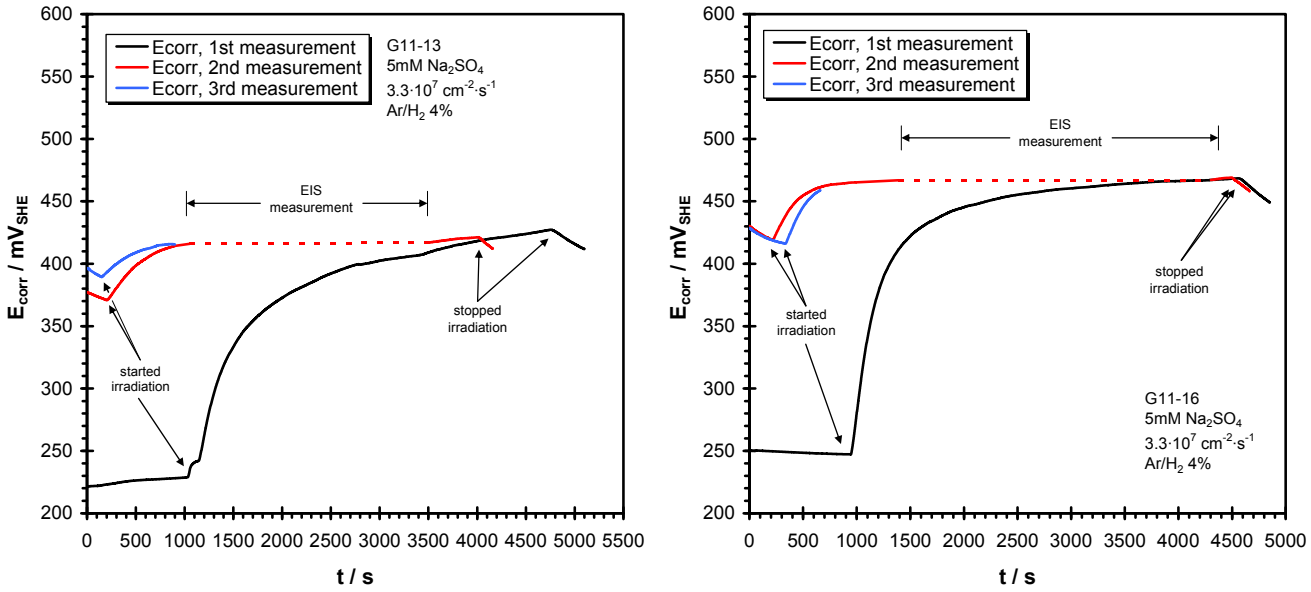

Fig. A.5 Corrosion potential during irradiation with 45MeV He^{2+} beam (flux $3.3 \cdot 10^7$ $cm^{-2} \cdot s^{-1}$) under Ar/H_2 atmosphere

Corrosion potentials during irradiation with 45 MeV He^{2+} beam (flux $3.3 \cdot 10^7$ and $3.3 \cdot 10^8$ $cm^{-2} \cdot s^{-1}$) under Ar atmosphere when cracking / leaking occurred (samples G11-06, I11-02)

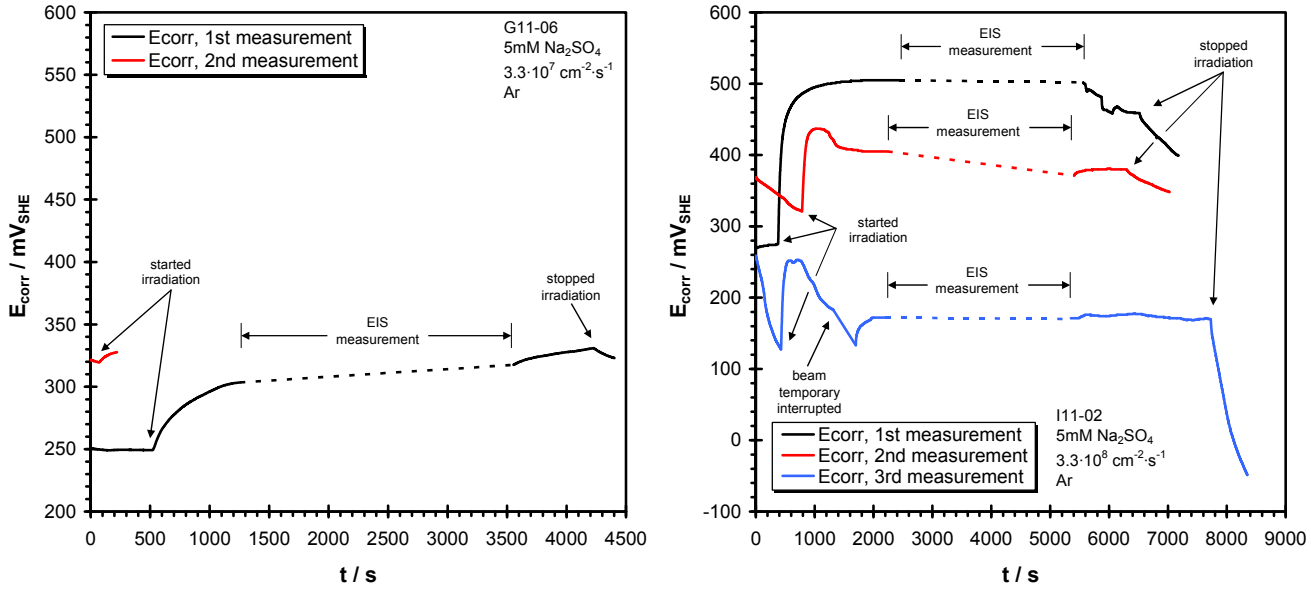

Fig. A.6 Leaking electrodes during irradiation with 45MeV He^{2+} beam (flux $3.3 \cdot 10^7$ and $3.3 \cdot 10^8 cm^{-2} \cdot s^{-1}$) under Ar atmosphere

A.2. Potentiostatic polarisation curves

Glove box experiments

Anodic polarisation curves on natural UO_2 under Ar/H_2 atmosphere (sample name UO_2 – X)

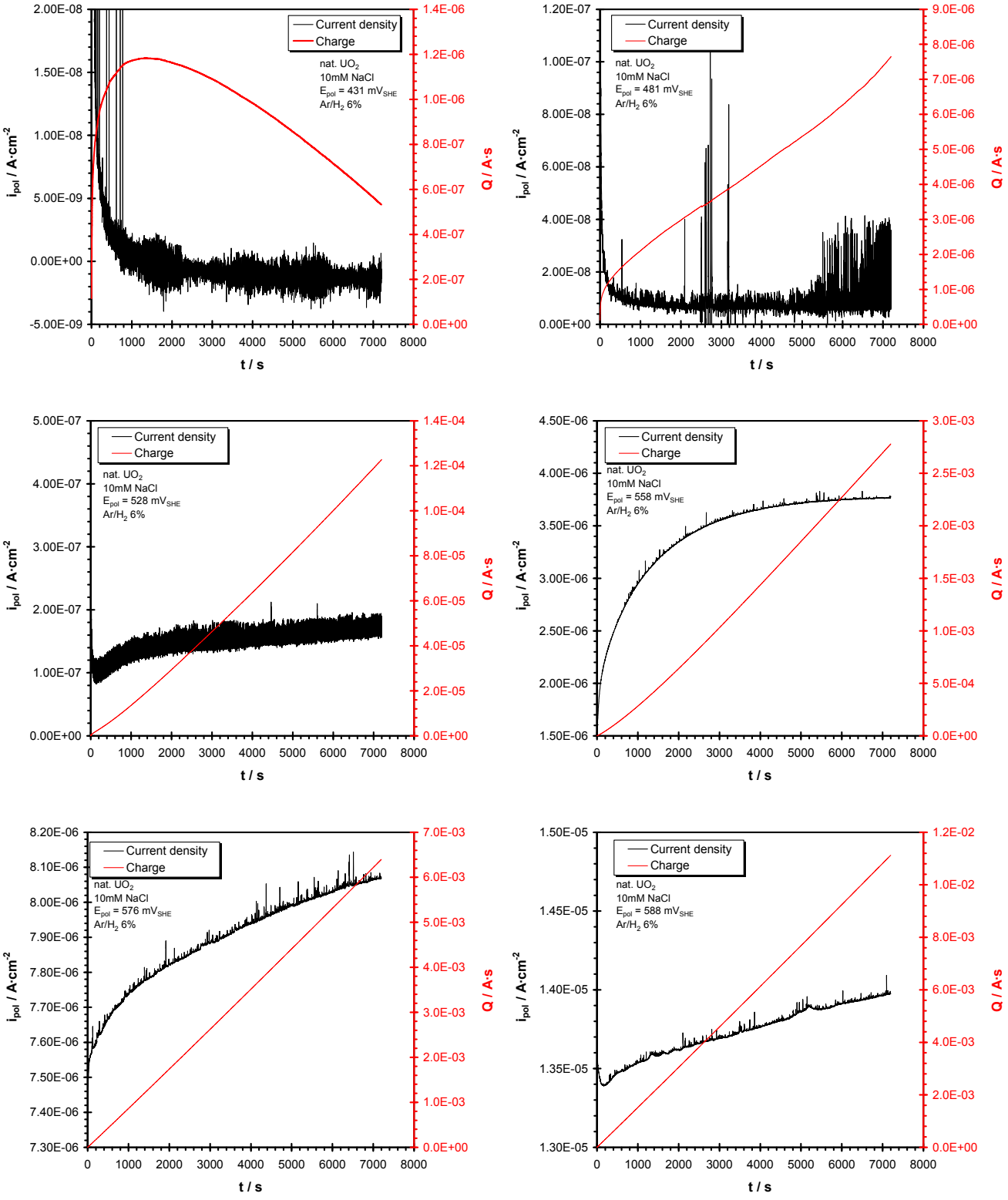

Fig. A.7.a Polarisation current density curves and polarisation charge curves for natural UO_2 under Ar/H_2 atmosphere

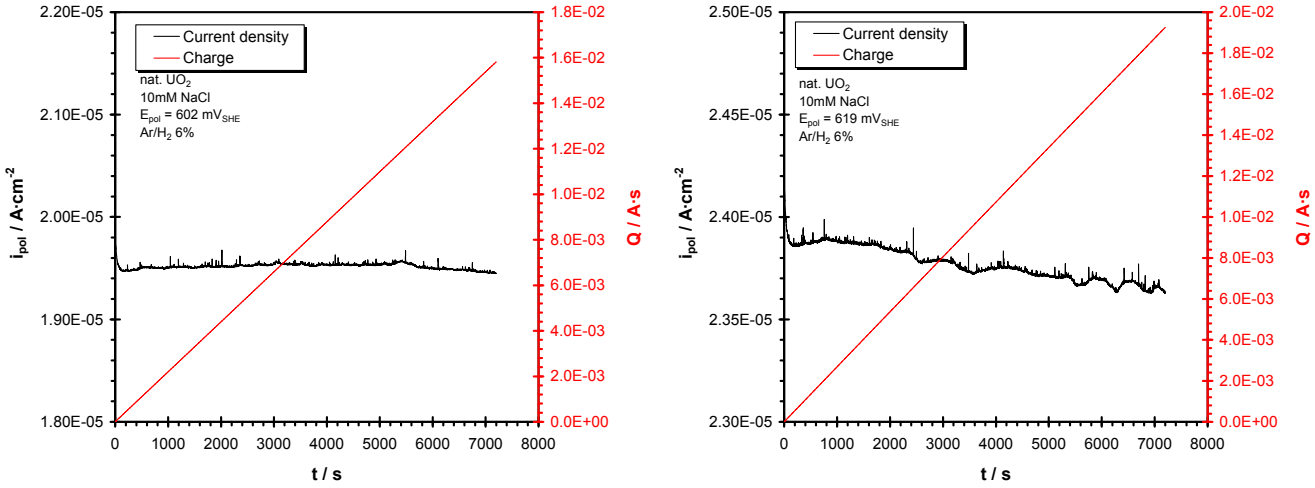

Fig. A.7.b Polarisation current density curves and polarisation charge curves for natural UO_2 under Ar/H_2 atmosphere

Anodic polarisation curves on 1% ^{233}U doped UO_2 under Ar/H_2 atmosphere (sample name U – V)

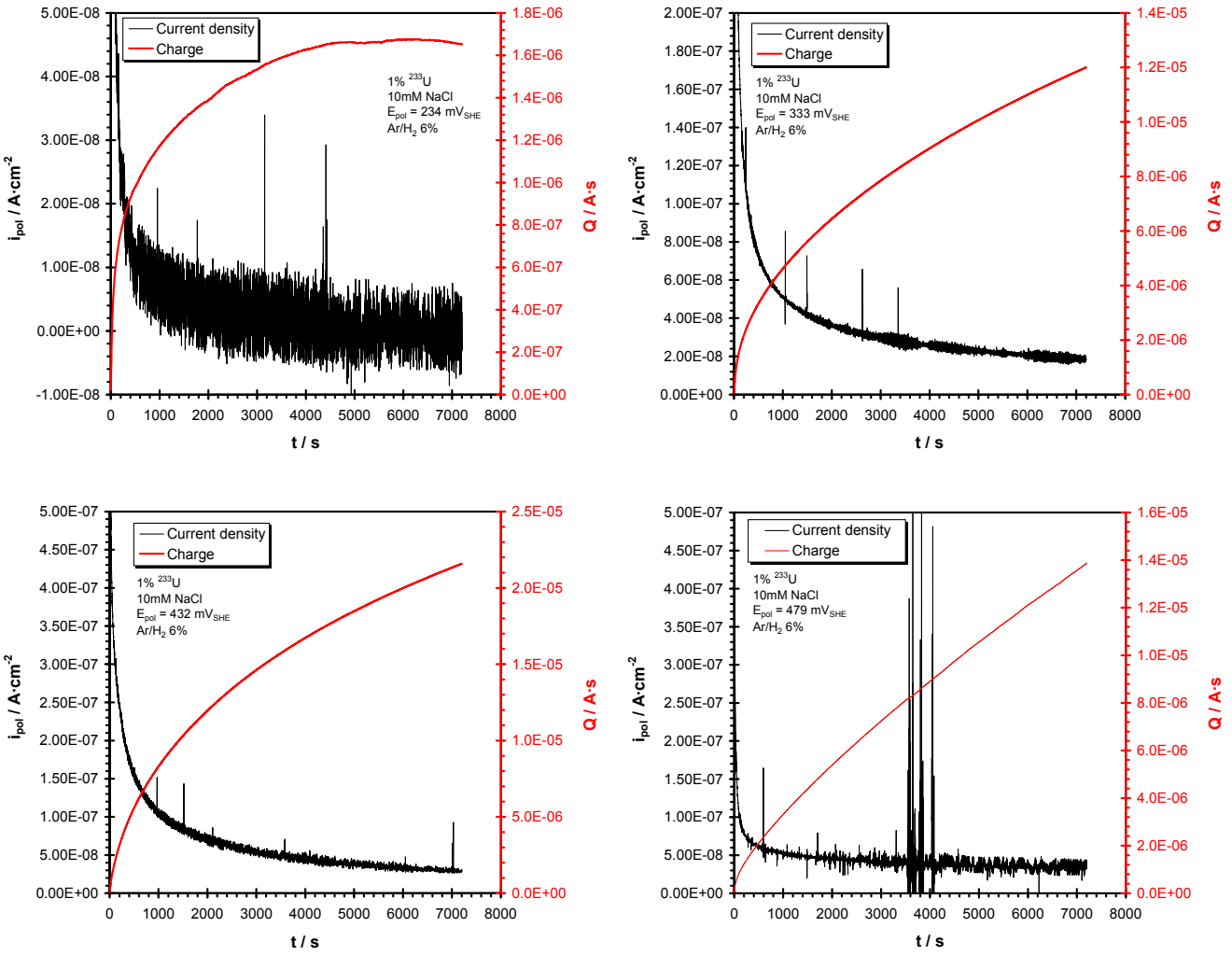

Fig. A.8.a Polarisation current density curves and polarisation charge curves for 1% ^{233}U doped UO_2 under Ar/H_2 atmosphere

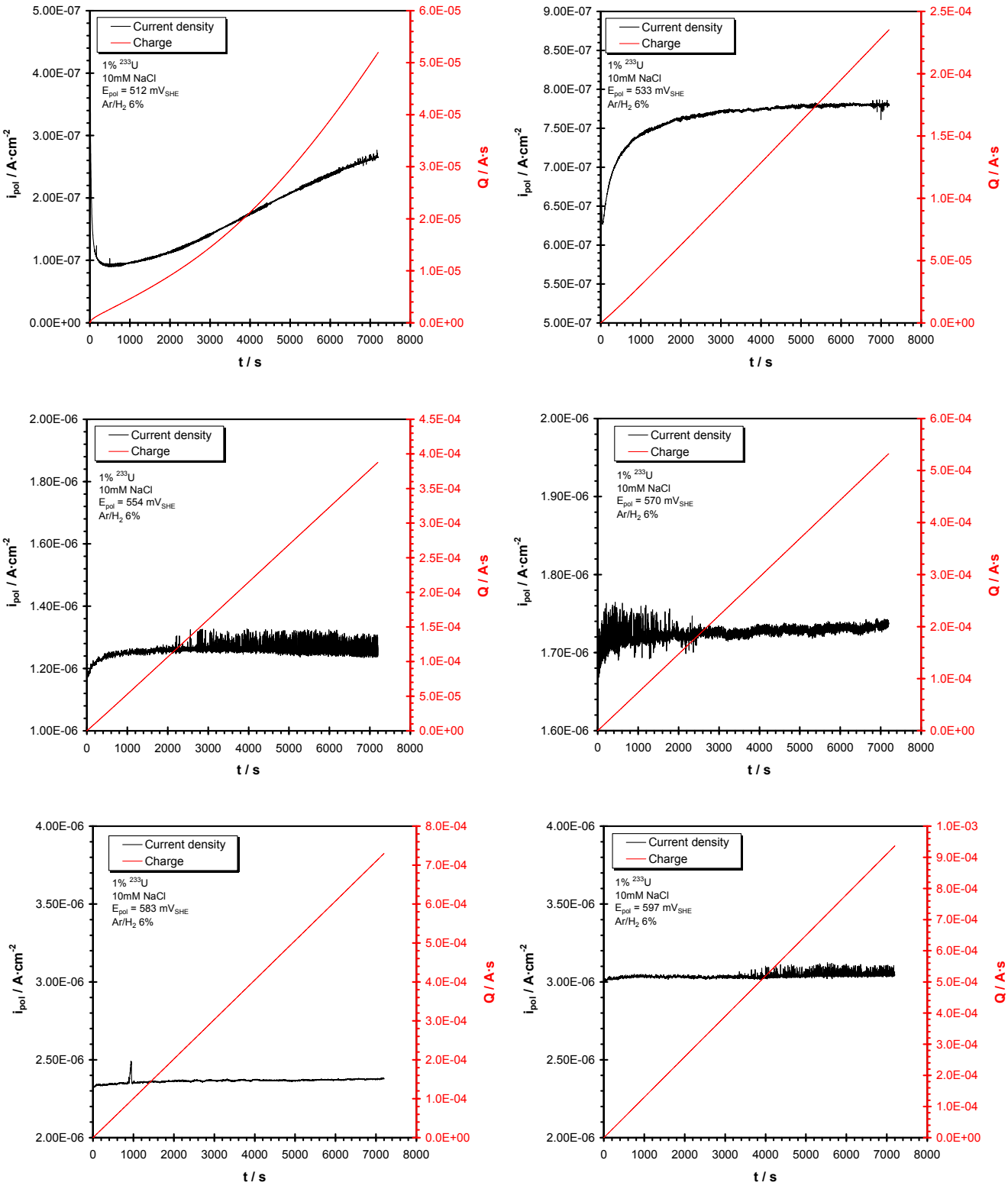

Fig. A.8.b Polarisation current density curves and polarisation charge curves for 1% ^{233}U doped UO_2 under Ar/H_2 atmosphere

Anodic polarisation curves on 10% ^{233}U doped UO_2 under Ar/H_2 atmosphere (sample name U – I)

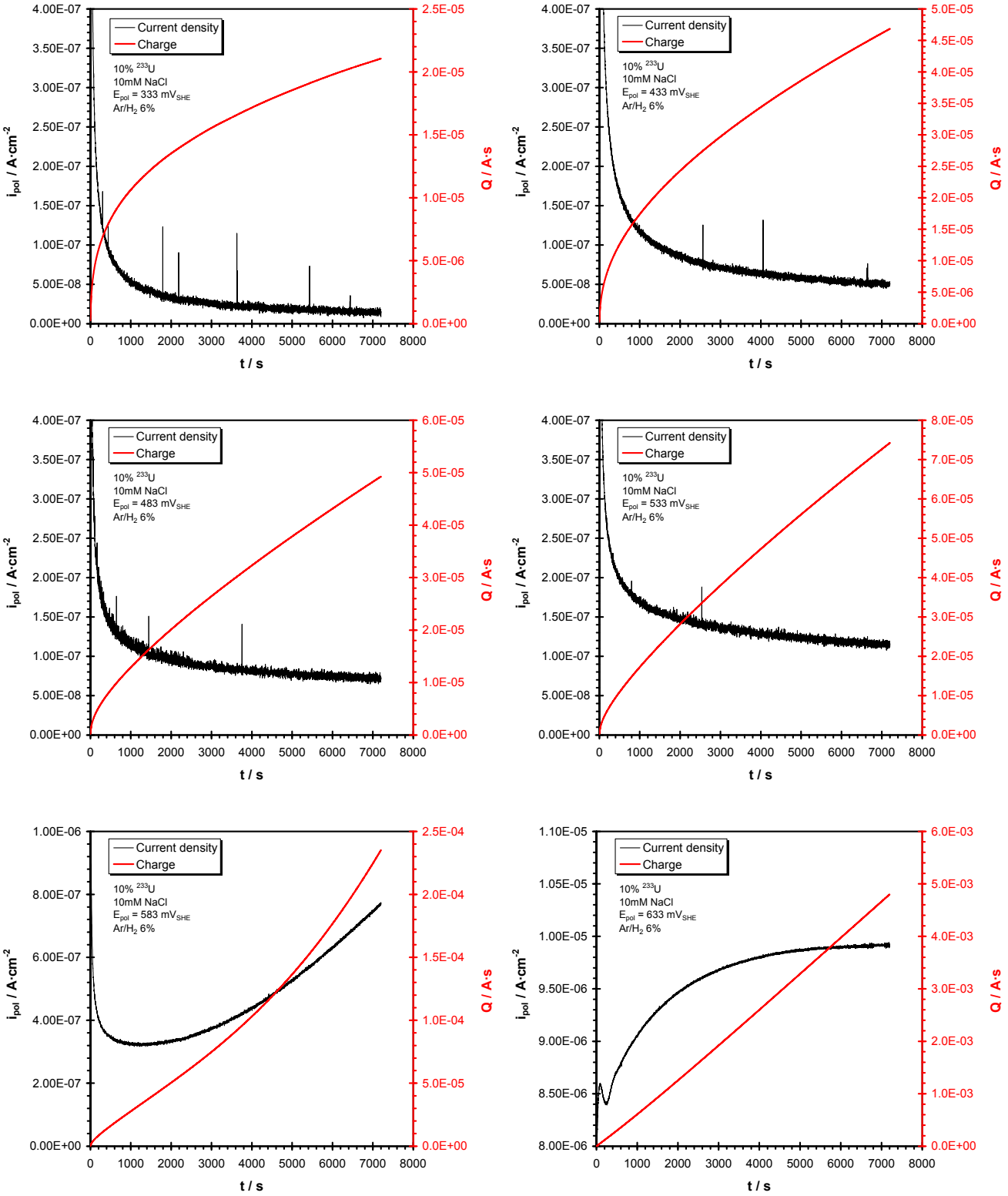

Fig. A.9.a Polarisation current density curves and polarisation charge curves for 10% ^{233}U doped UO_2 under Ar/H_2 atmosphere

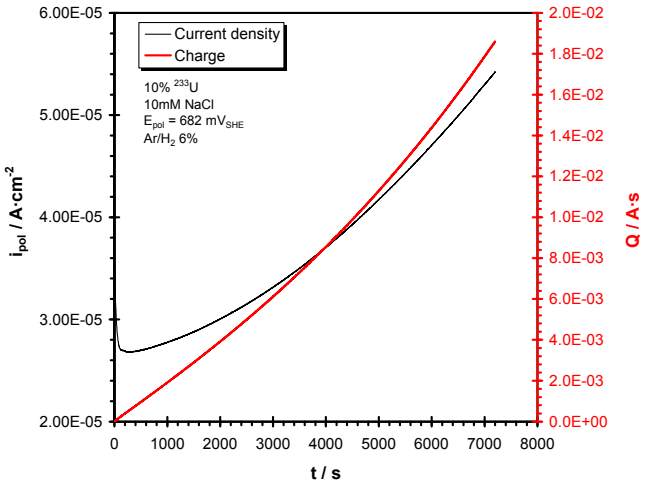

Fig. A.9.b Polarisation current density curves and polarisation charge curves for 10% ^{233}U doped UO_2 under Ar/H_2 atmosphere

Cyclotron experiments

Cathodic and anodic polarisations without beam irradiation under Ar atmosphere (sample G11-01)

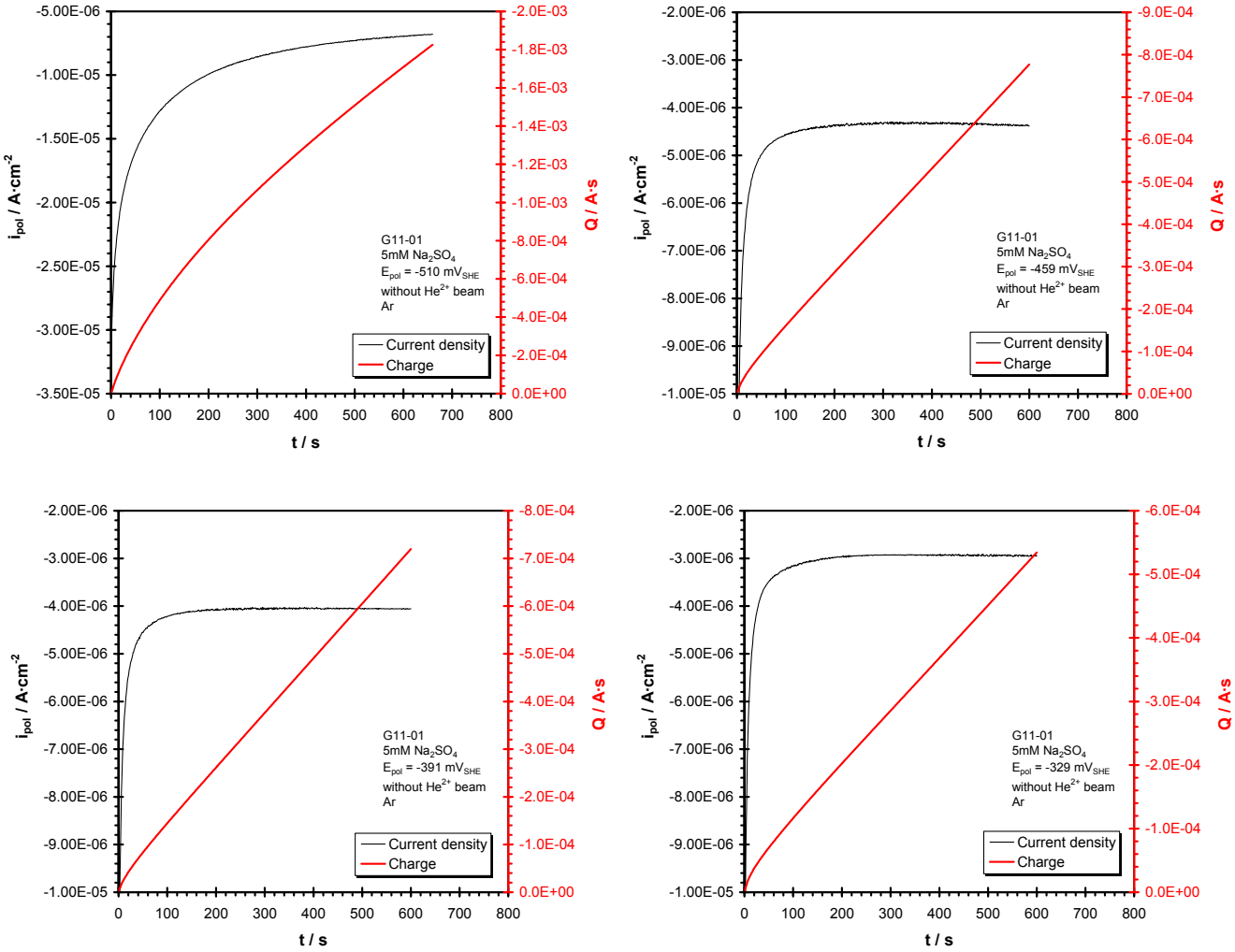

Fig. A.10.a Polarisation current density curves and polarisation charge curves for depleted UO_2 without He^{2+} beam irradiation under Ar atmosphere

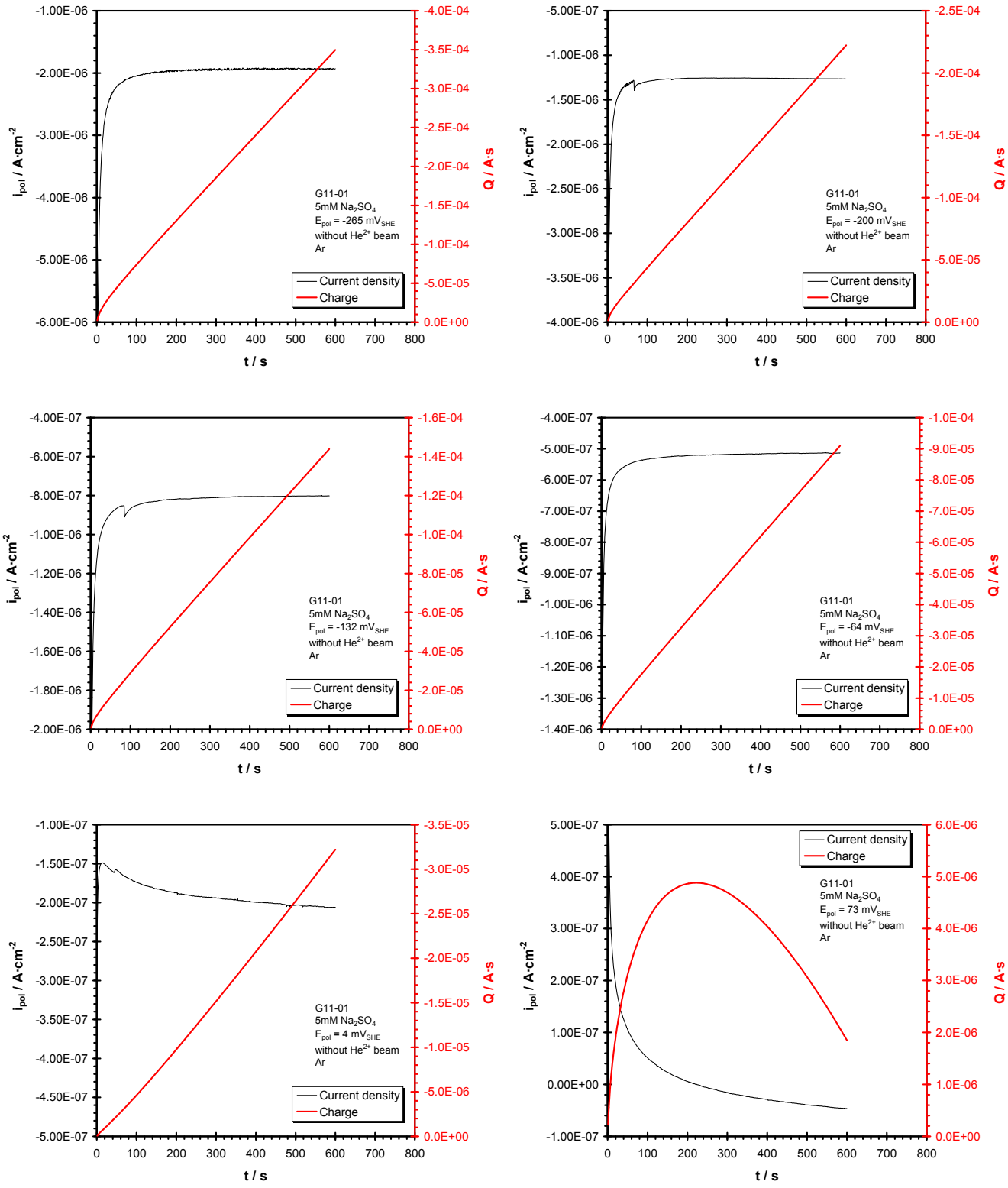

Fig. A.10.b Polarisation current density curves and polarisation charge curves for depleted UO_2 without He^{2+} beam irradiation under Ar atmosphere

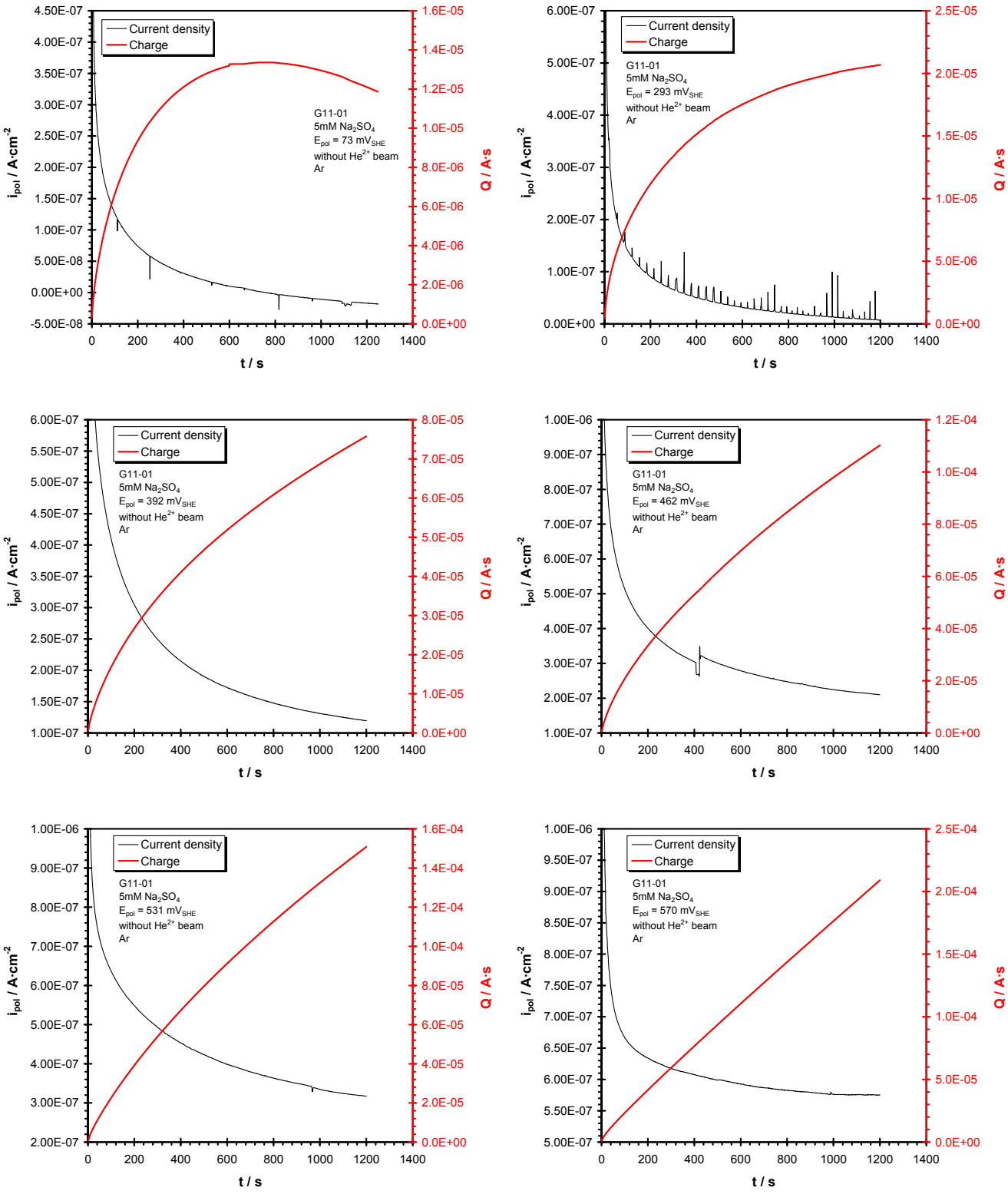

Fig. A.10.c Polarisation current density curves and polarisation charge curves for depleted UO_2 without He^{2+} beam irradiation under Ar atmosphere

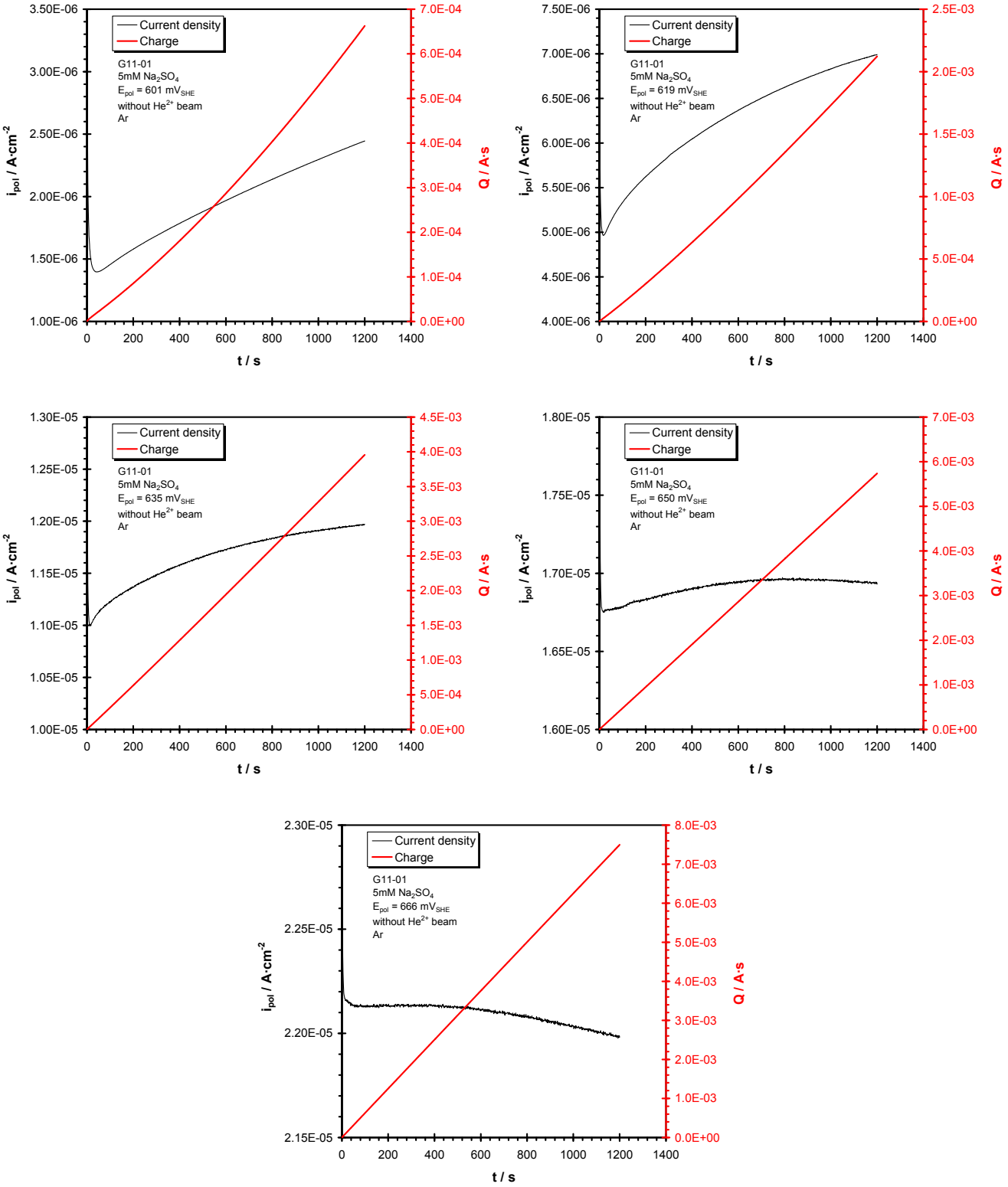

Fig. A.10.d Polarisation current density curves and polarisation charge curves for depleted UO_2 without He^{2+} beam irradiation under Ar atmosphere

Cathodic polarisations during irradiation with 45 MeV He^{2+} beam (flux $3.3 \cdot 10^7$ $cm^{-2} \cdot s^{-1}$) under Ar atmosphere (sample G11-05)

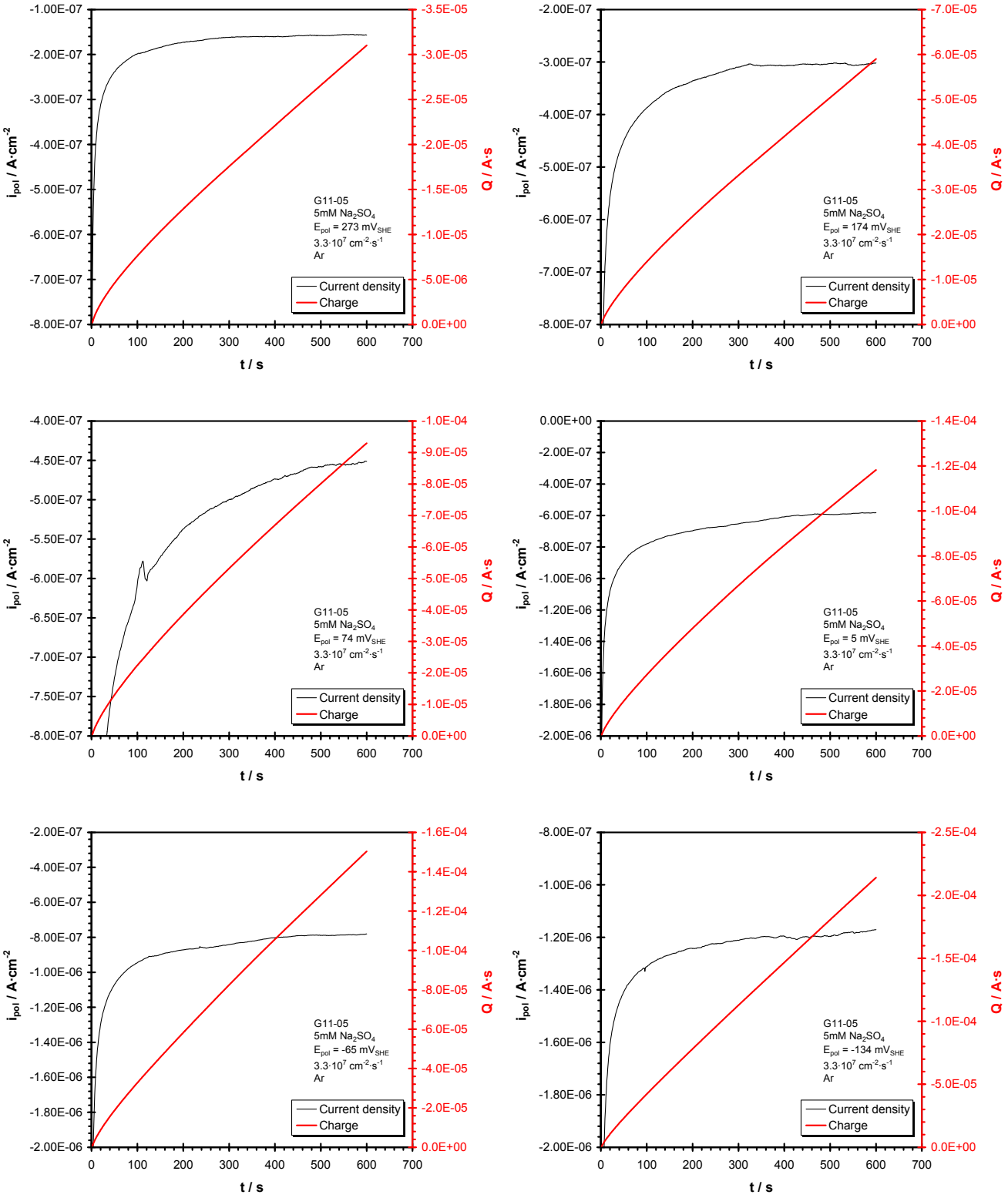

Fig. A.11.a Cathodic polarisation current density curves and polarisation charge curves for depleted UO_2 during irradiation with 45 MeV He^{2+} beam (flux $3.3 \cdot 10^7$ $cm^{-2} \cdot s^{-1}$) under Ar atmosphere (scanning from E_{corr} to negative potentials)

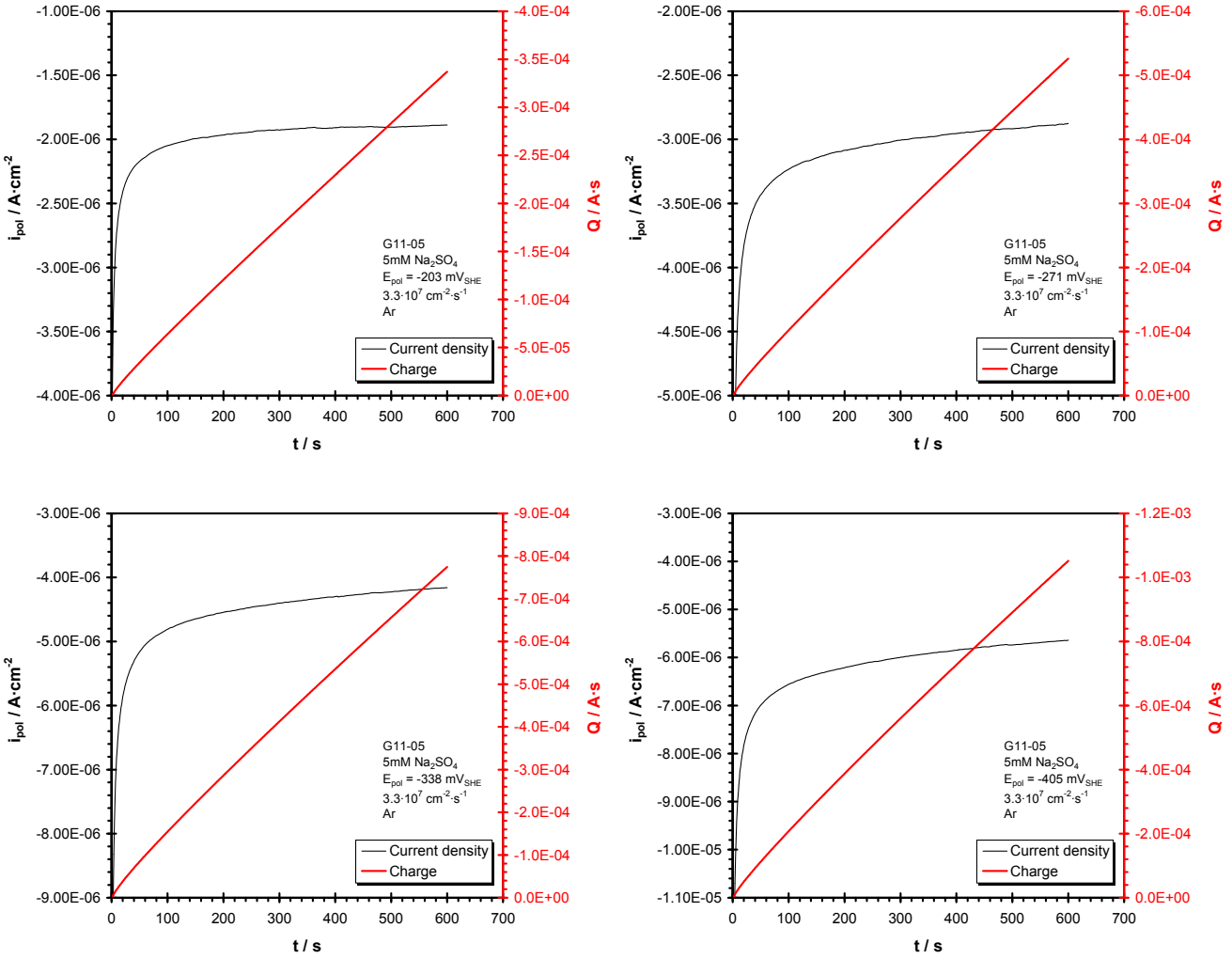

Fig. A.11.b Cathodic polarisation current density curves and polarisation charge curves for depleted UO_2 during irradiation with 45 MeV He^{2+} beam (flux $3.3 \cdot 10^7$ $cm^{-2} \cdot s^{-1}$) under Ar atmosphere (scanning from E_{corr} to negative potentials)

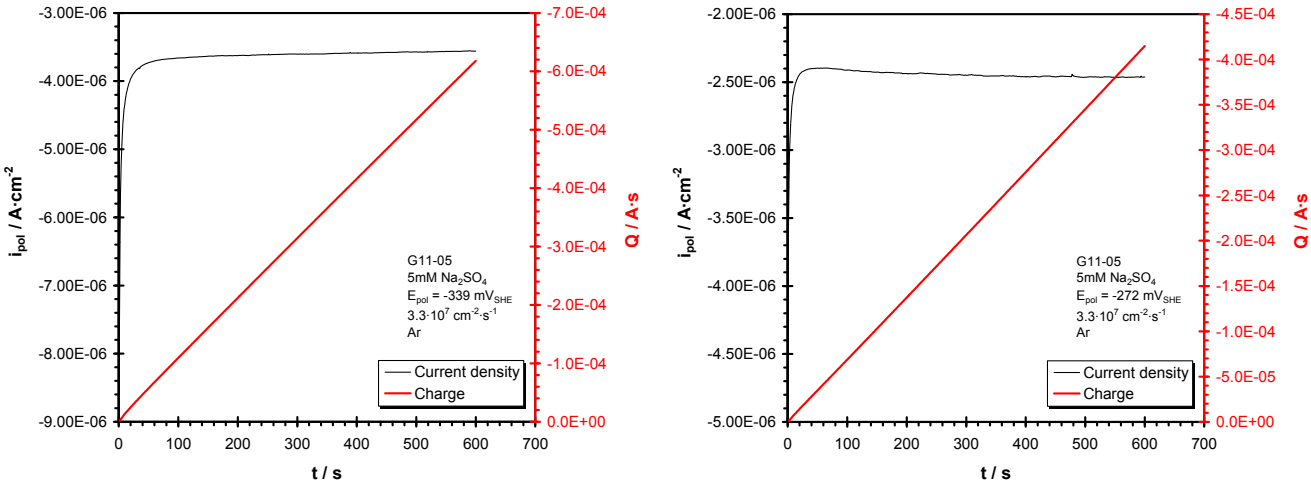

Fig. A.12.a Cathodic polarisation current density curves and polarisation charge curves for depleted UO_2 during irradiation with 45 MeV He^{2+} beam (flux $3.3 \cdot 10^7$ $cm^{-2} \cdot s^{-1}$) under Ar atmosphere (scanning from negative potentials to E_{corr})

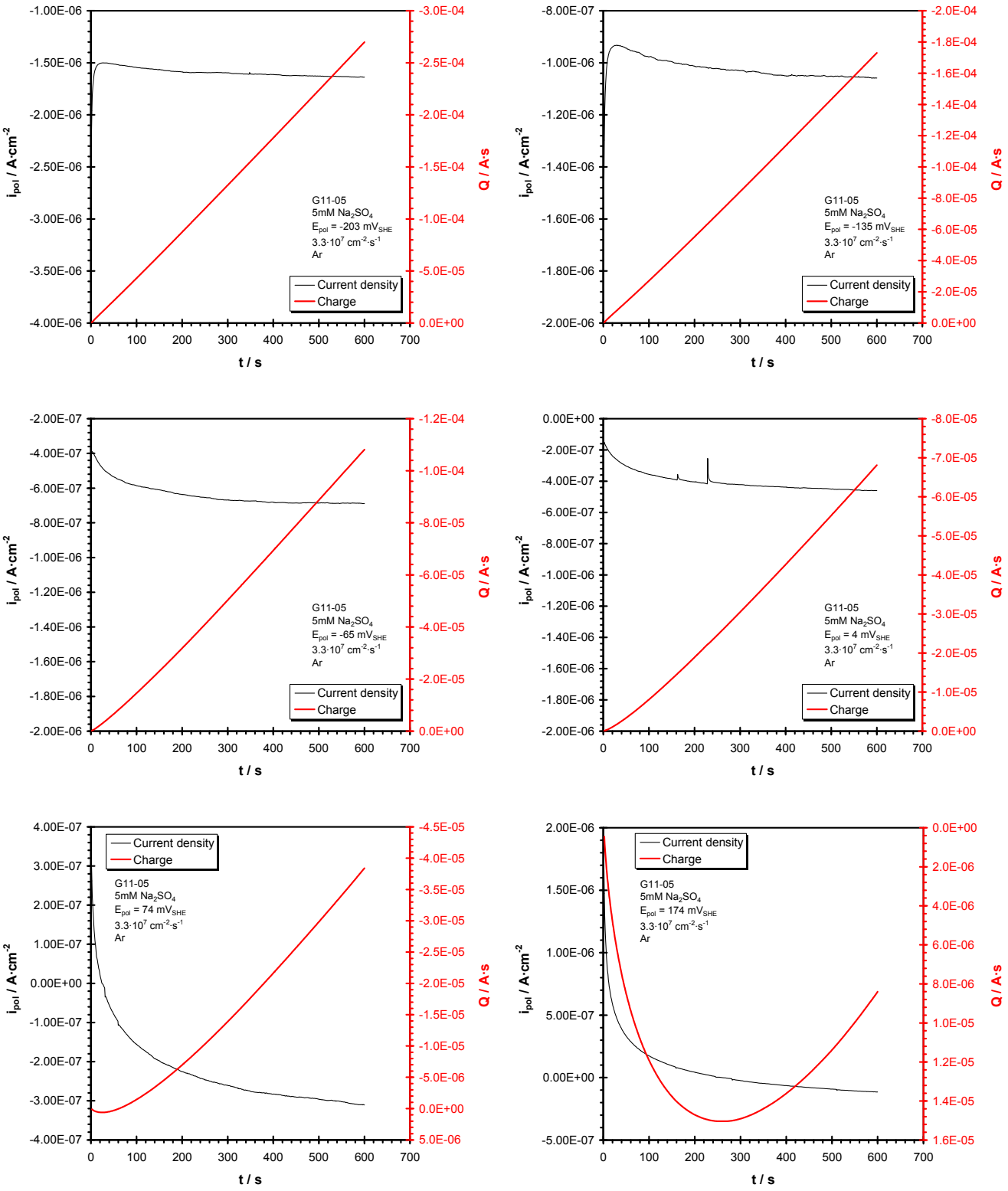

Fig. A.12.b Cathodic polarisation current density curves and polarisation charge curves for depleted UO_2 during irradiation with 45 MeV He^{2+} beam (flux $3.3 \cdot 10^7$ $cm^{-2} \cdot s^{-1}$) under Ar atmosphere (scanning from negative potentials to E_{corr})

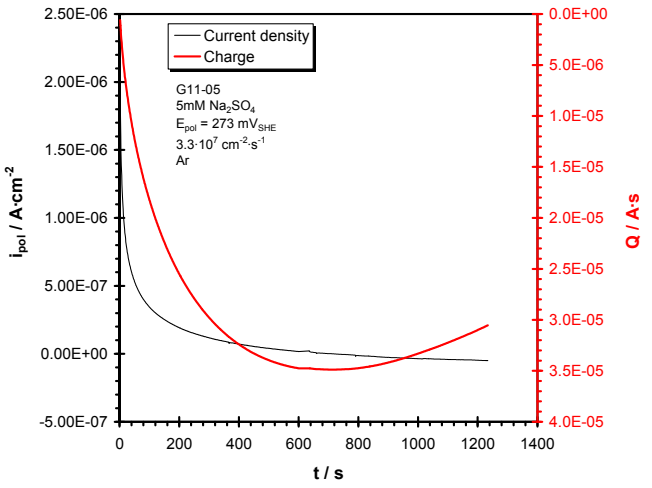

Fig. A.12.c Cathodic polarisation current density curves and polarisation charge curves for depleted UO_2 during irradiation with 45 MeV He^{2+} beam (flux $3.3 \cdot 10^7$ $cm^{-2} \cdot s^{-1}$) under Ar atmosphere (scanning from negative potentials to E_{corr})

Anodic polarisations during irradiation with 45 MeV He^{2+} beam (flux $3.3 \cdot 10^7$ $cm^{-2} \cdot s^{-1}$) under Ar atmosphere (sample G11-04)

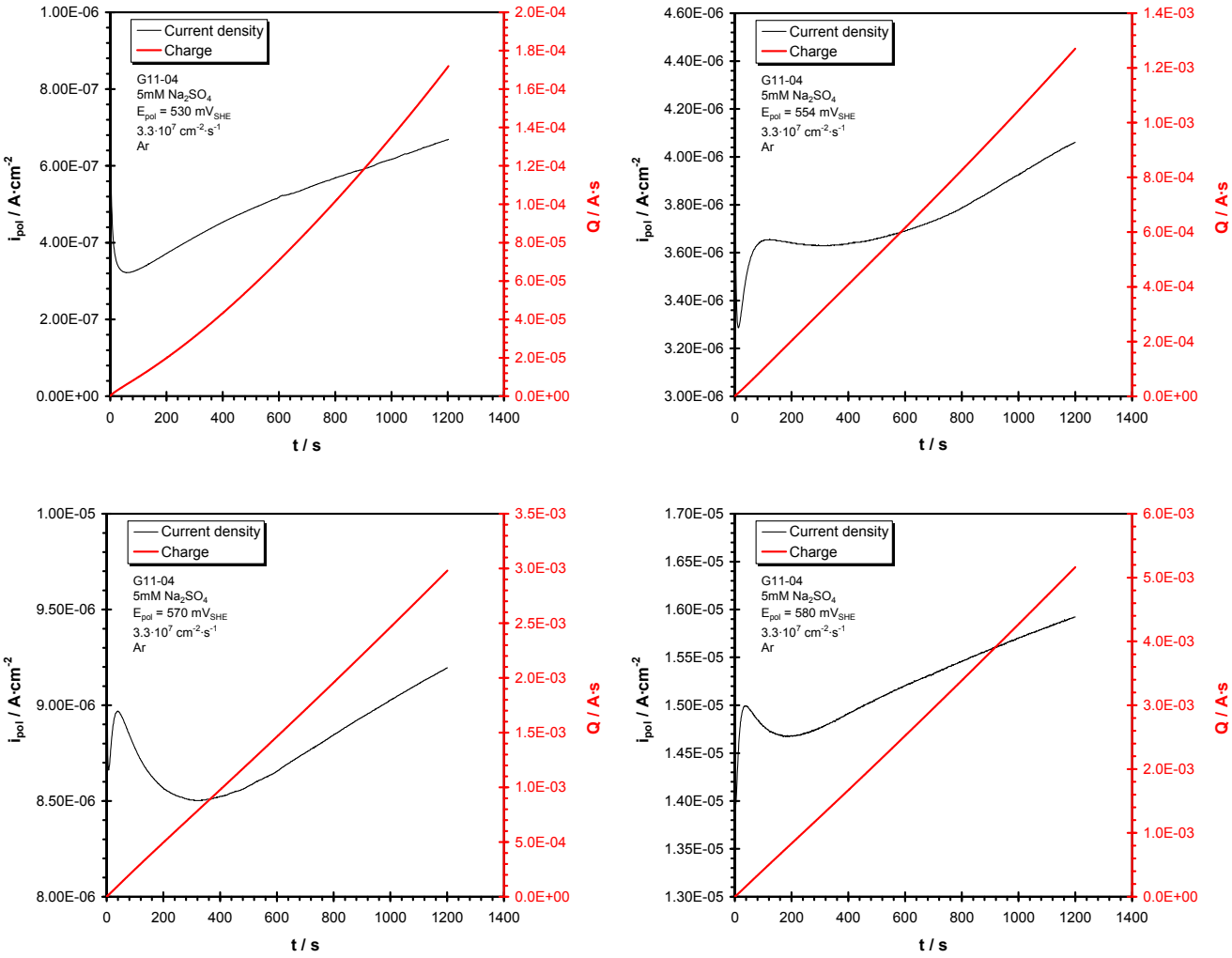

Fig. A.13.a Anodic polarisation current density curves and polarisation charge curves for depleted UO_2 during irradiation with 45 MeV He^{2+} beam (flux $3.3 \cdot 10^7$ $cm^{-2} \cdot s^{-1}$) under Ar atmosphere

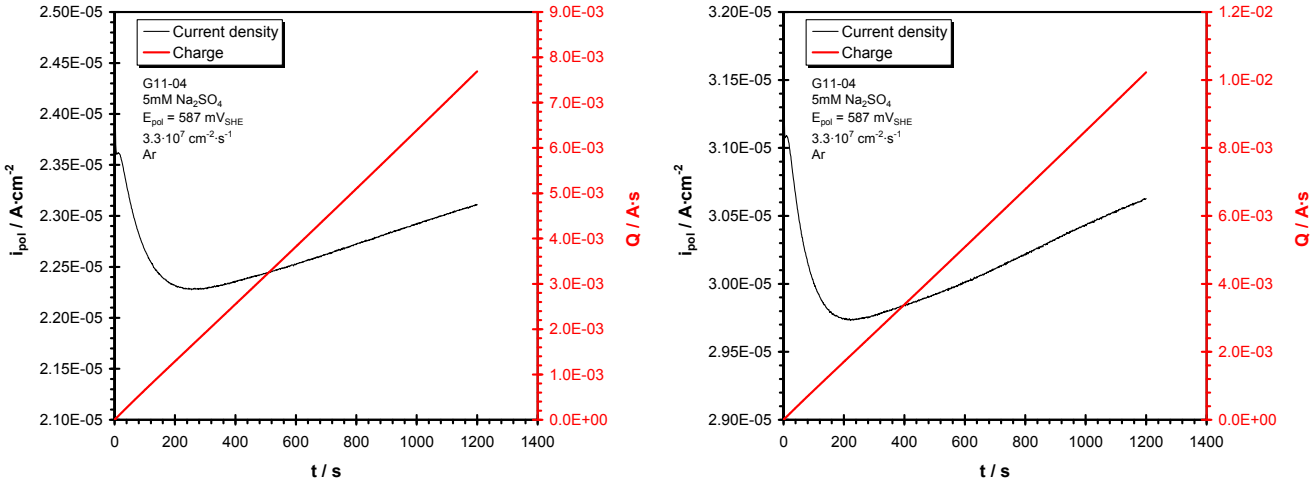

Fig. A.13.b Anodic polarisation current density curves and polarisation charge curves for depleted UO_2 during irradiation with 45 MeV He^{2+} beam (flux $3.3 \cdot 10^7$ $cm^{-2} \cdot s^{-1}$) under Ar atmosphere

Anodic polarisations without beam irradiation under Ar/H_2 6% atmosphere (sample G11-15)

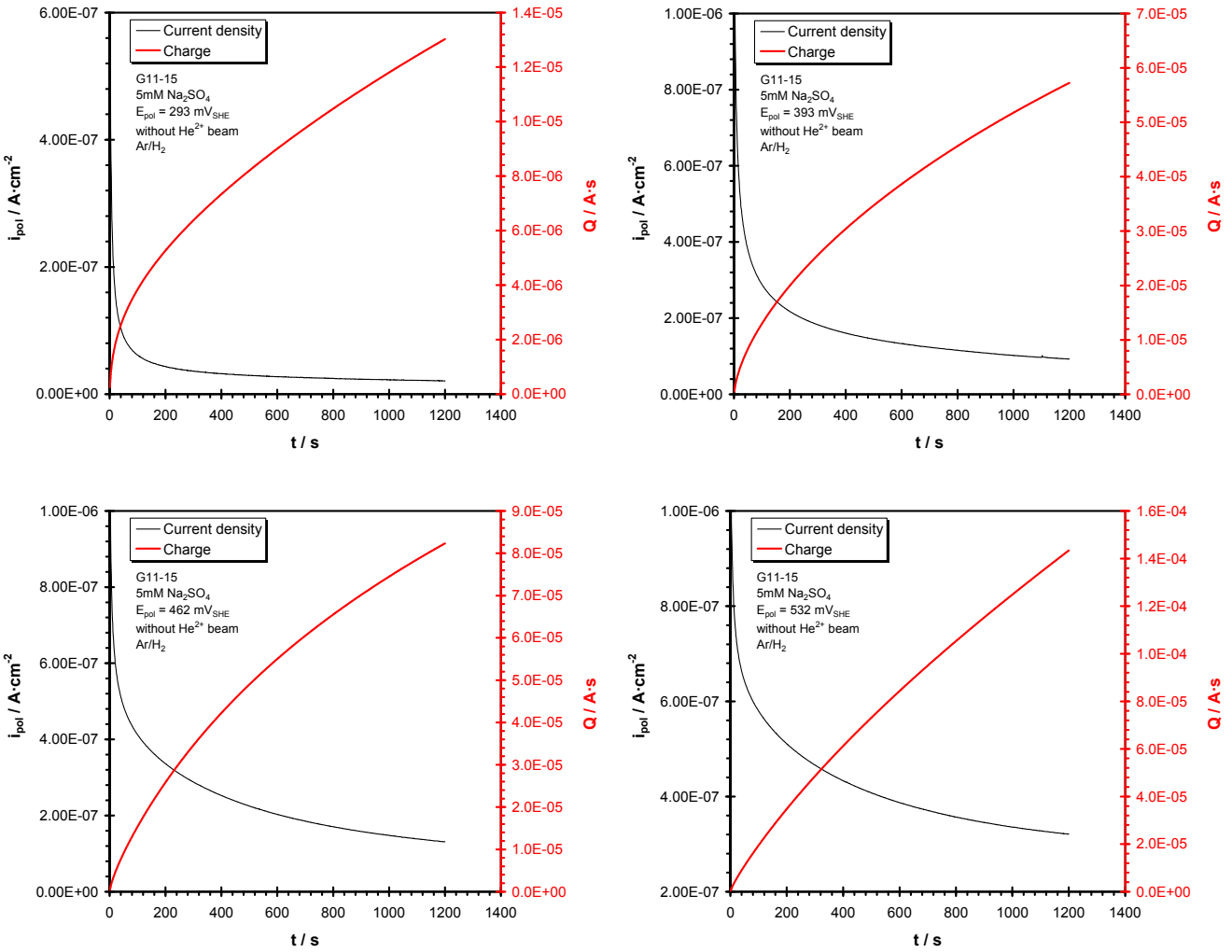

Fig. A.14.a Anodic polarisation current density curves and polarisation charge curves for depleted UO_2 without He^{2+} beam irradiation under Ar/H_2 atmosphere

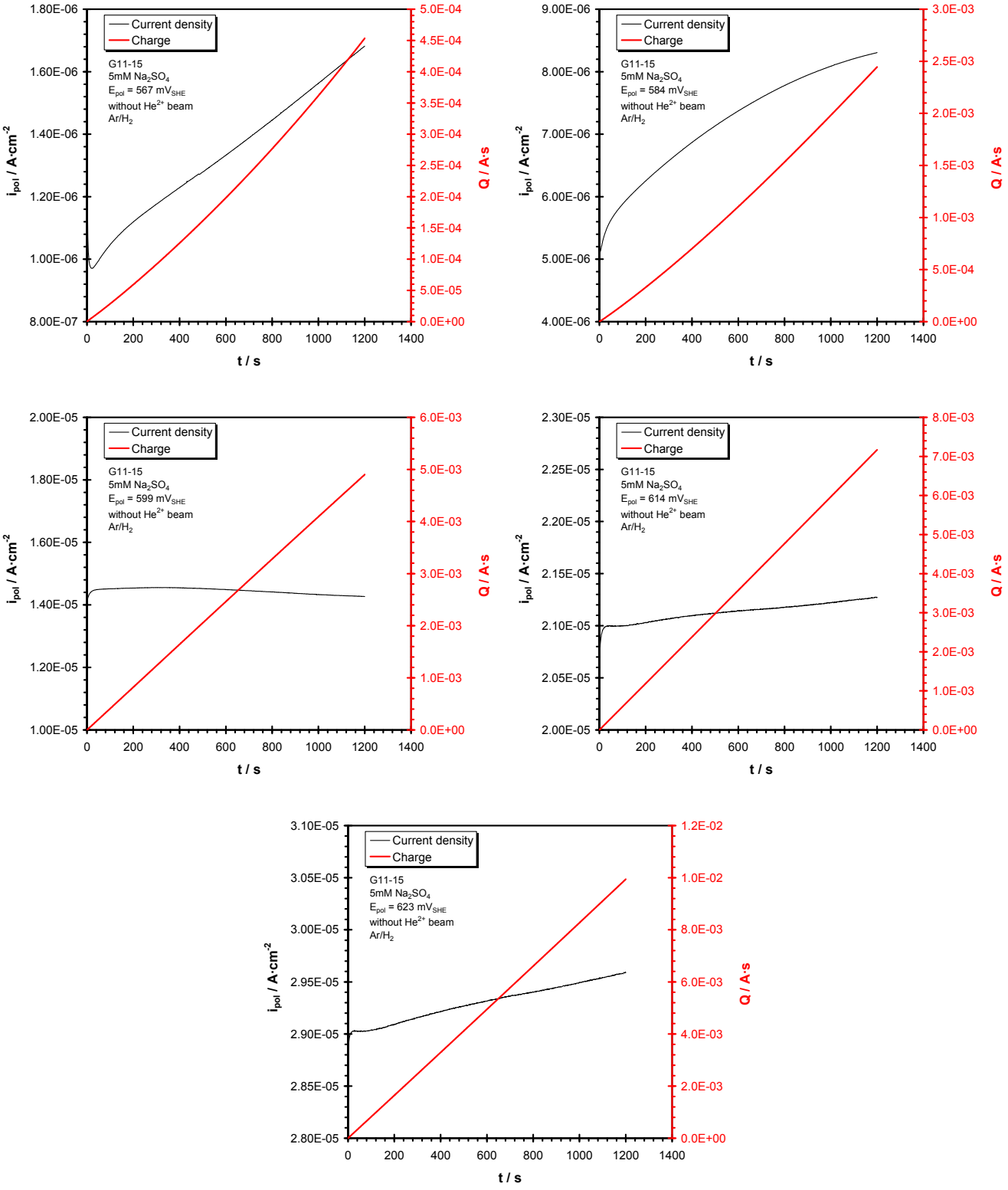

Fig. A.14.b Anodic polarisation current density curves and polarisation charge curves for depleted UO_2 without He^{2+} beam irradiation under Ar/H_2 atmosphere

Anodic polarisations during irradiation with 45 MeV He^{2+} beam (flux $3.3 \cdot 10^7$ $cm^{-2} \cdot s^{-1}$) under Ar/H_2 6% atmosphere (sample G11-16)

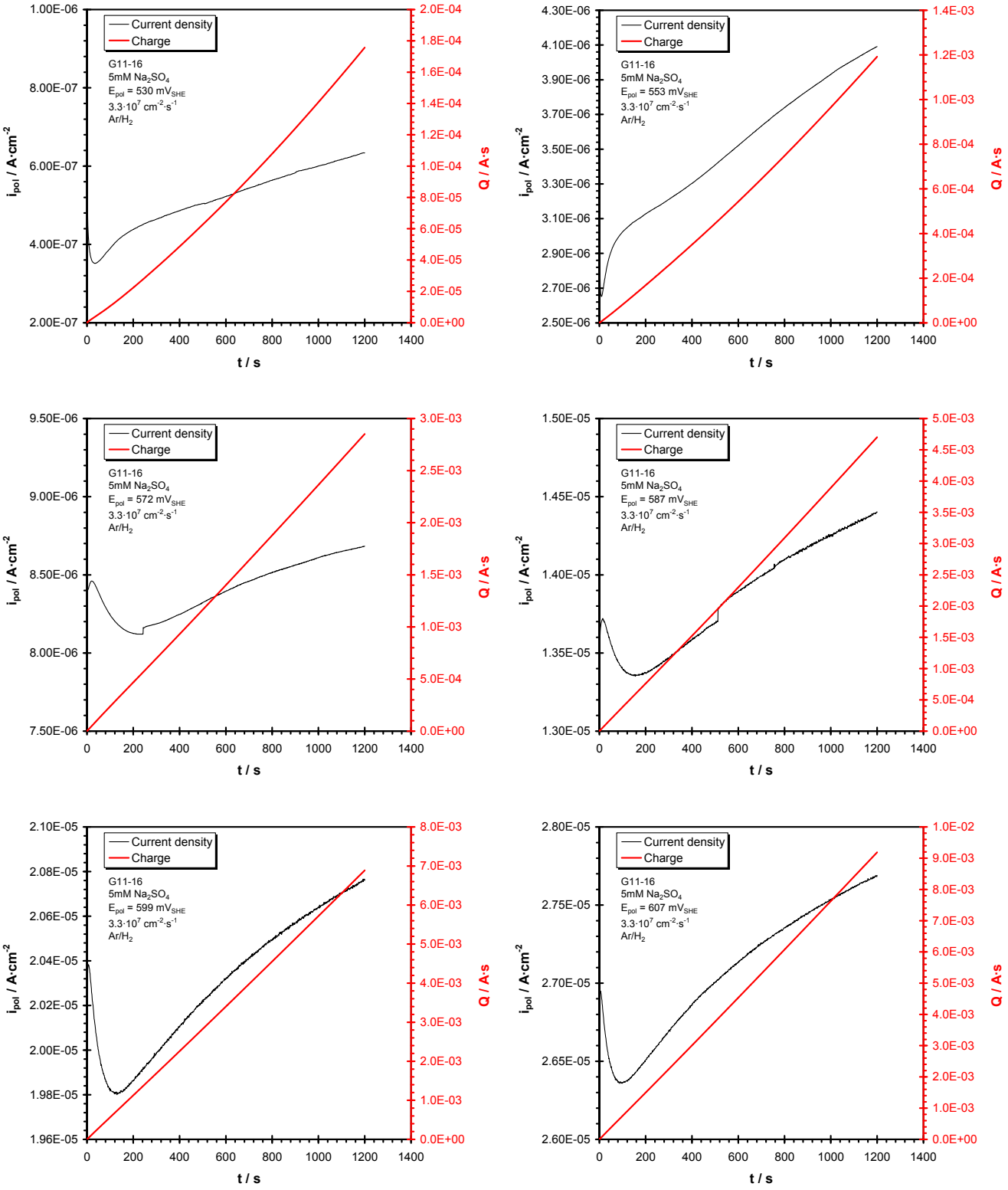

Fig. A.15 Anodic polarisation current density curves and polarisation charge curves for depleted UO_2 during irradiation with 45 MeV He^{2+} beam (flux $3.3 \cdot 10^7$ $cm^{-2} \cdot s^{-1}$) under Ar/H_2 atmosphere

A.3. Tafel slopes and corrosion rates calculations from polarisation curves

Glove box experiments[1)]

Anodic polarisation on natural UO_2 under Ar/H_2 atmosphere (sample name UO_2 – X)

Nr. crt.	$E_{pol,th.}$	$\|I_{pol}\|$	$\|i_{pol}\|$	lg $\|i_{pol}\|$	R_{bulk} *	$(I \cdot R)_{drop}$	$E_{pol, real}$	r_{corr}	Tafel slope
	[mV_{SHE}]	[A]	[$A \cdot cm^{-2}$]	-	[Ω]	[mV]	[mV_{SHE}]	[$moles \cdot cm^{-2} \cdot d^{-1}$]	[mV/decade]
1	431.4	5.104E-10	4.536E-09	-8.343	6.346E+04	0.0	431.4	2.031E-09	
2	481.4	3.378E-09	3.002E-08	-7.523	7.167E+04	0.2	481.2	1.344E-08	
3	531.4	5.915E-08	5.257E-07	-6.279	6.498E+04	3.8	527.6	2.354E-07	
4	581.4	3.839E-07	3.412E-06	-5.467	6.019E+04	23.1	558.3	1.528E-06	**42.04**
5	631.4	9.079E-07	8.069E-06	-5.093	6.149E+04	55.8	575.6	3.613E-06	
6	681.4	1.573E-06	1.398E-05	-4.855	5.922E+04	93.1	588.3	6.257E-06	
7	731.4	2.189E-06	1.945E-05	-4.711	5.906E+04	129.3	602.1	8.710E-06	
8	781.4	2.660E-06	2.364E-05	-4.626	6.097E+04	162.2	619.2	1.058E-05	

*) Values determined by fitting of EIS plots

Anodic polarisation on 1% ^{233}U doped UO_2 under Ar/H_2 atmosphere (sample name U – V)

Nr. crt.	$E_{pol,th.}$	$\|I_{pol}\|$	$\|i_{pol}\|$	lg $\|i_{pol}\|$	R_{bulk} *	$(I \cdot R)_{drop}$	$E_{pol, real}$	r_{corr}	Tafel slope
	[mV_{SHE}]	[A]	[$A \cdot cm^{-2}$]	-	[Ω]	[mV]	[mV_{SHE}]	[$moles \cdot cm^{-2} \cdot d^{-1}$]	[mV/decade]
1	234.0	1.032E-10	2.409E-09	-8.618	1.627E+06	0.2	233.8	1.079E-09	
2	334.0	7.902E-10	1.844E-08	-7.734	1.625E+06	1.3	332.7	8.257E-09	
3	434.0	1.236E-09	2.883E-08	-7.540	1.657E+06	2.0	432.0	1.291E-08	
4	484.0	2.998E-09	6.995E-08	-7.155	1.653E+06	5.0	479.0	3.132E-08	
5	534.0	1.339E-08	3.124E-07	-6.505	1.594E+06	21.3	512.7	1.399E-07	**51.21**
6	584.0	3.345E-08	7.803E-07	-6.108	1.536E+06	51.4	532.6	3.495E-07	
7	634.0	5.407E-08	1.261E-06	-5.899	1.484E+06	80.2	553.8	5.649E-07	
8	684.0	7.444E-08	1.737E-06	-5.760	1.526E+06	113.6	570.4	7.778E-07	

*) Values determined by fitting of EIS plots

Anodic polarisation on 10% ^{233}U doped UO_2 under Ar/H_2 atmosphere (sample name U – I)

Nr. crt.	$E_{pol,th.}$	$\|I_{pol}\|$	$\|i_{pol}\|$	lg $\|i_{pol}\|$	R_{bulk} *	$(I \cdot R)_{drop}$	$E_{pol, real}$	r_{corr}	Tafel slope
	[mV_{SHE}]	[A]	[$A \cdot cm^{-2}$]	-	[Ω]	[mV]	[mV_{SHE}]	[$moles \cdot cm^{-2} \cdot d^{-1}$]	[mV/decade]
1	333.0	1.045E-09	1.500E-08	-7.824	2.414E+02	0.000	333.0	6.729E-09	
2	433.0	3.486E-09	5.006E-08	-7.301	2.455E+02	0.001	433.0	2.246E-08	
3	483.0	3.486E-09	5.006E-08	-7.301	2.543E+02	0.001	483.0	2.246E-08	
4	533.0	6.486E-09	9.312E-08	-7.031	2.551E+02	0.002	533.0	4.178E-08	
5	583.0	5.340E-08	7.667E-07	-6.115	2.562E+02	0.014	583.0	3.440E-07	**50.88**
6	633.0	5.906E-07	8.480E-06	-5.072	2.687E+02	0.159	632.8	3.805E-06	
7	683.0	3.763E-06	5.402E-05	-4.267	2.683E+02	1.010	682.0	2.424E-05	

*) Values determined by fitting of EIS plots

[1] The samples characteristics (thicknesses, electrode surfaces, masses) are presented in Chapter 4

Cyclotron experiments[2)]

Cathodic and anodic polarisations without beam irradiation under Ar atmosphere (sample G11-01)

Nr. crt.	$E_{pol,th.}$	$\|I_{pol}\|$	$\|i_{pol}\|$	lg $\|i_{pol}\|$	R_{bulk} *	$(I \cdot R)_{drop}$	$E_{pol, real}$	r_{corr}	Tafel slope
	[mV_{SHE}]	[A]	[$A \cdot cm^{-2}$]	-	[Ω]	[mV]	[mV_{SHE}]	[$moles \cdot cm^{-2} \cdot d^{-1}$]	[mV/decade]
1	-557	1.958E-06	6.926E-06	-5.159	2.281E+04	-44.67	-512.33	3.101E-06	
2	-487	1.233E-06	4.361E-06	-5.360	2.245E+04	-27.68	-459.32	1.952E-06	
3	-417	1.147E-06	4.055E-06	-5.392	2.210E+04	-25.34	-391.66	1.816E-06	
4	-347	8.313E-07	2.940E-06	-5.532	2.174E+04	-18.07	-328.93	1.316E-06	
5	-277	5.464E-07	1.932E-06	-5.714	2.138E+04	-11.68	-265.32	8.652E-07	**-359.83**
6	-207	3.575E-07	1.265E-06	-5.898	2.103E+04	-7.52	-199.48	5.662E-07	
7	-137	2.267E-07	8.019E-07	-6.096	2.067E+04	-4.69	-132.31	3.590E-07	
8	-67	1.453E-07	5.140E-07	-6.289	2.032E+04	-2.95	-64.05	2.301E-07	
9	3	5.791E-08	2.048E-07	-6.689	1.996E+04	-1.16	4.16	9.171E-08	
10	73	1.221E-08	4.318E-08	-7.365	1.961E+04	-0.24	73.24	1.933E-08	
11	143	4.798E-09	1.697E-08	-7.770	1.925E+04	-0.09	143.09	7.598E-09	
12	293	2.398E-09	8.481E-09	-8.072	1.870E+04	0.04	292.96	3.797E-09	
13	393	3.453E-08	1.221E-07	-6.913	1.838E+04	0.63	392.37	5.468E-08	
14	463	6.030E-08	2.133E-07	-6.671	1.816E+04	1.09	461.91	9.550E-08	
15	533	9.062E-08	3.205E-07	-6.494	1.793E+04	1.63	531.37	1.435E-07	
16	573	1.627E-07	5.754E-07	-6.240	1.781E+04	2.90	570.10	2.576E-07	
17	613	6.813E-07	2.410E-06	-5.618	1.768E+04	12.04	600.96	1.079E-06	**44.98**
18	653	1.967E-06	6.956E-06	-5.158	1.755E+04	34.52	618.48	3.114E-06	
19	693	3.380E-06	1.196E-05	-4.922	1.742E+04	58.90	634.10	5.353E-06	
20	733	4.790E-06	1.694E-05	-4.771	1.730E+04	82.86	650.14	7.586E-06	
21	773	6.219E-06	2.200E-05	-4.658	1.717E+04	106.78	666.22	9.848E-06	

*) Values determined by fitting of EIS plots

Anodic polarisations during irradiation with 45 MeV He^{2+} beam (flux $3.3 \cdot 10^7$ $cm^{-2} \cdot s^{-1}$) under Ar atmosphere (sample G11-04)

Nr. crt.	$E_{pol,th.}$	$\|I_{pol}\|$	$\|i_{pol}\|$	lg $\|i_{pol}\|$	R_{bulk} *	$(I \cdot R)_{drop}$	$E_{pol, real}$	r_{corr}	Tafel slope
	[mV_{SHE}]	[A]	[$A \cdot cm^{-2}$]	-	[Ω]	[mV]	[mV_{SHE}]	[$moles \cdot cm^{-2} \cdot d^{-1}$]	[mV/decade]
1	533	1.855E-07	6.559E-07	-6.183	1.681E+04	3.12	529.88	2.937E-07	
2	573	1.140E-06	4.030E-06	-5.395	1.651E+04	18.81	554.19	1.805E-06	
3	613	2.589E-06	9.155E-06	-5.038	1.632E+04	42.25	570.75	4.099E-06	**44.30**
4	653	4.487E-06	1.587E-05	-4.799	1.617E+04	72.56	580.44	7.106E-06	
5	693	6.522E-06	2.307E-05	-4.637	1.614E+04	105.26	587.74	1.033E-05	
6	733	8.647E-06	3.058E-05	-4.515	1.612E+04	139.38	593.62	1.369E-05	

[2] The samples characteristics (thicknesses, electrode surfaces, masses) are presented in Chapter 4

Cathodic polarisations during irradiation with 45 MeV He^{2+} beam (flux $3.3 \cdot 10^7$ $cm^{-2} \cdot s^{-1}$) under Ar atmosphere (sample G11-05)

Nr. crt.	$E_{pol,th.}$	$\|I_{pol}\|$	$\|i_{pol}\|$	lg $\|i_{pol}\|$	R_{bulk}*	$(I \cdot R)_{drop}$	$E_{pol, real}$	r_{corr}	Tafel slope
	[mV_{SHE}]	[A]	[$A \cdot cm^{-2}$]	-	[Ω]	[mV]	[mV_{SHE}]	[$moles \cdot cm^{-2} \cdot d^{-1}$]	[mV/decade]
1	273	4.410E-08	1.560E-07	-6.807	6.582E+03	-0.29	273.29	6.983E-08	
2	173	8.612E-08	3.046E-07	-6.516	6.550E+03	-0.56	173.56	1.364E-07	
3	73	1.284E-07	4.540E-07	-6.343	6.518E+03	-0.84	73.84	2.033E-07	
4	3	1.654E-07	5.850E-07	-6.233	6.495E+03	-1.07	4.07	2.619E-07	
5	-67	2.219E-07	7.850E-07	-6.105	6.473E+03	-1.44	-65.56	3.515E-07	
6	-137	3.331E-07	1.178E-06	-5.929	6.451E+03	-2.15	-134.85	5.275E-07	
7	-207	5.353E-07	1.893E-06	-5.723	6.428E+03	-3.44	-203.56	8.476E-07	**-371.33**
8	-277	8.167E-07	2.888E-06	-5.539	6.406E+03	-5.23	-271.77	1.293E-06	
9	-347	1.181E-06	4.176E-06	-5.379	6.383E+03	-7.54	-339.46	1.870E-06	
10	-417	1.603E-06	5.669E-06	-5.247	6.361E+03	-10.20	-406.80	2.538E-06	
11	-417	1.603E-06	5.669E-06	-5.247	6.361E+03	-10.20	-406.80	2.538E-06	
12	-347	1.007E-06	3.562E-06	-5.448	6.299E+03	-6.34	-340.66	1.595E-06	
13	-277	6.965E-07	2.463E-06	-5.608	6.237E+03	-4.34	-272.66	1.103E-06	
14	-207	4.622E-07	1.635E-06	-5.787	6.176E+03	-2.85	-204.15	7.319E-07	**-371.85**
15	-137	2.985E-07	1.056E-06	-5.976	6.114E+03	-1.82	-135.18	4.727E-07	
16	-67	1.942E-07	6.868E-07	-6.163	6.052E+03	-1.18	-65.82	3.075E-07	
17	3	1.295E-07	4.581E-07	-6.339	5.990E+03	-0.78	3.78	2.051E-07	
18	73	8.660E-08	3.063E-07	-6.514	5.928E+03	-0.51	73.51	1.371E-07	
19	173	3.115E-08	1.102E-07	-6.958	5.840E+03	-0.18	173.18	4.933E-08	
20	273	1.346E-08	4.759E-08	-7.322	5.752E+03	-0.08	273.08	2.131E-08	

Anodic polarisations without beam irradiation under Ar/H_2 atmosphere (sample G11-15)

Nr. crt.	$E_{pol,th.}$	$\|I_{pol}\|$	$\|i_{pol}\|$	lg $\|i_{pol}\|$	R_{bulk}*	$(I \cdot R)_{drop}$	$E_{pol, real}$	r_{corr}	Tafel slope
	[mV_{SHE}]	[A]	[$A \cdot cm^{-2}$]	-	[Ω]	[mV]	[mV_{SHE}]	[$moles \cdot cm^{-2} \cdot d^{-1}$]	[mV/decade]
1	293	6.012E-09	2.126E-08	-7.672	1.543E+04	0.09	292.91	9.520E-09	
2	393	2.683E-08	9.491E-08	-7.023	1.497E+04	0.40	392.60	4.249E-08	
3	463	3.808E-08	1.347E-07	-6.871	1.458E+04	0.56	462.44	6.030E-08	
4	533	9.166E-08	3.242E-07	-6.489	1.429E+04	1.31	531.69	1.452E-07	
5	573	4.673E-07	1.653E-06	-5.782	1.385E+04	6.47	566.53	7.399E-07	
6	613	2.155E-06	7.622E-06	-5.118	1.352E+04	29.14	583.86	3.413E-06	
7	653	4.038E-06	1.428E-05	-4.845	1.341E+04	54.16	598.84	6.395E-06	**67.38**
8	693	6.011E-06	2.126E-05	-4.672	1.328E+04	79.83	613.17	9.519E-06	
9	733	8.359E-06	2.957E-05	-4.529	1.314E+04	109.84	623.16	1.324E-05	

Anodic polarisations during irradiation with 45 MeV He^{2+} beam (flux $3.3 \cdot 10^7$ $cm^{-2} \cdot s^{-1}$) under Ar/H_2 atmosphere (sample G11-16)

Nr. crt.	$E_{pol,th.}$	$\|I_{pol}\|$	$\|i_{pol}\|$	lg $\|i_{pol}\|$	R_{bulk}*	$(I \cdot R)_{drop}$	$E_{pol, real}$	r_{corr}	Tafel slope
	[mV_{SHE}]	[A]	[$A \cdot cm^{-2}$]	-	[Ω]	[mV]	[mV_{SHE}]	[$moles \cdot cm^{-2} \cdot d^{-1}$]	[mV/decade]
1	533	1.770E-07	6.258E-07	-6.204	1.841E+04	3.26	529.74	2.802E-07	
2	573	1.146E-06	4.055E-06	-5.392	1.739E+04	19.94	553.06	1.815E-06	
3	613	2.450E-06	8.666E-06	-5.062	1.668E+04	40.87	572.13	3.880E-06	
4	653	4.061E-06	1.436E-05	-4.843	1.622E+04	65.87	587.13	6.431E-06	**65.10**
5	693	5.862E-06	2.073E-05	-4.683	1.612E+04	94.50	598.50	9.283E-06	
6	733	7.819E-06	2.765E-05	-4.558	1.611E+04	125.96	607.04	1.238E-05	

A.4. Bode plots from EIS measurements and fitted parameters

Glove box experiments

EIS on natural UO_2 under Ar and Ar/H_2 atmosphere at open circuit potential (sample name UO_2 – X)

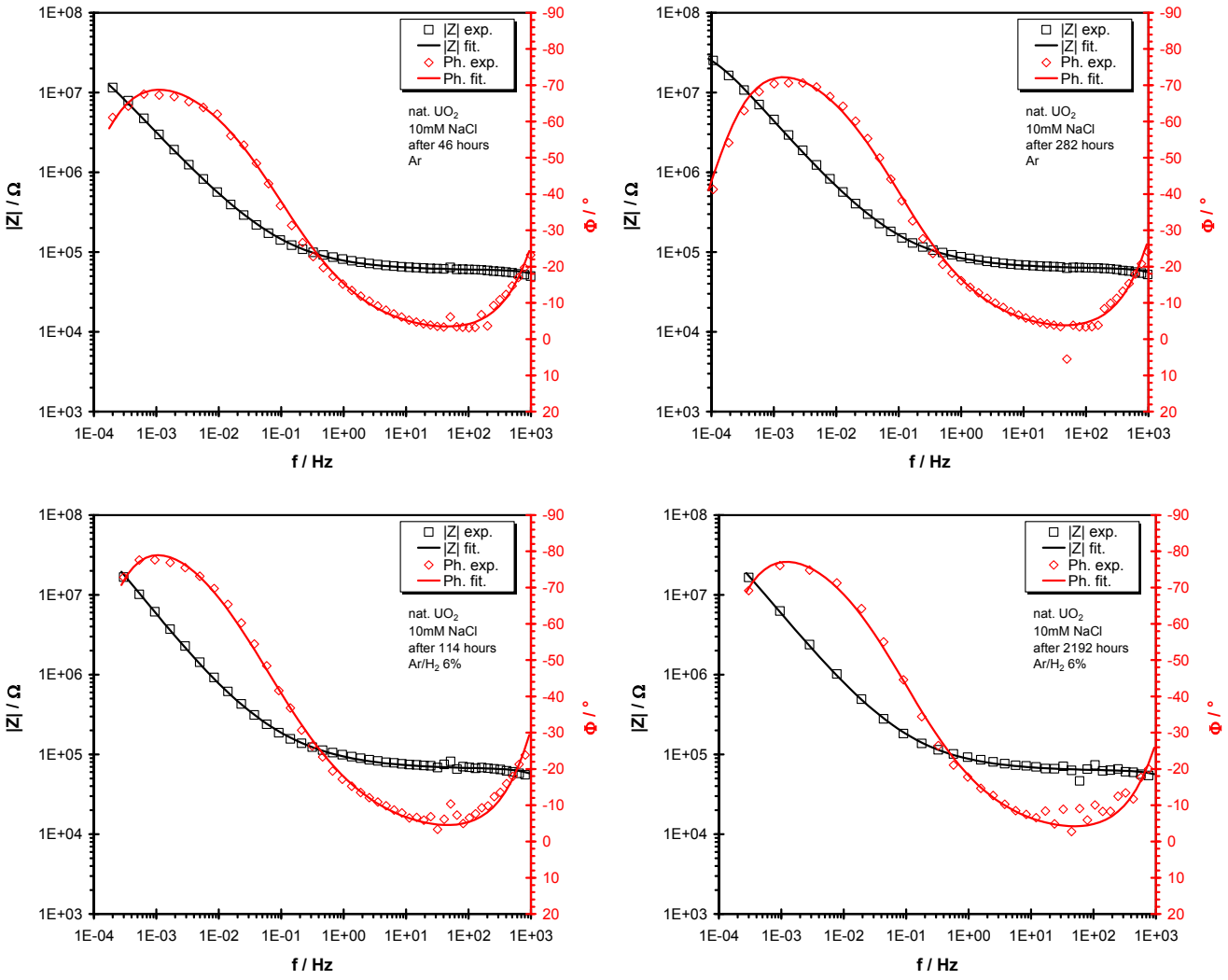

Fig. A.16 Bode plots from EIS measurements on natural UO_2 at open circuit potential under Ar (up) and Ar/H_2 (down) atmosphere

		Ar		Ar/H_2 6%	
Relative time [h]		46	282	114	2192
Global fitting error [%]		5.6	7.1	6.9	6.8
R_{bulk} [Ω]		5.896E+04	6.149E+04	6.518E+04	6.166E+04
C_{bulk} [F]		1.272E-09	1.322E-09	1.434E-09	1.303E-09
R_{pol} [Ω]		3.018E+07	3.380E+07	5.701E+07	5.808E+07
C_{dl} [F^p]	C^0 [F]	3.772E-05	3.195E-05	3.598E-05	2.907E-05
	P	0.902	0.943	1.000	0.984
N_{dif}	A_N [$\Omega \cdot s^{-1/2}$]	5.534E+04	6.526E+04	8.720E+04	7.713E+04
	k_N [s^{-1}]	3.501E-05	4.401E-05	3.211E-05	2.590E-05

EIS on natural UO_2 under Ar/H_2 atmosphere during polarisation (sample name UO_2 – X)

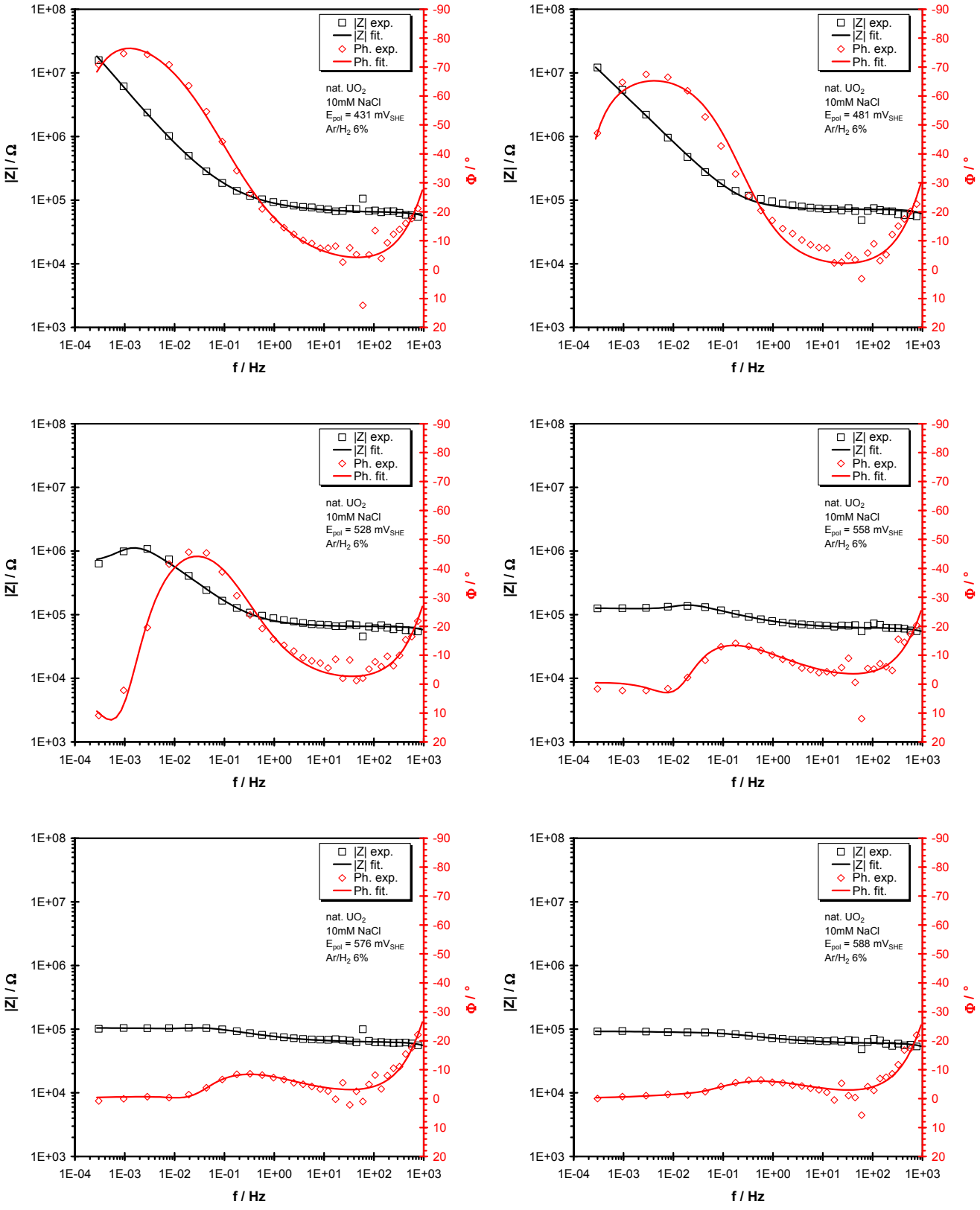

Fig. A.17.a Bode plots from EIS measurements on natural UO_2 during polarisation under Ar/H_2 atmosphere

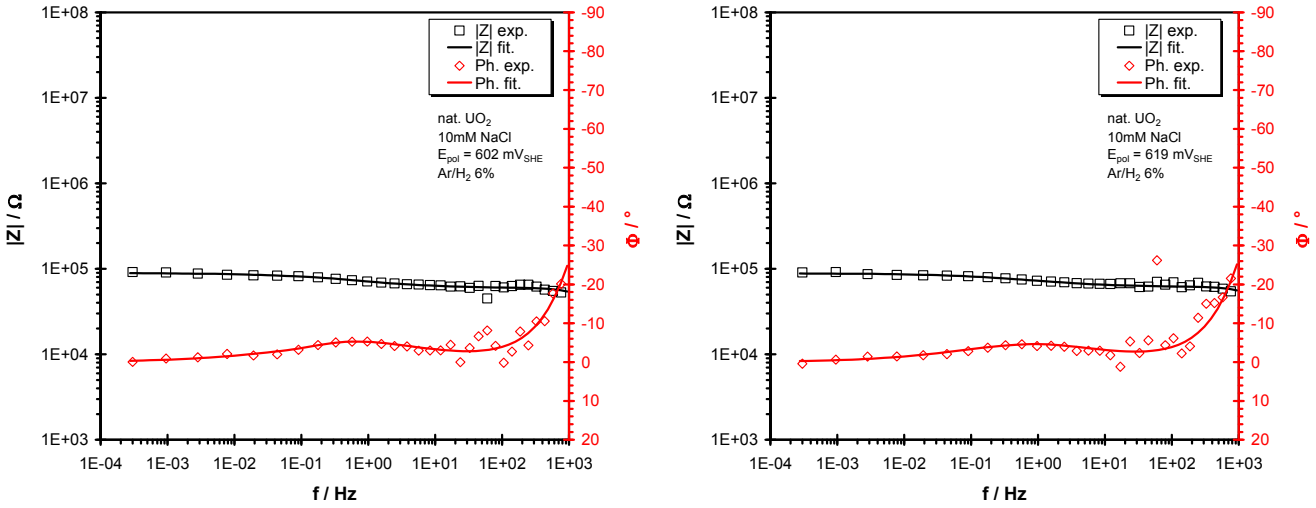

Fig. A.17.b Bode plots from EIS measurements on natural UO_2 during polarisation under Ar/H_2 atmosphere

		Ar/H_2 6%							
E_{pol} [mV_{SHE}]		431	481	528	558	576	588	602	619
Global fitting error [%]		8.0	17.1	13.5	5.2	4.5	3.7	3.9	4.5
R_{bulk} [Ω]		6.346E+04	7.167E+04	6.498E+04	6.019E+04	6.149E+04	5.922E+04	5.906E+04	6.097E+04
C_{bulk} [F]		1.361E-09	1.358E-09	1.306E-09	1.308E-09	1.345E-09	1.341E-09	1.309E-09	1.283E-09
R_{pol} [Ω]		5.709E+07	7.937E+06	4.956E+05	1.423E+05	6.363E+04	3.802E+04	3.364E+04	2.924E+04
C_{dl} [F^p]	C^0 [F]	3.862E-05	1.074E-05	1.095E-05	1.556E-05	1.761E-05	1.826E-05	2.038E-05	1.987E-05
	P	0.977	0.777	0.676	0.500	0.516	0.516	0.504	0.515
N_{dif}	A_N [$\Omega \cdot s^{-1/2}$]	7.681E+04	-	-	-	-	-	-	-
	k_N [s^{-1}]	2.704E-05	-	-	-	-	-	-	-
R_{relax} [Ω]		-	2.263E+07	1.058E+06	1.310E+05	1.402E+05	2.836E+05	3.118E+05	4.874E+05
L_{relax} [H]		-	3.951E+10	3.067E+08	2.249E+06	1.033E+06	9.947E+05	3.630E+05	1.146E+05

EIS on 1% ^{233}U doped UO_2 under Ar and Ar/H_2 atmosphere at open circuit potential (sample U – V)

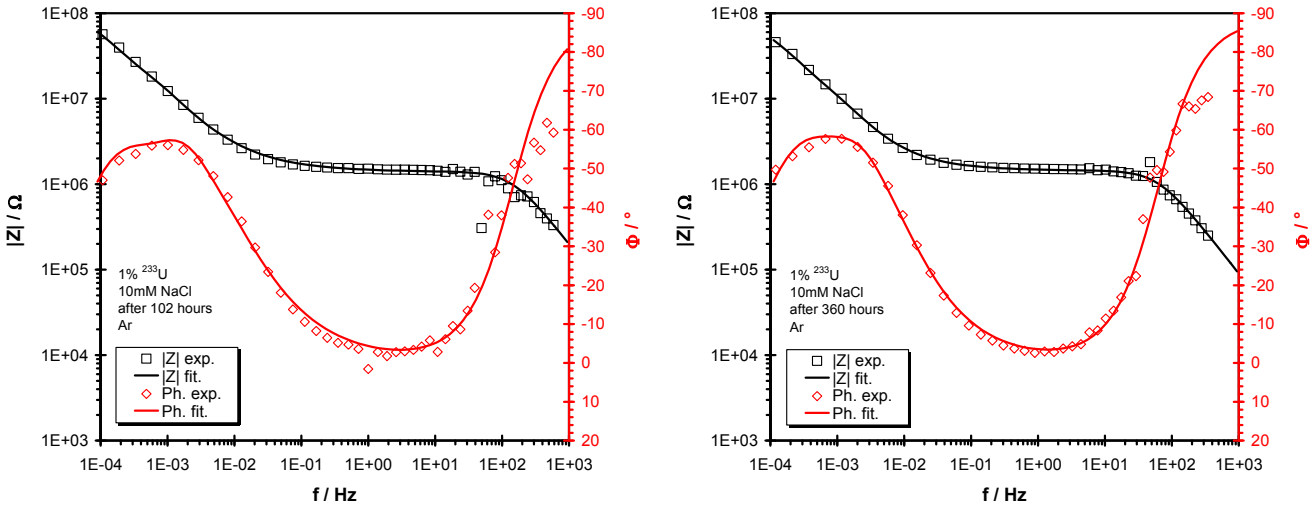

Fig. A.18.a Bode plots from EIS measurements on 1% ^{233}U doped UO_2 at open circuit potential under Ar (up) and Ar/H_2 (down) atmosphere

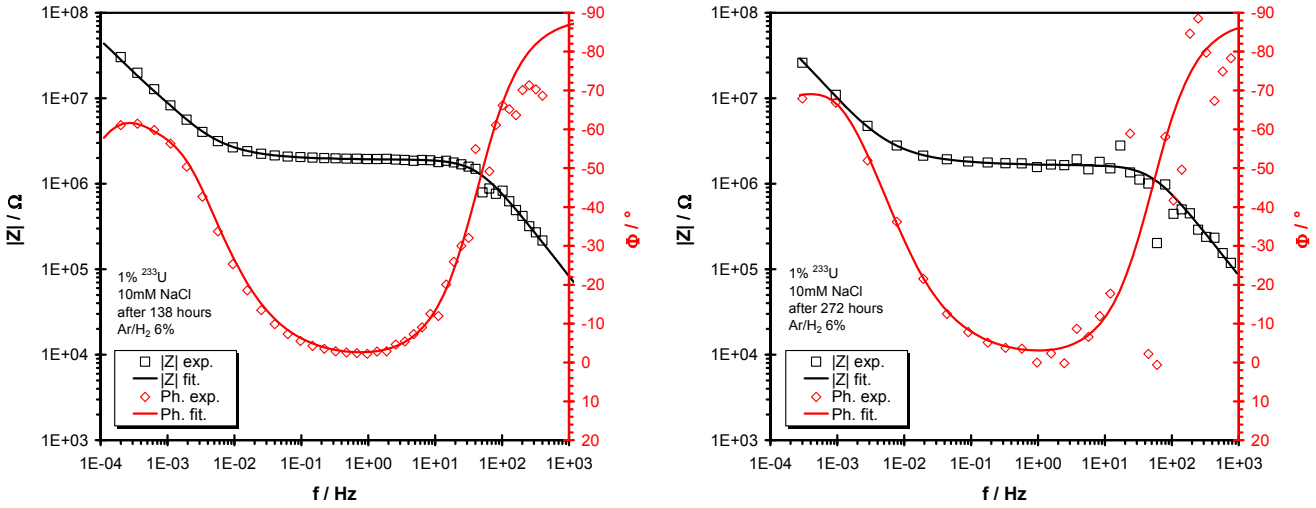

Fig. A.18.b Bode plots from EIS measurements on 1% ^{233}U doped UO_2 at open circuit potential under Ar (up) and Ar/H_2 (down) atmosphere

		Ar		Ar/H_2 6%	
Relative time [h]		102	360	138	272
Global fitting error [%]		9.0	4.7	8.0	7.4
R_{bulk} [Ω]		1.384E+06	1.425E+06	1.898E+06	1.627E+06
C_{bulk} [F]		8.018E-10	1.794E-09	1.935E-09	1.919E-09
R_{pol} [Ω]		1.179E+08	9.304E+07	1.433E+08	2.092E+08
C_{dl} [F^p]	C^0 [F]	1.088E-05	1.046E-05	1.277E-05	1.651E-05
	P	0.884	0.880	0.878	0.954
N_{dif}	A_N [$\Omega \cdot s^{-1/2}$]	2.995E+05	1.761E+05	1.114E+05	1.710E+05
	k_N [s^{-1}]	2.077E-03	2.743E-03	2.457E-03	1.049E-03

EIS on 1% ^{233}U doped UO_2 under Ar/H_2 atmosphere during polarisation (sample name U – V)

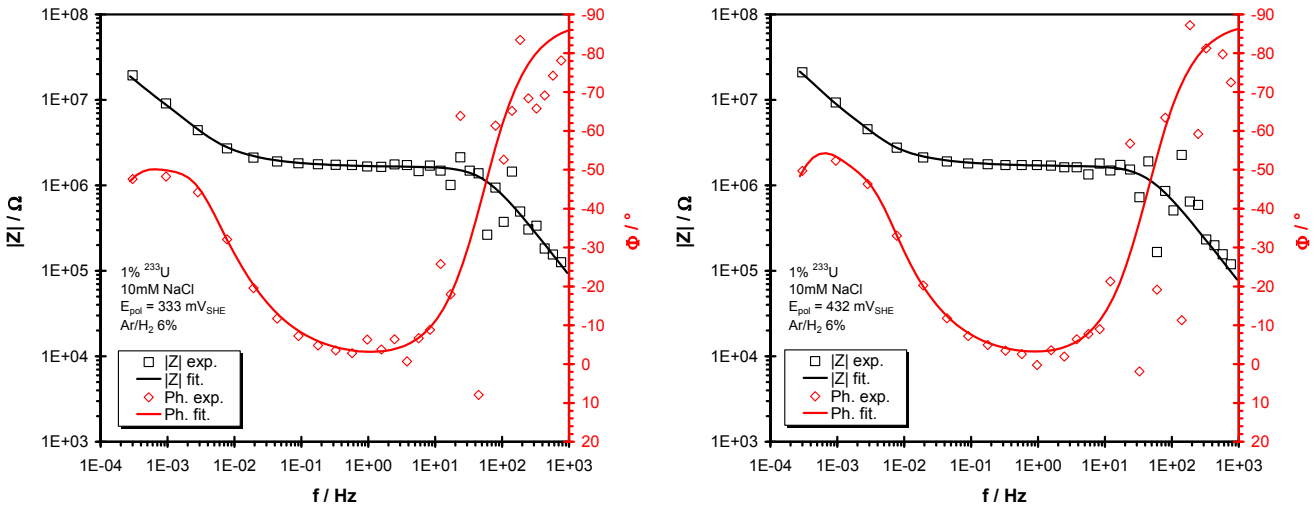

Fig. A.19.a Bode plots from EIS measurements on 1% ^{233}U doped UO_2 during polarisation under Ar/H_2 atmosphere

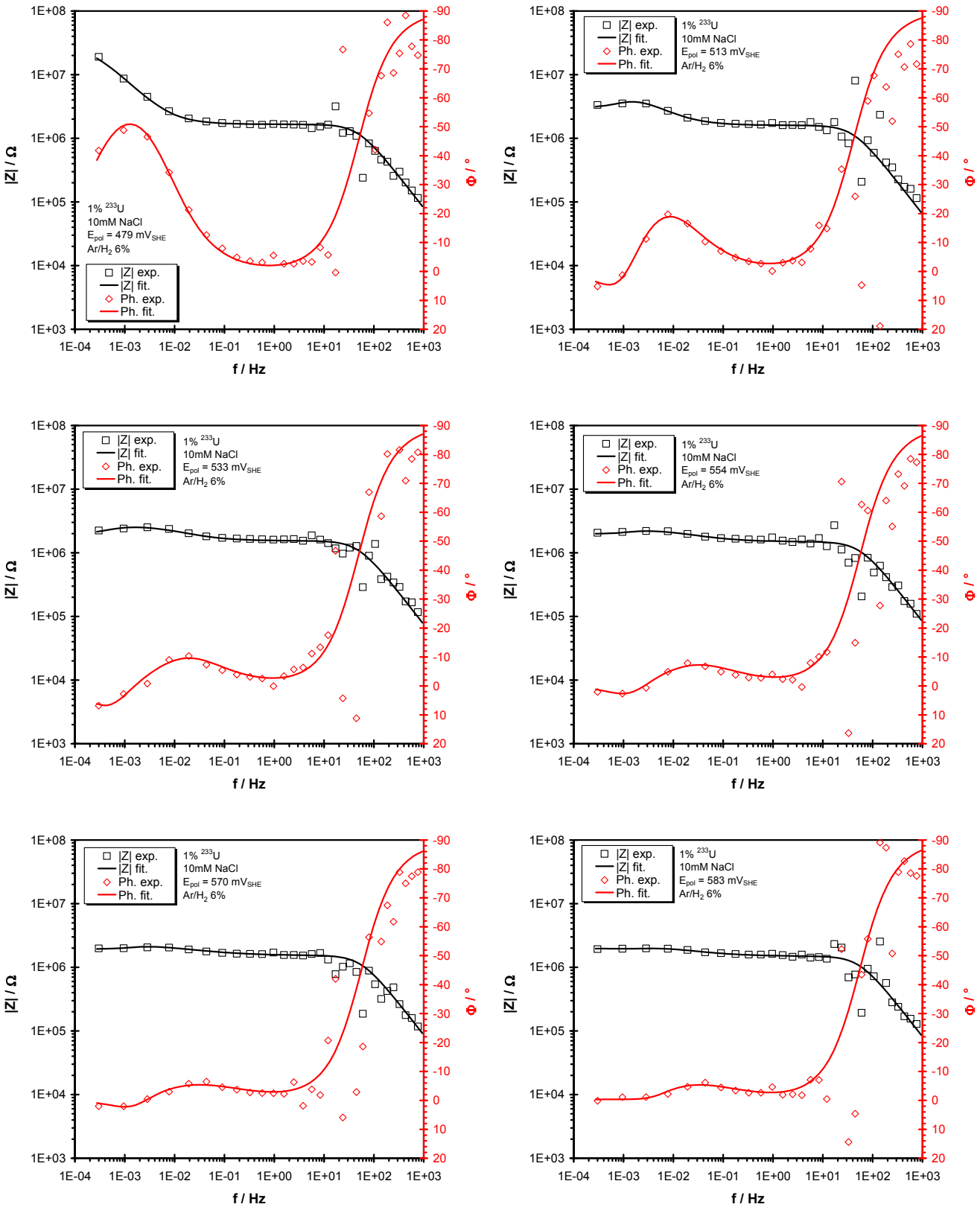

Fig. A.19.b Bode plots from EIS measurements on 1% ^{233}U doped UO_2 during polarisation under Ar/H_2 atmosphere

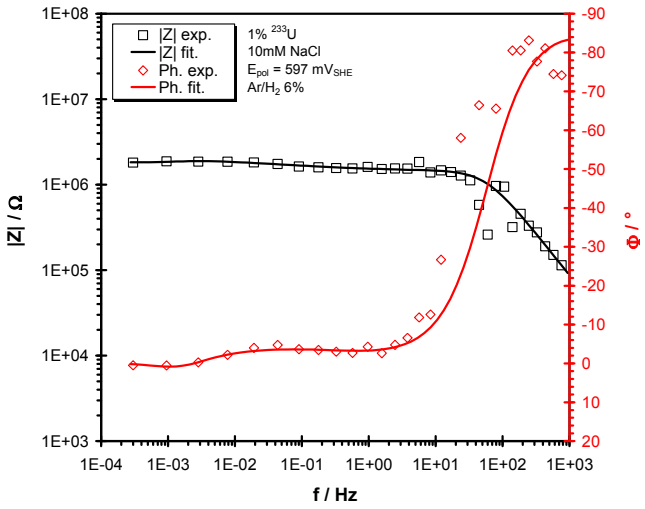

Fig. A.19.c Bode plots from EIS measurements on 1% ^{233}U doped UO_2 during polarisation under Ar/H_2 atmosphere

		Ar/H2 6%								
E_{pol} [mV_{SHE}]		333	432	479	513	533	554	570	583	597
Global fitting error [%]		15.6	4.3	12.8	12.4	18.6	6.1	4.3	5.4	4.9
R_{bulk} [Ω]		1.625E+06	1.657E+06	1.653E+06	1.594E+06	1.536E+06	1.484E+06	1.526E+06	1.485E+06	1.435E+06
C_{bulk} [F]		1.815E-09	2.169E-09	1.972E-09	2.460E-09	2.122E-09	1.929E-09	1.860E-09	1.963E-09	1.924E-09
R_{pol} [Ω]		1.029E+08	3.890E+07	1.065E+07	2.808E+06	1.105E+06	8.562E+05	7.470E+05	6.677E+05	6.031E+05
C_{dl} [F^p]	C^0 [F]	1.655E-05	1.935E-05	7.808E-06	5.964E-06	5.524E-06	4.354E-06	4.470E-06	5.226E-06	3.118E-06
	P	0.897	0.954	0.824	0.762	0.713	0.652	0.568	0.607	0.438
N_{dif}	A_N [$\Omega \cdot s^{-1/2}$]	1.826E+05	1.770E+05	-	-	-	-	-	-	-
	k_N [s^{-1}]	3.633E-03	5.364E-03	-	-	-	-	-	-	-
R_{relax} [Ω]		-	-	3.535E+09	3.120E+06	7.886E+05	1.254E+06	9.665E+05	1.914E+06	1.307E+06
L_{relax} [H]		-	-	2.111E+08	8.419E+08	5.279E+08	2.144E+08	1.576E+08	8.724E+07	1.595E+08

EIS on 10% ^{233}U doped UO_2 under Ar and Ar/H_2 atmosphere at open circuit potential (sample U – I)

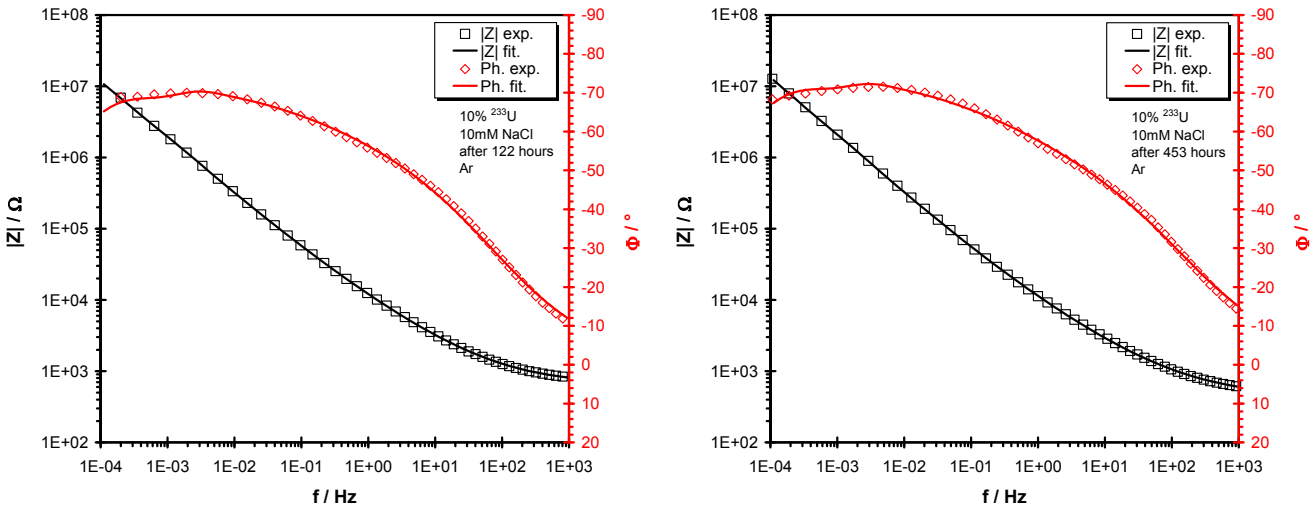

Fig. A.20.a Bode plots from EIS measurements on 10% ^{233}U doped UO_2 at open circuit potential under Ar atmosphere

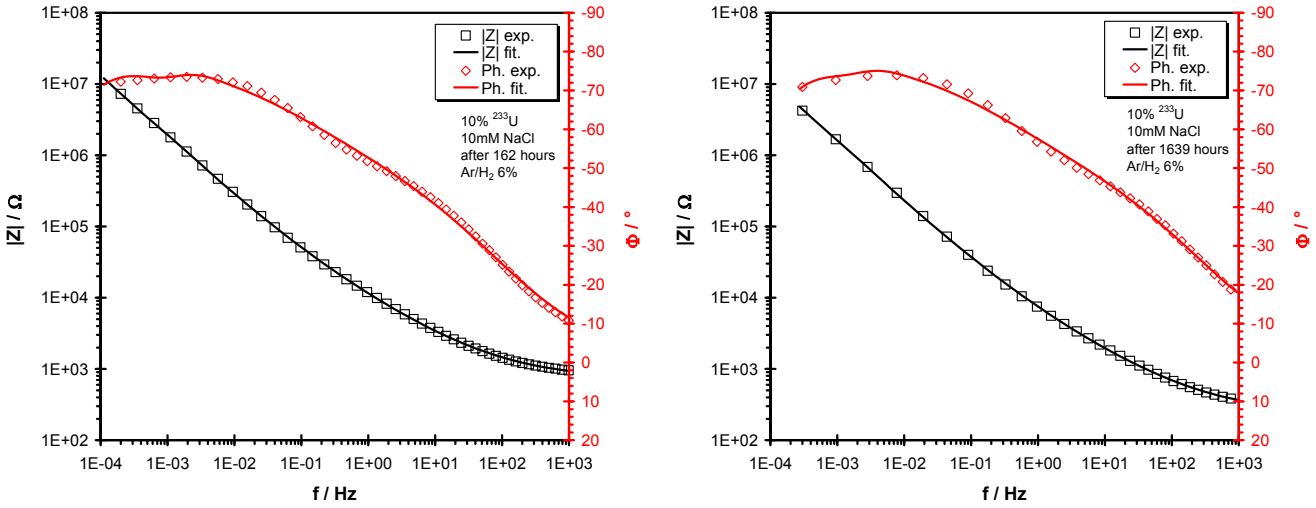

Fig. A.20.b Bode plots from EIS measurements on 1% ^{233}U doped UO_2 at open circuit potential under Ar/H_2 (down) atmosphere

		Ar		Ar/H_2 6%	
Relative time [h]		122	453	162	1639
Global fitting error [%]		2.3	3.6	3.3	3.5
R_{bulk} [Ω]		6.422E+02	4.406E+02	7.407E+02	2.429E+02
C_{bulk} [F]		8.706E-10	1.245E-09	6.362E-10	2.075E-09
R_{pol} [Ω]		7.019E+07	8.160E+07	9.203E+07	9.725E+07
C_{dl} [F^p]	C^0 [F]	3.825E-05	3.906E-05	5.427E-05	6.254E-05
	P	0.833	0.853	0.895	0.898
N_{dif}	A_N [$\Omega \cdot s^{-1/2}$]	1.635E+04	1.573E+04	2.011E+04	1.171E+04
	k_N [s^{-1}]	2.861E-03	2.963E-03	2.612E-03	4.128E-03

EIS on 10% ^{233}U doped UO_2 under Ar/H_2 atmosphere during polarisation (sample name U – V)

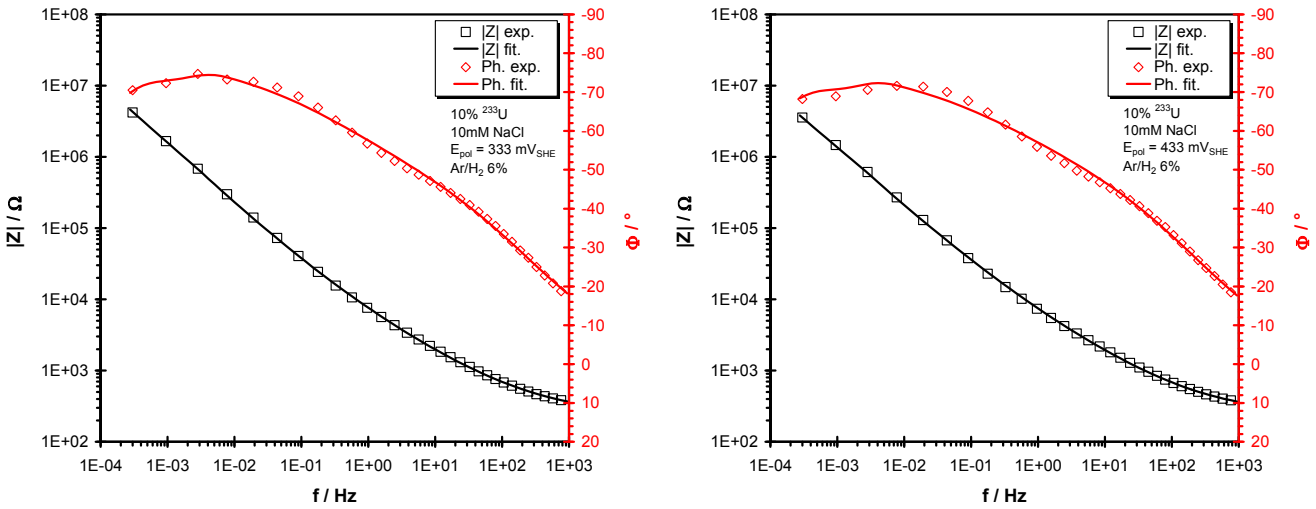

Fig. A.21.a Bode plots from EIS measurements on 10% ^{233}U doped UO_2 during polarisation under Ar/H_2 atmosphere

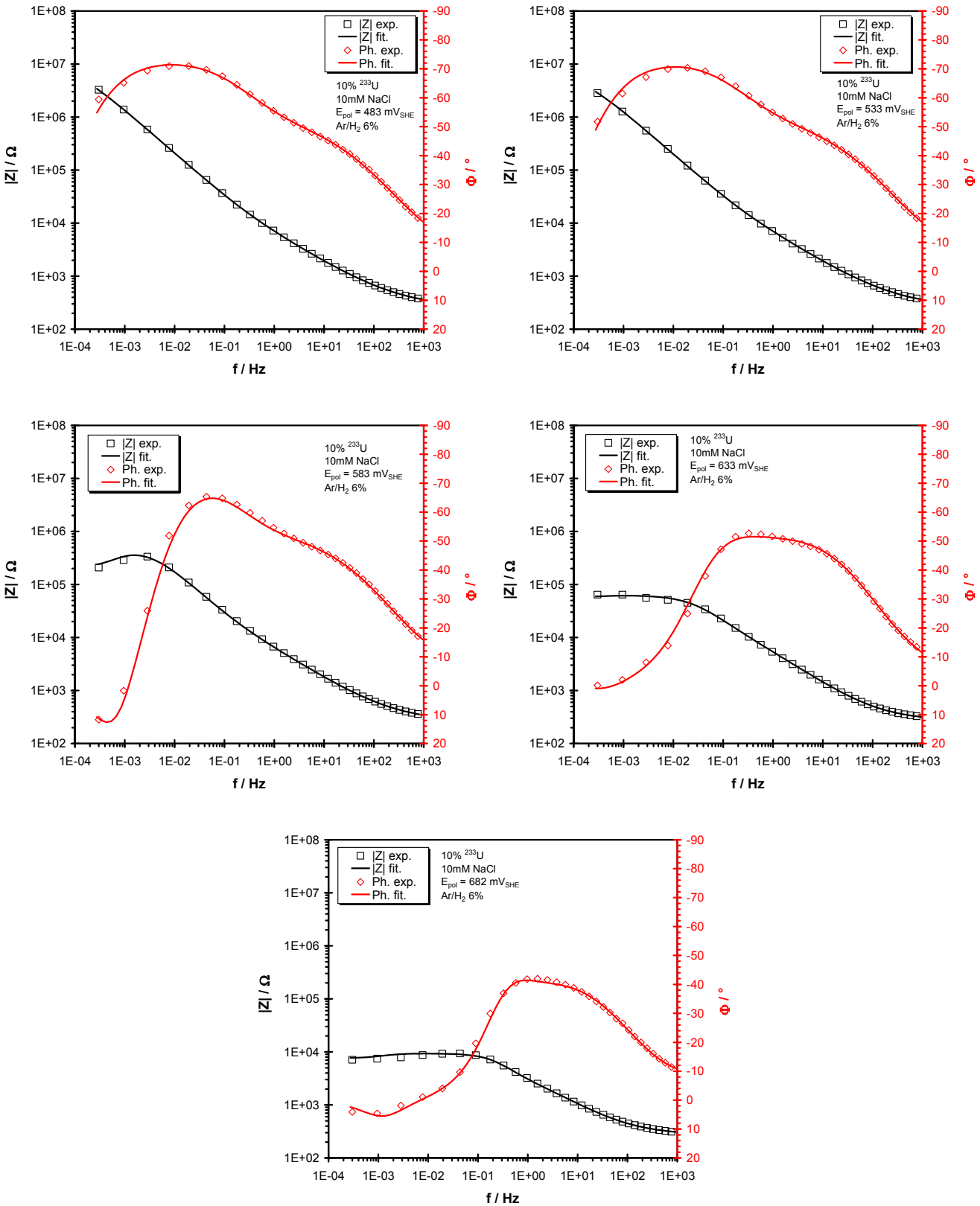

Fig. A.21.b Bode plots from EIS measurements on 10% ^{233}U doped UO_2 during polarisation under Ar/H_2 atmosphere

		Ar/H_2 6%						
E_{pol} [mV_{SHE}]		333	433	483	533	583	633	682
Global fitting error [%]		3.8	5.7	2.5	2.8	5.8	6.9	4.7
R_{bulk} [Ω]		2.414E+02	2.455E+02	2.543E+02	2.551E+02	2.562E+02	2.687E+02	2.683E+02
C_{bulk} [F]		2.016E-09	1.837E-09	3.174E-09	2.421E-09	3.803E-09	3.595E-09	2.307E-08
R_{pol} [Ω]		3.069E+07	2.833E+07	2.006E+07	4.420E+06	4.076E+05	5.687E+04	5.960E+03
C_{dl} [F^p]	C^0 [F]	6.138E-05	6.419E-05	4.681E-05	4.817E-05	5.656E-05	7.517E-05	1.277E-04
	P	0.891	0.868	0.823	0.829	0.869	0.821	0.970
N_{dif}	A_N [$\Omega \cdot s^{-1/2}$]	1.171E+04	1.119E+04	-	-	-	-	-
	k_N [s^{-1}]	4.233E-03	4.229E-03	-	-	-	-	-
R_{relax} [Ω]		-	-	2.004E+07	3.138E+07	4.141E+05	5.888E+05	1.407E+04
L_{relax} [H]		-	-	6.048E+07	5.141E+07	1.452E+08	2.190E+08	2.324E+06

Cyclotron experiments

EIS on depleted UO_2 without beam irradiation under Ar atmosphere (samples G11-01, G11-04, G11-05, H11-06, H11-09, H11-10, I11-03, I11-08, I11-13)

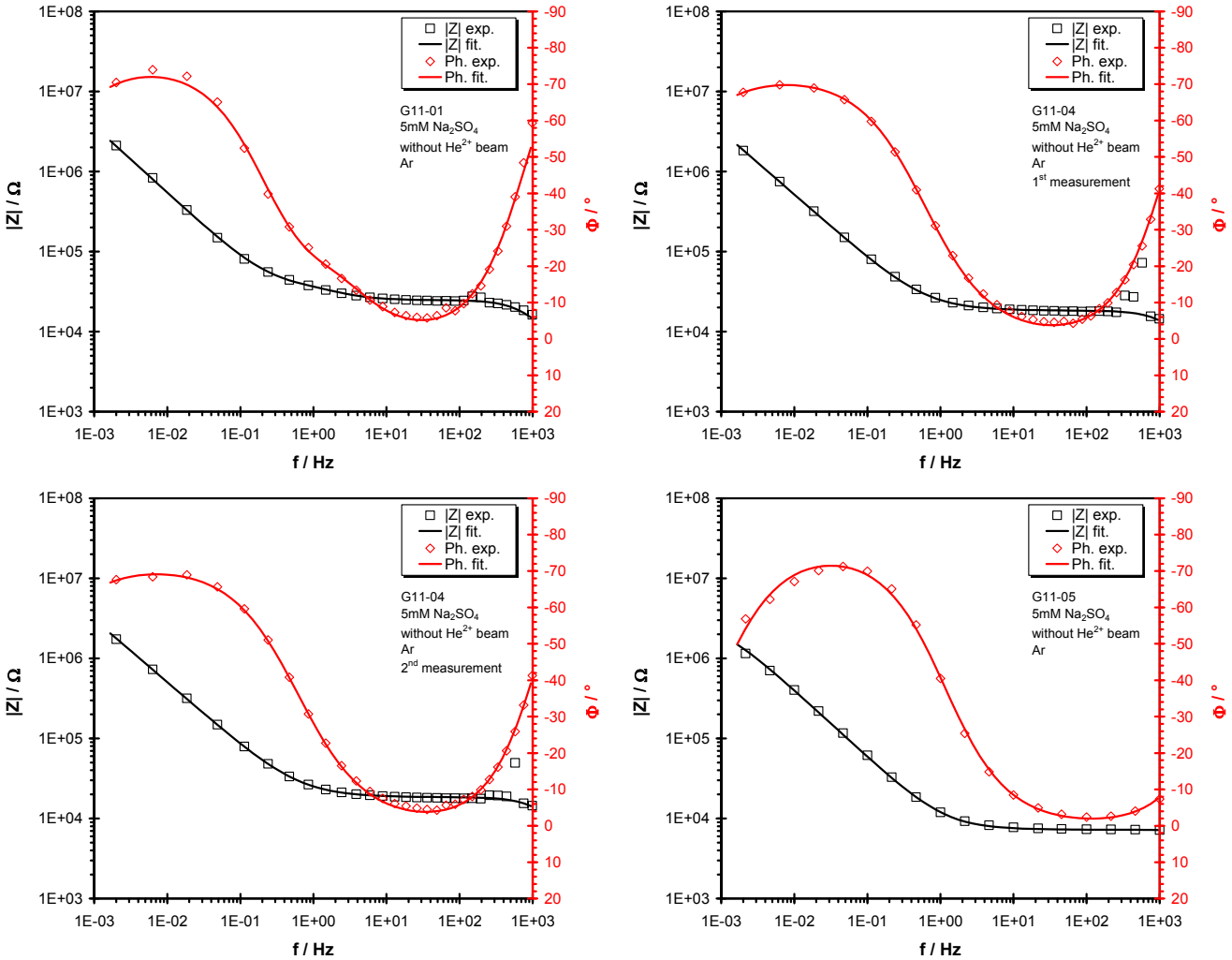

Fig. A.22.a Bode plots from EIS measurements on depleted UO_2 without He^{2+} beam irradiation under Ar atmosphere

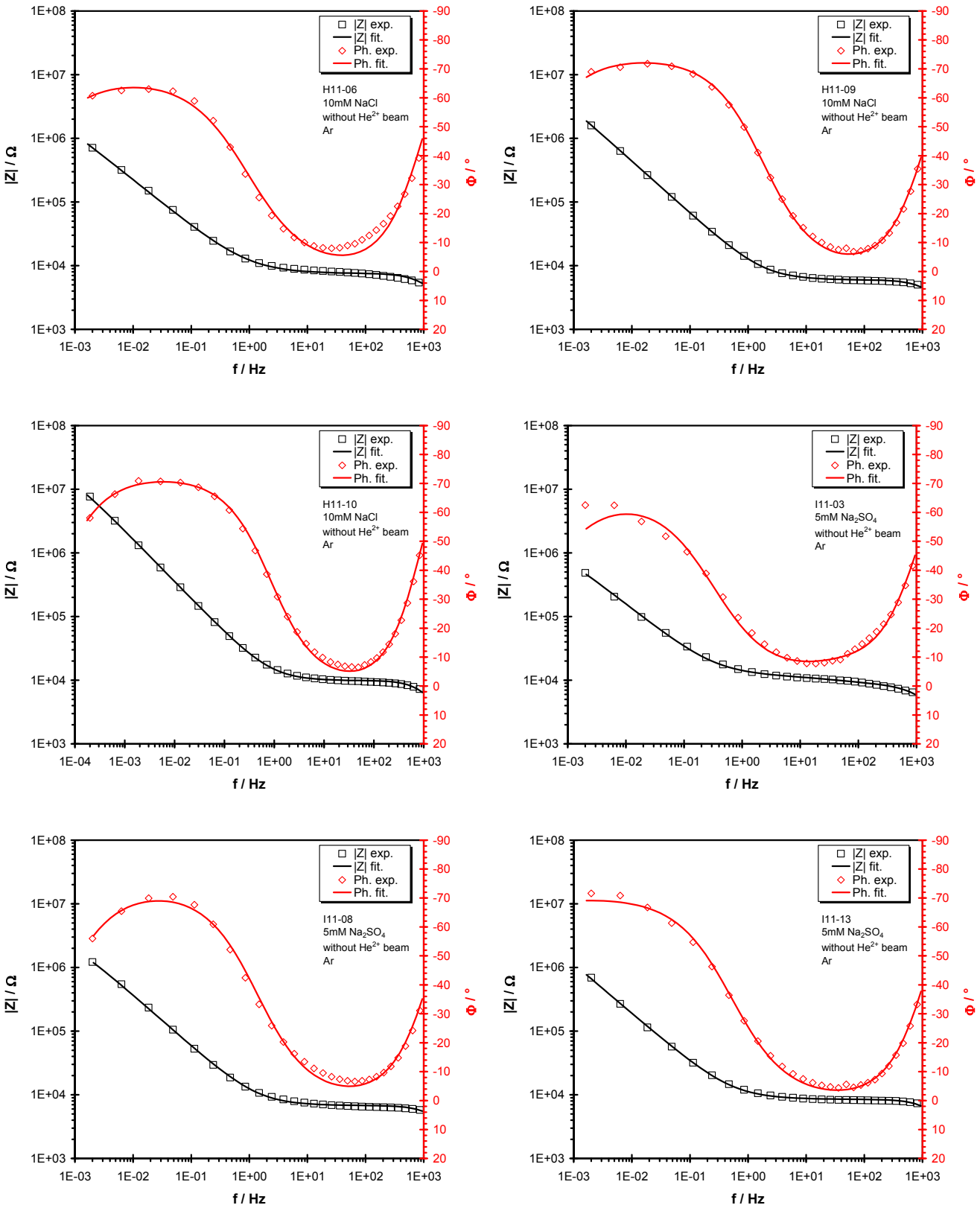

Fig. A.22.b Bode plots from EIS measurements on depleted UO_2 without He^{2+} beam irradiation under Ar atmosphere

Electrode sample		Ar								
		G11-01	G11-04 (1)	G11-04 (2)	G11-05	H11-06	H11-09	H11-10	I11-03	I11-08
Global fitting error [%]		4.3	3.3	4.0	11.6	9.0	4.8	6.8	8.5	7.8
R_{bulk} [Ω]		2.462E+04	1.821E+04	1.835E+04	6.612E+03	7.471E+03	5.923E+03	9.775E+03	1.190E+04	6.733E+03
C_{bulk} [F]		8.879E-09	7.615E-09	7.442E-09	3.573E-09	2.301E-08	2.320E-08	1.992E-08	1.909E-08	1.745E-08
R_{pol} [Ω]		2.077E+07	2.145E+07	2.325E+07	3.241E+06	6.448E+06	1.479E+07	2.939E+07	2.156E+06	4.051E+06
C_{dl} [F^p]	C^0 [F]	1.942E-05	1.831E-05	1.835E-05	2.588E-05	3.513E-05	2.223E-05	2.630E-05	4.869E-05	2.553E-05
	p	0.849	0.810	0.802	0.852	0.745	0.825	0.806	0.747	0.816

EIS on depleted UO_2 during irradiation with 45MeV He^{2+} beam (flux $3.3 \cdot 10^7 cm^{-2} \cdot s^{-1}$) under Ar atmosphere (samples G11-04, G11-05, H11-06, I11-08, I11-12)

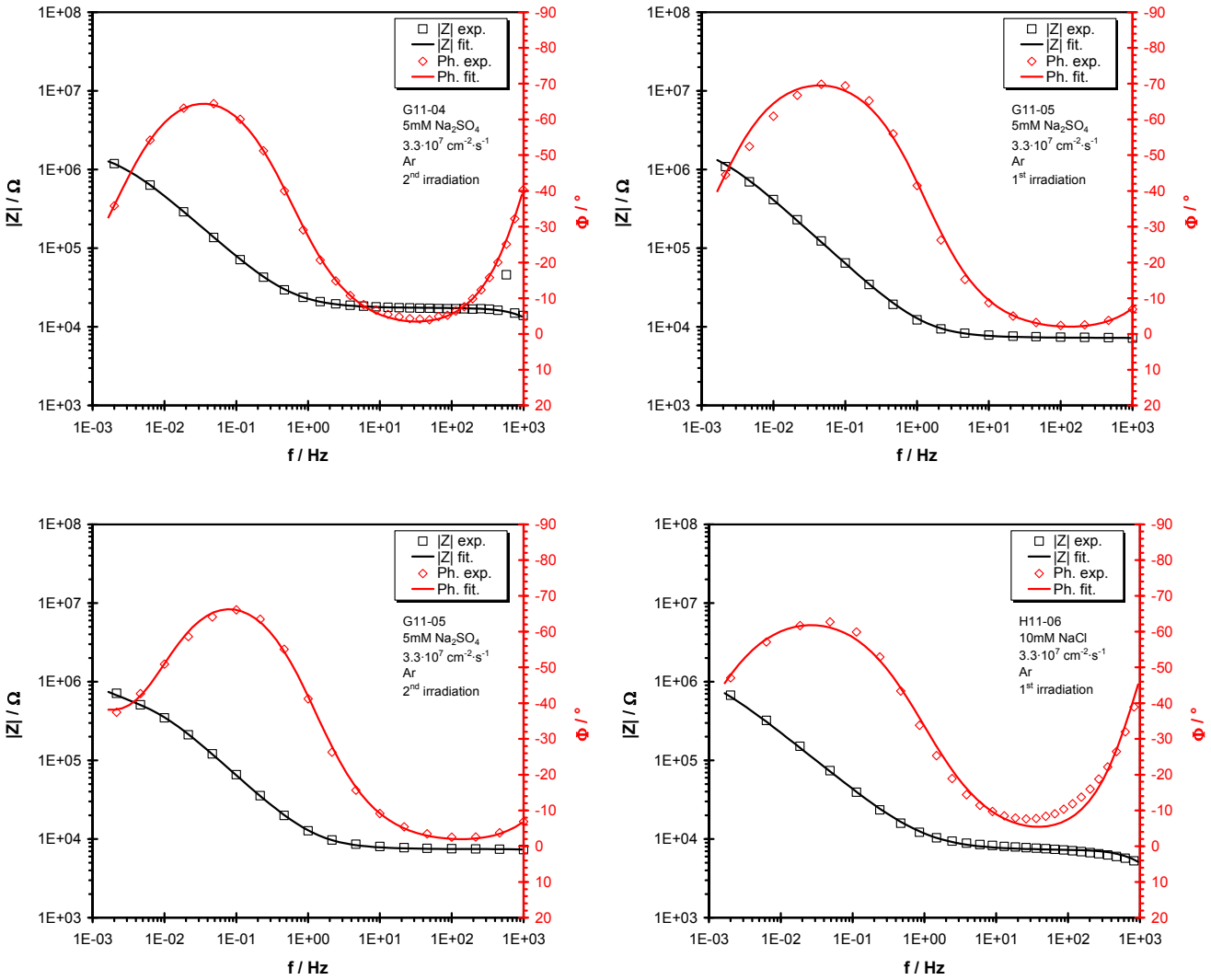

Fig. A.23.a Bode plots from EIS measurements on depleted UO_2 during irradiation with 45MeV He^{2+} beam (flux $3.3 \cdot 10^7 cm^{-2} \cdot s^{-1}$) under Ar atmosphere

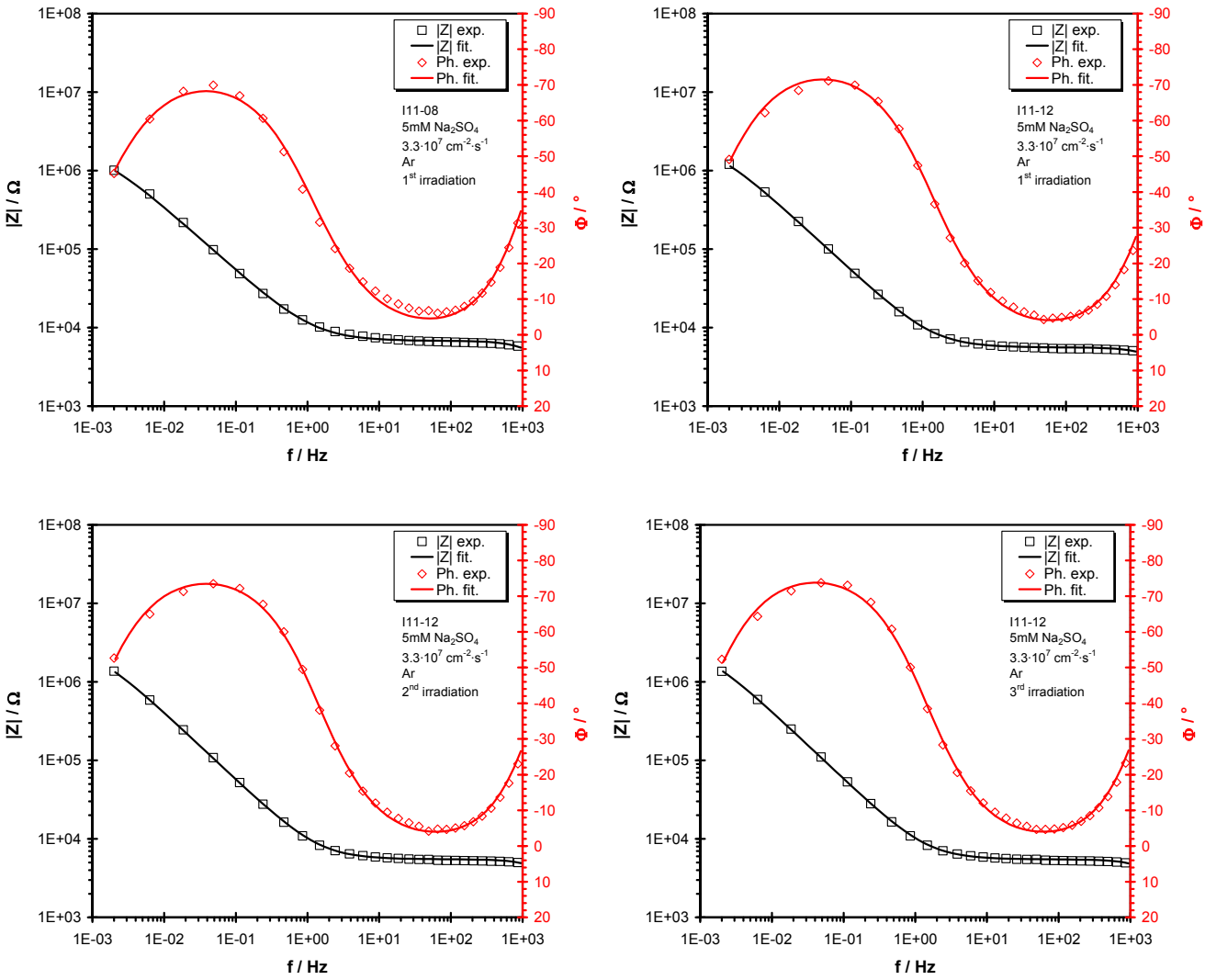

Fig. A.23.b Bode plots from EIS measurements on depleted UO_2 during irradiation with 45MeV He^{2+} beam (flux $3.3 \cdot 10^7 cm^{-2} \cdot s^{-1}$) under Ar atmosphere

		Ar						
Electrode sample		G11-04	G11-05	H11-06	I11-08	I11-12 (1)	I11-12 (2)	I11-12 (3)
Global fitting error [%]		3.0	11.5	8.7	6.2	7.6	6.9	7.0
R_{bulk} [Ω]		1.731E+04	6.603E+03	7.231E+03	6.724E+03	5.561E+03	5.470E+03	5.454E+03
C_{bulk} [F]		7.816E-09	3.252E-09	2.335E-08	1.717E-08	1.562E-08	1.528E-08	1.549E-08
R_{pol} [Ω]		1.815E+06	2.170E+06	1.724E+06	2.032E+06	2.363E+06	2.985E+06	2.922E+06
C_{dl} [F^p]	C^0 [F]	2.005E-05	2.377E-05	3.523E-05	2.778E-05	2.800E-05	2.666E-05	2.621E-05
	p	0.832	0.843	0.761	0.828	0.854	0.869	0.873

EIS on depleted UO_2 during irradiation with 45MeV He^{2+} beam (flux $3.3 \cdot 10^8 cm^{-2} \cdot s^{-1}$) under Ar atmosphere (samples I11-03, I11-15)

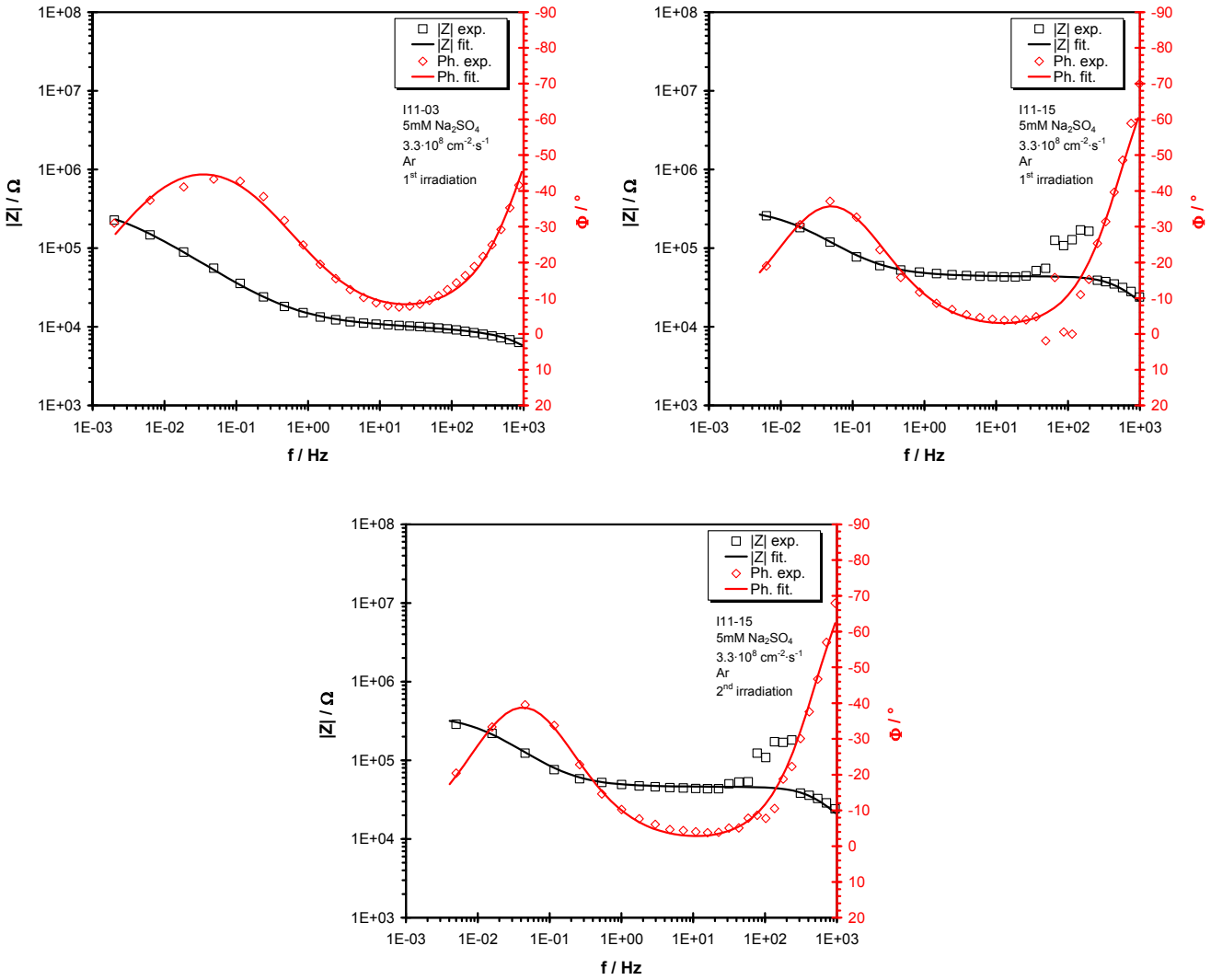

Fig. A.24 Bode plots from EIS measurements on depleted UO_2 during irradiation with 45MeV He^{2+} beam (flux $3.3 \cdot 10^8 cm^{-2} \cdot s^{-1}$) under Ar atmosphere

Electrode sample		Ar		
		I11-03	I11-15 (1)	I11-15 (2)
Global fitting error [%]		6.2	4.2	12.5
R_{bulk} [Ω]		1.057E+04	4.361E+04	4.590E+04
C_{bulk} [F]		1.942E-08	6.773E-09	6.986E-09
R_{pol} [Ω]		3.928E+05	2.785E+05	3.309E+05
C_{dl} [F^p]	C^0 [F]	4.324E-05	2.387E-05	2.504E-05
	p	0.660	0.775	0.802

EIS on depleted UO_2 during irradiation with 45MeV He^{2+} beam (flux $3.3 \cdot 10^9 cm^{-2} \cdot s^{-1}$) under Ar atmosphere (sample I11-13)

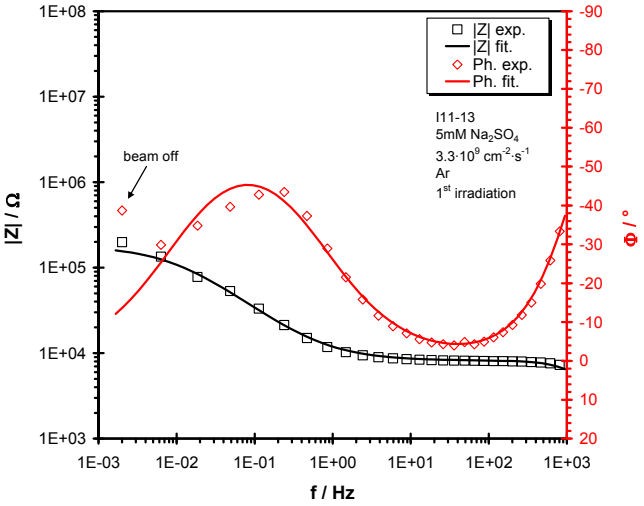

Electrode sample	Ar
	I11-13

Global fitting error [%]	8.1

R_{bulk} [Ω]		8.110E+03
C_{bulk} [F]		1.575E-08
R_{pol} [Ω]		1.727E+05
C_{dl} [F^p]	C^0 [F]	4.433E-05
	p	0.726

Fig. A.25 Bode plot from EIS measurement on depleted UO_2 during irradiation with 45MeV He^{2+} beam (flux $3.3 \cdot 10^9 cm^{-2} \cdot s^{-1}$) under Ar atmosphere

EIS on depleted UO_2 after irradiation with 45MeV He^{2+} beam under Ar atmosphere (samples G11-04, G11-05, H11-06, I11-03, I11-08, I11-12, I11-13)

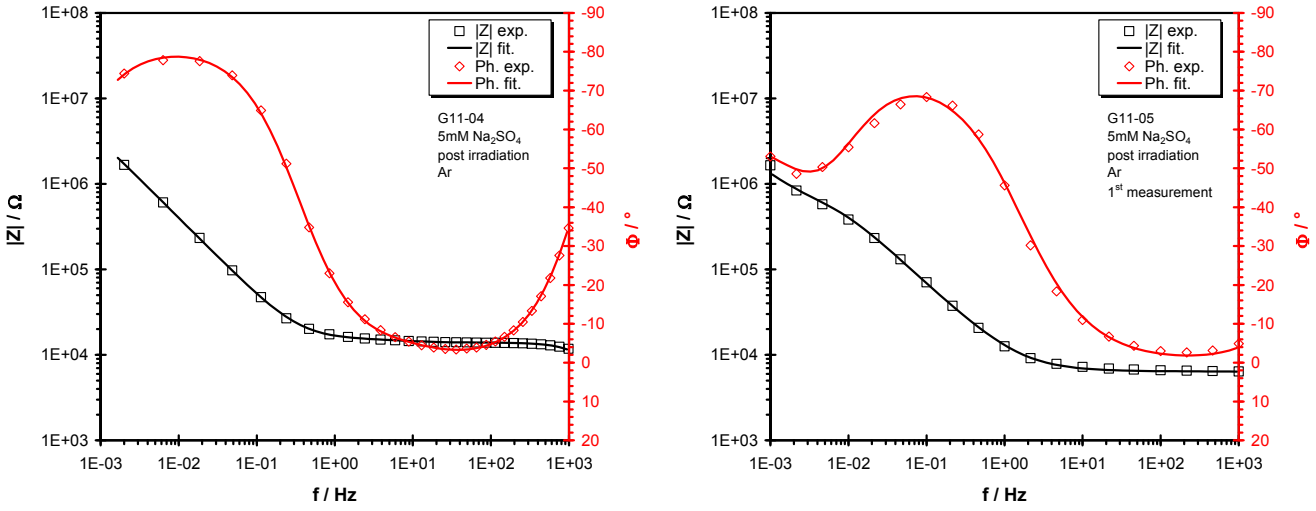

Fig. A.26.a Bode plots from EIS measurements on depleted UO_2 after irradiation with 45MeV He^{2+} beam under Ar atmosphere

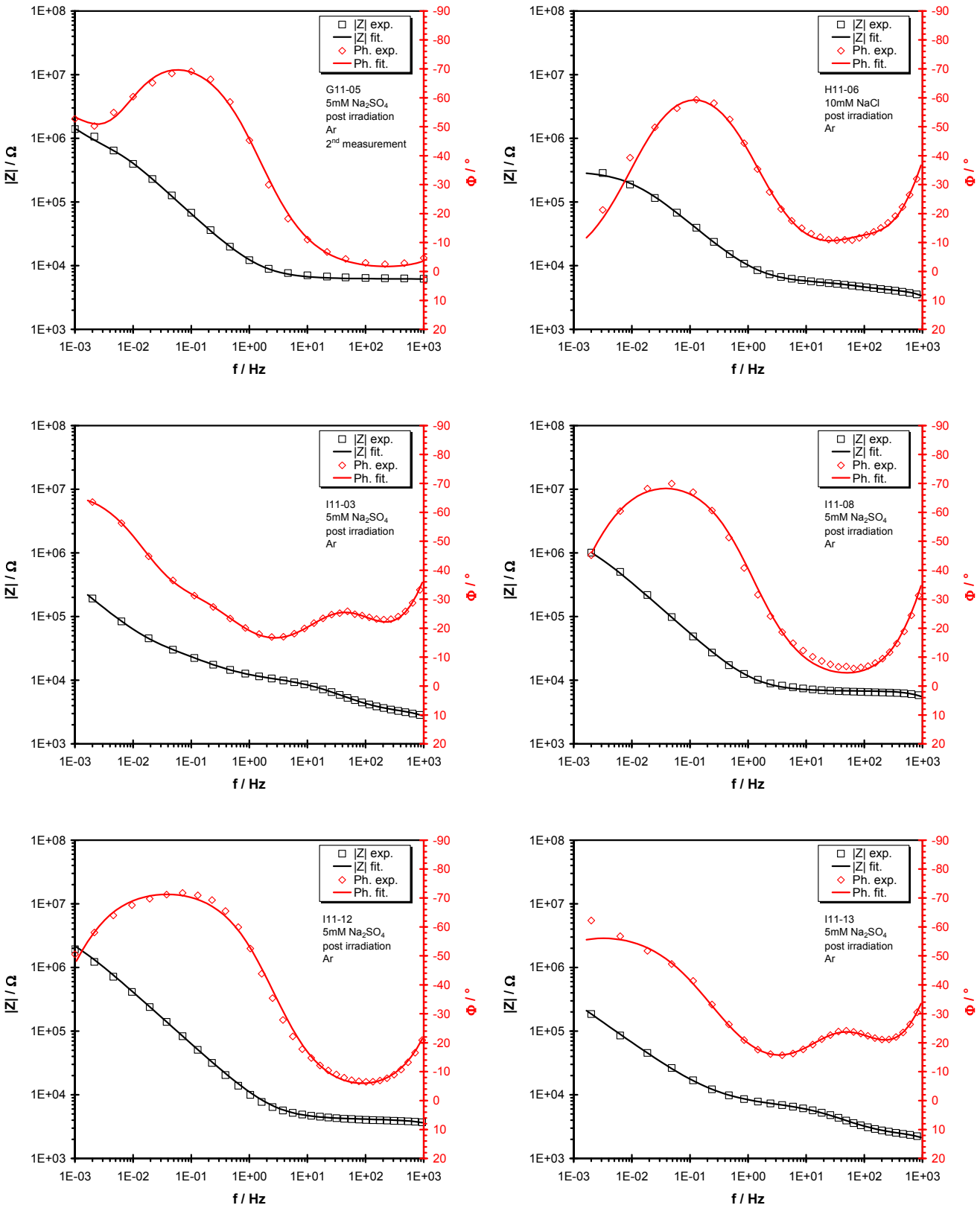

Fig. A.26.b Bode plots from EIS measurements on depleted UO_2 after irradiation with 45MeV He^{2+} beam under Ar atmosphere

Electrode sample		Ar							
		G11-04	G11-05 (1)	G11-05 (2)	H11-06	I11-03	I11-08	I11-12	I11-13
Global fitting error [%]		2.8	9.2	7.9	3.5	3.3	2.7	6.3	2.1
R_{bulk} [Ω]		1.389E+04	5.771E+03	5.529E+03	3.998E+03	3.030E+03	3.834E+03	3.090E+03	2.176E+03
C_{bulk} [F]		8.019E-09	1.942E-09	1.862E-09	2.950E-08	3.655E-08	2.804E-08	2.094E-08	4.303E-08
R_{pol} [Ω]		1.201E+07	2.114E+07	1.873E+07	3.028E+05	1.810E+07	1.148E+05	4.557E+06	2.800E+06
C_{dl} [F^p]	C^0 [F]	3.185E-05	4.186E-05	4.069E-05	3.150E-05	3.979E-05	3.402E-05	2.361E-05	1.020E-04
	p	0.919	0.762	0.770	0.812	0.708	0.847	0.828	0.676
R_{film} [Ω]		1.126E+03	3.473E+05	3.821E+05	-	9.666E+03	2.069E+03	1.077E+03	4.512E+03
C_{film} [F^p]	C^0 [F]	2.458E-05	4.585E-05	5.368E-05	-	3.656E-06	5.930E-06	2.272E-06	5.255E-06
	p	0.921	0.929	0.937	-	0.746	0.759	0.633	0.758

EIS on depleted UO_2 without beam irradiation under Ar/H_2 atmosphere (samples G11-13, G11-15, G11-16)

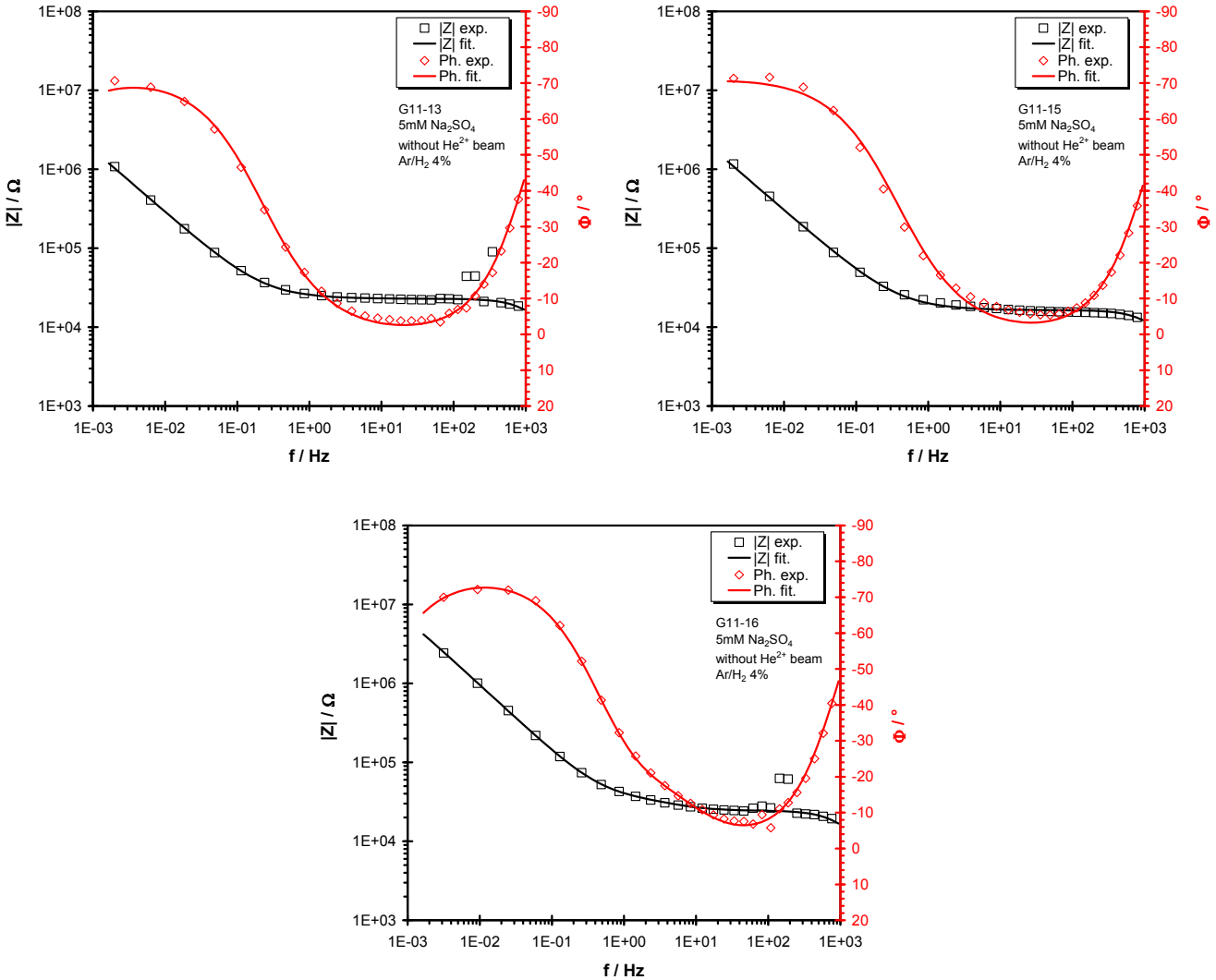

Fig. A.27 Bode plots from EIS measurements on depleted UO_2 without He^{2+} beam irradiation under Ar/H_2 atmosphere

Electrode sample		Ar/H_2 4%		
		G11-13	G11-15	G11-16
Global fitting error [%]		5.1	5.6	7.9
R_{bulk} [Ω]		2.283E+04	2.416E+04	1.632E+04
C_{bulk} [F]		6.868E-09	7.317E-09	9.082E-09
R_{pol} [Ω]		4.965E+07	2.154E+07	1.297E+08
C_{dl} [F^p]	C^0 [F]	3.282E-05	1.112E-05	3.026E-05
	p	0.806	0.855	0.797

EIS on depleted UO_2 during irradiation with 45MeV He^{2+} beam (flux $3.3 \cdot 10^7 cm^{-2} \cdot s^{-1}$) under Ar/$H_2$ atmosphere (samples G11-13, G11-16)

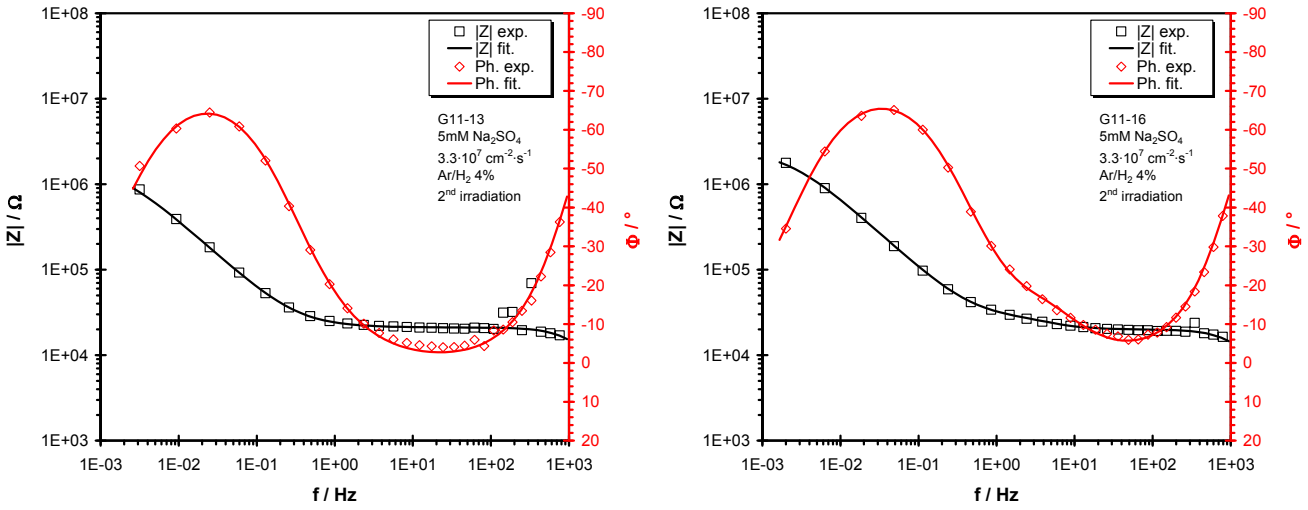

Fig. A.28 Bode plots from EIS measurements on depleted UO_2 during irradiation with 45MeV He^{2+} beam (flux $3.3 \cdot 10^7 cm^{-2} \cdot s^{-1}$) under Ar/$H_2$ atmosphere

Electrode sample		Ar/H_2 4%	
		G11-13	G11-16
Global fitting error [%]		5.3	4.9
R_{bulk} [Ω]		2.116E+04	1.984E+04
C_{bulk} [F]		7.420E-09	7.891E-09
R_{pol} [Ω]		4.566E+06	2.477E+06
C_{dl} [F^p]	C^0 [F]	2.657E-05	1.480E-05
	p	0.845	0.849

EIS on depleted UO_2 after irradiation with 45MeV He^{2+} beam under Ar/H_2 atmosphere (samples G11-13, G11-16)

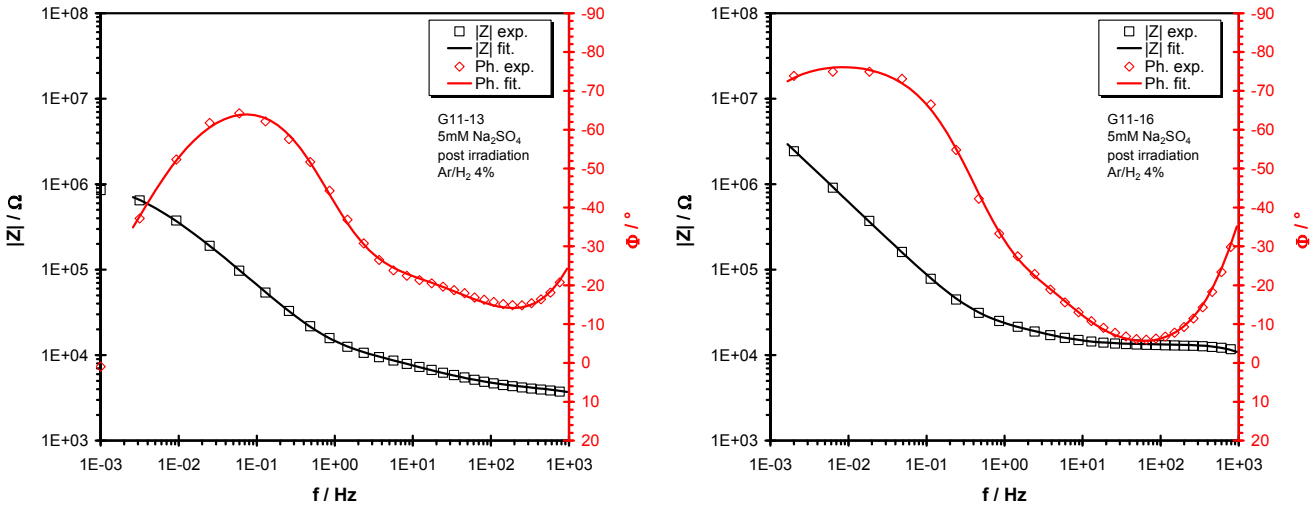

Fig. A.29 Bode plots from EIS measurements on depleted UO_2 after irradiation with 45MeV He^{2+} beam under Ar/H_2 atmosphere

Electrode sample		Ar/H2 4% G11-13	Ar/H2 4% G11-16
Global fitting error [%]		4.3	4.9
R_{bulk} [Ω]		7.431E+03	1.322E+04
C_{bulk} [F]		1.661E-08	8.870E-09
R_{pol} [Ω]		4.817E+07	2.611E+07
C_{dl} [F^p]	C^0 [F]	1.746E-05	1.843E-05
	p	0.882	0.880
R_{film} [Ω]		5.154E+03	6.223E+03
C_{film} [F^p]	C^0 [F]	1.201E-05	1.394E-05
	P	0.632	0.842

EIS measurements on depleted UO_2 during anodic polarisation and irradiation with 45MeV He^{2+} beam (flux $3.3 \cdot 10^7 cm^{-2} \cdot s^{-1}$) under Ar atmosphere (sample G11-04)

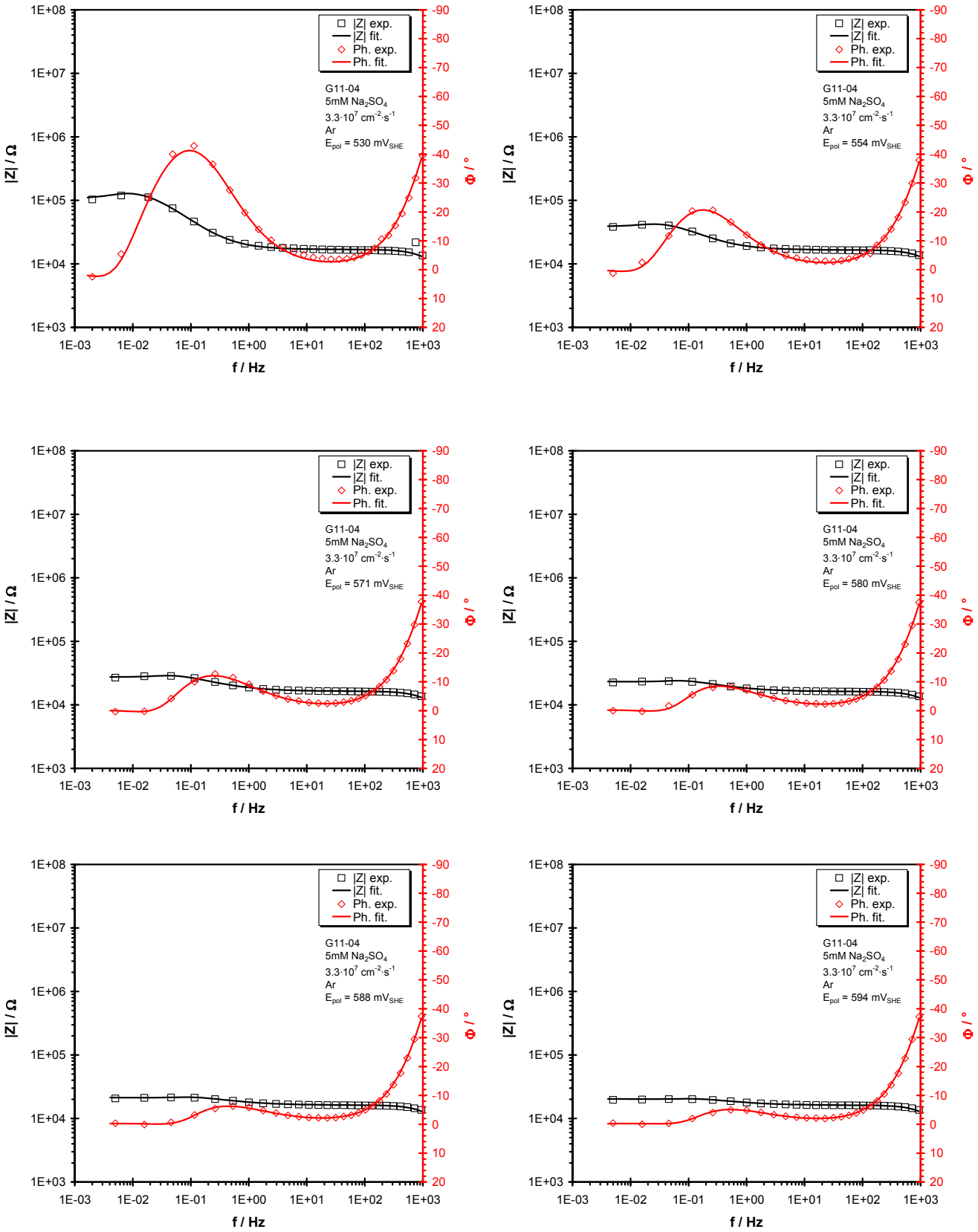

Fig. A.30 Bode plots from anodic polarisation on depleted UO_2 during irradiation with 45MeV He^{2+} beam (flux $3.3 \cdot 10^7 cm^{-2} \cdot s^{-1}$) under Ar atmosphere

E_{pol} (mV_{SHE})		Ar					
		530	554	571	580	587	594
Global fitting error [%]		5.5	2.8	2.6	2.6	2.6	2.5
R_{bulk} [Ω]		1.681E+04	1.651E+04	1.632E+04	1.617E+04	1.614E+04	1.612E+04
C_{bulk} [F]		7.951E-09	7.759E-09	7.794E-09	7.798E-09	7.769E-09	7.778E-09
R_{pol} [Ω]		1.393E+05	3.331E+04	1.725E+04	1.144E+04	8.151E+03	6.310E+03
C_{dl} (F^p)	C^0 (F)	3.400E-05	5.077E-05	6.869E-05	8.283E-05	9.483E-05	1.042E-04
	p	0.817	0.765	0.697	0.670	0.651	0.655
R_{relax} [Ω]		2.737E+05	7.349E+04	3.378E+04	1.970E+04	1.517E+04	1.270E+04
L_{relax} [H]		1.002E+07	7.432E+05	2.080E+05	6.910E+04	3.960E+04	2.596E+04

EIS measurements on depleted UO_2 during anodic polarisation without irradiation with He^{2+} beam under Ar/H_2 atmosphere (sample G11-15)

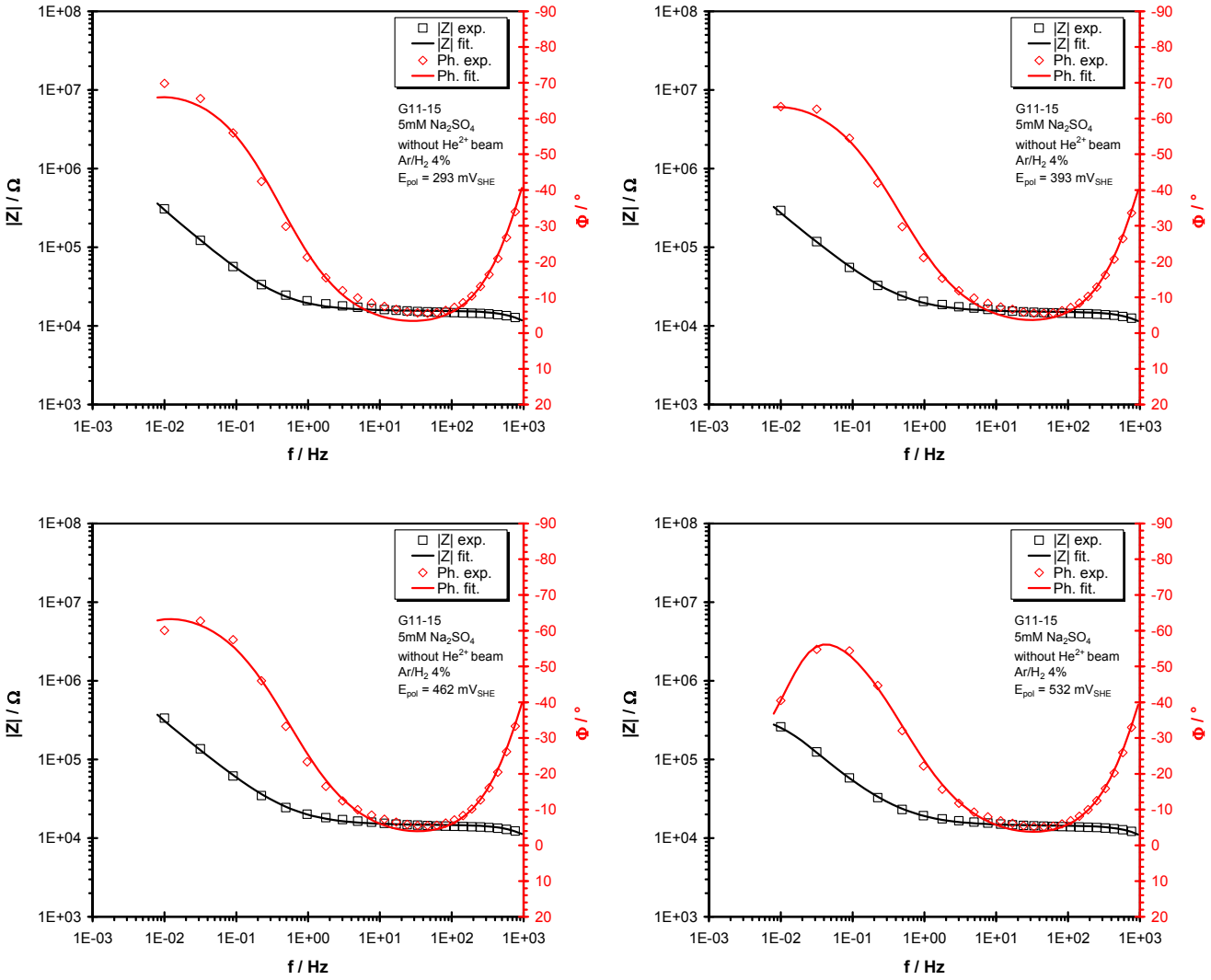

Fig. A.31.a Bode plots from anodic polarisation on depleted UO_2 without irradiation with He^{2+} beam under Ar/H_2 atmosphere

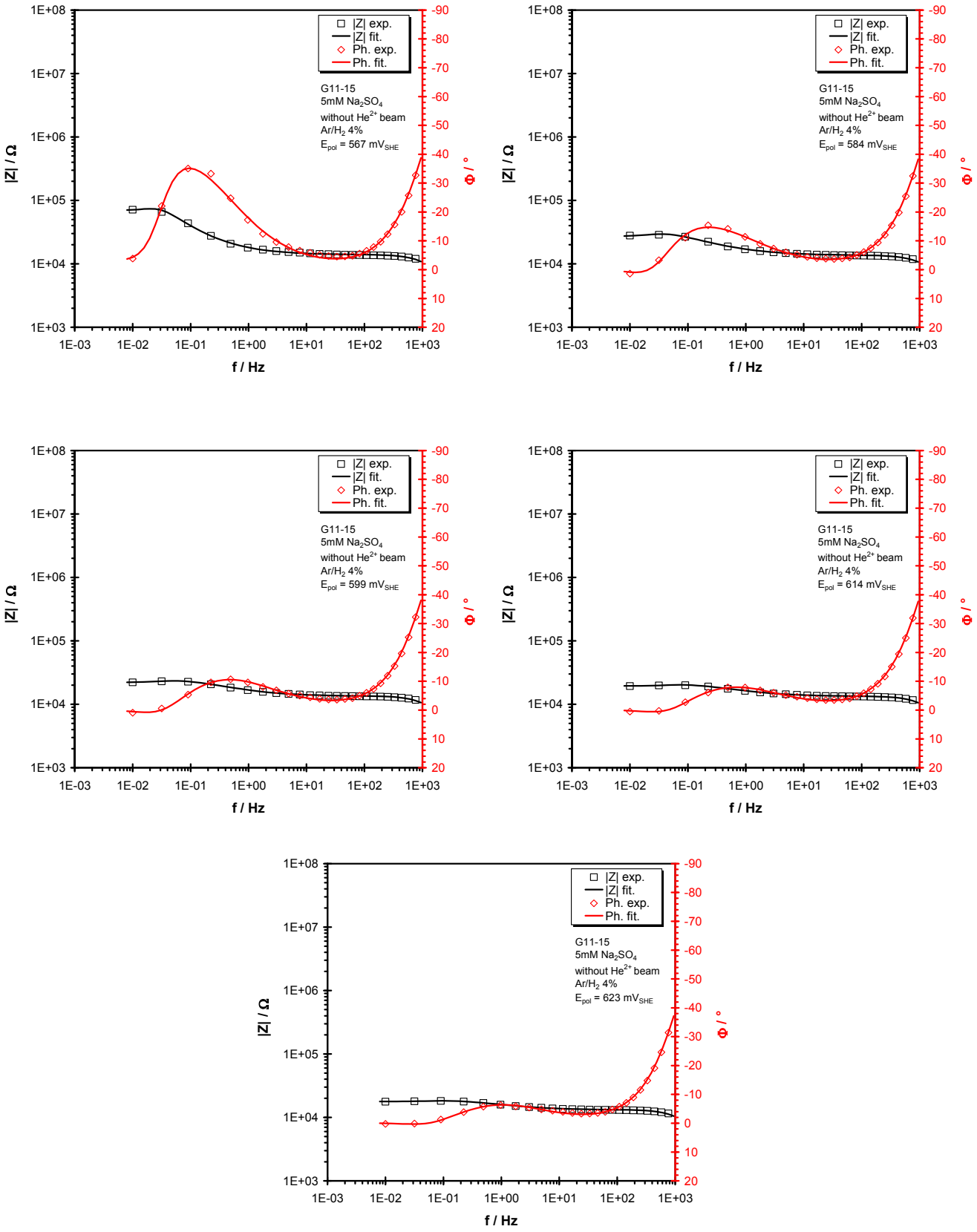

Fig. A.31.b Bode plots from anodic polarisation on depleted UO_2 without irradiation with He^{2+} beam under Ar/H_2 atmosphere

	Ar/H_2 4%								
E_{pol} (mV_{SHE})	293	393	462	532	567	584	599	614	623
Global fitting error [%]	8.0	6.6	6.2	4.9	4.0	3.3	3.0	2.9	2.7
R_{bulk} [Ω]	1.543E+04	1.497E+04	1.458E+04	1.429E+04	1.385E+04	1.352E+04	1.341E+04	1.328E+04	1.314E+04
C_{bulk} [F]	9.316E-09	9.400E-09	9.530E-09	9.586E-09	9.701E-09	9.778E-09	9.777E-09	9.744E-09	9.678E-09
R_{pol} [Ω]	1.012E+07	1.004E+07	8.676E+06	3.216E+06	2.181E+05	2.526E+04	1.293E+04	8.906E+03	6.175E+03
C_{dl} [F^p] C^0 [F]	3.038E-05	3.069E-05	2.723E-05	3.044E-05	4.457E-05	6.292E-05	5.706E-05	6.106E-05	5.720E-05
C_{dl} [F^p] p	0.786	0.756	0.758	0.750	0.668	0.609	0.649	0.639	0.670
R_{relax} [Ω]	1.702E+05	1.712E+05	2.077E+05	5.950E+05	8.730E+04	3.340E+04	2.957E+04	2.180E+04	2.078E+04
L_{relax} [H]	1.956E+08	1.832E+08	1.516E+08	5.429E+06	6.665E+05	2.537E+05	1.662E+05	8.665E+04	6.176E+04

EIS measurements on depleted UO_2 during anodic polarisation and irradiation with 45MeV He^{2+} beam (flux $3.3 \cdot 10^7 cm^{-2} \cdot s^{-1}$) under Ar/$H_2$ atmosphere (sample G11-16)

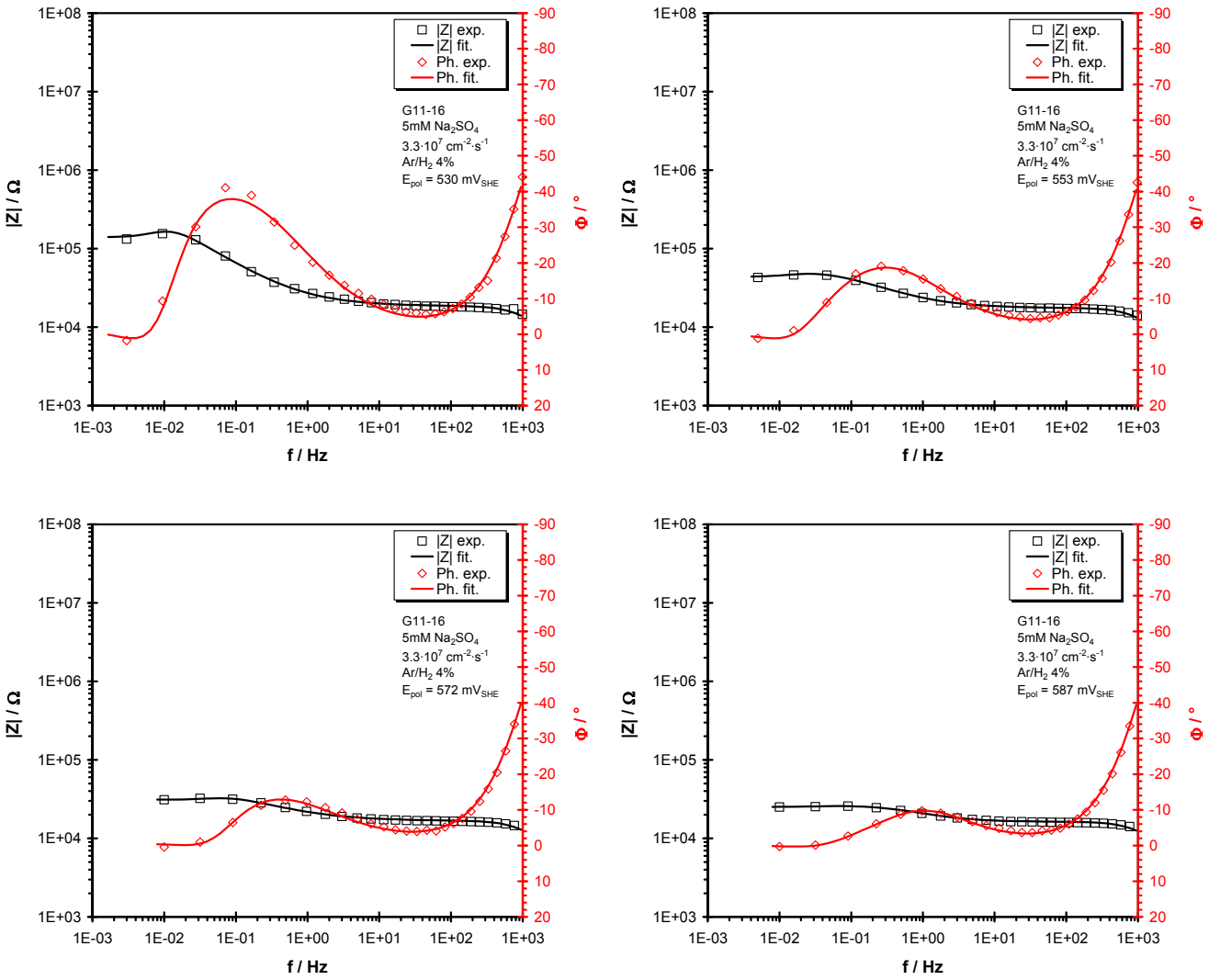

Fig. A.32.a Bode plots from anodic polarisation on depleted UO_2 during irradiation with 45MeV He^{2+} beam (flux $3.3 \cdot 10^7 cm^{-2} \cdot s^{-1}$) under Ar/$H_2$ atmosphere

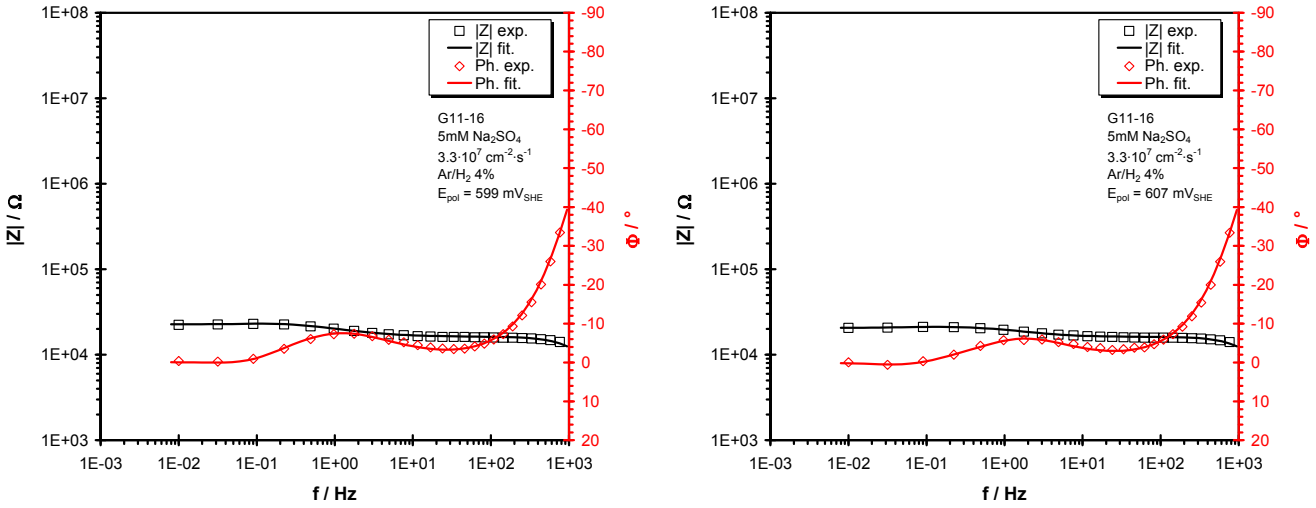

Fig. A.32.b Bode plots from anodic polarisation on depleted UO_2 during irradiation with 45MeV He^{2+} beam (flux $3.3 \cdot 10^7 cm^{-2} \cdot s^{-1}$) under Ar/H_2 atmosphere

		Ar/H_2					
E_{pol} (mV_{SHE})		530	553	572	587	599	607
Global fitting error [%]		6.7	4.3	4.6	4.2	4.2	4.2
R_{bulk} [Ω]		1.841E+04	1.739E+04	1.668E+04	1.622E+04	1.612E+04	1.611E+04
C_{bulk} [F]		7.985E-09	8.224E-09	8.369E-09	8.490E-09	8.518E-09	8.513E-09
R_{pol} [Ω]		3.071E+05	3.953E+04	2.325E+04	1.056E+04	8.087E+03	5.441E+03
C_{dl} [F^p]	C^0 [F]	2.350E-05	3.099E-05	4.055E-05	2.965E-05	3.457E-05	3.048E-05
	p	0.658	0.665	0.631	0.764	0.733	0.805
R_{relax} [Ω]		2.182E+05	8.705E+04	4.373E+04	6.135E+04	3.655E+04	2.709E+04
L_{relax} [H]		4.895E+06	9.482E+05	1.664E+05	2.838E+05	7.813E+04	8.106E+04

EIS measurements on leaking UO_2 electrode during and after irradiation with He^{2+} beam (I11-02)

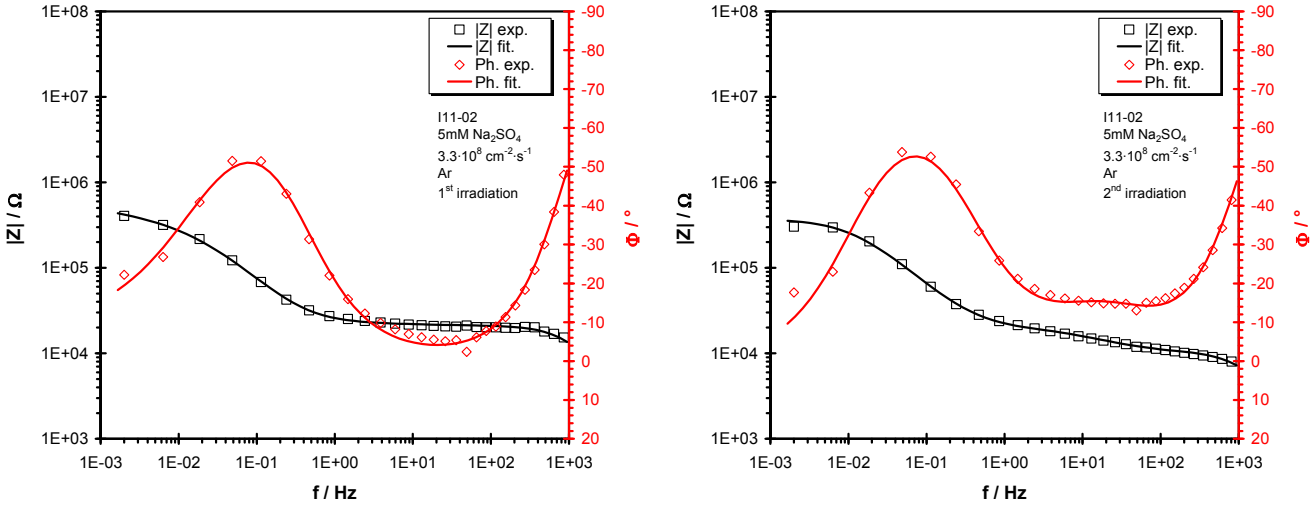

Fig. A.33.a Bode plots from EIS measurements on depleted UO_2 leaking electrode during and after irradiation with He^{2+} beam under Ar atmosphere

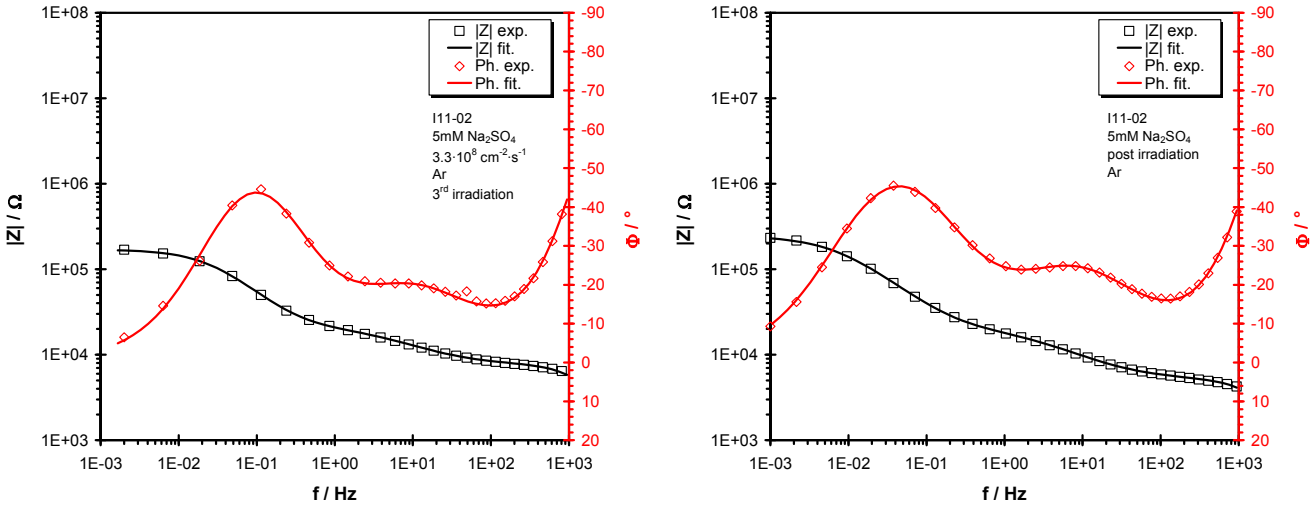

Fig. A.33.b Bode plots from EIS measurements on depleted UO_2 leaking electrode during and after irradiation with He^{2+} beam under Ar atmosphere

		Ar			
		45 MeV He^{2+} 3.3·10^8 $cm^{-2}·s^{-1}$			post irradiation
Electrode sample		I11-02 (1)	I11-02 (2)	I11-02 (3)	I11-02 (4)
Global fitting error [%]		6.7	7.5	2.8	1.8
R_{bulk} [Ω]		2.480E+04	2.121E+04	2.316E+04	2.236E+04
C_{bulk} [F]		9.282E-09	1.639E-08	1.856E-08	2.428E-08
R_{pol} [Ω]		9.203E+05	2.070E+06	3.017E+05	7.789E+05
C_{dl} [F^p]	C^0 [F]	1.824E-05	2.171E-05	2.512E-05	3.691E-05
	p	0.878	0.845	0.860	0.793
$R_{pol, steel}$ [Ω]		1.704E+07	4.415E+05	3.515E+05	3.556E+05
$C_{dl, steel}$ [F^p]	C^0 [F]	4.409E-06	1.232E-06	2.899E-06	5.164E-06
	p	0.279	0.725	0.702	0.682
$R_{cr, pores}$ [Ω]		1.052E+05	1.967E+04	1.139E+04	6.675E+03

Note: For fitting of the experimental data a fitting program created and developed by Dr. Detlef Wegen from ITU was used

A.5. Electrode properties and reaction parameters from EIS data

Glove box experiments

EIS on natural UO_2 under Ar and Ar/H_2 atmosphere at open circuit potential (sample name UO_2 – X)

	Ar		Ar/H_2 6%	
Relative time [h]	46	282	114	2192
Electrode resistivity [KΩ·cm]	29.88	31.17	33.04	31.25
Electrode relative capacitance [$F \cdot cm^{-2}$]	11.30	11.75	12.74	11.58
Double layer thickness [nm]	0.211	0.249	0.222	0.274
Oxygen concentration at interface [$\cdot 10^{-6}$ M]	4.342	3.682	2.756	3.116
Nernst diffusion layer thickness [mm]	8.322	7.422	8.689	9.675
Corrosion rate [$\cdot 10^{-9}$ moles$\cdot cm^{-2} \cdot d^{-1}$]	2.497	2.230	1.322	1.298

EIS on natural UO_2 under Ar/H_2 atmosphere during polarisation (sample name UO_2 – X)

	Ar/H_2 6%							
E_{pol} [mV_{SHE}]	431.6	481.6	529.8	556.4	572.6	585.8	603.2	617.4
lg $1/(R_{pol} \cdot A_{el})$	-6.704	-5.951	-4.746	-4.204	-3.855	-3.631	-3.578	-3.517
Slope [mV/decade]			**49.62**					
Electrode resistivity [KΩ·cm]	32.17	36.33	32.94	30.51	31.17	30.02	29.94	30.90
Electrode relative capacitance [$F \cdot cm^{-2}$]	12.10	12.07	11.61	11.62	11.95	11.92	11.63	11.40
Double layer thickness [nm]	0.206	0.742	0.728	0.512	0.453	0.437	0.391	0.401
Corrosion rate [$\cdot 10^{-9}$ moles$\cdot cm^{-2} \cdot d^{-1}$]	1.675	9.496	152.1	529.6	1184	1982	2240	2577

EIS on 1% ^{233}U doped UO_2 under Ar and Ar/H_2 atmosphere at open circuit potential (sample U – V)

	Ar		Ar/H_2 6%	
Relative time [h]	102	360	138	272
Electrode resistivity [KΩ·cm]	361.7	372.4	496.0	425.2
Electrode relative capacitance [$F \cdot cm^{-2}$]	18.71	41.86	45.15	44.77
Double layer thickness [nm]	0.279	0.290	0.238	0.184
Oxygen concentration at interface [$\cdot 10^{-6}$ M]	2.106	3.583	5.663	3.689
Nernst diffusion layer thickness [mm]	1.080	0.940	0.993	1.520
Corrosion rate [$\cdot 10^{-9}$ moles$\cdot cm^{-2} \cdot d^{-1}$]	1.811	2.295	1.490	1.021

EIS on 1% ^{233}U doped UO_2 under Ar/H_2 atmosphere during polarisation (sample name U – V)

	Ar/H_2 6%								
E_{pol} [mV_{SHE}]	333.8	432.9	482.9	515.9	536.0	558.2	569.8	581.7	595.9
lg $1/(R_{pol} \cdot A_{el})$	-6.644	-6.222	-5.659	-5.080	-4.675	-4.565	-4.505	-4.457	-4.412
Slope [mV/decade]			**54.14**						
Electrode resistivity [KΩ·cm]	424.7	433.1	432.0	416.6	401.4	387.8	398.8	388.1	375.0
Electrode relative capacitance [$F \cdot cm^{-2}$]	42.35	50.61	46.01	57.40	49.51	45.01	43.40	45.80	44.89
Double layer thickness [nm]	0.183	0.157	0.389	0.509	0.550	0.697	0.679	0.581	0.974
Corrosion rate [$\cdot 10^{-9}$ moles$\cdot cm^{-2} \cdot d^{-1}$]	2.075	5.488	20.05	76.03	193.2	249.4	285.8	319.8	354.0

EIS on 10% ^{233}U doped UO_2 under Ar and Ar/H_2 atmosphere at open circuit potential (sample U – I)

	Ar		Ar/H_2 6%	
Relative time [h]	122	453	162	1639
Electrode resistivity [KΩ·cm]	0.234	0.161	0.270	0.089
Electrode relative capacitance [$F \cdot cm^{-2}$]	12.50	17.88	9.13	29.79
Double layer thickness [nm]	0.13	0.13	0.09	0.08
Oxygen concentration at interface [$\cdot 10^{-6}$ M]	23.75	24.68	19.31	33.15
Nernst diffusion layer thickness [mm]	0.921	0.905	0.963	0.766
Corrosion rate [$\cdot 10^{-9}$ moles$\cdot cm^{-2} \cdot d^{-1}$]	4.771	4.104	3.638	3.443

EIS on 10% ^{233}U doped UO_2 under Ar/H_2 atmosphere during polarisation (sample name U – V)

	Ar/H_2 6%						
E_{pol} [mV_{SHE}]	333.0	433.0	483.0	533.0	583.0	632.8	680.9
lg $1/(R_{pol} \cdot A_{el})$	-6.330	-6.295	-6.145	-5.488	-4.453	-3.598	-2.618
Slope [mV/decade]				**52.09**			

Electrode resistivity [KΩ·cm]	0.088	0.090	0.093	0.093	0.093	0.098	0.098
Electrode relative capacitance [$F \cdot cm^{-2}$]	28.95	26.38	45.57	34.76	54.60	51.62	331.2
Double layer thickness [nm]	0.08	0.08	0.11	0.10	0.09	0.07	0.04
Corrosion rate [$\cdot 10^{-9}$ moles$\cdot cm^{-2} \cdot d^{-1}$]	10.91	11.82	16.69	75.76	821.5	5888	56183

Cyclotron experiments

EIS measurements on depleted UO_2 during anodic polarisation and irradiation with 45 MeV He^{2+} beam (flux $3.3 \cdot 10^7 cm^{-2} \cdot s^{-1}$) under Ar atmosphere (sample G11-04)

	Ar					
E_{pol} [mV_{SHE}]	528.7	552.5	568.4	577.5	585.0	591.0
lg $1/(R_{pol} \cdot A_{el})$	-4.595	-3.974	-3.688	-3.510	-3.363	-3.251
Slope [mV/decade]			**51.72**			

Electrode resistivity [KΩ·cm]	157.9	155.1	153.3	151.9	151.6	151.4
Electrode relative capacitance [$F \cdot cm^{-2}$]	28.12	27.44	27.57	27.58	27.48	27.51
Double layer thickness [nm]	0.177	0.118	0.087	0.073	0.063	0.058
Corrosion rate [$\cdot 10^{-9}$ moles$\cdot cm^{-2} \cdot d^{-1}$]	195.4	817.2	1578	2379	3339	4314

EIS measurements on depleted UO_2 during anodic polarisation without irradiation with He^{2+} beam under Ar/H_2 atmosphere (sample G11-15)

	Ar/H_2								
E_{pol} [mV_{SHE}]	292.8	392.6	462.5	531.6	565.3	580.6	599.0	612.7	622.3
lg $1/(R_{pol} \cdot A_{el})$	-6.457	-6.453	-6.390	-5.959	-4.790	-3.854	-3.563	-3.401	-3.242
Slope [mV/decade]						**69.21**			

Electrode resistivity [KΩ·cm]	146.9	142.5	138.8	136.0	131.9	128.7	127.7	126.4	125.1
Electrode relative capacitance [$F \cdot cm^{-2}$]	32.95	33.25	33.71	33.90	34.31	34.58	34.58	34.46	34.23
Double layer thickness [nm]	0.198	0.196	0.221	0.197	0.135	0.095	0.105	0.098	0.105
Corrosion rate [$\cdot 10^{-9}$ moles$\cdot cm^{-2} \cdot d^{-1}$]	3.857	3.888	4.499	12.14	179.0	1545	3019	4383	6321

EIS measurements on depleted UO_2 during anodic polarisation and irradiation with 45MeV He^{2+} beam (flux $3.3 \cdot 10^7 cm^{-2} \cdot s^{-1}$) under Ar/H_2 atmosphere (sample G11-16)

	Ar/H_2					
E_{pol} [mV_{SHE}]	528.9	551.3	571.0	585.5	596.5	605.0
lg $1/(R_{pol} \cdot A_{el})$	-4.939	-4.048	-3.818	-3.475	-3.359	-3.187
Slope [mV/decade]		**60.44**				

Electrode resistivity [KΩ·cm]	174.7	165.0	158.3	153.9	152.9	152.9
Electrode relative capacitance [$F \cdot cm^{-2}$]	28.24	29.09	29.60	30.03	30.13	30.11
Double layer thickness [nm]	0.256	0.194	0.148	0.203	0.174	0.197
Corrosion rate [$\cdot 10^{-9}$ moles$\cdot cm^{-2} \cdot d^{-1}$]	0.124	0.964	1.639	3.608	4.711	7.002

A.6. Solution analysis results and calculations

Glove box experiments

Solution analysis from experiments on natural UO_2 under Ar and Ar/H_2 atmosphere (sample electrode UO_2 – X)

Nr. Crt.	Sample name	Observations	t_{rel}	$[U]_{total}$	m_{sample}	$m_{total, sol}$	$m_{U, total}$	r_{corr}
-	-	-	[h]	[M]	[g]	[g]	[g]	[moles·cm^{-2}·s^{-1}]
1	EC00201	Ar	0.00	2.384E-06	3.523	100.0	5.673E-05	
2	EC00202		1.92	2.406E-06	4.387	96.48	5.723E-05	2.076E-07
3	EC00203		144.87	2.540E-06	3.440	92.09	6.018E-05	1.884E-08
4	EC00204		475.75	2.771E-06	4.125	88.65	6.506E-05	1.383E-08
5	EC00205		835.88	2.997E-06	3.203	84.52	6.960E-05	1.216E-08
					Theoretically left:	81.32	(practically ~80g)	
6	EC00206	Ar/H_2 6%	0.00	3.791E-11	3.804	120.0	1.083E-09	
7	EC00207		95.25	7.985E-08	4.352	116.2	2.198E-06	1.822E-08
8	EC01001		2181.00	2.959E-07	3.490	111.8	7.981E-06	3.279E-09
9	EC01010	after polarisation		1.154E-05	3.595	80.58		
					Theoretically left:	76.98	(practically ~80g)	
		E_{pol} (mV_{SHE})						
10	EC01002	431.63	19.88	3.015E-07	3.555	108.4	8.121E-06	5.541E-09
11	EC01003	481.59	29.20	3.301E-07	3.573	104.8	8.836E-06	2.312E-08
12	EC01004	529.77	36.07	3.786E-07	3.588	101.2	1.000E-05	4.432E-08
13	EC01005	556.40	42.95	1.336E-06	3.601	97.64	3.230E-05	4.473E-07
14	EC01006	572.58	49.82	2.276E-06	3.701	94.04	5.333E-05	7.190E-07
15	EC01007	585.82	56.70	5.645E-06	2.575	90.34	1.274E-04	1.663E-06
16	EC01008	603.16	63.57	8.994E-06	3.626	87.76	1.960E-04	2.337E-06
17	EC01009	617.40	70.45	1.308E-05	3.559	84.13	2.782E-04	3.030E-06

Nr. Crt.	Sample name	Observations	t_{rel}	[Fe]	[Si]	[Ag]	[Au]
-	-	-	[h]	[M]	[M]	[M]	[M]
1	EC00201	Ar	0.00	1.298E-05	2.773E-05	1.242E-07	<
2	EC00202		1.92	8.757E-06		1.303E-07	<
3	EC00203		144.87	9.981E-06		1.306E-07	<
4	EC00204		475.75	1.840E-05		1.646E-07	3.619E-10
5	EC00205		835.88	1.765E-05	9.029E-05	1.637E-07	<
6	EC00206	Ar/H_2 6%	0.00	1.043E-05	2.026E-05	1.688E-09	<
7	EC00207		95.25	5.251E-06		1.211E-08	<
8	EC01001		2181.00	2.892E-05	8.253E-05	9.137E-08	<
9	EC01010	after polarisation		2.699E-05	9.155E-05	3.424E-08	<
		E_{pol} (mV_{SHE})					
10	EC01002	431.63	19.88	2.848E-05		8.997E-08	<
11	EC01003	481.59	29.20	2.821E-05		8.854E-08	<
12	EC01004	529.77	36.07	2.748E-05		7.822E-08	<
13	EC01005	556.40	42.95	3.224E-05		7.250E-08	<
14	EC01006	572.58	49.82	4.124E-05		5.654E-08	<
15	EC01007	585.82	56.70	2.802E-05		5.210E-08	<
16	EC01008	603.16	63.57	2.949E-05		4.475E-08	<
17	EC01009	617.40	70.45	2.709E-05		4.235E-08	<

Solution analysis from experiments on 1% ^{233}U doped UO_2 under Ar and Ar/H_2 atmosphere (sample electrode U – V)

Nr. Crt.	Sample name	Observations	t_{rel}	$[U]_{total}$	m_{sample}	$m_{total, sol}$	$m_{U, total}$	r_{corr}
-	-	-	[h]	[M]	[g]	[g]	[g]	[moles·cm^{-2}·s^{-1}]
1	EC00301	Ar	0.00	2.889E-08	3.350	100.0	6.875E-07	
2	EC00302		20.65	3.168E-08	4.107	96.65	7.517E-07	7.325E-09
3	EC00303		144.88	4.196E-08	3.533	92.54	9.781E-07	4.721E-09
4	EC00304		475.80	7.111E-08	3.593	89.01	1.596E-06	4.492E-09
5	EC00305		835.95	7.349E-08	3.337	85.42	1.644E-06	2.693E-09
					Theoretically left:	82.08	(practically ~80g)	
6	EC00306	Ar/H_2 6%	0.00	3.631E-10	4.294	120.0	1.037E-08	
7	EC00307		95.42	1.231E-08	4.062	115.7	3.395E-07	8.116E-09
8	EC00601		270.08	1.283E-08	3.385	111.6	3.531E-07	2.986E-09
9	EC00308		2275.25	1.289E-08	3.353	108.3	3.547E-07	3.561E-10
					Theoretically left:	80.54	(practically ~76g)	
		E_{pol} (mV_{SHE})						
10	EC00602	333.78	8.12	1.295E-08	3.325	104.9	3.562E-07	9.298E-10
11	EC00603	432.90	15.17	1.325E-08	3.341	101.6	3.634E-07	1.606E-09
12	EC00604	482.94	23.32	1.428E-08	3.269	98.24	3.876E-07	3.483E-09
13	EC00605	515.90	32.58	3.115E-08	3.275	94.97	7.688E-07	3.003E-08
14	EC00606	536.00	41.63	9.167E-08	2.451	91.70	2.090E-06	9.815E-08
15	EC00607	558.24	51.15	1.705E-07	1.065	89.25	3.763E-06	1.569E-07
16	EC00608	569.79	60.80	2.398E-07	0.467	88.18	5.219E-06	1.883E-07
17	EC00609	581.67	69.88	3.531E-07	4.008	87.71	7.583E-06	2.434E-07
18	EC00610	595.91	79.53	7.763E-07	3.165	83.71	1.601E-05	4.634E-07

Nr. Crt.	Sample name	Observations	t_{rel}	[Fe]	[Si]	[Ag]	[Au]
-	-	-	[h]	[M]	[M]	[M]	[M]
1	EC00301	Ar	0.00	2.737E-05	7.906E-05	1.060E-07	1.436E-09
2	EC00302		20.65	3.912E-05		1.249E-07	1.273E-09
3	EC00303		144.88	8.066E-05		1.640E-07	1.244E-09
4	EC00304		475.80	6.998E-05		9.392E-08	8.140E-10
5	EC00305		835.95	1.071E-04	2.491E-04	1.174E-07	5.709E-10
6	EC00306	Ar/H_2 6%	0.00	1.795E-06	1.350E-05	8.001E-11	<
7	EC00307		95.42	7.315E-06		8.865E-09	<
8	EC00601		270.08	1.773E-05		8.611E-09	<
9	EC00308		2275.25	1.264E-05	2.660E-05	1.005E-08	<
		E_{pol} (mV_{SHE})					
10	EC00602	333.78	8.12	1.693E-05		7.611E-09	<
11	EC00603	432.90	15.17	1.961E-05		7.861E-09	<
12	EC00604	482.94	23.32	1.751E-05		8.495E-09	<
13	EC00605	515.90	32.58	1.392E-05		7.944E-09	<
14	EC00606	536.00	41.63	2.572E-05		9.245E-09	<
15	EC00607	558.24	51.15	1.950E-05		1.546E-08	<
16	EC00608	569.79	60.80	1.584E-04		2.149E-08	<
17	EC00609	581.67	69.88	1.660E-05		1.373E-08	<
18	EC00610	595.91	79.53	1.951E-05		6.489E-08	3.486E-10

Solution analysis from experiments on 10% ^{233}U doped UO_2 under Ar and Ar/H_2 atmosphere (sample electrode U – I)

Nr. Crt.	Sample name	Observations	t_{rel}	$[U]_{total}$	m_{sample}	$m_{total, sol}$	$m_{U, total}$	r_{corr}
-	-	-	[h]	[M]	[g]	[g]	[g]	[moles·cm^{-2}·s^{-1}]
1	EC00401	Ar	0.00	1.498E-08	3.278	100.0	3.566E-07	
2	EC00402		21.60	1.677E-08	3.576	96.72	3.978E-07	2.770E-09
3	EC00403		144.87	2.226E-08	3.519	93.15	5.195E-07	1.631E-09
4	EC00404		475.87	2.381E-08	3.641	89.63	5.524E-07	5.971E-10
5	EC00405		836.05	2.894E-08	3.240	85.99	6.575E-07	5.222E-10
					Theoretically left:	82.75	(practically ~80g)	
6	EC00406	Ar/H_2 6%	0.00	5.607E-11	4.304	120.0	1.601E-09	
7	EC00407		95.58	2.615E-10	4.049	115.7	7.257E-09	8.586E-11
8	EC00408		432.90	9.057E-10	3.216	111.6	2.438E-08	7.633E-11
9	EC00409		1626.43	2.794E-09	3.108	108.4	7.311E-08	6.379E-11
10	EC00510	after polarisation	1796.67	1.449E-04	3.316	76.43	3.922E-03	3.580E-05
					Theoretically left:	73.12	(practically ~68g)	
		E_{pol} (mV_{SHE})						
11	EC00501	333.00	7.65	4.824E-09	3.375	105.3	1.240E-07	9.652E-09
12	EC00502	433.00	15.13	6.934E-09	3.256	101.9	1.752E-07	9.788E-09
13	EC00503	483.00	23.28	9.857E-09	3.173	98.69	2.438E-07	1.064E-08
14	EC00504	533.00	30.17	1.271E-08	3.259	95.52	3.087E-07	1.133E-08
15	EC00505	582.99	37.07	4.663E-08	3.268	92.26	1.053E-06	3.837E-08
16	EC00506	632.82	43.93	3.701E-07	2.555	88.99	7.905E-06	2.586E-07
17	EC00507	680.94	51.10	1.007E-05	3.269	86.44	2.076E-04	5.891E-06

Nr. Crt.	Sample name	Observations	t_{rel}	[Fe]	[Si]	[Ag]	[Au]
-	-	-	[h]	[M]	[M]	[M]	[M]
1	EC00401	Ar	0.00	5.413E-06	2.662E-05	3.305E-08	<
2	EC00402		21.60	9.710E-06		3.700E-08	<
3	EC00403		144.87	9.750E-06		3.690E-08	1.120E-09
4	EC00404		475.87	7.031E-06		3.883E-08	1.749E-09
5	EC00405		836.05	1.386E-05	6.821E-05	4.577E-08	1.201E-09
6	EC00406	Ar/H_2 6%	0.00	7.147E-07	1.492E-05	8.789E-11	<
7	EC00407		95.58	1.332E-06		5.626E-09	<
8	EC00408		432.90	8.547E-06		3.474E-09	<
9	EC00409		1626.43	2.380E-05	1.829E-04	4.174E-08	1.032E-09
10	EC00510	after polarisation	1796.67	2.125E-05		1.567E-08	<
		E_{pol} (mV_{SHE})					
11	EC00501	333.00	7.65	7.126E-05		4.463E-08	9.321E-10
12	EC00502	433.00	15.13	2.716E-05		4.376E-08	9.900E-10
13	EC00503	483.00	23.28	4.045E-05		4.759E-08	1.321E-09
14	EC00504	533.00	30.17	2.454E-05		4.578E-08	1.200E-09
15	EC00505	582.99	37.07	2.464E-05		4.261E-08	1.026E-09
16	EC00506	632.82	43.93	2.344E-05		4.014E-08	<
17	EC00507	680.94	51.10	2.491E-05		3.749E-08	<

Cyclotron experiments

Solution analysis from experiments on depleted UO_2 during irradiation with 45MeV He^{2+} beam (flux $3.3 \cdot 10^7 cm^{-2} \cdot s^{-1}$) under Ar atmosphere (sample electrode G11-04)

Nr. Crt.	Sample name	Observations	t_{rel}	$[U]_{total,ICP-MS}$	$[U]_{total,ICP-OES}$	$V_{solution}$	r_{corr}
-	-	-	[h]	[M]	[M]	[mL]	$[moles \cdot cm^{-2} \cdot s^{-1}]$
1	G11-04-D5	dissolution without beam	0.915	2.097E-08		20	3.890E-08
2	G11-04-D6		1.061	1.672E-08		20	2.675E-08
3	G11-04-I7	dissolution during irradiation	0.797	2.345E-08		20	4.993E-08
4	G11-04-I9		0.894	3.252E-08		20	6.178E-08
5	G11-04-D23	post irradiation	9.696	6.471E-08		20	1.133E-08
		E_{pol} (mV_{SHE})					
6	G11-04-I11	529.88	1.151	1.450E-07	3.151E-07	20	4.649E-07
7	G11-04-I13	554.19	0.724		3.529E-07	20	8.277E-07
8	G11-04-I15	570.75	0.716		5.126E-07	20	1.215E-06
9	G11-04-I17	580.44	0.813		7.941E-07	20	1.658E-06
10	G11-04-I19	587.74	0.726		1.172E-06	20	2.743E-06
11	G11-04-I21	593.62	0.721		1.672E-06	20	3.940E-06

Solution analysis from experiments on depleted UO_2 during irradiation with 45MeV He^{2+} beam (flux $3.3 \cdot 10^7 cm^{-2} \cdot s^{-1}$) under Ar/H_2 atmosphere (sample electrode G11-16)

Nr. Crt.	Sample name	Observations	t_{rel}	$[U]_{total,ICP-MS}$	$[U]_{total,ICP-OES}$	$V_{solution}$	r_{corr}
-	-	-	[h]	[M]	[M]	[mL]	$[moles \cdot cm^{-2} \cdot s^{-1}]$
1	G11-16-D1	dissolution without beam	2.035	7.605E-09		20	6.343E-09
2	G11-16-D2		0.294	4.874E-09		20	2.810E-08
3	G11-16-D3		0.296	5.000E-09		20	2.864E-08
4	G11-16-D4		1.215	5.000E-09		20	6.986E-09
5	G11-16-I5	dissolution during irradiation	1.348	1.088E-08		20	1.370E-08
6	G11-16-I7		1.003	1.223E-08		20	2.071E-08
7	G11-16-D21	post irradiation	11.260	5.378E-08		20	8.108E-09
		E_{pol} (mV_{SHE})					
8	G11-16-I9	528.90	1.004	9.790E-08	2.899E-07	20	4.904E-07
9	G11-16-I11	551.26	0.781		3.866E-07	20	8.401E-07
10	G11-16-I13	570.98	0.657		4.706E-07	20	1.216E-06
11	G11-16-I15	585.51	0.599		6.723E-07	20	1.906E-06
12	G11-16-I17	596.53	0.635		9.118E-07	20	2.437E-06
13	G11-16-I19	604.96	0.687		1.126E-06	20	2.782E-06

A.7. Oxygen sensor calibration

Factory calibration

Factory Calibration data are provided by manufacturer (at 1 atm and 1024 ms integration time)

p = 1 [atm]

Int. time = 1024 [ms]

	O_2 conc. [%]	T[K]			
		288.15	293.15	298.15	303.15
Signal intensity, I	0.0	736.0	711.0	684.0	656.0
	0.2	660.0	617.0	588.0	560.0
	0.4	570.0	544.0	513.0	489.0
	0.6	512.0	489.0	456.0	437.0
	0.8	466.0	447.0	420.0	398.0
	1.0	430.0	412.0	383.0	365.0

Due to saturation of spectrophotometer while using 1024 ms integration time a lower integration time was selected, 512 ms. At this integration time the calibration data are the following

Int. time = 512 [ms]

	O_2 conc. [%]	T[K]			
		288.15	293.15	298.15	303.15
Signal intensity, I	0.0	368.0	355.5	342.0	328.0
	0.2	330.0	308.5	294.0	280.0
	0.4	285.0	272.0	256.5	244.5
	0.6	256.0	244.5	228.0	218.5
	0.8	233.0	223.5	210.0	199.0
	1.0	215.0	206.0	191.5	182.5

The ratio I_0/I is calculated using the signal intensity at 0% oxygen concentration:

	O_2 conc. [%]	T[K]			
		288.15	293.15	298.15	303.15
Signal intensity ratio, I_0/I	0.0	1.000	1.000	1.000	1.000
	0.2	1.115	1.152	1.163	1.171
	0.4	1.291	1.307	1.333	1.342
	0.6	1.438	1.454	1.500	1.501
	0.8	1.579	1.591	1.629	1.648
	1.0	1.712	1.726	1.786	1.797

The calibration curves as I_0/I vs. oxygen concentration (in percentage) are drawn at different temperatures. A second order polynomial is fitted at each temperature. The calibration curves are presented in figure A.34.

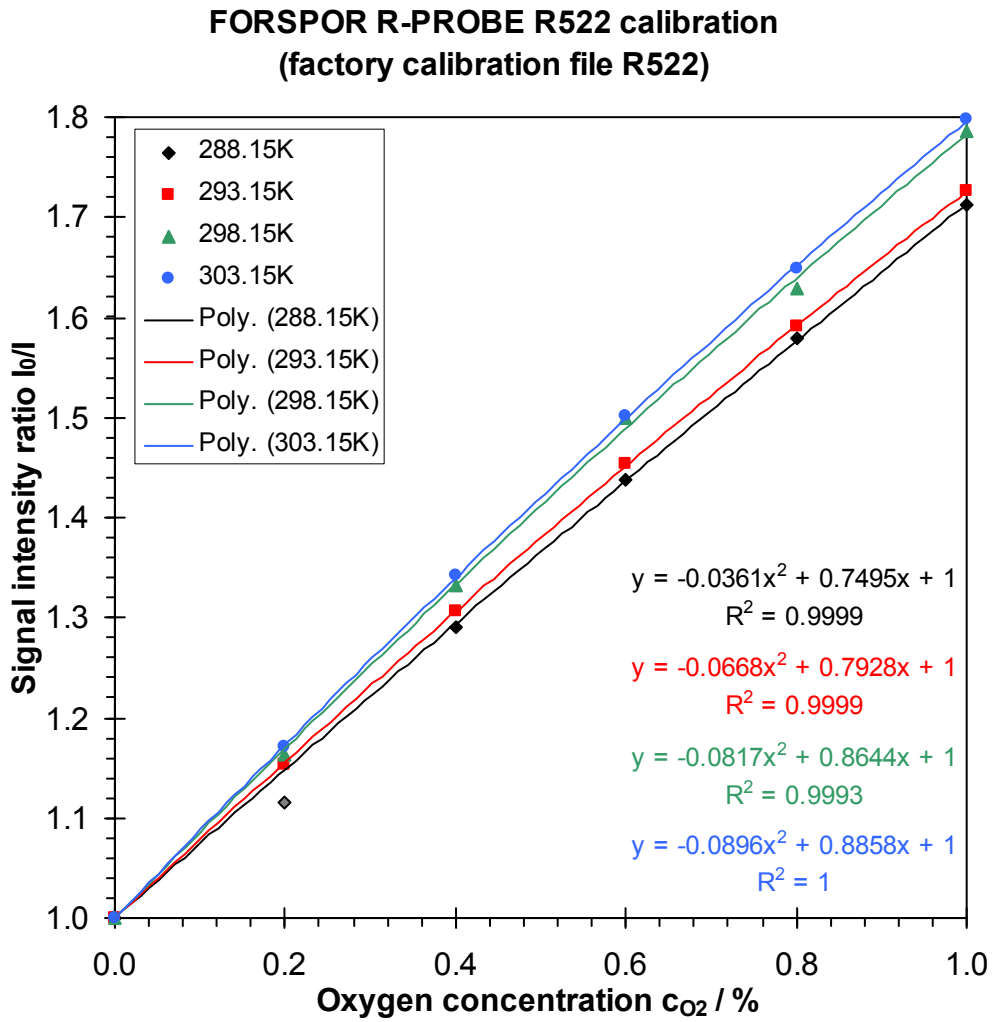

Fig. A.34 Factory calibration curves for oxygen concentration

The dependency between I_0/I and oxygen concentration is given by the equation:

$$\frac{I_0}{I} = 1 + K_1 \cdot c_{O_2} + K_2 \cdot c_{O_2}^2 \qquad \text{(A.7.1)}$$

I_0 and also the two constants K_1 and K_2 are temperature dependent:

$$I_0 = a_0 + b_0 \cdot T + c_0 \cdot T^2 \qquad \text{(A.7.2)}$$

$$K_1(T) = a_1 + b_1 \cdot T + c_1 \cdot T^2 \qquad \text{(A.7.3)}$$

$$K_2(T) = a_2 + b_2 \cdot T + c_2 \cdot T^2 \qquad \text{(A.7.4)}$$

From the factory calibration the following data are determined:

T[K]	288.15	293.15	298.15	303.15
K_1 [K^{-1}]	0.7495	0.7928	0.8644	0.8858
K_2 [K^{-2}]	-0.0361	-0.0668	-0.0817	-0.0896
R^2	0.9999	0.9999	0.9993	1.0000

By plotting this data the following curves resulted:

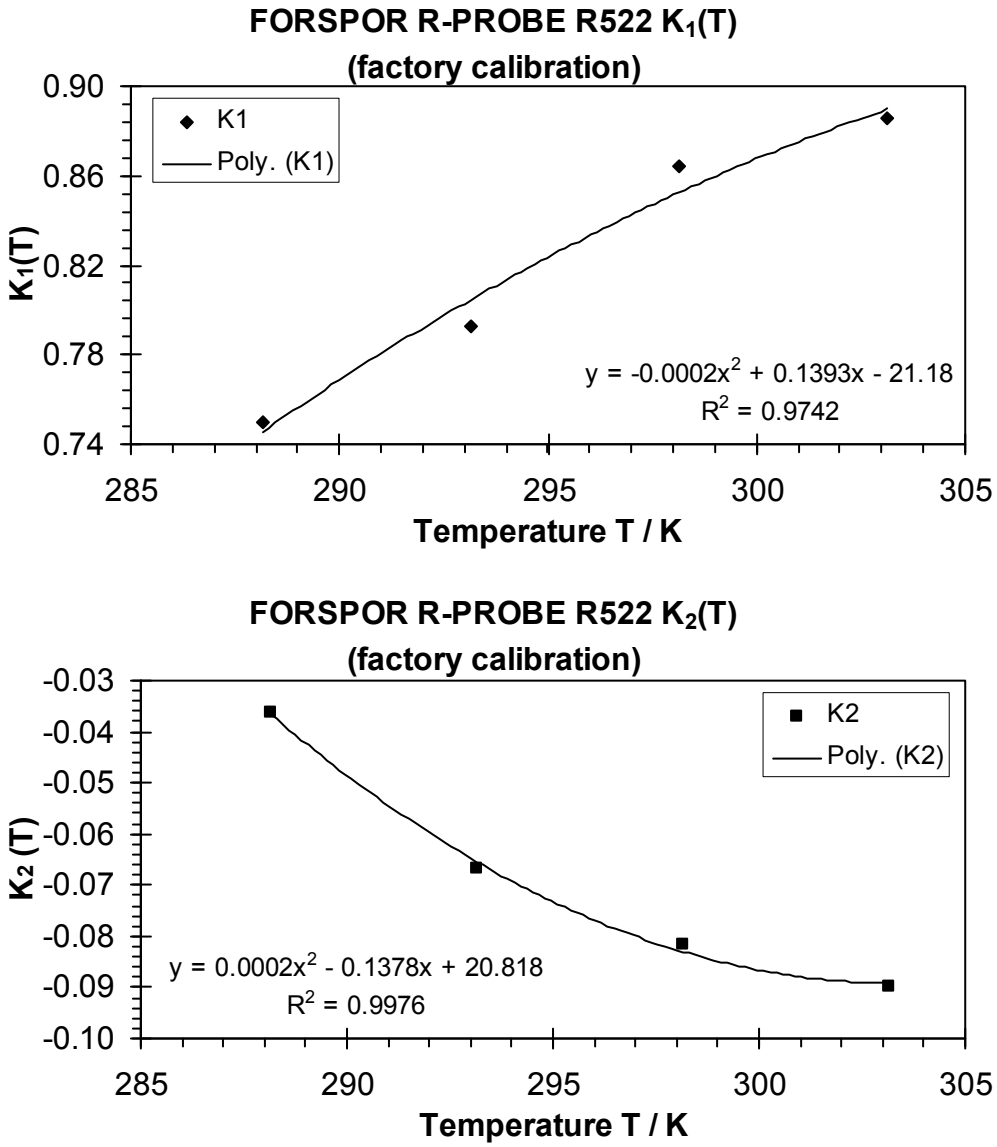

Fig. A.35 Temperature dependant coefficients determined from the factory calibration data

From fitting of the curves in figure A.35 the coefficients for the equations (A.7.3) and (A.7.4) were determined:

j	a	b	c	R^2
1 (K_1)	***-21.1799***	***0.1393***	***-0.0002***	0.9742
2 (K_2)	***20.8179***	***-0.1378***	***0.0002***	0.9976

By using of these coefficients in the respective equations, the constants K_1 and K_2 were calculated:

T[K]	288.15	293.15	298.15	303.15
K_1 [K^{-1}]	0.746	0.805	0.853	0.890
K_2 [K^{-2}]	-0.037	-0.065	-0.083	-0.089
err K_1	-0.52	1.49	-1.36	0.44
err K_2	1.24	-2.01	1.65	-0.50

With these determined constants K_1 and K_2 the I_0/I is calculated at the given oxygen concentrations:

	O_2 conc. [%]	T[K]			
		288.15	293.15	298.15	303.15
Signal intensity ratio, Io/I	0.0	1.000	1.000	1.000	1.000
	0.2	***1.148***	***1.158***	***1.167***	***1.174***
	0.4	***1.292***	***1.311***	***1.328***	***1.342***
	0.6	***1.434***	***1.459***	***1.482***	***1.502***
	0.8	***1.573***	***1.602***	***1.629***	***1.655***
	1.0	***1.709***	***1.739***	***1.770***	***1.801***

The error between the values of I_0/I determined from the calibration data and by calculation is very low as shown below:

	O_2 conc. [%]	T[K]			
		288.15	293.15	298.15	303.15
Signal intensity ratio error, err I_0/I	0.0	0.00	0.00	0.00	0.00
	0.2	2.91	0.52	0.34	0.25
	0.4	0.09	0.33	-0.42	0.01
	0.6	-0.23	0.36	-1.22	0.04
	0.8	-0.40	0.70	0.03	0.39
	1.0	-0.15	0.78	-0.91	0.18

The temperature dependence of I_0 is also determined from the calibration data:

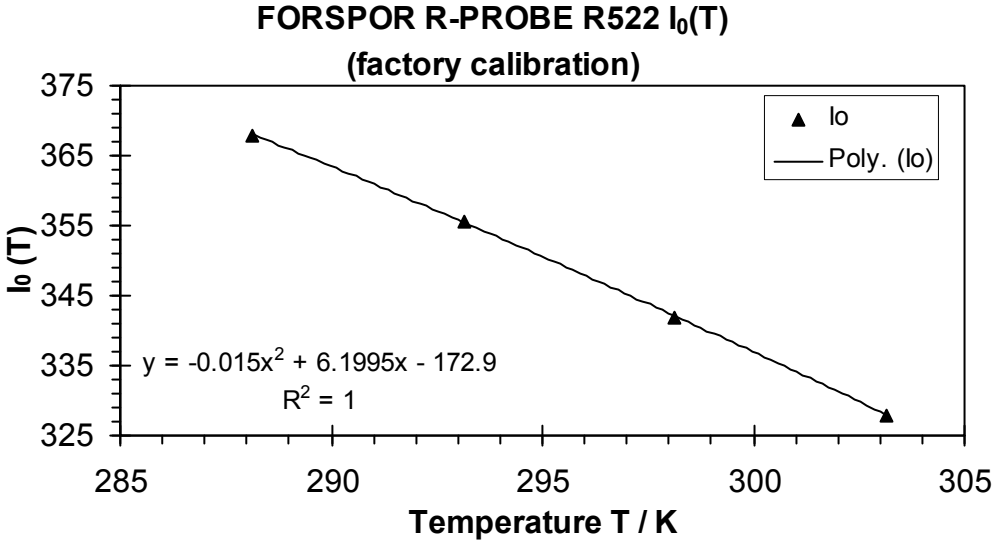

Fig. A.36 Factory calibration curve for temperature dependence of I_0

The coefficients from the equation (A.7.2) are determined:

j	a	b	c	R^2
0 (I_0)	***-172.9046***	***6.1995***	***-0.0150***	1.0000

The error between the values of I_0 from the calibration data and from calculations is also very low:

T[K]	288.15	293.15	298.15	303.15
I_0 [cnts]	368.0	355.4	342.1	328.0
err I_0	0.01	-0.02	0.02	-0.01

Laboratory calibration

Since the actual experimental conditions differ from the conditions during sensor calibration the adjustment of the calibration curves is necessary. In order to calibrate the oxygen sensor to the new environmental conditions only one measurement at a known oxygen concentration is needed.

For this matter a WTW CellOx 325 electrochemical oxygen sensor was used. Although very accurate the main problem with this type of sensor is that it can only be calibrated in water saturated air. The atmosphere inside the glove box is very different from the normal atmospheric one. As a consequence the electrochemical sensor can not be calibrated inside the glove box. This means that the CellOx 325 oxygen sensor can be used inside the glove box only a short time after the calibration.

The oxygen concentration inside an aqueous solution was measured:

$c_{O2,dis,cal}$ =	**30**	[µg/L]
(measured with WTW CellOx 325)		
t =	**23.1**	[°C]
ΔP_{Lab} =	**-0.5**	[mbar]
$\Delta P_{glove\ box}$ =	**-2**	[mbar]
P_{total} =	**1010.75**	[mbar]
I =	**2673**	[cnts]
Int. time =	**512**	[ms]
M_{O2} =	**32**	[g/mole]

By using of the Henry law the oxygen concentration in the gaseous phase above the solution can be determined:

$$p_{O2}^{T} = K_{H,pc,O2}^{T} \cdot \frac{c_{O_2,dis}}{M_{O_2}} \tag{A.7.5}$$

$$K_{H,pc,O_2}^{T} = K_{H,pc,O_2}^{T_0} \cdot e^{C_{O_2} \cdot \left(\frac{1}{T} - \frac{1}{T_0}\right)} \tag{A.7.6}$$

At 25°C the following parameters are known:

$K_{H,pc,O2}^{(25°C)}$ =	769.23	[atm·L/mole]
C_{O2} =	1700	[K]
T_0 =	298.15	[°C]

The following parameters were calculated for the experimental conditions mentioned above:

T =	296.25	[K]
$K_{H,pc,O2}^{(23.1°C)}$ =	48.55	[atm·L/mole]
$p_{O2,cal}^{(23.1°C)}$ =	4.55E-05	[atm]
P_{total} =	0.998	[atm]
$c_{\%,O2,g,cal}$ =	4.56E-03	[%]

Also the values of K_1 and K_2 were determined by interpolation at 23.1°C:

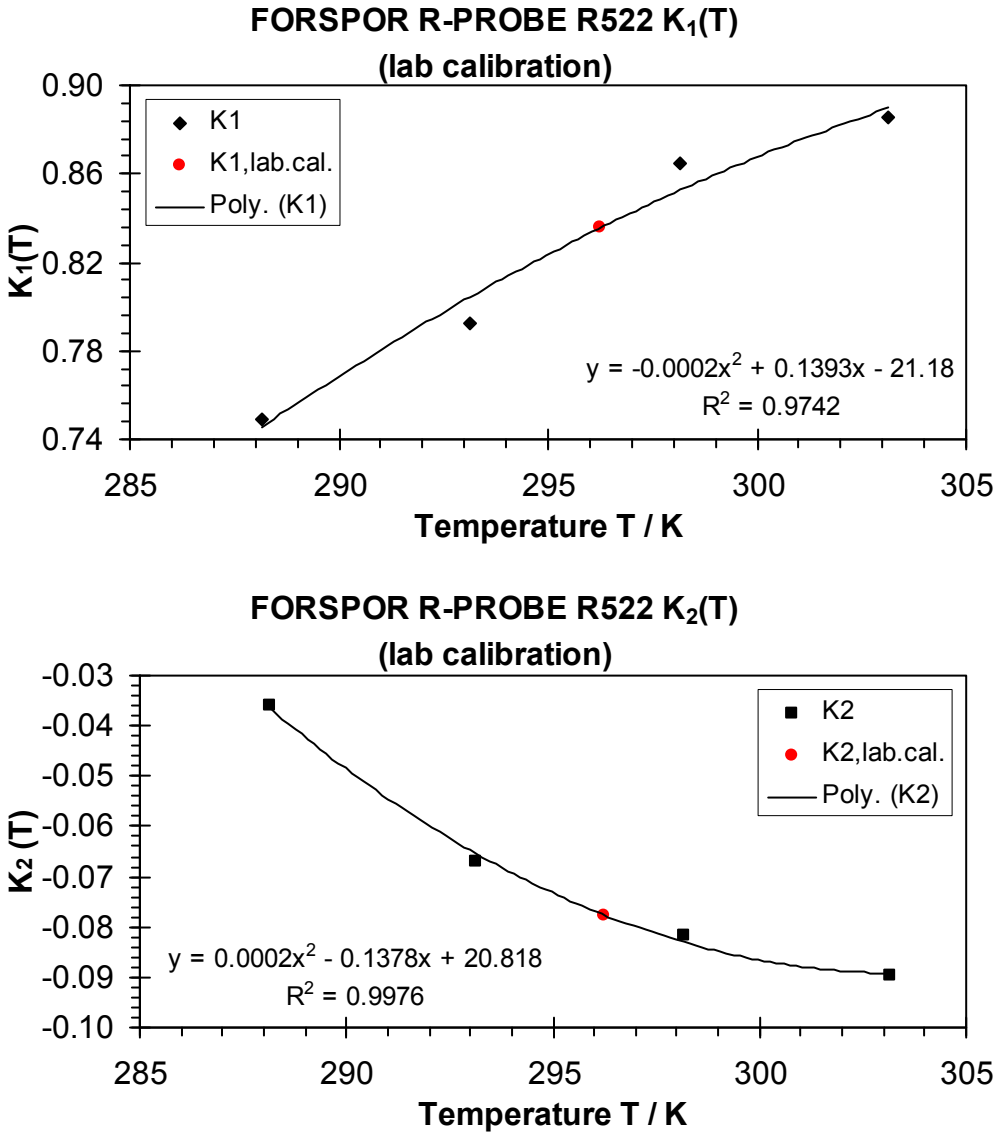

Fig. A.37 Laboratory calibration curves for temperature dependants coefficients

The following values were determined:

$K_1^{(23.1°C)}$ = 0.836 [K^{-1}]
$K_2^{(23.1°C)}$ = -0.078 [K^{-2}]

The value of I_0/I for the laboratory calibration is calculated:

$I_0/I_{lab.cal.,new}$ = 1.058

Subsequently the value of I_0 in laboratory conditions is calculated:

$I_{0,lab.cal.}^{(23.1°C)}$ = 2827.7 [cnts]

At the same temperature the calculated I_0 value from factory calibration data is:

$I_{0,fab.cal.}^{(23.1°C)}$ = 347.2 [cnts]

The ratio of I_0 values from laboratory and factory calibration data is:

$I_{0,lab.}/I_{0,fab.}$ = 8.143

The new coefficients for equation (A.7.2) in laboratory conditions are:

	a	b	c	R^2
0	***-1408.0274***	***50.4849***	***-0.1222***	1.0000

The equation (A.7.1) can be transformed in the following form:

$$\left(c_{\%,O_2,g}\right)^2 + \frac{K1}{K2}\cdot\left(c_{\%,O_2,g}\right) + \frac{1}{K_2}\cdot\left(1-\frac{I_0}{I}\right) = 0$$

The discriminant of this equation is:

$$\Delta = \left(\frac{K_1}{K_2}\right)^2 - 4\cdot\frac{1}{K_2}\cdot\left(1-\frac{I_0}{I}\right)$$

The mathematical solutions of the quadratic equation above are:

$$c_{\%,O_2,g} = -\frac{1}{2}\cdot\left(\frac{K_1}{K_2} \pm \sqrt{\Delta}\right)$$

From these two solutions one solution is selected as the one having physical meaning in the experimental environment.

A.8. List of figures

1. Introduction and objectives

2. Theoretical aspects and literature review

3. Experimental methods

4. Experimental set-up

5. Results

6. Discussions

Appendices

A.9. List of tables

2. Theoretical aspects and literature review

4. Experimental set-up

5. Results

I herewith declare that the presented doctoral thesis was written by me and that I have used no other sources and aids except those mentioned in the text. I herewith declare that I have neither requested an examination nor submitted the manuscript in this or other form as a document for obtaining a doctoral title at another faculty.

Ich erkläre hiermit, dass ich die vorgelegte Dissertation selbst verfasst und mich keiner anderen als der von mir ausdrücklich bezeichneten Quellen und Hilfen bedient habe. Ich erkläre hiermit, dass ich an keiner anderen Stelle ein Prüfungsverfahren beantragt bzw. die Dissertation in dieser oder anderer Form bereits anderweitig als Prüfungsarbeit verwendet oder einer anderen Fakultät als Dissertation vorgelegt habe.

Heidelberg, 07. November 2008

Cătălin – Gabriel Alecu

Distribution List:

This report was printed in 9 unnumbered copies.

		Copy
Prof. Dr. Th. Fanghänel	Univ. Heidelberg / ITU	1x
Mr. O. Cromboom (QM Office)	ITU	1x
Mr. J.-P. Glatz (Head of Unit)	ITU	1x
Mr. V.V. Rondinella (Action leader)	ITU	1x
Mr. D.H. Wegen (Project coordinator)	ITU	1x
Mrs. P. Jäger (Management and Support Unit)	ITU	1x
Mrs. G. Weber (Registration+Archives)	ITU	3x

European Commission– Joint Research Centre – Institute for Transuranium Elements
Title: Studies of electrochemical corrosion processes of UO_2 and mixed oxide fuels in aqueous solutions in the view of final storage of spent nuclear fuel

Author: Cătălin – Gabriel ALECU
2008 – 218 pp. – 21.0 x 29.7 cm

Abstract

Keywords: Uranium dioxide, electrochemistry, corrosion, radiolysis, leaching, irradiation, Impedance Spectroscopy, polarisation curve

The possible release of toxic and radioactive species from spent nuclear fuel in contact with water in a deep geological repository is expected to depend mainly on the rate of dissolution of the UO_2 matrix. At the depth of the repository very low oxygen concentrations are expected. Moreover, large amounts of hydrogen are expected to be generated from the corrosion of iron containing canisters and containers. In this reducing groundwater environment UO_2 has very low solubility. However, radiolysis of the ground water will produce reactive radicals and molecular products and can thereby alter the redox conditions. In this work different electrochemical techniques were used to study the corrosion behaviour of UO_2 based materials in aqueous solutions in anoxic and reducing conditions. The possible influence of hydrogen on the corrosion mechanism of UO_2 was investigated. In order to study the importance of the alpha activity level on the corrosion of the matrix, UO_2 electrode samples doped with different concentrations of short-lived alpha emitters were used. In the frame of ACTINET Network of Excellence the collaboration between Institute for Transuranium Elements (ITU) in Karlsruhe, Germany and The Centre for Studies and Research by Irradiation (CERI) in Orléans, France made possible the use of a cyclotron generated He^{2+} beam to simulate high levels of alpha activities. Impedance Spectroscopy, together with potentiostatic polarization and cyclic voltammetry measurements were used on a variety of materials, ranging from depleted UO_2 to 10% ^{233}U doped UO_2. A comparison was made between the electrochemical results and the results provided by the solution analysis and surface characterization. The good concordance of the results shows that the electrochemical techniques can be taken into consideration for the safety assessment of the final spent nuclear fuel repository.

The mission of the JRC is to provide customer-driven scientific and technical support for the conception, development, implementation and monitoring of EU policies. As a service of the European Commission, the JRC functions as a reference centre of science and technology for the Union. Close to the policy-making process, it serves the common interest of the Member States, while being independent of special interests, whether private or national.